QCD Studies at L3

Swagato Banerjee

Tata Institute of Fundamental Research

Mumbai 400 005

2002

QCD Studies at L3

Swagato Banerjee

Tata Institute of Fundamental Research
Mumbai 400 005

A Thesis submitted to the

University of Mumbai

for the degree of
Doctor of Philosophy in Physics

March, 2002

To my parents

Acknowledgement

It has been an extremely enlightening and enriching experience working with Sunanda Banerjee, supervisor of this thesis. I would like to thank him for his forbearance and encouragement and for teaching me the different aspects of the subject with lots of patience.

I thank all the members of the Department of High Energy Physics of Tata Institute of Fundamental Research (TIFR) for providing various facilities and support, and ideal ambiance for research. In particular, I would like to thank B.S. Acharya, T. Aziz, Sudeshna Banerjee, B.M. Bellara, P.V. Deshpande, S.T. Divekar, S.N. Ganguli, A. Gurtu, M.R. Krishnaswamy, K. Mazumdar, M. Maity, N.K. Mondal, V.S. Narasimham, P.M. Pathare, K. Sudhakar and S.C. Tonwar.

Asesh Dutta, Dilip Ghosh, S. Gupta, Krishnendu Mukherjee, Sreerup Ray Chaudhuri, D.P. Roy, Sourov Roy, Gavin Salam and K. Sridhar provided valuable theoretical insight on various occasions. My heartfelt thanks to them.

I thank the European Organisation for Nuclear Research (CERN) for its kind hospitality and all the members of the Large Electron Positron (LEP) accelerator group for successful operation over the last decade.

The members of the L3 collaboration and the LEP QCD Working Group provided me a stimulating working environment. In particular, I thank Pedro Abreu, Satyaki Bhattacharya, Gerard Bobbink, Ingrid Clare, Robert Clare, Glen Cowan, Aaron Dominguez, Dominique Duchesneau, John Field, Ian Fisk, Roger Jones, Mehnaz Hafeez, Stephan Kluth, Wolfgang Lohmann, Wesley Metzger, Peter Molnar, Oliver Passon, Martin Pohl, Subir Sarkar, Chris Tully and Micheal Unger.

I thank all my friends who helped me on many occasions with various issues, and made my graduate days worthwhile and interesting.

Finally, I thank my parents for their love, understanding, patience and encouragement, without which this thesis would have never been completed.

Contents

List of Figures

List of Tables

SYNOPSIS

Title of the Thesis	:	QCD STUDIES AT L3
Name of the Candidate	:	SWAGATO BANERJEE
Registration Number	:	TIFR−181 (28/7/1998)
Degree	:	DOCTOR OF PHILOSOPHY
Subject	:	PHYSICS
Thesis Supervisor	:	PROF. SUNANDA BANERJEE
Institution	:	TATA INSTITUTE OF
	:	FUNDAMENTAL RESEARCH,
	:	MUMBAI 400 005, INDIA.

Introduction

LEP (Large Electron Positron) is an ideal laboratory to study Quantum Chromodynamics (QCD) [1], the theory of strong interaction between particles carrying color quantum number. This is primarily due to *two* reasons: the initial state (e^-e^+) is clean, and the hadronization corrections (which are inversely proportional to the energy) are small at the high center of mass energies ($\sqrt{s}$) accessible at LEP.

At LEP 1 ($\sqrt{s} \simeq M_Z$), hadronic cross section is large owing to large hadronic branching fraction of Z (70%). At LEP 2 ($\sqrt{s} > 2M_W$), the process $e^+e^- \rightarrow$ *hadrons* through $\gamma/Z^\star$ exchange is the dominant background to the W^-W^+ pair production. At both these phases and at LEP 1.5 ($\sqrt{s}$ between 130 to 136 GeV), there are sufficient number of hadronic events recorded by each of the 4 detectors at LEP (ALEPH, DELPHI, L3, OPAL), from which different aspects of QCD can be studied.

This work is based on hadronic events recorded by the L3 detector [2], at different center of mass energies from LEP 1, LEP 1.5 and LEP 2 data, collected between 1991 and 1999. L3 detector, equipped with a central tracking device, excellent electromagnetic and hadron calorimeters, and a precise muon tracking system, all immersed in an uniform 0.5 Tesla magnetic field along the beam direction, is a hermetic detector with 99% of the 4π angular coverage. This study of $e^+e^- \rightarrow$ *hadrons* events is based on the clusters reconstructed from energy deposited in the calorimeters alone, and also with super-clusters obtained from a non-linear combination of energies of charged tracks and calorimetric clusters.

The signatures of hadronic events are large number of particles observed in the final states and large visible energy measured in the detector. The hadronic events are characterized by two, three or more jet topology, corresponding to zero, one or more hard gluon radiations. The jet properties of hadronic events have manifestly direct correspondence with the global event shape variables of the hadronic events. These collinear and infrared safe variables, like *thrust (T), heavy jet mass (ρ), total and wide jet broadening (*B_T, B_W*), C-parameter, etc.* can thus be exploited to study the characteristic topology of the hadronic events: while the variables (y = 1−T, ρ, B_T, B_W, C) vanish in the two jet regime, they take on well distinguished values for the multi-jet topologies.

In order to compare the data with theoretical predictions at the parton level, event shape variables are corrected for finite detector resolution and acceptance effects. Several Monte Carlo programs are available to model the underlying process using parton shower or matrix element calculations for the perturbative phase and string, cluster or independent fragmentation model for the non-perturbative hadronization phase. Using a few uncorrelated event shape variables, optimised parameter sets are obtained by tuning [3] the models at a fixed center of mass energy, chosen to be $\sqrt{s} = M_Z$, where statistics available is large. Then all the other event shape variables at different center of mass energies are used to test the predictive power of the models.

The energy dependence of the event shape variables come from two distinct sources: logarithmic dependence from the running of strong coupling constant (α_s), and $1/Q^n$ de-

pendence from non-perturbative effects in the hadronization phase. The energy evolutions of the mean values of the event shape variables are seen to be well described by the QCD coherent parton shower models with string or cluster fragmentation.

Determination of α_s from 30 to 189 GeV

For this analysis [11], three event samples collected by the L3 detector have been used:

1. at $\sqrt{s} = M_Z$ from hadronic decays at the Z resonance. Since the cross-section is large, this channel can be isolated with high efficiency (98%), and high purity (99%) [4].

2. at $\sqrt{s} < M_Z$ from events with isolated energetic photon in hadronic decays of Z. After removing the photon, the event is boosted to the rest frame of the remaining hadronic system with an effective reduced center of mass energy of $\sqrt{s'} = \sqrt{s\left(1 - \frac{2E_\gamma}{\sqrt{s}}\right)}$. A neural network is used for π^o/η rejection, and the hadronic system is studied at $\sqrt{s'} = 30{-}50$, $50{-}60$, $60{-}70$, $70{-}80$, $80{-}84$, $84{-}86$ GeV with efficiency of $50{-}30\%$, and purity of $70{-}90\%$ [5].

3. at $\sqrt{s} > M_Z$ from LEP 1.5 & 2 at $\sqrt{s} = 130, 136, 161, 172, 183, 189$GeV. The events from radiative return to the Z are removed by tagging the high energetic photon observed in the detector, or cutting on parallel energy imbalance if the photon escapes down the beam pipe. Above W^-W^+ (ZZ) threshold, well-balanced high multiplicity events compatible with 4 jet topology from W^-W^+ (ZZ) decays are also removed. True high energy hadronic events are identified with efficiency of $90{-}80\%$, and purity of $80{-}84\%$ [6].

The experimental systematic errors are then different and uncorrelated between the three data sets, but are taken as fully correlated between individual low energy or high energy measurements.

α_s from Event Shape Distributions:

Distributions of event shape variables are analytically calculable [7] and have expansion in terms of α_s, the only free parameter of the theory. Complete calculations upto second order exist for these event shape variables, and the leading and next-to-leading order logarithmic terms have been resummed to all orders. By combining these two calculations, the data can be described over a wide range. This furnishes a method for one of the most precise determination of α_s [4], where the event shape distributions from the total event sample can be exploited to obtain a measurement of α_s, as opposed to using a sub-sample, eg. 3 jet events used to extract α_s from the 3 jet rate. The experimental

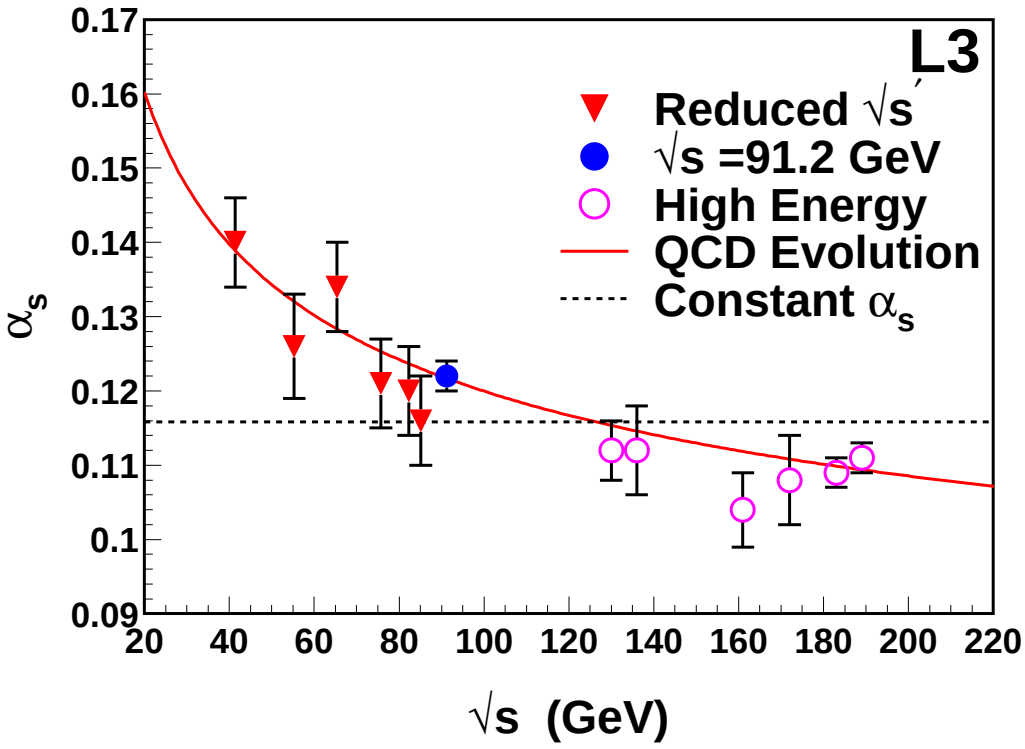

Figure 1: *Running of* α_s *as determined from four event shapes at different center of mass energies.*

accuracy, estimated to be 1% from detector systematics and background contamination, is superseded by the theoretical uncertainty ($\simeq 5\%$) which comes from uncalculated higher order terms. The theoretical error is estimated by varying the renormalization scale, matching algorithms for second order and resummed calculations, and the modelling of the hadronization phase.

α_s is measured at each center of mass energy by taking the unweighted average of the α_s values obtained from 1−T, ρ, B_T and B_W. In this approach, the hadronization effects are folded in, using Parton Shower Monte Carlo.

From a combined fit to the QCD evolution equation [8] of the 13 α_s measurements at $\sqrt{s}$ between 30 to 189 GeV(see figure 1):

$$\alpha_s(M_Z) \;=\; 0.1215 \;\pm\; 0.0012\ (\text{exp}) \;\pm\; 0.0061\ (\text{theo})$$

is obtained with a χ^2 of 13.5 for 12 degrees of freedom.

Using the same covariance matrix determined from experimental and overall errors on α_s in the fit, one can study the effect of enhanced degrees of flavours, in presence of light gluinos, from the slope in the energy evolution of α_s. A fit with the slope as an additional free parameter, along with α_s, furnishes the number of active flavours as:

$$N_f \;=\; 5.0 \;\pm\; 1.3\ (\text{exp}) \;\pm\; 2.0\ (\text{theo})$$

α_s from Moments of Event Shape Distributions:

In an alternative approach, one assumes that soft gluon emission is controlled by an effective $\alpha_{\rm eff}$, different from α_s only below an infrared matching scale (μ_I). Then the non-perturbative contributions to the *first moment* of the event shape variables can be parametrised as [9]: $\langle V \rangle = \langle V \rangle_{\rm PT} + c_V * \mathcal{P}$, where second order calculations are used for the perturbative part, and c_V is a shape dependent parameter. For linear observables, the "shift" given by $\mathcal{P}$, is supposed to have a universal form proportional to α_0/Q, where $\alpha_0(\mu_I)$ $(= \frac{1}{\mu_I}\int_0^{\mu_I} dq \alpha_{\rm eff}(q))$ accounts for contributions below μ_I (chosen to be 2GeV in this study). For the broadening variables, the non-perturbative corrections involve additional "logarithmic skew" given by an extra multiplicative factor to $\mathcal{P}$.

The fit to the first moment of *five* event shapes (1−T, ρ, B_T, B_W, C) from L3 data [11] at 30−196 GeVwith correlated systematic errors are in agreement with the predicted universality of the power law behaviour within 10% accuracy. The five estimates of α_0 and α_s values can be combined to get an overall α_0 and α_s from the power law fit as:

$$\begin{aligned} \alpha_0 &= 0.537 \pm 0.069 \pm 0.079\,, \\ \alpha_s(M_Z) &= 0.1110 \pm 0.0045 \pm 0.0067\,. \end{aligned}$$

Using the measured energy evolution of second moment from L3 data, the prediction for the power law behaviour has been extended to the second moment of the event shape variables [10]: $\langle V^2 \rangle = \langle V^2_{\rm pert} \rangle + 2\langle V_{\rm pert} \rangle \cdot c_V \mathcal{P} + \mathcal{O}\left(\frac{1}{Q^2}\right)$. Using α_0 and α_s from the corresponding fits to the first moments, the fit to the *second moment* admits sizable contributions from the $(\frac{1}{Q^2})$ term, which was initially predicted to be small. The fits for thrust are shown in figure 2 as an illustration.

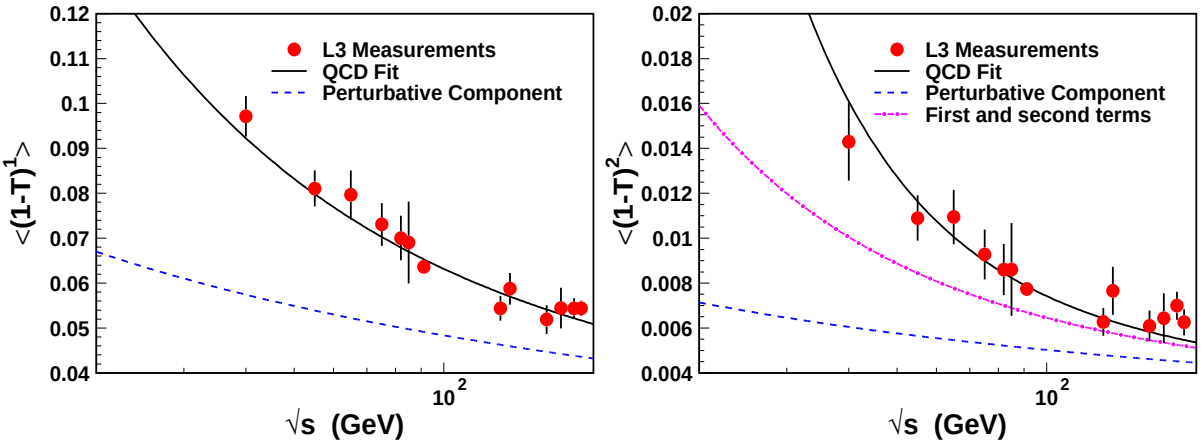

Figure 2: *Fit to energy evolution of the moments of (1-thrust).*

Intrajet Coherence

Intrajet coherence phenomena arising from destructive interference between the soft gluon emission within the jets, affect the hadronic event topology in e^-e^+ annihilation. The effect is to reduce the phase space available for parton emission to an angular ordered region. This dynamical suppression of the momenta in the infrared region leads to energy and emission angle ordering of the successive parton radiations. As a result, one expects reduced parton multiplicities and a dip in the parton momenta in the low momentum region, both of which have been observed in e^-e^+ annihilation by the L3 detector. The inclusive charged particle momentum spectra has been studied in terms of the variable $\xi = -\ln(\frac{2|\vec{p}|}{\sqrt{s}})$ [12] (where $\vec{p}$ is the momentum), and peak position ($\xi^\star$) of spectra, corrected for detector effects, has been measured between 130 and 189 GeV [6, 11]. The energy evolution of the measured peak position ($\xi^\star$) is well described by infrared sensitive modified leading logarithmic QCD calculations, as shown in figure 3.

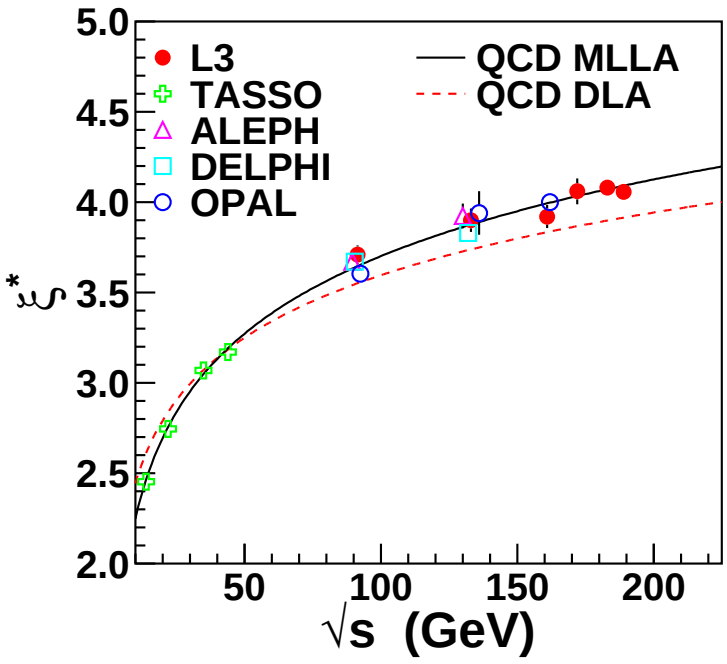

Figure 3: *Energy evolution of $\xi^\star$ compared to QCD predictions.*

Rapidity Gap Events

Recently, large *rapidity gap* events, observed in $p\overline{p}$ and e^-p collisions at DØ and HERA experiments, have been attributed to color singlet exchanges. The gaps in 3 jet events from hadronic Z decays collected by the L3 detector have been studied to search for

color singlet exchange in e^-e^+ annihilation [13]. Using the jade algorithm (with $y_{cut} = 0.05$), well separated 3 jet events of Mercedes type are selected for this study. The angles (θ_{ij}) between the jets (i and j) projected onto the event plane, defined by the two most energetic jets, are restricted to lie within 30° interval with respect to a perfect Mercedes 120° separation. A fixed degree cone is defined around each jet and the remaining region in the event plane is taken as *gaps*.

The Monte Carlo for color singlet exchange is made by generating $q\overline{q}\gamma$ events with the photon having a mass distribution as a gluon, and then by replacing the photon with a boosted 2-jet event. In terms of string fragmentation, colored strings are thus confined to the $q\overline{q}$ gap, whereas in usual gluon exchange colored strings are stretched between the qg and $\overline{q}g$ gaps. In the usual case, destructive interference occurs the $q\overline{q}$ gap because of inter-jet coherence and further reduces the hadronic activity in this gap. We thus expect increased multiplicity and smaller opening angles between the particles in the $q\overline{q}$ gap in the color singlet exchange scenario as compared to the other two gaps, and a reverse effect in the color octet case. Asymmetries, defined with respect to the angular and particle distributions in these gaps, are found to be sensitive to the exchange of color singlet instead of emission of a color octet gluon.

Hadronic Z decays from the 1994-1995 data taking period are compared with fully reconstructed and detector simulated QCD models (eg, JETSET) and the Monte Carlo with color singlet exchange. Anti-b tagged jets in $b\overline{b}$ events are used to improve the gluon jet identification (88%) from energy ordering based criteria (64%) in these Mercedes events.

From a comparison of the distributions between data and QCD Monte Carlo, one can set a limit on the production rate of color singlet exchanges.

Reference

[1] M. Gell-Mann, Acta Phys. Austriaca Suppl. **IX** (1972) 733;
H. Fritzsch, M. Gell-Mann and H. Leytwyler, Phys. Lett. **B47** (1973) 365;
D.J. Gross and F. Wilczek, Phys. Rev. Lett. **30** (1973) 1343;
D.J. Gross and F. Wilczek, Phys. Rev. **D8** (1973) 3633;
H.D. Politzer, Phys. Rev. Lett. **30** (1973) 1346.

[2] L3 Collaboration, B. Adeva *et al.*, Nucl. Inst. Meth. **A 289** (1990) 35;
M. Chemarin *et al.*, Nucl. Inst. Meth. **A 349** (1994) 345;
M. Acciarri *et al.*, Nucl. Inst. Meth. **A 351** (1994) 300;
G. Basti *et al.*, Nucl. Inst. Meth. **A 374** (1996) 293;
A. Adam *et al.*, Nucl. Inst. Meth. **A 383** (1996) 342.

[3] L3 Collaboration, B. Adeva *et al.*, Z. Phys. **C55** (1992) 39;
Swagato Banerjee, "Tuning of QCD Model Parameters Using LEP Data of Hadronic Z Decays", M.Sc. thesis (1998).

[4] L3 Collaboration, B. Adeva *et al.*, Phys. Lett. **B248** (1990) 464;
L3 Collaboration, B. Adeva *et al.*, Phys. Lett. **B284** (1992) 471;
L3 Collaboration, B. Adeva *et al.*, Z. Physik **C55** (1992) 39;
S. Banerjee, S.Müller, L3 Note # 1441 (1993).

[5] L3 Collaboration, M. Acciarri *et al.*, Phys. Lett. **B411** (1997) 339;
Subir Sarkar, "Study of Hadronic Events in e^-e^+ Collisions using L3 Detector at Large Electron Positron (LEP) Collider at CERN", Ph.D. thesis (1997).

[6] L3 Collaboration, M. Acciarri *et al.*, Phys. Lett. **B371** (1996) 137;
L3 Collaboration, M. Acciarri *et al.*, Phys. Lett. **B404** (1997) 390;
L3 Collaboration, M. Acciarri *et al.*, Phys. Lett. **B444** (1998) 569.

[7] S. Catani *et al.*, Phys. Lett. **B263** (1991) 491;
S. Catani *et al.*, Phys. Lett. **B272** (1991) 368;
S. Catani *et al.*, Phys. Lett. **B295** (1992) 269;
S. Catani *et al.*, Nucl. Phys. **B407** (1993) 3;
S. Catani *et al.*, CERN-TH-98-14, HEP-PH-9801350;
Z. Kunszt *et al.*, "Z Physics at LEP 1", CERN Report 89-08, Vol.I., p. 373.

[8] Particle Data Group, R.M. Barnett *et al.*, Eur. Phys. J. **C3** (1998) 1.

[9] Yu. L. Dokshitzer, B. R. Webber, Phys. Lett. **B352** (1995) 451;
B. R. Webber, HEP-PH-9510283;
Yu. L. Dokshitzer *et al.*, Nucl. Phys. **B511** (1997) 396;
Yu. L. Dokshitzer *et al.*, J.HEP. 05 (1998) 3;
Yu. L. Dokshitzer *et al.*, HEP-PH-9812487.

[10] Yu.L. Dokshitzer and B.R. Webber, Phys. Lett. **B404** (1997) 321;
B.R. Webber, Nucl. Phys. Proc. Suppl. **71** (1999) 66;
G. Salam, private communication.

[11] Contributions to the summer conferences '99, L3 note #2414 (1999).

[12] A.H. Mueller, in *Proc. 1981 International Symposium on Lepton and Photon Interactions at High Energies*, ed. W. Pfeil (Bonn, 1981), p.689;
Yu.L. Dokshitzer, V.S. Fadin and V.A. Khoze, Phys. Lett. **B115** (1982) 242;
C. P. Fong and B. R. Webber, Phys. Lett. **B229** (1989) 289;
Yu. L. Dokshitzer *et al.*, Basics of Perturbative QCD, Editions Frontieres, Gif-sur-Yvette, 1991.

[13] L3-Note #2422d, June 1999.
"Rapidity gap events in 3jets", presentation at L3 Annual General Meeting 1999, Lyon, France.
– Swagato Banerjee.

Statement Required Under Ordinance 0.770

I hereby state that the work presented in this thesis has not been submitted to this or any other university for Ph.D or any other degree.

Statement Required Under Ordinance 0.771

Statement No. 1 regarding new facts :

Hadronic interactions at LEP II has been studied. Combining with data sets from LEP I and reduced center of mass energy studies, energy evolution of α_s has been studied using distributions and moments of some global event shape variables.

Inclusive charged particle momentum spectra has been studied between 130-189 GeV, and evidence of intra-jet gluon coherence has been observed.

Gaps in 3 jet events have been studied to search for color singlet exchange in e^+e^- interactions.

Statement No. 2 regarding author's contribution in joint work :

The L3 experiment is a huge collaborative effort comprising of around 500 physicists from about 50 institutes/laboratories all over the globe. Numerous individuals have contributed significantly towards the successful joint venture in the fields of detector design, building and maintenance as well as software development, both online and offline, without which this work would not have been realized. The scientists and engineers of the CERN accelerator divisions contributed towards the excellent performances of the LEP collider over the years.

I have carried out the analyses under the supervision of Prof. Sunanda Banerjee. The work where major responsibility towards the analyses rests on the author is described in this thesis.

References are properly cited at appropriate places whenever use has been made of earlier works. The principal aspects of the work of the author can be summarised as :

Study of hadronic interactions in e^+e^- annihilations at LEP 1.5 and LEP 2;

Study of power law behaviour of moments of event shapes from 30 to 189 GeV;

Study of charged particle momentum spectra from LEP 1.5 and LEP 2 data; and

Study of rapidity gap events from LEP 1 data.

Swagato Banerjee
Signature of the Candidate

Sunanda Banerjee
Signature of the Supervisor

Overview

The first 4 chapters are introductory.

- *A Brief History of QCD: from Pions to Jets* (chapter 1) traces the development of the study of *strong* interactions with a *strong* bias in the choice of topics.

- *Jets, Shapes and Asymmetries* (chapter 2) introduces the variables used in the analysis. The energy flow due to *hard gluon radiation* in hadronic events are conviniently studied in terms of the global event shape variables, while the inclusive momenta spectra are useful to study the *soft gluon radiations*. The singlet/octect nature of the color exchanges in strong interactions are studied in terms of particle and angular assymetries in *rapidity gaps events*.

- $\mathbf{e^-e^+}$ *Annihilation at LEP* (chapter 3) discusses how clean initial states in e^-e^+ annihilations make it an ideal laboratory to study strong interactions with smaller hadronization corrections, as we go up in energy at the LEP (Large Electron Positron) Collider.

- *L3: Apparatus and Data Taking* (chapter 4) describes the experiment set-up with the L3 detector located at the second interaction (IP2) at LEP.

The next 3 chapters describe the analysis.

- Energy response of the individual sub-detectors are calibrated off-line using hadronic events, which have large number of particles observed in the final state and large visible energy deposited in the detector. The modelling of the process, hadronic event characteristics are described in chapter 5: *The Process:* $\mathbf{e^-e^+ \rightarrow \gamma/Z^\star \rightarrow}$ *hadrons*.

- At LEP 1.5 and LEP 2 phase, the dominant backgrounds come from ISR events from radiative return to the Z and hadronic decays of the weak boson pair-production (W^-W^+/ZZ). Chapter 6 describes *Hadronic Event Selection at* $\mathbf{\sqrt{s} > M_Z}$.

- Chapter 7: *Systematics and Corrections* deals with finite detector resolution and acceptance effects and sources of systematic error and statictical fluctuations in systematic error study.

The next 3 chapters describe the results.

- Chapter 8: *Aspects of Hard Gluon Radiation* discusses jetrates, evolution of event shapes and determination of the strong coupling constant between 30-189 GeV, along with the power law behaviour.
- Chapter 9: *Aspects of Soft Gluon Radiation* discusses the charged particle multiplicity and intra-jet coherance studied from inclusive charged particle momenta spectra.
- Chapter 10: *Search for Colour Singlet Exchange* describes the study of rapidity gap events in e^-e^+ events using Mercedes 3-jet events from hadronic Z-decays.

Finally, *Summary* (chapter 11) summarizes the thesis.

Chapter 1

A Brief History of QCD: from pions to jets

1.1 The Illustrious 1947

It was known for a long time that four building blocks of matter are electron, photon, proton, neutron: the first one, the electron, being discovered by J.J. Thomson in 1897 and the last one, the neutron, by J. Chadwick in 1932. Following the presentation of theory of beta decay in 1933, there was a strong conviction that a fifth particle also exist: neutrino (proposed by Pauli, named by Fermi). These were not only sufficient to explain the physical and chemical properties of matter that we encounter in everyday life, but also to perceive the processes inside the Sun and the stars, to study condensed matter and plasma, to build reactors, etc.

However, the dense packing of like-charged mutually repelling protons in the small core of an atom called nucleus, led physicists to seek for a understanding of the forces of *strong interaction* between the nucleons: an interaction strong enough to overcome the electrostatic repulsions between protons at distances, (10^{-15} cm), smaller than the radius of the nucleus, i.e. an interaction with a lifetime $\sim 10^{-23}$ sec.

The idea of global SU(2) isospin invariance, that proton and neutron are two components of an isospin doublet, had been proposed the same year neutron was discovered (1932), and the hypothesis that the carrier of this nucleon force is the π-meson was proposed by Yukawa in 1934. It was realized that a triplet of π-mesons must exist (1938): π^+, π^0, π^- (π^0 is the first particle predicted on the basis of internal symmetry). But the experimental connection between the "mesotron" (discovered in cosmic ray by two groups: Anderson and Neddermeyer, and Street and Stevenson, in 1937) with the theoretically wanted triplet of π-mesons was unclear.

Three discoveries in 1947 marked the birth of beginning of our current knowledge about the proliferation of matter:

- By exposing photographic emulsions on mountain tops, Powell and his co-workers at Bristol [1] discovered *two* particles of mass between electron and proton masses

in cosmic rays: first, the pion (π^+), and second, the muon (μ^+) (for the preceding ten years they "coexisted as mesotron");

- Thirdly, strange particles were discovered: the first two V^0-decay events were seen in cloud chamber photographs by Rochester and Butler [2].

These three discoveries started the process of shifting high energy physics from its cosmic ray cradle to the huge detectors in today's big accelerators.

1.2 1947 onwards

In 1948, the first man-made charged **pions** were produced, and the neutral ones were discovered in 1950. The first man-made kaons and hyperons were produced in 1954. By the end of 1960, the list of strongly interacting or decaying particles discovered had grown to hundreds.

Finally, in 1961, the "Eightfold Way" was invented by Gell-Mann and Ne'eman [3], and the discovered mesons (spin-0, 1 bound states) and baryons (spin-$\frac{1}{2}$, $\frac{3}{2}$ bound states) started to get explained in terms of a model of 3 quarks (u, d, s) with fractional values of baryonic number and electric charge. The next decade witnessed the transformation of our understanding of the nature of strong interaction: from the QPM, Quark Parton Model (1964) [4] to QCD, Quantum Chromodynamics [5] - a local field theory based on the non-abelian group SU(3) of internal gauge symmetry of *colour* degrees of freedom, which was introduced [6] in order to lift degeneracy of 3 quarks in similar spin states in an anti-symmetric baryon.

Till date, six flavours of quarks have been observed: (u,d), (c,s) and (t,b), and written this way they correspond to the *three* observed families of leptons in the electro-weak sector of Standard Model [7]. The quarks take part in the electro-weak interaction as well, while, the leptons are characterised by the abstinence from the strong interaction.

The non-abelian nature of QCD manifests itself in two characteristic features of the strong interaction: *asymptotic freedom* and *colour confinement*. While the first one says that at small distances, the strong coupling constant (α_s) lies well within the domain of perturbative calculations, the latter postulates that only colour singlet states exist independently in nature.

In the present day high energy experiments, strong interaction between hadrons (as mesons and baryons are collectively called), are observed as **jets**: *colour singlet final states* in the end product of particle collisions. Electron-positron (e^-e^+) annihilation is an extremely pure and efficient method in probing high energy, and jets observed in e^-e^+ annihilations have provided valuable information on QCD.

1.2.1 The Theory of Strong Interaction

A few words about notations are in order:

$$\begin{aligned}
\textit{Flavour indices} &: i, j, k \\
\textit{Color indices} &: \mathrm{m}, \mathrm{n}, \mathrm{l} \\
\textit{Spinor indices} &: \mathrm{I}, \mathrm{J}, \mathrm{K} \\
\textit{Lorentz indices} &: \mu, \nu, \lambda \\
\textit{Quarks} &: \psi_i = \begin{pmatrix} \psi_1 \\ \psi_2 \\ \psi_3 \end{pmatrix}_i \\
\textit{Gluons} &: \mathrm{A}_\mu = \mathrm{T}^\mathrm{a}\mathrm{A}^\mathrm{a}_\mu,\ \mathrm{T}^\mathrm{a} = \frac{\lambda^\mathrm{a}}{2}\ (\lambda^\mathrm{a}:\ \mathrm{Gell-Mann\ Matrices})
\end{aligned}$$

The matter and the gauge fields of the theory are called *quarks and gluons* respectively. They can be written in the fundamental and adjoint representations of SU(3) respectively. Thus, the colour index runs from 1 to 3 for quarks and from 1 to 8 for gluons.

The QCD Lagrangian reads:

$$\mathcal{L} = -\frac{1}{2} tr\ \mathrm{F}_{\mu\nu}\mathrm{F}^{\mu\nu} + \sum_i \overline{\psi_i}(i\not{D} - m_i)\psi_i.$$

Here, $\not{D} = \not{\partial} - ig\not{A}$, and $\mathrm{F}_{\mu\nu} = \mathrm{T}^\mathrm{a}F^\mathrm{a}_{\mu\nu}$, where $F^\mathrm{a}_{\mu\nu} = \partial_\mu \mathrm{A}^\mathrm{a}_\nu - \partial_\nu \mathrm{A}^\mathrm{a}_\mu + g f^{\mathrm{abc}} \mathrm{A}^\mathrm{b}_\mu \mathrm{A}^\mathrm{c}_\nu$.

This gives us the following *three* basic amplitudes:

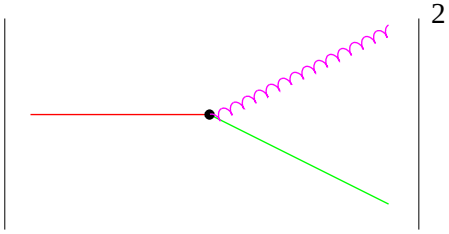

Quark Bremsstrahlung
$\sim \mathrm{C_F} \cdot \alpha_\mathrm{s}$

$\mathrm{C_F} = \frac{\mathrm{N_C}^2 - 1}{2\mathrm{N_C}} = \frac{4}{3}$

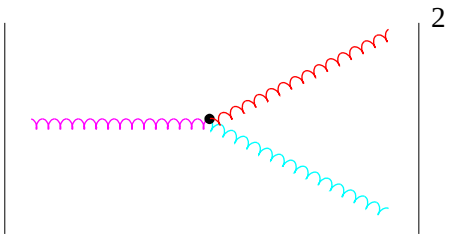

Gluon Bremsstrahlung
$\sim \mathrm{C_A} \cdot \alpha_\mathrm{s}$

$\mathrm{C_A} = \mathrm{N_C} = 3$

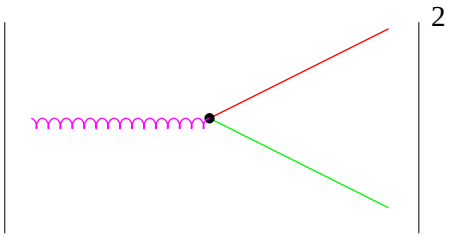

Gluon Splitting
$\sim \mathrm{T_F} \cdot \alpha_\mathrm{s}$

$\mathrm{T_F} = \frac{1}{2}$

1.2.2 QCD with e^-e^+ Annihilations

$e^-e^+ \rightarrow$ *hadrons* data have provided vital experimental evidences in the discoveries of new quarks, and understanding the theory of QCD that describes the quarks. Some of them are listed below :

- In November 1974, two experiments, one studying e^-e^+ annihilations led by Burton Richter at SLAC and and the other studying e^-e^+ pairs produced in proton-beryllium collisions led by Samuel Ting at Brookhaven, discovered the *fourth* quark: charm, by observing the J/ψ bound state at 3.1 GeV [8]. This is referred to as the "November Revolution" in particle physics.

  After a statistically significant di-muon peak in 9.5 GeV region with a observed width of 1.2 GeV had been observed by a team led by L. Lederman in mid 1977 [9] studying collisions of 400 GeV protons on nuclear targets at Fermilab, in May 1978 [10] two groups at the DORIS e^-e^+ storage ring at DESY were able to observe the Υ in the PLUTO and DASP II detectors. The clean environment in an e^-e^+ annihilation reaction allowed for testing the width of this narrow peak, and thus, unambiguously marked the experimental observation of *fifth* quark: beauty.

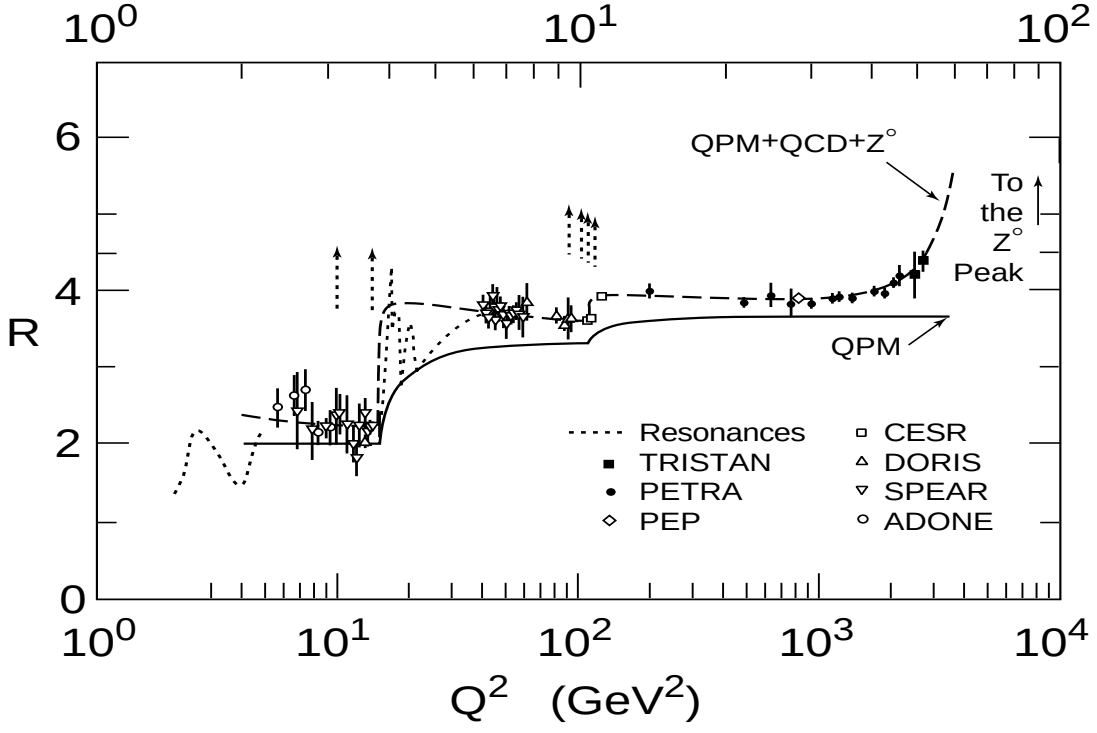

Figure 1.1: Measurements of the ratio R_{had} compared with theoretical predictions.

- According to QED and the QPM, in e^-e^+ annihilations, the quantity:

$$R_{had} \equiv \frac{\sigma(e^+e^- \rightarrow \text{hadrons})}{\sigma_{QED}(e^+e^- \rightarrow \mu^+\mu^-)}$$

should be equal to $N_C \, \Sigma_f \, q_f^2$, where q_f is the charge of the quark of flavour f and the sum runs over all active flavours at a given centre-of-mass energy. A summary of R measurements as a function of energy, shows (figure 1.1 [11]):

  - Step-wise jump of cross section corresponding to the threshold of new quarks, thus providing evidence that $q\overline{q}$ production is the underlying process;
  - Along with assignment of fractional charge of the quarks, this provides experimental support to the number of colours $N_C = 3$;
  - For $Q^2 > 1000$GeV, it shows that $e^-e^+ \rightarrow$ *hadrons* process mediates through the Z boson in addition to the photon as the propagator;
  - Residual excess in the data relative to QED + QPM expectation, and decrease of this excess with increasing Q^2, hints for some mechanism which causes an increase in the 'phase-space' for hadron production beyond QED + QPM, but at a rate that decreases with Q^2. The R-ratio thus provides indirect evidence for the existence of the gluon, as well as for the non-abelian 'running' of the strong coupling.

- In 1975, first evidence of "jet" structure was observed at the SPEAR e^-e^+ collider at $\sqrt{s} = 6.2$ - 7.4 GeV. An illustrative result from the MARK I experiment [12] is shown in figure 1.2, which uses the event shape variable sphericity [13]:

$$\text{Sphericity(S)} = \frac{3(\sum_a |\vec{p}_{a\perp}|^2)}{2(\sum_a |\vec{p}_a|^2)}\text{min}$$

One can expect S = 0 or 1 for 2-jet or spherical events, respectively. With increasing centre of mass energy, the jets will more be collimated and thus, $\langle S \rangle$ *decreases* with $\sqrt{s}$, as has been observed [12].

- Hadronic data from e^-e^+ annihilations also demonstrated that in the underlying reaction $e^-e^+ \rightarrow$ *hadrons*, spin 1/2 quarks were involved. An illustrative result from the TASSO experiment [14] is shown in figure 1.3. Here the distribution of the polar-angle (θ_S) of the sphericity axis is shown at centre-of-mass energies of 14, 22 and 35 GeV. A fit to the data at $\sqrt{s} = 35$ GeV to the functional form:

$$\frac{dN}{d\cos\theta_S} \propto 1 + a_S \cos^2\theta_S$$

yields $a_S = 1.03 \pm 0.07$, which is characteristic of the production of spin $\frac{1}{2}$ particles in the e^-e^+ annihilation. Also shown in figure 1.3 is a second example of an event

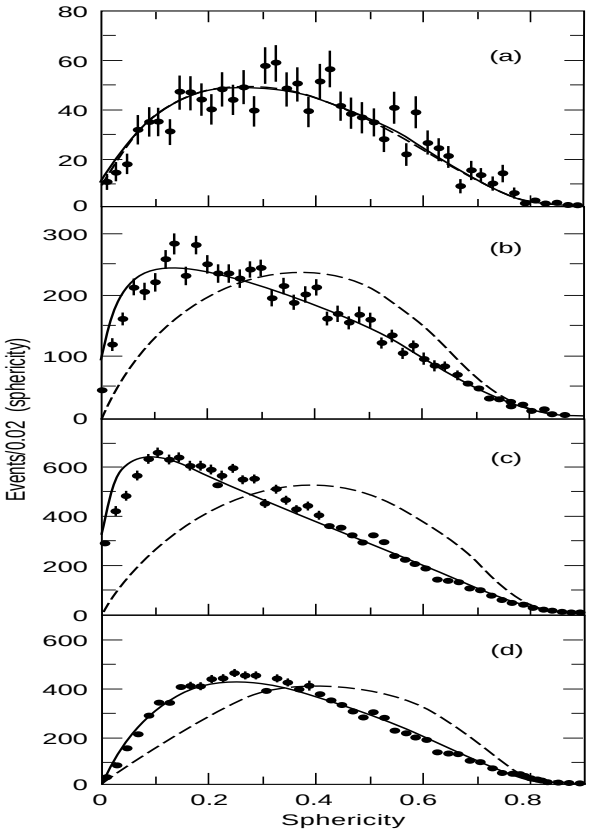

QCD predictions (solid line) of the sphericity distributions overlayed with data as measured by the MARK I experiment at SPEAR [12] at c.m. energies of (a) 3.0, (b) 6.2, (c) 7.4 GeV. The narrowing of the distributions, and the trend of the peak towards smaller values with increase of the centre-of-mass energy, provides evidence for collimated hadron production in e^-e^+ annihilation. The dashed line represents the expectation from a 'phase-space model' of hadron production. Figure (d) is same as figure (c) but for a subset of events containing particles with scaled momentum, $2p/Q$, less than 0.4.

Figure 1.2: Evidence of jet structure at MARK I.

shape observable in the form of the thrust-axis [15] polar-angle (θ_T) distribution. Thrust is defined qualitatively similar to sphericity in that it can be used to quantify the degree of collimation of particle production, and is collinear and infra-red safe making it more attractive theoretically. The thrust-axis polar-angle distribution in figure 1.3 was fitted (to similar functional form as θ_S) to obtain, at 35 GeV $a_T = 1.01 \pm 0.06$, in good agreement with the result using the sphericity axis.

- Study of the energy flow and relative transverse momenta of the jets in hadronic events at centre of mass energy around 20 GeV, led to observation of *three* distinct jets of hadrons at the PETRA electron-positron collider [16] in 1979. Such events were interpreted [17] in terms of the fundamental process $e^-e^+ \rightarrow q\bar{q}g$, providing *direct evidence* for the existence of the gluon and its coupling to quarks.

  Study of the angle between the thrust direction and the light jet direction (boosted to the rest frame of the 2 lighter jets) in a 3-jet decay system from e^-e^+ annihilation study at TASSO, PLUTO and CELLO collaboration, gave experimental confirmation to the spin-1 property of gluons [18].

  With the high statistics available from hadronic Z decays at LEP, the scalar spin-0 model of gluons has been ruled out with probability $< 10^{-10}$ using L3 data alone [19].

Polar angle distribution of sphericity and thrust axes from TASSO experiment [14]
$d\sigma/d\Omega \propto (1 + \alpha\, cos^2\,\theta)$
$\Rightarrow$ Spin-1/2 quarks

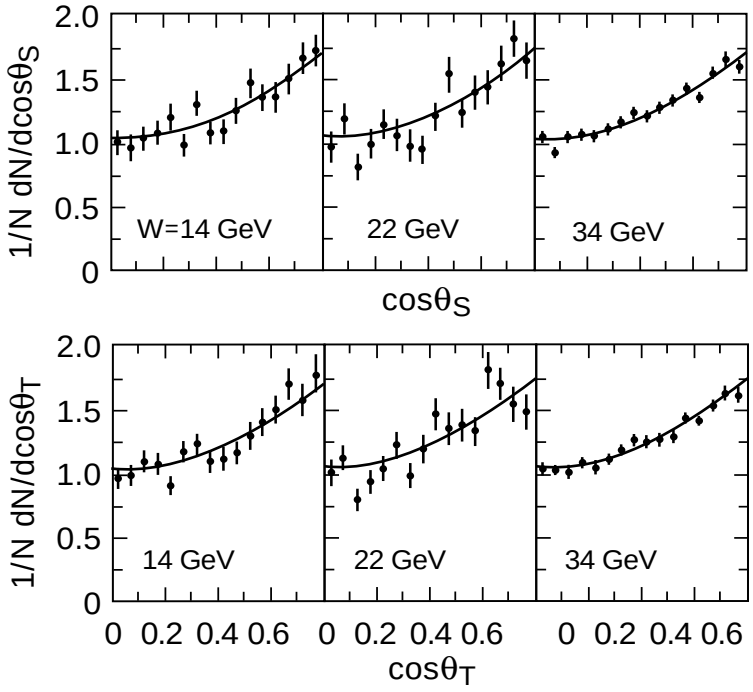

Figure 1.3: Production of spin 1/2 particles in $e^-e^+ \rightarrow$ *hadrons* process at TASSO.

Numerous other experimental evidences from hadron spectroscopy, deep-inelastic scattering, etc. along with developments from the theoretical side [5] (like Yang-Mills's non-abelian gauge theory, concept of colour, quark-parton model, scaling and its violation, renormalisibility, asymptotic freedom, etc.) now lead us to believe that SU(3) based QCD describes the force of strong interaction. Along with the SU(2)$\otimes$U(1) electro-weak theory of Glashow, Salam, and Weinberg [7], it forms the basis of our understanding of the theory of elementary particles, known as the Standard Model of particle physics.

References

[1] C.M.G. Lattes *et al.*, Nature **159** (1947) 694; **160** (1947) 453, 486.

[2] G.D. Rochester and C.C. Butler, Nature **160**, (1947) 855.

[3] M. Gell-Mann and Y. Ne'eman, "The Eightfold Way", New York: Benjamin, 1964.

[4] O.W. Greenberg, Am. J. Physics **50** (1982) 1074;
D.B. Lichentenberg and S.P. Rosen, eds., "Developments in the Quark Theory of Hadrons", Nonantum: Hadronic Press, (1980).

[5] J.D. Bjorken, Physical Review Letters **16** (1966) 408;
R.P. Feynman, Physical Review Letters **23** (1969) 1515;
M. Gell-Mann, Acta Physica Austriaca Suppl. **IX** (1972) 733;
H. Fritzsch, M. Gell-Mann, H. Leutwyler, Physics Letters **B47** (1973) 365;
D.J. Gross and F. Wilczek, Physical Review Letters **30** (1973) 1343;
H.D. Politzer, Physical Review Letters **30** (1973) 1346;
G. 't Hooft, Nuclear Physics **B33** (1971) 173.

[6] O.W. Greenberg, Phys. Rev. Lett. **13**, (1964) 598;
D.B. Lichentenberg, "Unitary Symmetry and Elementary Particle", New York: Academic Press, (1970).

[7] S.L. Glashow, Nucl. Phys. **22** (1961) 579;
S. Weinberg, Phys. Rev. Lett. **19** (1967) 1264;
A. Salam, "Elementary Particle theory", ed. N. Svartholm (Stockholm 1968), 367.

[8] J.J. Aubert *et al.*, Phys. Rev. Lett. **33** (1974) 1404;
J.-E. Augustin *et al.*, Phys. Rev. Lett. **33** (1974) 1406.

[9] S.W. Herb *et al.*, Phys. Rev. Lett. **39** (1977) 252.

[10] Pluto Collaboration, Ch. Berher *et al..*, Phys. Lett. **B76** (1978) 243;
C.W. Darden *et al.*, Phys. Lett. **B76** (1978) 246; *ibid*, **B78** (1978) 364.

[11] R. Marshall, Zeitschrift für Physik **C43** (1989) 595.

[12] Mark I Collaboration, G. Hanson *et al.*, Physical Review Letters **35** (1975) 1609.

[13] J.D. Bjorken, S.J. Brodsky, Physics Reports **D1** (1970) 1416.

[14] TASSO Collaboration, M. Althoff *et al.*, Zeitschrift für Physik **C22** (1984) 307.

[15] S. Brandt *et al.*, Phys. Lett. **12** (1964) 57.
E. Farhi, Phys. Rev. Lett. **39** (1977) 1587.

[16] TASSO Collaboration, R. Brandelik *et al.*, Phys. Lett. **B86** (1979) 243.
MARK J Collaboration, D.P. Barber *et al.*, Phys. Rev. Lett. **43** (1979) 830.
PLUTO Collaboration, Ch. Berger *et al.*, Phys. Lett. **B86** (1979) 418.
JADE Collaboration, W. Bartel *et al.*, Phys. Lett. **B91** (1980) 142.

[17] J. Ellis, M.K. Gaillard, G.G. Ross, Nucl. Phys. **B111** (1976) 253.

[18] J. Ellis and I. Karliner, Nuclear Physics **B148** (1979) 141;
TASSO Collaboration, R. Brandelik *et al.*, Physics Letters **B97** (1980) 453;
PLUTO Collaboration, C. Berger *et al.*, Physics Letters **B97** (1980) 459;
CELLO Collaboration, H.J. Behrend *et al.*, Physics Letters **B110** (1982) 329.

[19] L3 Collaboration, B. Adeva *et al.*, Phys. Lett. **B263** (1991) 551.

Chapter 2

Jets, Shapes and Asymmetries

2.1 Jets in e^-e^+ Annihilation

Studies of jets in e^-e^+ interactions have been very important in understanding QCD. Two, three and four jet events are understood to arise out of $e^-e^+ \to q\overline{q}$, $e^-e^+ \to q\overline{q}g$ and $e^-e^+ \to q\overline{q}q\overline{q}$ or $e^-e^+ \to q\overline{q}gg$ type of processes at the underlying level. This widespread correspondence has resulted in associating the word *jet* almost interchangeably with the quarks and gluons (generically termed *partons*) in the event description.

A "jet" is one or several nearby partons lumped together according to some jet reconstruction criterion - while the actual number of partons produced is an ill-defined concept, and might as well be infinite, the number of jets for a given jet definition is well defined.

The jet characteristics are most intuitively studied using cone algorithms. Sterman and Weinberg [1] defined a two-jet event if $(1 - \varepsilon)$ fraction of the total centre-of-mass energy lies inside two opposite cones (of half-angle δ). According to the Kinoshita-Lee-Nauenberg theorem [2], which states that the infrared singularities cancel each other if all the degenerate initial and final state diagrams are summed up, the jet cross section defined in this manner, is free of collinear and soft singularities. For example, the full second order cross section involves both real parton emission terms and the vertex and propagator corrections (see figure 2.1), which modify the three and four jet cross sections.

One may also define a single-jet inclusive cross section by finding the distribution of the maximum amount of energy which lies in a cone of half-angle δ. Because the treatment adopted experimentally for overlapping jets has proved difficult to standardise, "Snowmass Accord" [3] on jet cone definitions has been set up, which helps to make more reliable comparison between the full next-to-leading order perturbative calculations for hadronic cross section and experiments.

Alternatively, jets may be reconstructed using the JADE [4] or the DURHAM ($k_\perp$) [5] clustering algorithms. These algorithms cluster the final state particles into pseudo-particles by comparing their separation with the chosen resolution measure. This approach

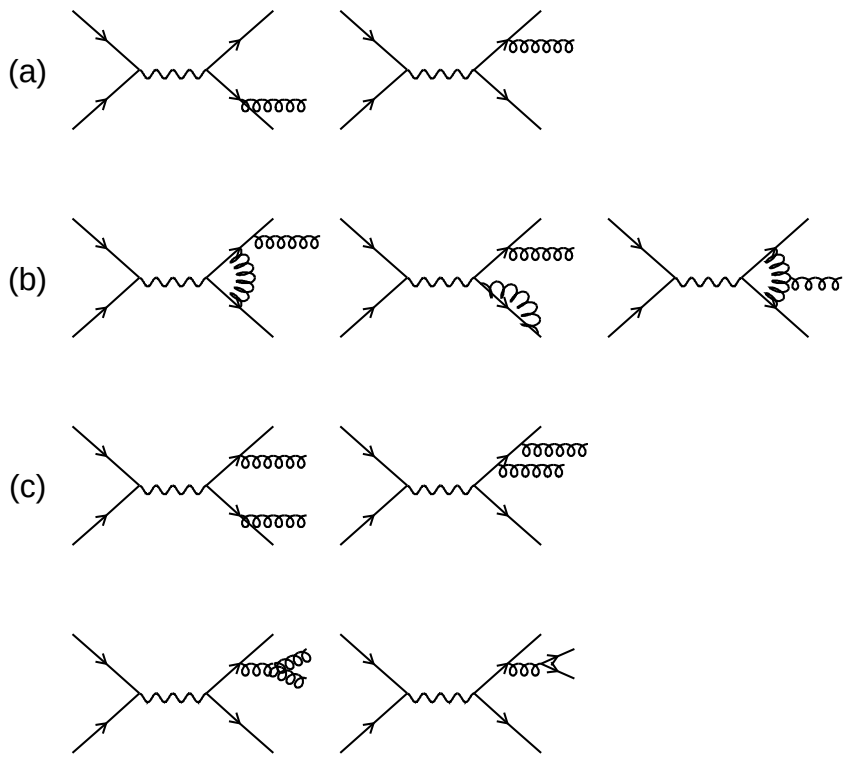

Figure 2.1: $\mathcal{O}(\alpha_s)$ & $\mathcal{O}({\alpha_s}^2)$ diagrams for three and four jet cross sections: (a) contribution to three jets in first order; (b) vertex and propagator corrections to three jets in second order; (c) second order contributions to four jet production (using symmetry more diagrams may be generated).

is both infrared and collinear safe, because the algorithms start off by combining the softest and most collinear particles, which thereafter do not affect the analysis at all. The measure of separation (y_{cut}) is related to the invariant mass in the JADE algorithm or transverse momentum in the DURHAM algorithm, both scaled with respect to the centre-of-mass energy ($\sqrt{s}$).

In the JADE clustering algorithm, the separation (y_{ab}) between a pair of particles is measured using invariant mass of a pair of particles (ignoring particles masses):

$$y_{ab}^{\text{JADE}} = \frac{2E_a E_b}{s}(1-\cos\theta_{ab})$$

where E_a and E_b are the energies of the particles, θ_{ab} is the angle between them and $\sqrt{s}$ is the centre-of-mass energy. In the DURHAM clustering algorithm jets are reconstructed using scaled transverse momenta between a pair of particles as the measure of separation between the particles (y_{ab}):

$$y_{ab}^{\text{DURHAM}} = 2\,\frac{\min(E_a^2, E_b^2)}{s}(1-\cos\theta_{ab}).$$

The pair with the smallest value of the jet resolution variable is replaced by a pseudo-particle c with 4-momentum:

$$p_c = p_a + p_b.$$

This procedure is repeated until the resolution measure y_{ab}^{JADE} or y_{ab}^{DURHAM} for all the final state particles exceed a predefined jet resolution parameter y_{cut}. The remaining pseudo-particles at the end of this recombination procedure are called jets in the clustering algorithms. The 3-jet resolution parameter y_{23}^{JADE} (y_{23}^{DURHAM}) for JADE (DURHAM) algorithm is defined as that value of the maximum jet resolution parameter y_{cut} for which the event still has 3-jet structure.

Besides the fact that use of invariant mass related measure can lead to a unnatural assignments of particles (particularly back-to-back final state low momenta ones) to jets, theoretical criteria of good resolution parameters (like leading to smaller hadronisation corrections, resummability of large logarithms at small values of y_{cut}) have favoured the DURHAM algorithm.

In the JADE algorithm, a fixed y_{cut} corresponds to a minimum mass between any two jets which grows linearly with the centre-of-mass energy: for example, at $y_{\text{cut}} = 0.01$ the mass separation between jets is 3.5 GeVat PETRA/PEP energies, while at LEP I it corresponds to 9 GeV, which is worth comparing to the 1 GeVscale below which the non-perturbative fragmentation process sets in, irrespective of centre-of-mass energy. At this y_{cut} value, with $\alpha_s = 0.12$, second order QCD calculations give a $2:3:4$ jet composition as approximately $11\% : 77\% : 12\%$, with the individual contributions from $e^-e^+ \to q\overline{q}gg$ and $e^-e^+ \to q\overline{q}q\overline{q}$ processes to 4 jet rate estimated to be 11.5% and 0.5% respectively [6].

2.2 Global Event Shape Variables

Energy flow in hadronic events are conveniently studied in terms of global event shape variables. These variables are collinear and infrared safe variables and hence, analytically calculable in QCD. Resummed perturbative calculations for the event shapes [7] are more complete than that of jet-rates (R_{jet}^{n}) [8], and thus theoretical uncertainty associated with the measurement of these event shapes is more controlled.

The non-perturbative effects of hadronisation on some of the event shape variables, are estimated using Monte Carlo programs, which use: (a) independent, or (b) string, or (c) cluster fragmentation. The power law behaviour of the moments of these event shapes has been recently calculated [9], and the non-perturbative terms can be expanded in inverse powers of energy.

Improved analytical QCD calculations are available for five variables, thrust (T) [10], scaled heavy jet mass (ρ_{H}) [11], total (B_{T}) and wide (B_{W}) jet broadening variables [12] and the C-parameter [13]. These variables are defined as:

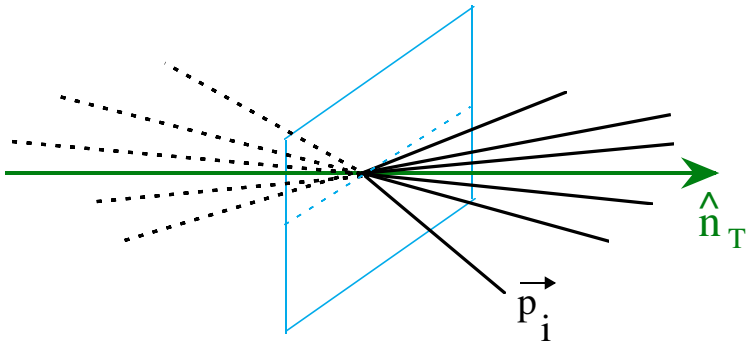

Figure 2.2: Orientation of the two hemispheres w.r.t thrust axis.

Thrust: The global event shape variable thrust, T, [14] is defined as:

$$T \;=\; \max \frac{\sum |\vec{p}_i \cdot \vec{n}_T|}{\sum |\vec{p}_i|} \;,$$

where $\vec{p}_i$ is the momentum vector of the particle i. The thrust axis $\vec{n}_T$ is the unit vector which maximises the above expression (see figure 2.2). The value of the thrust can vary between 0.5 and 1.

Scaled heavy jet mass: The heavy jet mass M_H [15] is defined as:

$$M_H \;=\; \max[M_+(\vec{n}_T), M_-(\vec{n}_T)] \;,$$

where $M_\pm$ are the invariant masses in the two hemispheres, $S_\pm$, defined by the plane normal to the thrust axis (see figure 2.2):

$$M_\pm^2 \;=\; \left(\sum_{i \in S_\pm} p_i \right)^2$$

where p_i is the four momentum of particle i. The scaled heavy jet mass ρ is defined as:

$$\rho \;=\; M_H^2/s \;.$$

Jet broadening variables: These variables are defined [12] by computing in each hemisphere the quantity:

$$B_\pm \;=\; \frac{\sum_{i \in S_\pm} |\vec{p}_i \times \vec{n}_T|}{2 \sum_i |\vec{p}_i|} \;.$$

The observables used to study α_s are

$$\mathrm{B_T} \;=\; B_+ + B_- \quad \text{and} \quad \mathrm{B_W} \;=\; \max(B_+, B_-)$$

referred to as 'total jet broadening' and 'wide jet broadening', respectively.

***C*-Parameter:** The C parameters is derived from the eigenvalues of the linearised sphericity momentum tensor [16]:

$$\theta^{ij} = \frac{\sum_a p_a^i p_a^j / \mid \vec{p_a} \mid}{\sum_a \mid \vec{p_a} \mid} \quad i,j = 1,2,3 \ ;$$

It is defined in terms of the eigenvalues of θ^{ij}, λ_1, λ_2, and λ_3, as:

$$C = 3(\lambda_1\lambda_2 + \lambda_2\lambda_3 + \lambda_3\lambda_1) \ ;$$

Neglecting the masses, one can express this in terms of centre-of-mass energy fractions of the final state particles, $x_i = 2E_i/\sqrt{\mathrm{s}}$, as [13]:

$$C = (\frac{3}{8})\sum_{i,j} x_i x_j \sin^2(\theta_{ij})$$

2.2.1 Relative Contributions from n-jet Configurations

Hadronic event topologies are characterised by hard gluon radiations. These different jet topologies appear differently in the distributions of the event shape variables. Relative contributions to the event shapes for two-jet, three-jet and four-jet topologies are shown in the figures 2.3, 2.4 and 2.5.

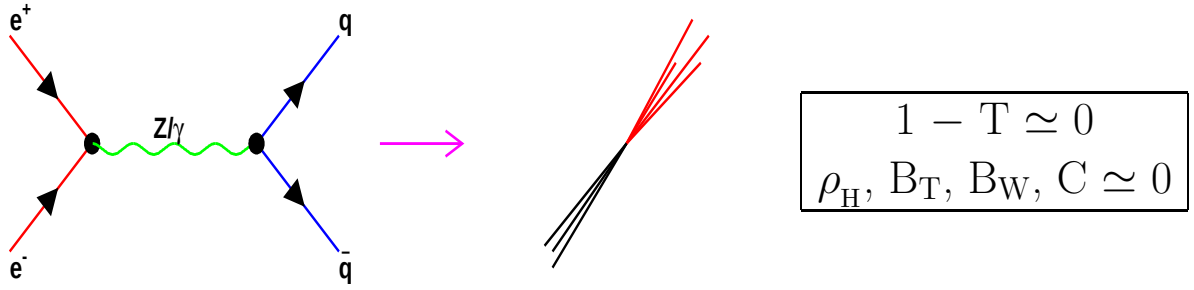

Figure 2.3: Two jet contributions to event shapes.

2.2.2 α_s from Event Shapes

By studying the distributions and moments of event shapes from hadronic events, one can estimate the relative composition of the multi-jet configurations. This provides one of the most precise method for determination of α_s. Some of the advantages of these variables are:

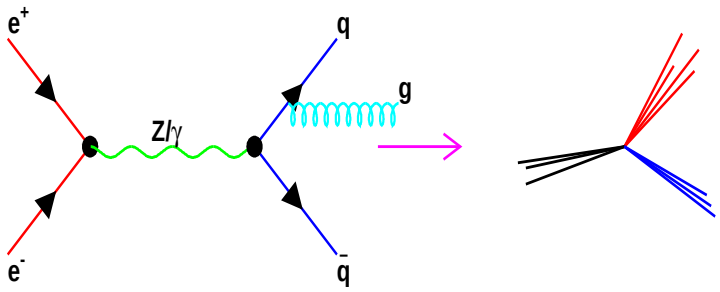

$$\begin{array}{c} \mathrm{T} \in [\frac{2}{3}, 1] \\ \rho_{\mathrm{H}} \approx 1 - \mathrm{T} \\ \mathrm{B_T} \in [0, \frac{1}{2\sqrt{3}}] \\ \mathrm{C} \in [0, \frac{3}{4}] \end{array}$$

Figure 2.4: Three jet contributions to event shapes.

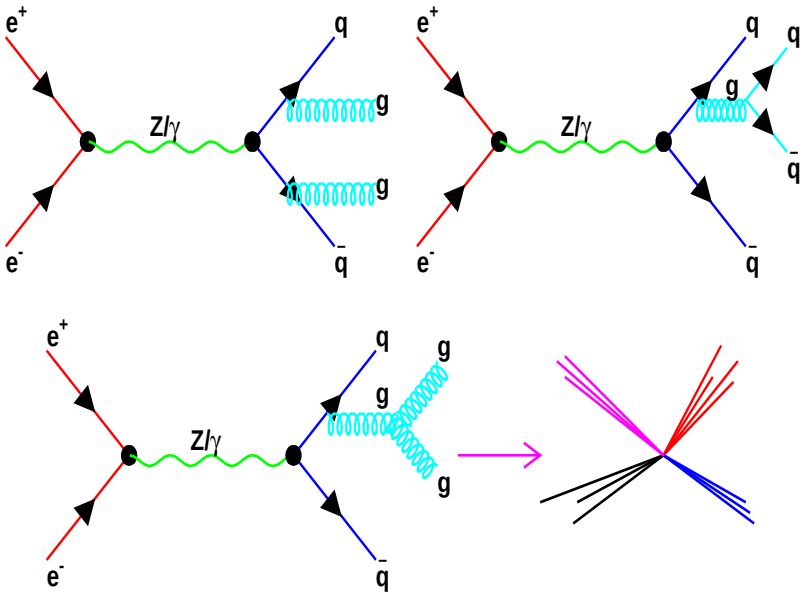

$$\begin{array}{c} \mathrm{T} \in [\frac{1}{\sqrt{3}}, 1] \\ \underline{\text{Planar Topology}} \\ (\mathrm{C})_{max} = 1 \\ \underline{\text{Spherical Topology}} \\ (\mathrm{B_T})_{max} = \frac{\pi}{8} \\ (\mathrm{B_W})_{max} = \frac{\pi}{16} \end{array}$$

Figure 2.5: Four jet contributions to event shapes.

Smaller theoretical errors: Improved resummation calculations of the events shape variables are responsible for the better control of theoretical uncertainties in determination of α_{s} than from $\mathrm{R}^{\mathrm{n}}_{jet}$;

Smaller statistical errors: As one can use the distribution the event shape variable for the *total* hadronic event sample, as opposed to only 3-jet sub-sample alone being used for extraction of α_{s} from 3-jet rates, the statistical fluctuation in the estimation of α_{s} is reduced. By matching the complete second order with resummations of leading and next to leading order terms up to all order, the whole dynamic range of the variables can be fitted to estimate α_{s} from event shapes.

2.3 Inclusive Momenta Variables

The phenomenon of colour coherence in QCD implies a destructive interference of soft gluon emission in the region of disordered emission angles. This reduction of the available phase space for parton radiation to an angular ordered region corresponds to a suppression of hadron production to the leading infrared order, ie, at momenta ($x = \frac{2|p|}{\sqrt{s}}$) much less than the beam-energy.

The charged particle momenta can be studied in terms of the variable $\xi = \ln(1/x)$ at various centre-of-mass energies. The predicted dip in the small x region will translate into a hunched-back peak in the ξ distribution.

The asymptotic behaviour of the ξ spectra is expected to be Gaussian [17, 18]. The moments of the ξ distribution are of relative order $\sqrt{\alpha_s}$ in the next-to-leading order corrections rather than α_s (for mean charged particle multiplicity, the corrections are of the order $\sqrt{\alpha_s}\ln\alpha_s$). Fong and Webber [19] have calculated higher order moments in the next-to-leading orders. They have predicted a *Platykurtic* shape for the ξ distribution using a saddle-point expansion. This implies a narrower ξ-peak shifted towards lower x-values, skewed and flattened towards higher x-values, and the tail falling off faster than Gaussian.

2.3.1 Theoretical Predictions for ξ Distribution

The asymptotic form of the ξ-distribution at a momentum scale Q is predicted to be Gaussian, with the peak evolving linearly like $\ln(Q/\Lambda)$, and the width increasing like $[\ln(Q/\Lambda)]^{3/4}$ [17]. The next-to-leading order corrections have been found to be important. The corrections to the mean [18] and those for the width and higher moments [19] are now available.

In terms of the QCD scale, Λ, and active number of flavours, N_f, and colours, N_c, the mean ($\bar{\xi}$), width (σ), skewness (s) and kurtosis (k) of the ξ-distribution are given as :

$$\begin{aligned}
\bar{\xi} &= \frac{1}{2}\tau\left(1+\frac{\rho}{24}\sqrt{\frac{48}{\beta\tau}}\right)+C \\
\sigma &= \sqrt{\frac{\tau}{3}}\left(\frac{\beta\tau}{48}\right)^{\frac{1}{4}}\left(1-\frac{\beta}{24}\sqrt{\frac{48}{\beta\tau}}\right)+\mathcal{O}(\tau^{-\frac{1}{4}}) \\
\mathrm{s} &= -\frac{\rho}{16}\sqrt{\frac{3}{\tau}}\left(\frac{48}{\beta\tau}\right)^{\frac{1}{4}}+\mathcal{O}(\tau^{-\frac{5}{4}}) \\
\mathrm{k} &= -\frac{27}{5\tau}\left(\sqrt{\frac{\beta\tau}{48}}-\frac{\beta}{24}\right)+\mathcal{O}(\tau^{-\frac{3}{2}})
\end{aligned}$$

where

$$\begin{aligned}
\tau &= \ln(E_{jet}/\Lambda) \;\;;\;\; E_{jet} = E_{beam} = \sqrt{s}/2 \\
\beta &= 11 - 2N_f/N_c \;\;;\;\; \rho = 11 + 2N_f/{N_c}^3
\end{aligned}$$

and the parameter C is independent of scale Λ.

From the higher moments, Fong and Webber proposed the following parametrisation of the ξ-distribution (*platykurtic shape*):

$$F(\xi) \;=\; \frac{\mathrm{n_{ch}}}{\sigma\sqrt{2\pi}}\exp\left[\frac{1}{8}k-\frac{1}{2}s\delta-\frac{1}{4}(2+k)\delta^2+\frac{1}{6}s\delta^3+\frac{1}{24}k\delta^4\right]$$

where $\delta = (\xi-\bar{\xi})/\sigma$ and $\mathrm{n_{ch}}$ (mean charge multiplicity) is the overall normalisation constant.

Taking the active numbers of colours and flavours both to be three, one can fit the ξ-spectra near its peak to both Gaussian and skewed Gaussian form, where the suppression of hadrons due to soft gluon emission is dominant.

The skewed Gaussian parametrisation involves three free parameters to the leading order : $\mathrm{n_{ch}}$, Λ, and C. The peak position, $\xi^\star$, can be determined by differentiating the $F(\xi)$.

The $\xi^\star$ is given by:

$$\xi^\star = \sigma\delta^\star + \bar{\xi},$$

where $\delta^\star$ is a solution of the equation :

$$\delta^3 + 3\mathrm{A}\delta^2 - \mathrm{B}\delta + \mathrm{C} \;=\; 0$$

with

$$\begin{aligned}\mathrm{A} &= \frac{\mathrm{s}}{\mathrm{k}}\;;\\ \mathrm{B} &= -\frac{3(2+\mathrm{k})}{\mathrm{k}}\;;\\ \mathrm{C} &= -\frac{3\mathrm{s}}{\mathrm{k}}.\end{aligned}$$

In terms of $\mathrm{P} = \mathrm{B} - 3\mathrm{A}^2$, $\mathrm{Q} = 2\mathrm{A}^2 - \mathrm{AB} + \mathrm{C}$ and the cubic discriminant $\mathrm{D} = (27\mathrm{Q}^2 + 4\mathrm{P}^3)/27$, we have:

$$\delta^\star \;=\; \left(\frac{\sqrt{\mathrm{D}}-\mathrm{Q}}{2}\right)^{\frac{1}{3}} - \left(\frac{\sqrt{\mathrm{D}}+\mathrm{Q}}{2}\right)^{\frac{1}{3}} - \mathrm{A}$$

The error on $\xi^\star$ is obtained using the covariance matrix of the three fitted parameters. Thus, for the error on $\xi^\star = \xi^\star(\tau, \mathrm{n_{ch}}, \mathcal{O}(1))$, we have

$$\Delta\xi^\star \;=\; \left[\left(\frac{\partial\xi^\star}{\partial\tau}\right)^2\mathrm{Cov}(\tau,\tau) + 2\frac{\partial\xi^\star}{\partial\tau}\mathrm{Cov}(\tau,\mathcal{O}(1)) + \mathrm{Cov}(\mathcal{O}(1),\mathcal{O}(1))\right]^{\frac{1}{2}}$$

2.4 Gaps in e^-e^+ Annihilations

Bjorken [20] discussed the possibility of colour singlet exchange in hard diffractive hadron-hadron scattering characterised by large rapidity gap events. 1% of events with at least two high transverse energetic jets have been observed [21] to have no particle activity in large rapidity regions between the two jets in $p\overline{p}$ collisions at Tevatron, Fermilab. 10% of all photo-produced di-jet events in deep-inelastic scattering at the HERA ep collider have also been reported to contain large rapidity gaps [22]. In e^-e^+ annihilations, search for large rapidity gaps have been also conjured to arise out of colour singlet exchange [23].

In this thesis, gaps in three jet events from hadronic Z decays have been investigated. Using crossing symmetry arguments, gaps can be expected to arise out of colour singlet exchange in e^-e^+ annihilations as in $p\overline{p}$ collisions as depicted in the figure 2.6.

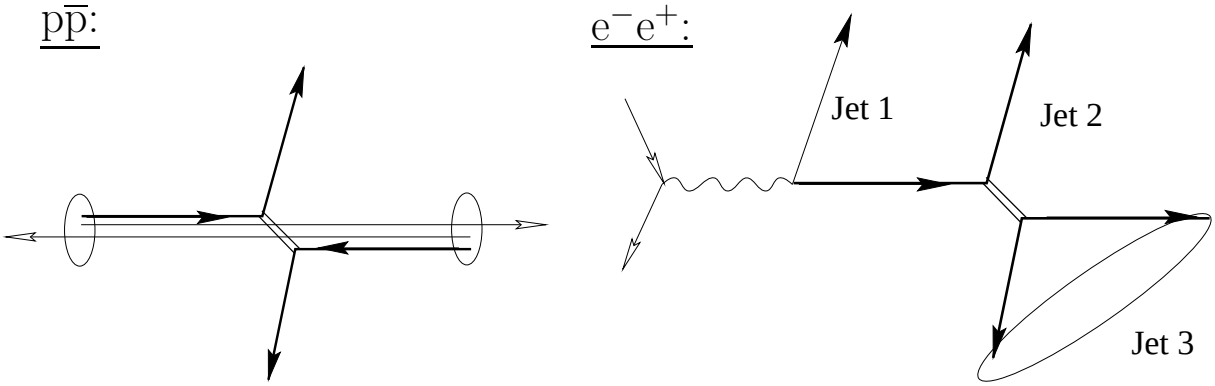

Figure 2.6: Colour singlet exchange in $p\overline{p}$ and in e^-e^+ reactions, depicted by double lines, as related by crossing symmetry.

2.4.1 Particles and Angles

In order to look for colour singlet exchanges, Mercedes type three jet events are studied, and gaps between jets are defined. The definition are motivated from expectations of different particle multiplicity and angular separation between the separation of the jets, as expected from colour flow. In 3 jet events, one expects different colour flow for colour singlet exchange and a colour octet exchange, as given below:

Colour Octet exchange	Colour Singlet Exchange
Colour flow between qg & $\overline{q}$g	–
Destructive interference between q$\overline{q}$	Colour flow between between q$\overline{q}$

Let the jets be ordered in energy, so that the first two most energetic jets are more probable to be from primary quarks. In order to have minimum bias from fragmentation,

the core of the jets is left out in the definition of the gaps. Accordingly, cone is constructed around the each of the 3 jets, with fixed opening angles. This study has been done for $\text{cone}_{\text{angle}} = 15°, 20°$.

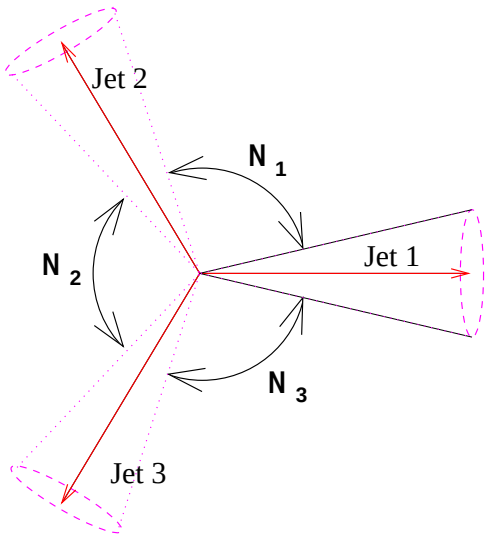

Figure 2.7: Particles in the gaps in Mercedes three jet events.

All the remaining particles between the jets constitute the gaps, as shown in the figure 2.7. Let the number of particles in the i^{th} gap be N_i ($i = 1, 2, 3$ stands for gap between the jets (1,2), (2,3) and (3,1) respectively). The colour exchange properties of the gaps can be studied using particle asymmetries [24]. The particle asymmetry in gap 1 is given by: $\mathcal{A}_{12} = \frac{-N_1+N_2+N_3}{N_1+N_2+N_3}$. Similarly, one can define $\mathcal{A}_{23}$ and $\mathcal{A}_{31}$.

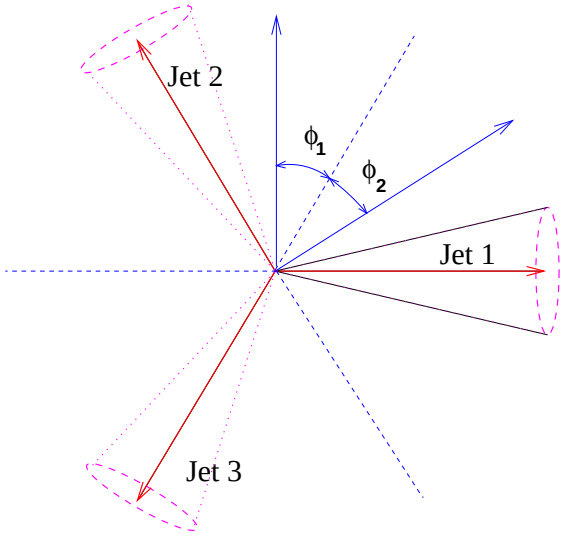

Figure 2.8: Angles in the gaps in Mercedes three jet events.

The properties of the gaps can also be studied in terms of the gap angles. Two definition of angles are used: minimum opening angle measured from the bisector in the gap (B-angle), and maximum separation angle of all the particles in the gap (S-angle). For example, B-angle in gap 1 is defined as: $B_{12} = \mathrm{Min}(\phi_1,\phi_2)$ (see figure 2.8). Let us define angular asymmetry in gap 1 as: $A^B_{12} = \frac{-B_{12}+B_{23}+B_{31}}{B_{12}+B_{23}+B_{31}}$. Similarly, define A^B_{23} and A^B_{31}. Alternatively, asymmetries can also be defined from the S-angle as: $A^S_{12} = \frac{-S_{12}+S_{23}+S_{31}}{S_{12}+S_{23}+S_{31}}$. Similarly, define A^S_{23} and A^S_{31}.

2.4.2 Octet vs Singlet

The colour flow in the gaps is expected to give more particles (N) and smaller angular separation (ψ_i stands for B-angle or S-angle of the i^{th} gap). Let us assume that the jets have been ordered such that the third jet is the gluon jet in the case of colour octet exchange. Lack of colour flow in gaps adjacent to color singlet exchange should thus be associated with reduced particle flow and larger gap angles. Typical ordering of variables as expected for the two scenarios are listed in the table 2.1 (see figure 2.9). Thus using these asymmetries one can distinguish between these two scenarios.

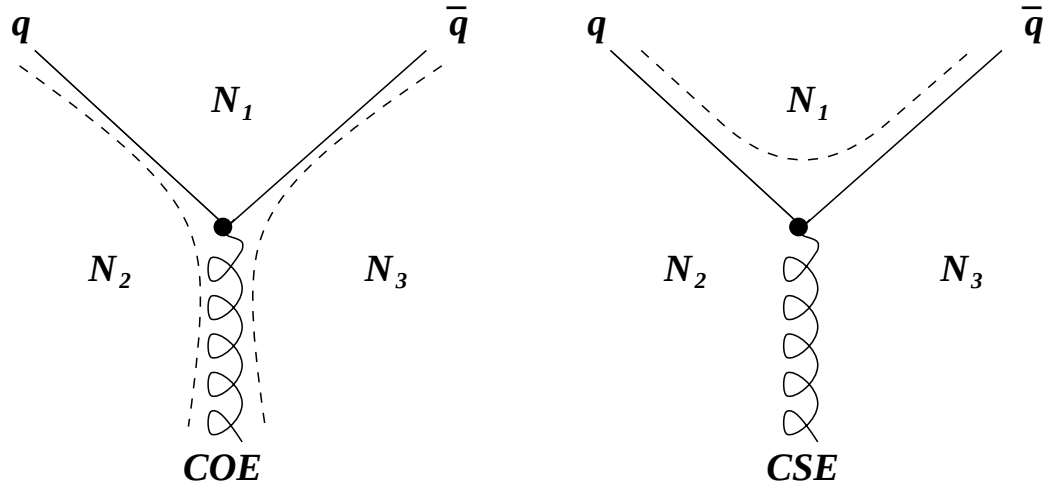

Figure 2.9: Comparison of variables in singlet and octet exchange.

Colour Octet exchange	Colour Singlet Exchange
$N_2 \approx N_3 > N_1$ $\mathcal{A}_{23} \approx \mathcal{A}_{31} < \mathcal{A}_{12}$	$N_2 \approx N_3 < N_1$ $\mathcal{A}_{23} \approx \mathcal{A}_{31} > \mathcal{A}_{12}$
$\psi_2 \approx \psi_3 < \psi_1$ $A_{23} \approx A_{31} > A_{12}$	$\psi_2 \approx \psi_3 > \psi_1$ $A_{23} \approx A_{31} < A_{12}$

Table 2.1: Ordering of variables in singlet and octet exchange.

References

[1] G. Sterman and S. Weinberg, Physical Review Letters **39** (1977) 1436.

[2] T. Kinoshita, J. Math. Phys. **3** (1962) 650;
T.D. Lee and M. Nauenberg, Phys. Rev. **B133** (1964) 1549.

[3] J.E. Huth *et al.*, *Proc. Summer Study on High Energy Physics*, Snowmass, Colorado, 1990, FERMILAB-Conf.-90/249-E.

[4] JADE Collaboration, W. Bartel *et al.*, Zeitschrift für Physik **C33** (1986) 23;
JADE Collaboration, S. Bethke *et al.*, Physics Letters **B213** (1988) 235.

[5] Yu.L. Dokshitzer, Contribution to the Workshop on Jets at LEP and HERA, Durham (1990);
N. Brown and W.J. Stirling, Rutherford Preprint RAL-91-049;
S. Catani *et al.*, Physics Letters **B269** (1991) 432;
S. Bethke *et al.*, Nuclear Physics **B370** (1992) 310.

[6] Z. Kunszt and P. Nason in "Z Physics at LEP 1", CERN Report 89-08, Vol.I., p. 373.

[7] S. Catani *et al.*, Nucl. Phys. **B407** (1993) 3.

[8] S. Bethke *et al.*, Nucl. Phys. **B370** (1992) 310.

[9] Yu.L. Dokshitzer, B. R. Webber, Phys. Lett. **B352** (1995) 451;
B.R. Webber, HEP-PH-9510283;
Yu.L. Dokshitzer *et al.*, Nucl. Phys. **B511** (1997) 396;
Yu.L. Dokshitzer *et al.*, J.HEP. 05 (1998) 3;
Yu.L. Dokshitzer *et al.*, HEP-PH-9812487.

[10] S. Catani *et al.*, Phys. Lett. **B263** (1991) 491.

[11] S. Catani *et al.*, Phys. Lett. **B272** (1991) 368.

[12] S. Catani *et al.*, Phys. Lett. **B295** (1992) 269.

[13] S. Catani and B.R. Webber, Phys. Lett. **B427** (1998) 377.

[14] S. Brandt *et al.*, Phys. Lett. **12** (1964) 57;
E. Fahri, Phys. Rev. Lett. **39** (1977) 1587.

[15] T. Chandramohan and L. Clavelli, Nucl. Phys. **B184** (1981) 365;
Mark II Collaboration, A. Peterson *et al.*, Phys. Rev. **D37** (1988) 1;
TASSO Collaboration, W. Braunschweig *et al.*, Z. Phys. **C45** (1989) 11.

[16] G. Parisi, Phys. Lett. **B74** (1978) 65;
J. F. Donoghue, F. E. Low, and S. Y. Pi, Phys. Rev. **D20** (1979) 2759.

[17] A.H. Mueller, in *Proc. 1981 International Symposium on Lepton and Photon Interactions at High Energies*, ed. W. Pfeil (Bonn, 1981), p.689; Yu.L. Dokshitzer, V.S. Fadin and V.A. Khoze, Phys. Lett. **B115** (1982) 242.

[18] A.H. Mueller, Nucl. Phys. **B213** (1983) 85, *ibid.* **B241** (1984) 141.

[19] C.P. Fong and B.R. Webber, Phys. Lett. **B229** (1989) 289.

[20] J.D. Bjorken, Physical Review **D47** (1993) 101.

[21] DØ collaboration, S. Abachi *et al.*, Physical Review Letters **72** (1994) 2332;
Cdf collaboration, F. Abe *et al.*, Physical Review Letters **74** (1995) 855;
DØ collaboration, S. Abachi *et al.*, Physical Review Letters **76** (1996) 734;
Cdf collaboration, F. Abe *et al.*, Physical Review Letters **78** (1997) 2698;
Cdf collaboration, F. Abe *et al.*, Physical Review Letters **79** (1997) 2636;
DØ collaboration, B. Abbott *et al.*, Physics Letters **B440** (1998) 189;
Cdf collaboration, F. Abe *et al.*, Physical Review Letters **81** (1998) 5278.

[22] H1 collaboration, T. Ahmed *et al.*, Nuclear Physics **B429** (1994) 477;
Zeus collaboration, M. Derrick *et al.*, Physics Letters **B332** (1994) 228;
Zeus collaboration, M. Derrick *et al.*, Physics Letters **B369** (1996) 55.

[23] J. Ellis and D.A. Ross, Zeitschrift für Physik **C70** (1996) 115.

[24] John Field, private communication.

Chapter 3

e^-e^+ Annihilation at LEP

3.1 Introduction

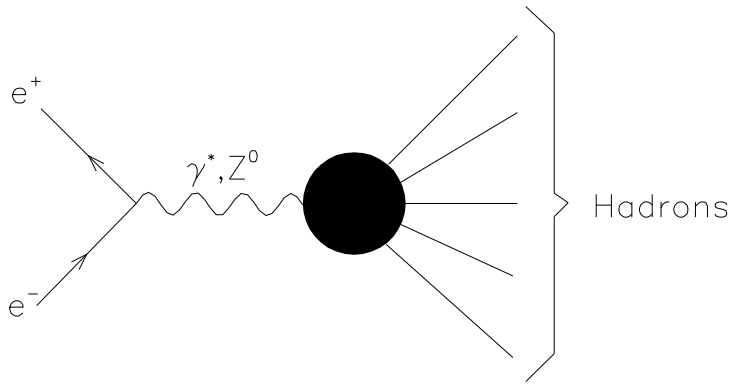

Figure 3.1: The reaction under study: $e^-e^+ \rightarrow$ *hadrons*.

e^-e^+ annihilation provides an ideal laboratory to study the processes of hard and soft gluon emissions and many other aspects of the strong interaction. A summary of the deep insights gained by studying strong interaction in e^-e^+ annihilations has already been listed in chapter 1.

Precise measurements of QCD are possible at high energy e^-e^+ annihilation machines because it offers:

★ *clean* initial state (e^-e^+); and

★ *small* hadronisation corrections ($\propto 1/E$).

3.2 Large Electron Positron Collider (LEP)

LEP was designed [1] to operate at beam energies between 40 and 100 GeV corresponding to the centre-of-mass energies of Z boson and W/Z boson pair production. It has been running for the last decade at CERN, the European Organisation for Nuclear Research, on the border of Switzerland and France, as illustrated in the figure 3.2.

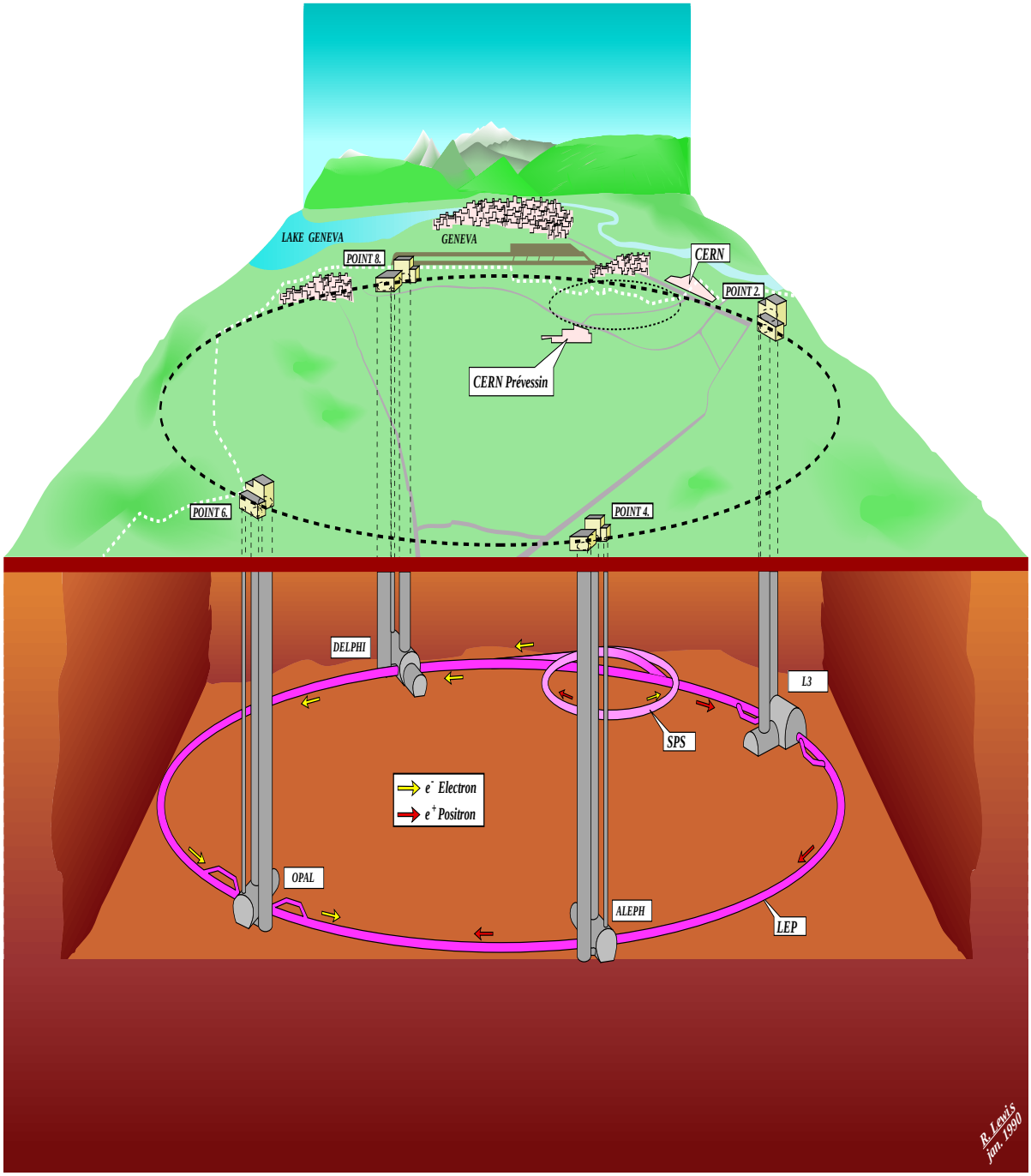

Figure 3.2: Schematic view of the LEP site.

3.2.1 Acceleration Stages

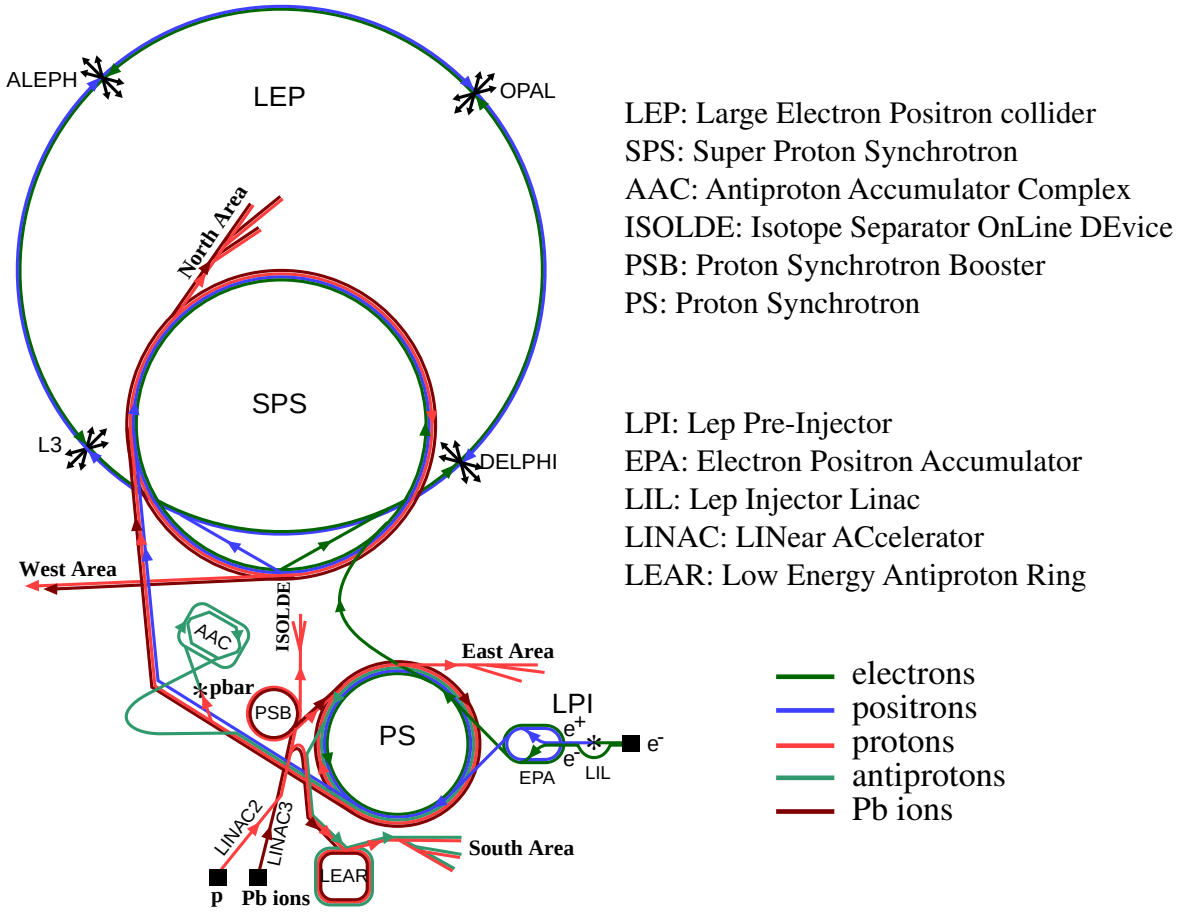

Figure 3.3: Different stages of injectors and accelerators at CERN.

Every circular accelerator has an optimal energy range. The minimum energy is constrained by betatron oscillation (amplitude is inversely proportional to the square root of magnetic field) and the beam spot size. The maximum beam energy is limited by the RF power available and the maximum bending power of the dipole magnets. Different stages of acceleration used to collide particles at the CERN accelerator complex are shown in the figure 3.3.

Electrons are generated by a high current tandem linac, and positrons are generated through bremsstrahlung (followed by pair production) by striking electrons from this 200 MeV linac on a tungsten target.

LEP is the last one in the sequence of the injector chains, the operational energy of the different component of chain being:

	Tandem	LIL	EPA	PS	SPS	LEP
e^-	200 MeV	600 MeV	600 MeV	3.5 GeV	20 GeV	40-100 GeV
e^+	—	600 MeV	600 MeV	3.5 GeV	20 GeV	40-100 GeV

3.2.2 LEP Specifications

Electrons and positrons travel around LEP almost with the speed of light lapping LEP over 11,200 times a second [2]. Some of the LEP parameters [3, 4] are given in the table 3.1.

Shape	:	8 straight + 8 circular
Circumference (m)	:	26,658.9
Depth of tunnel (m below Jura foothills)	:	50 to 175
Detectors	:	ALEPH, L3, DELPHI, OPAL
Data taking period	:	1989 - 2000
Crossing time (μs)	:	22 (4 x 4 bunch mode)
Beam size (μm,μm,cm)	:	(200, 8, 1) at LEP 1
Beam current (mA)	:	4/2.5 (LEP 1/2)
Beam Lifetime (hr)	:	10/5 (LEP 1/2)
Luminosity (10^{30}/cm^2 s)	:	24/100 (LEP 1/2)

Table 3.1: LEP parameters.

Some of the other specifications of LEP are:

Frequency: At LEP, the system of accelerators is based on the radio-frequency oscillation within conducting (and super-conducting) cavities. The operating frequency of the RF cavities is 352.209 MHz, an integral number of times (harmonic number = 31320) of the revolution frequency (time period = 88.9 μs).

Beam Power: To keep the bunches circulating around the LEP, power must be fed into the beam to exactly compensate for the losses. Due to synchrotron radiation, the energy loss per turn per electron is given by $eU_{synchrotron} = 99.5 \text{ X } 10^3 \text{ } E^4_{beam}/r = 262$ MeV (for $E_{beam} = 55$ GeV), and the associated power loss is $2IU_{synchrotron} = 1.57$ MW (for I = 3 mA). There are in addition parasitic mode power loses, coming from excitation to the higher modes due to RF cavities, vacuum systems and electrostatic separators, which contribute respectively 15.5, 1.4 and 1.8 MV (for a bunch length of 15.7 mm and number of particles per bunch $N_e = 4.2 \times 10^{11}$) to the decelerating voltages U_{pm} expressed in terms of charge per bunch (q) or average current per beam (I) as $U_{pm} = k_{pm}\ q = Z_{pm}\ I$. The associated power loss to parasitic modes is given by $P_{pm} = 2(I^2\ Z_{pm})$ (for number of electron/positron bunches $k_b = 4$) = 0.11 MW (for I = 3 mA). Thus, the total beam power is 1.57 + 0.11 = 1.68 MW.

Lifetime: The vacuum inside the LEP beam pipe, 10^{-9} torr, is a billionth of atmospheric pressure. High vacuum is needed to make sure that electrons and positrons circulating in LEP do not collide with molecules inside the beam pipe. The contribution to beam lifetime coming from beam-gas interaction is 200 hrs.

Other factors which contribute towards beam life time are interactions with thermal photons (100/50 hrs for LEP 1/2), and beam-beam bremsstrahlung (25/12.5 hrs for LEP 1/2). The total lifetime τ is obtained [5] by summing the individual contributions: $1/\tau = \sum 1/\tau_i$.

Magnets: The specifications of the LEP magnets are listed below:

Number of dipole bending magnets	:	3368
Number of focusing quadrupoles	:	816
Number of focusing sextupoles	:	504
Number of correcting magnets	:	700

All of these LEP components are aligned to an accuracy of 0.1 mm, and so precise is the measurement of the beam energy that LEP can detect the orbit of the moon, heavy rainfall, and changing water levels in Lake Geneva. Even the departure of the TGV from Geneva does not escape LEP's attention.

The number of LEP's accelerating cavities has undergone a gradual rise through the years, as given below:

Date	Number of Copper cavities	Number of Superconducting cavities	Accelerating voltage per lap in Megavolt (MV)
1990	128	0	300
Nov. 1995	120	60	750
June 1996	120	144	1600
Oct. 1996	120	172	1900
1997	86	240	2500
1998	52	272	2700

Luminosity: The luminosity for colliding beams is given by :

$$\mathcal{L} = \frac{N_e N_p n_b f_{rev}}{4\pi\sigma_x\sigma_y}$$

- $N_{e,p}$: number of e^-, e^+ per bunch,
- n_b : number of bunches per beam,
- f_{rev} : revolution frequency of the beams and
- $\sigma_{x,y}$: transverse beam sizes at the interaction point.

The rate of interactions is directly proportional to the luminosity :

$$\mathrm{N} = \sigma \ . \ \mathcal{L}$$

where σ is the interaction cross section.

The design luminosity of LEP, $1.3 \times 10^{31}\ cm^{-2}sec^{-1}$, has been exceeded in 1993 [6]. $17 \cdot 10^6$ Z decays have been recorded at LEP 1 by the 4 experiments between 1989-1995.

The target luminosity at LEP 2 was 500 pb^{-1}. Up to 1999, LEP has already delivered a luminosity of 12.1+11.3 ('96) + 63.8 ('97) + 196.4 ('98) + 253.7 ('99) = 537 pb^{-1} above the W^-W^+ threshold. A summary of LEP luminosity from 1993-1999 is given in the figure 3.4.

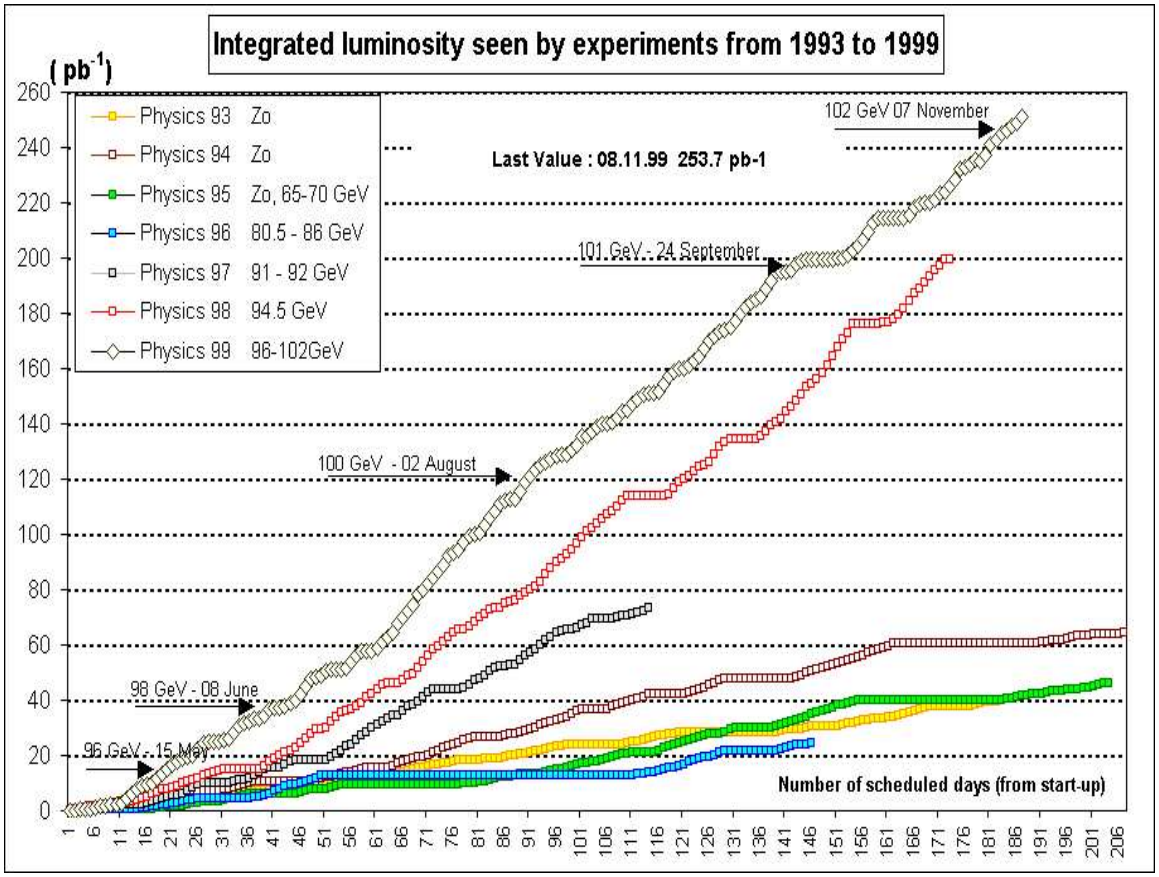

Figure 3.4: Summary of LEP luminosity from 1993-1999.

3.2.3 Energy Record at LEP

Every increase in energy brings the possibility of new discoveries or surprises, and physicists are eagerly waiting to see what the revamped LEP will reveal. A brief history of the energy upgrade at LEP is given below [7]:

1989 : On 13^{th} August 1989, the first collisions took place in experiments on CERN's 27km accelerator, LEP. Acceleration was performed using the room temperature copper

radio-frequency system which consisted of 128 five cell cavities with a potential voltage of 400MV. In parallel with the successful operation on the Z peak until 1995, research and development was being carried out to provide the technology and production techniques for high gradient superconducting cavities.

1995 : A few test modules of superconducting cavities were installed which allowed the energy to be raised to 70 GeV/beam.

1996 : The beam energy reached the W-pair production energy for the first time and physics data was taken at beam energies between 80.5 and 86 GeV.

1996-1997 : During the winter shutdown a further complement of superconducting cavities was installed, raising the total complement to 192 cavities.

1997 : The beam energies were at 91-92 GeV, well above the W-pair threshold.

1998 : LEP operated at 94.5 GeV with 272 superconducting cavities. Record integrated luminosity of 200 pb^{-1}.

1999 : Subsequent increases in beam energy from 96 GeV in May, to 98 GeV in July, culminating with 100 GeV on 2 August 1999 at 11h15 hrs. At this energy LEP operates at the limit on many fronts; in particular the radio-frequency system which, optimistically designed for gradients of 6 MV/m, must operate all 288 cavities at an average gradient of 7 MV/m. The total RF voltage per turn needed is 3400 MV, and the synchrotron radiation beam power at this energy is a staggering 18 MW, testing the vacuum components to the limit and requiring careful control of the experiments' background. Nevertheless the first physics run at 200 GeV collision energy was very successful, resulting in more than 320 nb^{-1} in each of the four detectors.

References

[1] LEP Design report CERN-LEP/84-01 (1984), Vol II.

[2] Press release PR 05.96 - 10.07.96 by CERN.

[3] Ian Wilson and Heino Henke, "The LEP Main Ring Accelerating Structure", CERN Yellow Report 89-09.

[4] Particle Data Group, C. Caso *et al.*, Eur. Phys. J. **C3** (1998) 1.

[5] Report by the working group on "Interaction Regions" *CERN Yellow Report 96-01, Vol.1* p. 45, eds. G. Altarelli, T. Sjöstrand and F. Zwirner.

[6] G. Arduini *et al.*, *LEP Operations, 1989-1995*, **CERN-SL/96-043**.

[7] Press release PR 09.99 - 04.08.99 by CERN.

Chapter 4

L3: Apparatus and Data Taking

4.1 L3 Detector

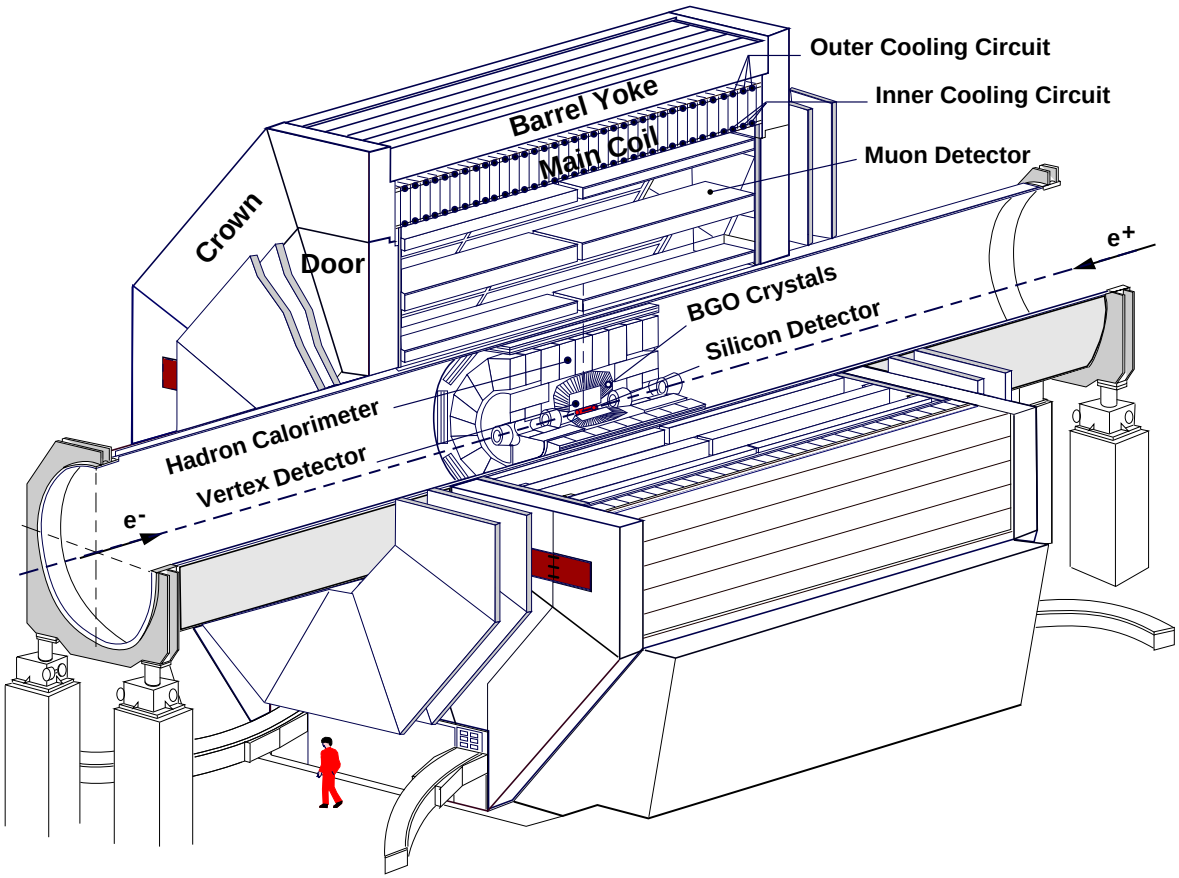

Figure 4.1: Perspective view of L3 detector.

The L3 detector (figure 4.1), located at the second interaction point (IP2), is the largest of the four experiments at LEP: ALEPH [1], DELPHI [2], L3 [3] and OPAL [4].

L3, 14 m long and 16 m in diameter, is a hermetic detector with 99% of the 4π angular coverage. The tracking system (consisting of the SMD, the TEC, the z-chambers and the FTC), barrel and endcaps of the electromagnetic calorimeter, the scintillating counters in the barrel and the endcap, the barrel and the endcap of the hadron calorimeter, the active lead rings, and the luminosity monitor are housed inside a 32 m long, 4.45 m diameter support tube (see figure 4.2). Around this support tube, the muon chamber forms three concentric layers in the barrel and a set of 3 layers in the endcap. All the sub-detectors (except a part of the endcap muon detector) are immersed in an uniform 0.5 Tesla magnetic field along the beam direction, provided by 7.8 Kton octagonally shaped solenoidal magnet; and there is an additional 1.5 Tesla toroidal magnetic field on the doors (for the endcap muon detector). The angular coverage of the different sub-detectors are also shown in the figure 4.2 in terms of the polar angle. The individual sub-detectors are described in the following sub-sections.

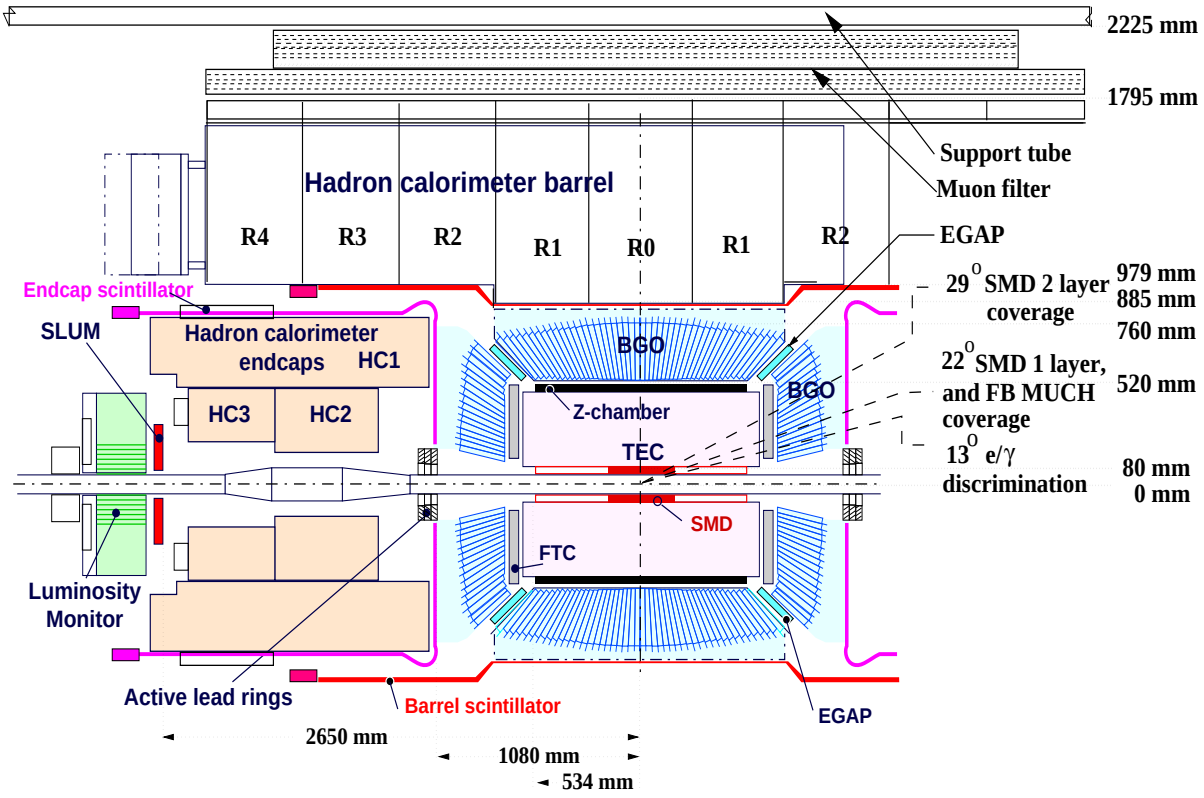

Figure 4.2: Inner components of the L3 detector.

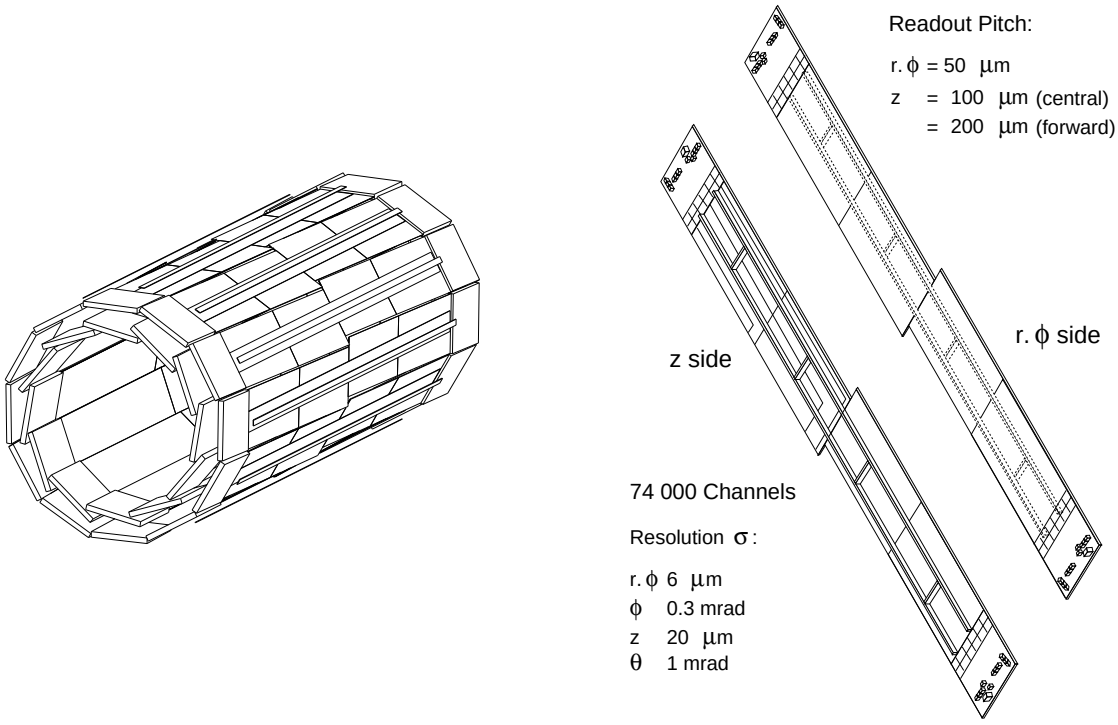

Figure 4.3: Perspective view of the Silicon microvertex detector and one of the ladders.

4.1.1 Silicon Microvertex Detector

Two layers of double sided Silicon Microstrip Detectors (SMD) [5], installed to record position information accurately, are positioned at 6 cm and 8 cm from the beam line, giving a ≈ 90 % solid angle coverage. Each layer has 12 modules which in turn has 4 sensors of dimensions 70 mm $\times$ 40 mm $\times$ 300 μm. The material corresponds to 0.012 radiation length (X_0) at normal incidence. The pitch and resolution are:

	readout pitch	resolution (λ = dip angle)
junction side (r-ϕ)	50 μm	10 μm
ohmic side (z)	150 μm	$(21 \oplus 15 \cdot \tan\lambda)$ μm
ohmic side (z)(forward region)	200 μm	$(21 \oplus 26 \cdot \tan\lambda)$ μm

4.1.2 Time Expansion Chamber

The Time Expansion Chamber (TEC) [6] measures the time of arrival of the ionisation electrons at the anode wires, relative to a marker reference, to reconstruct the curvature of a charged track bending in the magnetic field in which the detector is immersed. Slow drift velocity in a low diffusion gas in the drift region, followed by fast absorption by strong fields generated by focus wire near the anode characterise its modus operandi (see figure 4.4(a).

The volume occupied by the TEC is: 8.5 cm $< r <$ 47 cm, 63 cm $< |z|$, and it comprises of 12 inner sectors with 8 anodes, and 24 outer sectors with 54 anodes. The gas mixture

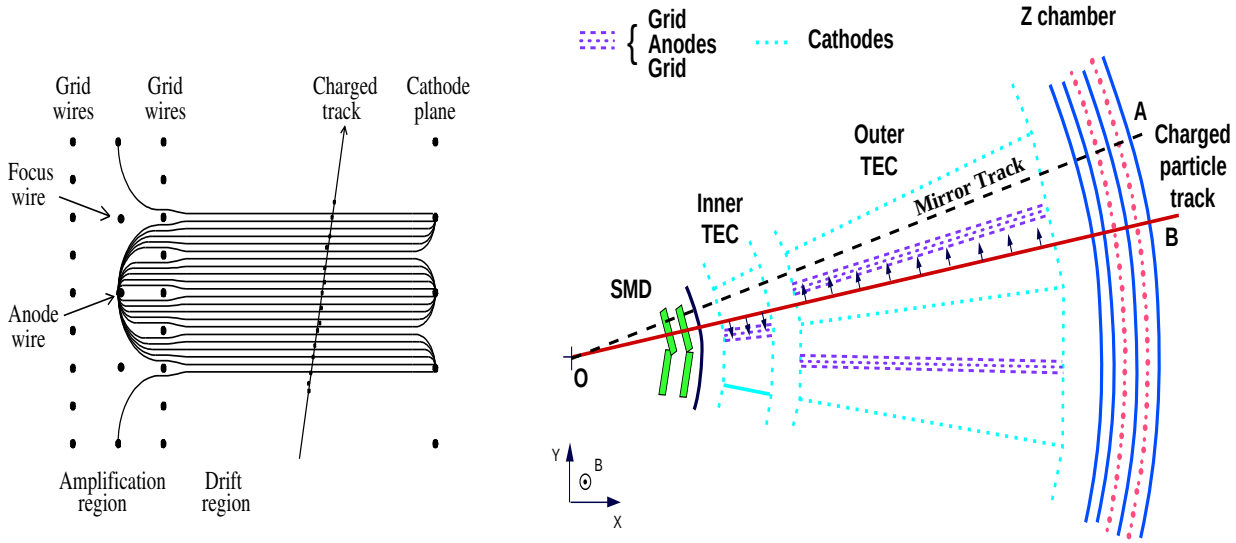

(a) Drift and amplification region of TEC.

(b) r-ϕ view of the central tracking system.

Figure 4.4: Time Expansion Chamber.

used is: 80% CO_2 + 20% iso-C_4H_{10} at pressure 2 bar with low diffusion coefficient, and low drift velocity ≈ 6 μm/ns. Measurement of the distance of the track from the anode plane is read out using Flash ADC with a centre-of-gravity method giving better spatial resolution.

The single wire resolution is 51 μm, and the double track resolution is 650 μm. Mirror tracks are resolved by matching the hits with the inner TEC and SMD (figure 4.4(b)). The transverse momenta resolution of the TEC is: $\frac{\sigma_{P_T}}{{P_T}^2} = 0.018/\text{GeV}$, and the effect of improvement by the inclusion of SMD is shown in the figure 4.5.

4.1.3 Z Chambers

Two layers of Z chambers surrounding the TEC, at radial distances between 48 cm and 49 cm and having $|z|$-extent $<$ 51cm, provide accurate measurements of z-coordinates of points along the trajectory of a charged particle. These chambers are proportional wire chambers with thickness 21.5 mm (~ 0.013 X_0). The wire chambers operate in drift mode, with gas mixture of 80% Ar + 20% CO_2. Ionisation signals are read out by cathode strips, inclined with respect to the beam axis by $0°, 90°, \pm 69°$. This gives us a z-coordinate resolution of 320 μm and double track resolution of 7 mm.

4.1.4 Forward Tracking Chambers

Two layers of Forward Tracking Chambers (FTC) were installed in 1991, at the two ends of the TEC (figure 4.2) and covers the polar angle region $9.5° < \theta$, $(180° - \theta) < 37.5°$.

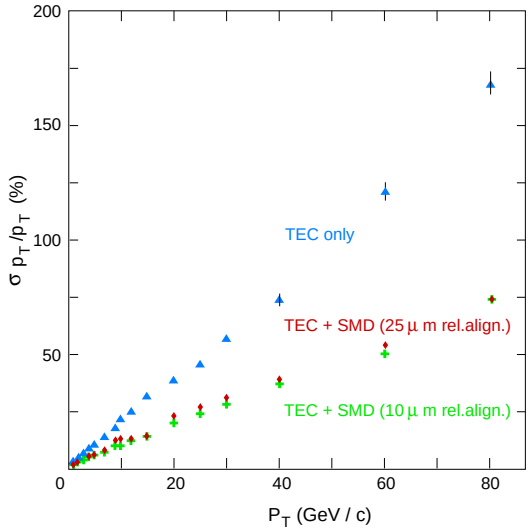

Figure 4.5: Transverse momentum resolution of the charged particles in the central tracking system before and after installation of the SMD.

The FTC uses a gas mixture of 38.5% ethane and 61.5% Ar and operates in drift mode. Spatial resolution of the FTC is better than 200 μm and angular resolution is better than 10 mrad [8].

4.1.5 Electromagnetic Calorimeter

The Electromagnetic Calorimeter (ECAL) [9] (figure 4.6), made of homogeneous Bismuth Germanium Oxide (BGO) crystals, measures total energy of electrons, positrons and photons accurately and serves as the first interaction length for measurements of hadrons along with the hadron calorimeter.

The front face of a BGO crystal in the barrel is $2cm \times 2$ cm, the back is $3cm \times 3$ cm and has a length of 24 cm ($\approx 22\ X_0$). The specifications of a BGO are:

Density	7.13 gm/cc
Radiation length	1.12 cm
Moliere radius	2.4 cm
Peak emission	480 nm
Decay time of light	300 ns
Temperature coefficient	$-1.55\%/^\circ$ C
Nuclear interaction length	22 cm

There are 7680 crystals in the barrel and 3054 in the endcap, the temperature is monitored for 1 in 12 crystals. The material before ECAL barrel is $0.3 - 0.4$ X_0.

Each crystal is read out by 2 photo-diodes, with a quantum efficiency of 70%, and gain close to unity. The hadron/electron rejection ratio $\sim 1000 : 1$.

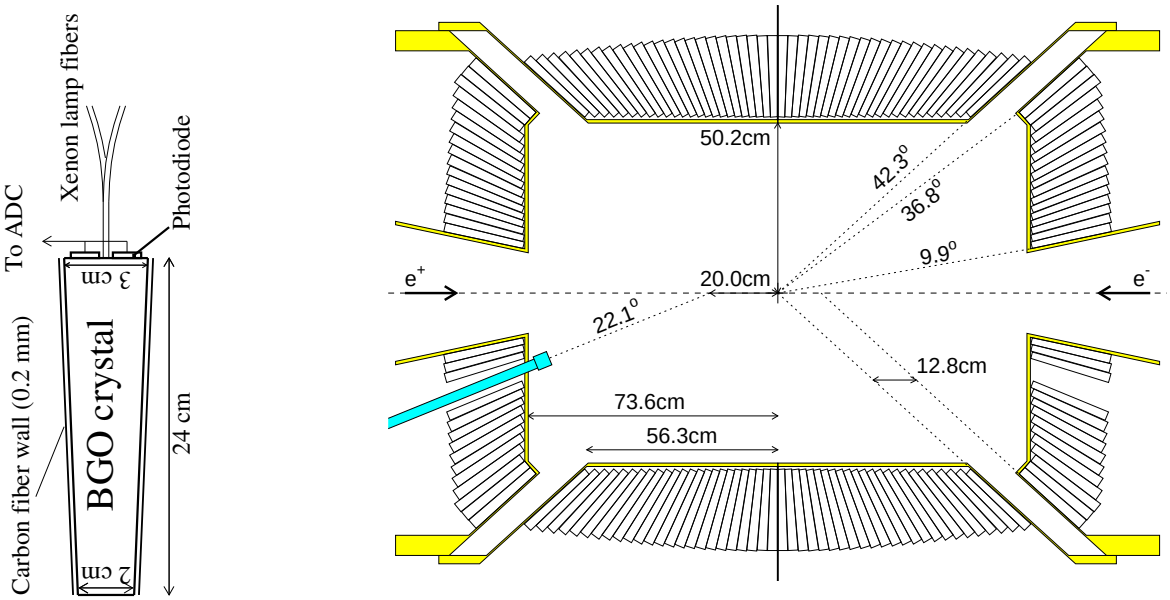

(a) A barrel BGO crystal.

(b) Longitudinal view of BGO detector.

Figure 4.6: BGO crystal and L3 electromagnetic calorimeter.

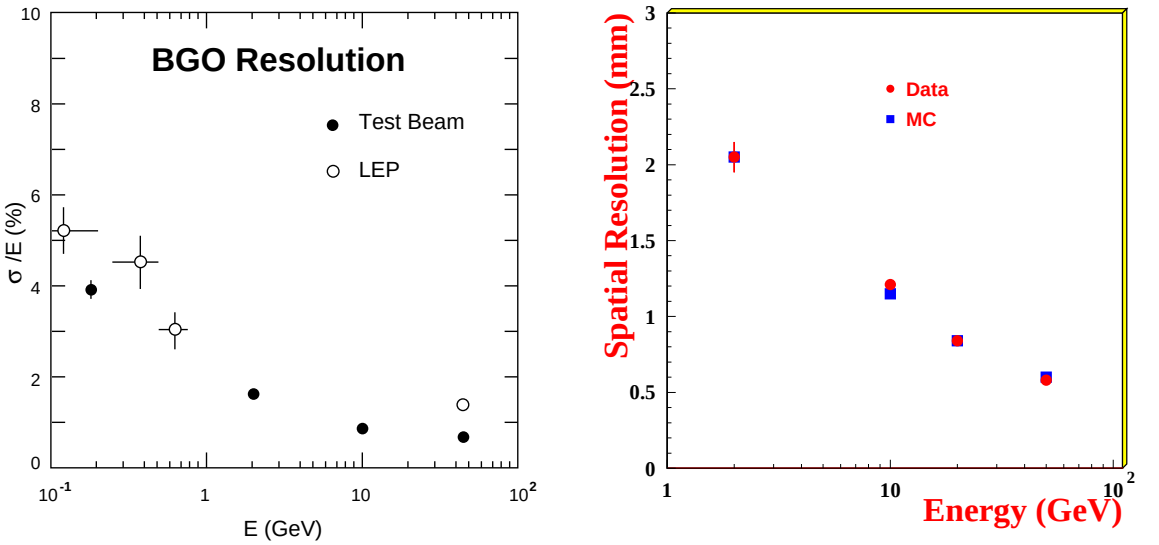

(a) Energy resolution of BGO calorimeter.

(b) Position resolution of BGO calorimeter.

Figure 4.7: Energy and position resolution of barrel BGO calorimeter.

Impact point measurement calculated by computing the energy weighted centroid position (centre of gravity method) gives a position resolution ~ 1 mm and angular resolution ~ 2 mrad.

The BGO barrel calorimeter was calibrated in test beams using electrons of energies 0.18, 2, 10, and 50 GeV. The energy resolution obtained is $\approx 5\%$ at 180 MeV, less than 2% above 2 GeV and about 1.2% at 45 GeV as shown in figure 4.7. The linearity is better than 1%. The position resolution is determined by the centre of gravity method to be $\sim$ 1 mm whereas the angular resolution is ~ 1 mrad for electromagnetic showers at 45 GeV.

4.1.6 Gap Calorimeter

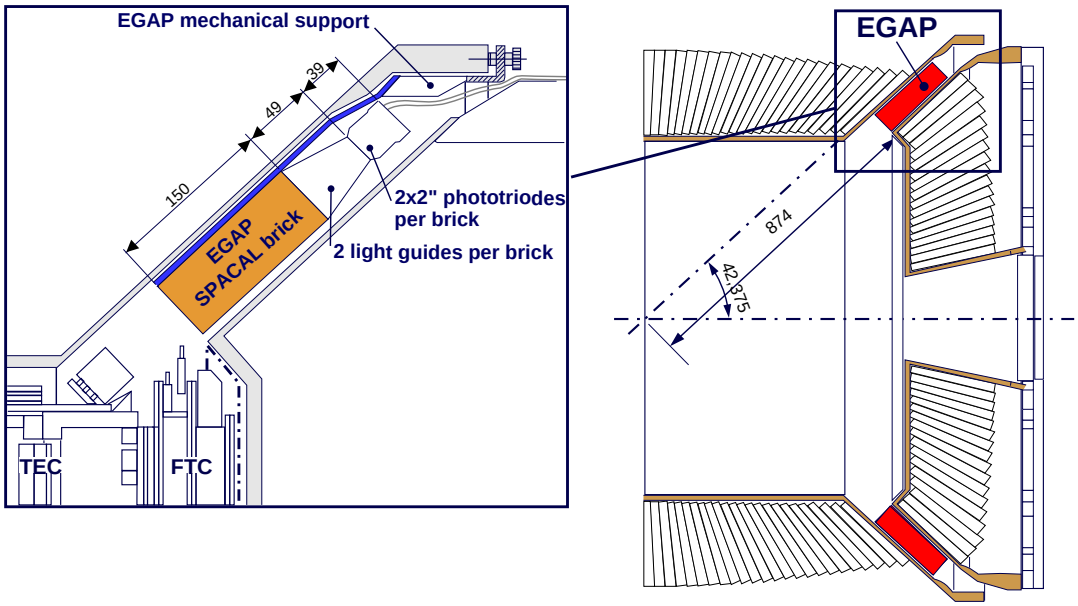

Figure 4.8: Lead-scintillating fibre calorimeter (EGAP).

During the 1995/96 shutdown period, lead-scintillating fibre calorimeter (EGAP) [10] were installed in the gap between ECAL barrel and endcap, to increase the angular coverage (see figure 4.8). Each gap is filled up with 24 modules of trapezoidal blocks. The gap between the modules is tilted by about 25 mrad with respect to the interaction vertex to avoid loss of particles in the cracks.

The ratio in volume between the lead and the fibres is 4:1, giving $X_\circ = 0.72$ cm, in order to ensure sufficient shower containment. The total thickness corresponds to $21\,X_\circ$.

From the test beam study one obtains the energy resolution as:

$$\frac{\sigma(\mathrm{E})}{\mathrm{E}} = \left(2.3 + \frac{11.6}{\sqrt{\mathrm{E(GeV)}}}\right) \%$$

4.1.7 Scintillation Counters

The excellent time resolution of plastic scintillators are used in the scintillation counters to measure the time of the flight of particles passing through the detector with respect to the beam crossing time. These are primarily used to distinguish the cosmic-ray events from the dimuon events, in addition to improving the trigger rate.

The barrel part consists of 30 plastic scintillation paddles of length 2.9 m and thickness 10 mm. Both ends of the paddles are connected by light-guides to photomultipliers. In the rz plane, the counters mark the boundary between the electromagnetic and hadron calorimeter and are at a radial distance of 886mm for $|\mathrm{z}| <$ 800 mm and 979 mm for 800 mm $< |\mathrm{z}| <$ 1000 mm from the beam axis (see figure 4.2). Polar angle coverage of the barrel counters is $34^\circ < \theta < 146^\circ$ ($|\cos\theta| < 0.83$).

The endcap scintillation counter system [11] consists of 16 counters located between the electromagnetic and hadron calorimeter endcaps on either side of the interaction point. Counters are made out of 3 plates of 5mm thick plastic scintillator. Light from each plate is collected by 10 wave-length shifting fibres of diameter 1mm glued into grooves of 1.5mm $\times$1.5mm. 30 fibres per counter-end are connected into an optical connector at the outer edge of the counters. A flexible guide of 30 fibres, each 1.7 m long, connects the counters to the photo tubes which are situated outside the hadron barrel. The counters having an inner (outer) radius of 230 mm (746 mm), are attached to the shielding of the BGO endcaps. The centre of the 2nd scintillator plate is located at a distance of z = $\pm$ 1132.5 mm from the nominal interaction point, giving a polar angle coverage of $11.5^\circ < \theta < 34.1^\circ$ ($0.83 < |\cos\theta| < 0.98$).

A time resolution of 460 ps has been achieved from the dimuon events in the barrel and 1.9 ns in the endcap (see figure 4.9 [8]). The efficiency of the scintillator hit for muon pair events is larger than 99 % [11].

4.1.8 Hadron Calorimeter

The Hadron Calorimeter (HCAL) [12] is a fine sampling calorimeter consisting of layers of uranium ($\lambda_{int} \sim$ 11cm) plates (5-10 mm) and brass plate proportional chambers (5.6 mm). The gas used is 80% Ar + 20% CO_2.

It has a length of 472.5 cm, inner radius of 88.5-97.9 cm, and outer radius of 179.5 cm, with angular coverage ($35^\circ < \theta < 145^\circ$) for the barrel part and ($5.5^\circ < \theta, 180^\circ - \theta < 35^\circ$) for the endcap region. The barrel consists 16 modules in ϕ and 9 modules in z, while the endcap consists of 6 modules made of 3 rings HC1, HC2, HC3. Corresponding to the barrel/endcap parts, there are 7968/2284 chambers, $\sim$ 370/54K wires and $\sim$ 23/4K

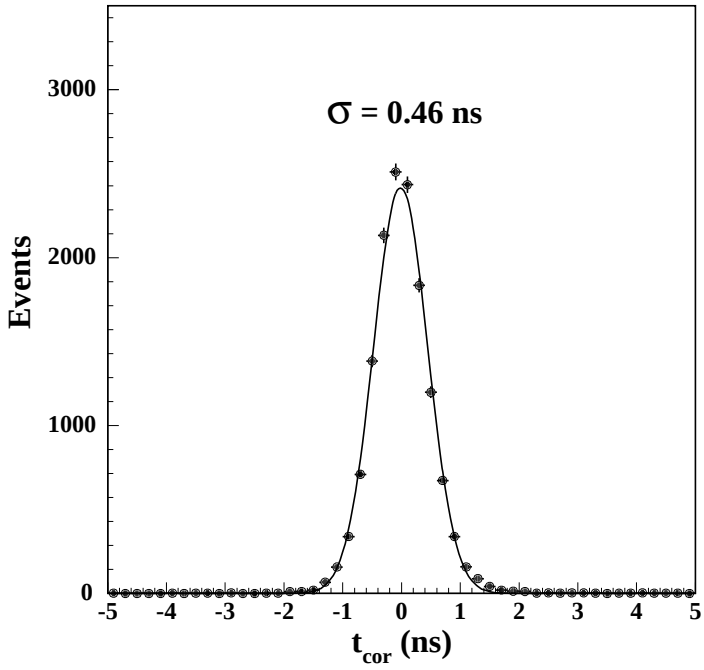

Figure 4.9: Timing resolution of the scintillation counters in the barrel part.

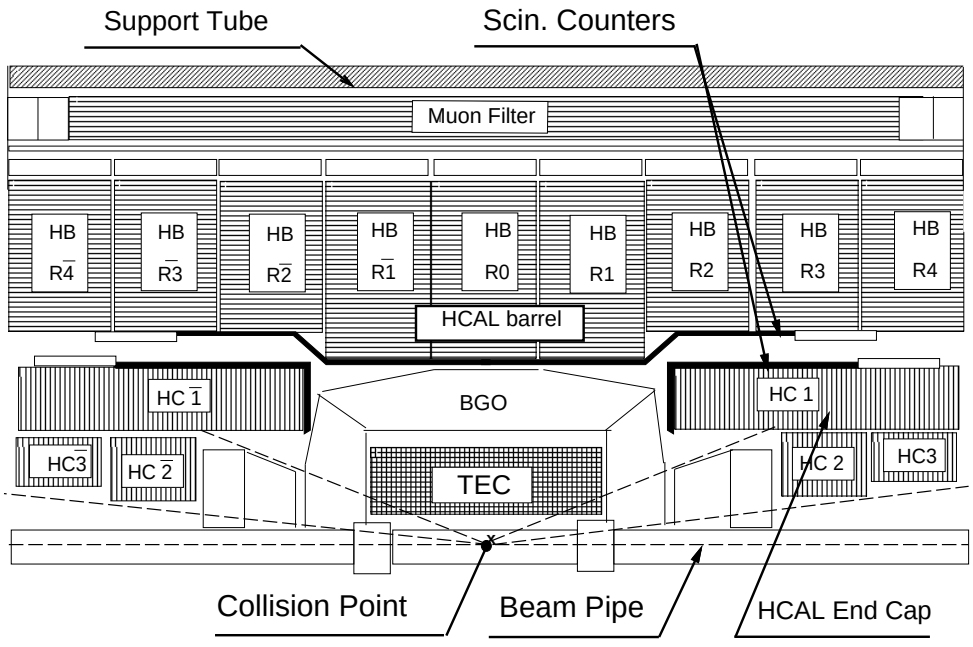

Figure 4.10: r-ϕ view of hadron calorimeter.

readout. The chambers are grouped into towers, with $\Delta\phi \approx 2.5°$, $\Delta z \approx 6$ cm, $\Delta r \approx 8$ cm.

The energy resolution of HCAL is $\frac{\sigma_E}{E} = \frac{55\%}{\sqrt{E}} + 5\%$, and the angular resolution is 2.5°.

Material transversed by a particle is $6 - 7\ \lambda_{int}$ depending upon the angle of incidence. Active Muon Filter [13], absorbing most of the residual hadron shower, adds 1.03 absorption length to HCAL. It comprises of 8 octants, 139 cm long. Each octant is made up of 6 layers of 1cm thick brass absorbers, interleaved with 5 layers of proportional tubes.

4.1.9 Muon Chambers

The Muon Chamber (MUCH) [14] system, made with drift chambers, consists of a barrel part and forward-backward part.

The barrel part comprises of 2 sets of 8 octants. Each Octant has 5 precision (P) chambers: (2 Outer (MO), 2 Middle (MM) and 1 Inner (MI)) and 6 Z-chambers (top and bottom covers of MI and MO) (see figure 4.11).

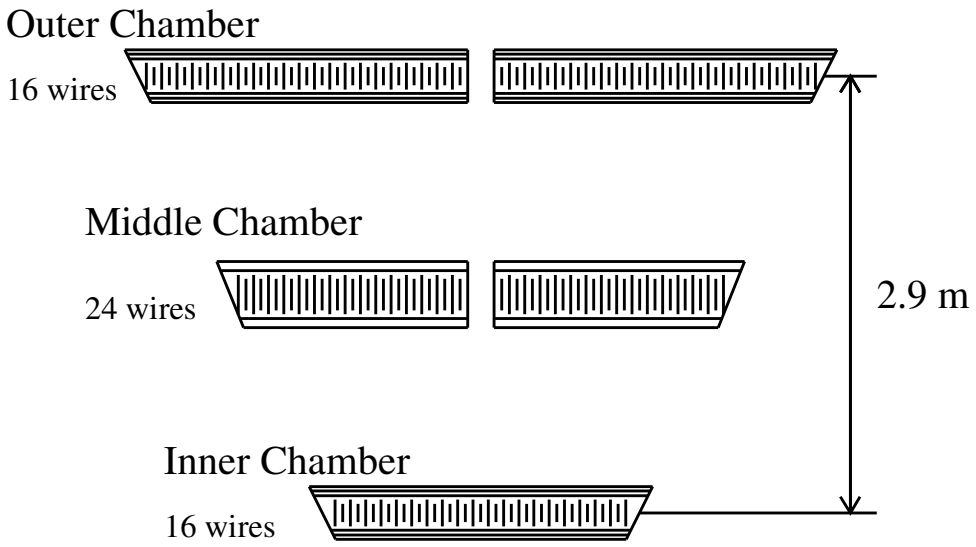

Figure 4.11: An octant of the muon chamber.

The gas mixture and drift velocity in the chambers are listed below:

Chambers	gas	$v_d(\mu m/ns)$
P	38.5% ethane, 61.5% Ar	50
Z	8.5% ethane, 91.5% Ar	30

The principal measurement of the MUCH is measurement of the sagitta of a track bending under the magnetic feild. In terms of the co-ordinate measurement in the different P segments, the sagitta is given by s = (X_{MI} + X_{MO})/2 - X_{MM}, each measurement having an uncertainity of $\varepsilon_i = 200\ \mu$m / $\sqrt{N_i}$ (i= MI, MM, MO). This propagates into the intrinsic error on the sagitta measurement as: $\Delta s = \sqrt{(\varepsilon_{MI}/2)^2 + (\varepsilon_{MO}/2)^2 + (\varepsilon_{MM})^2}$.

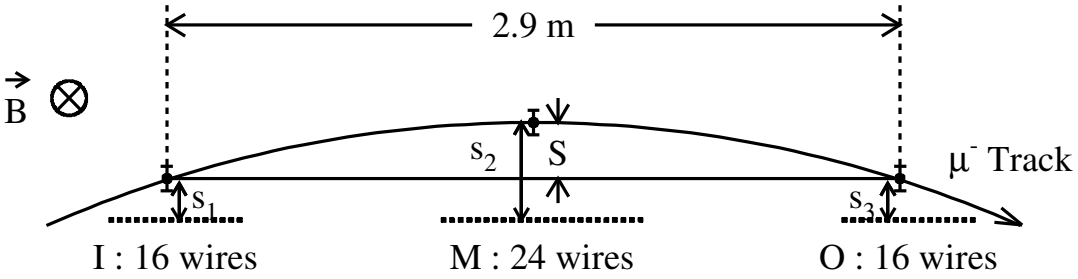

Figure 4.12: Sagitta measurement of a typical muon track.

The total error on the sagitta measurement is given by:

$$\begin{aligned} \Delta s &= (\text{intrinsic}) \oplus (\text{mult. scat.}) \oplus (\text{align syst.}) \\ &= 57\mu m \oplus 35\mu m(\text{at } 45\text{GeV}) \oplus 30\mu m \quad \sim 73\mu m \end{aligned}$$

This gives us momentum resolution of $\frac{\Delta p}{p} = \frac{\Delta s}{s} = 2.5\%$, and a corresponding di-muon mass resolution of $\frac{\Delta m}{m} = 1.8$ %. The precision of Z-chambers is $\simeq 500\mu m$.

The angular coverage of the barrel part in terms of the polar angle coverage is given by $< 44°(\text{MO}), 35°(\text{MM}), 24°(\text{MI})$ (figure 4.13).

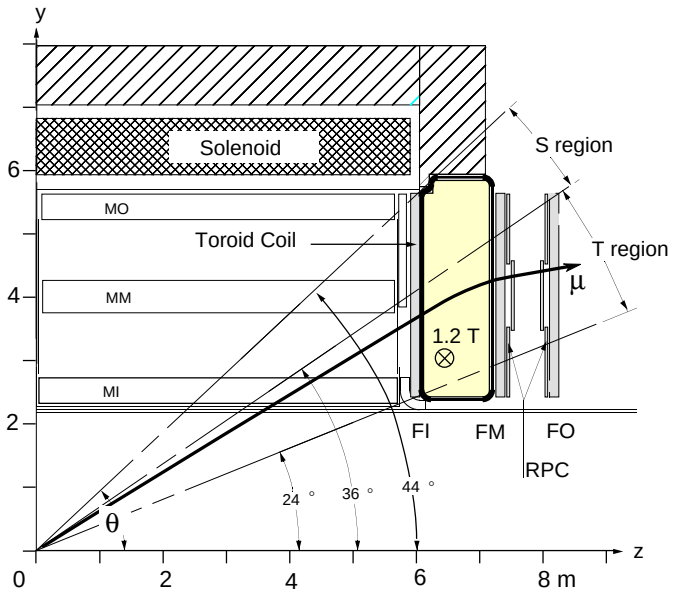

Figure 4.13: Side view of the muon chamber.

The forward backward muon chambers (FBMU) [15] are mounted on the magnet doors (figure 4.14), meseauring the bending of muons in solenoidal (S-region) and toroidal (T-region) of the magnetic feild. On either side of the interaction point, there are three layers of FBMU, each containing 16 drift chambers. The gas mixture used is 86% argon, 10% CO_2 and 4% isobutane.

The momentum resolution worsens in the FBMU due to multiple scattering in the 1m thick magnet doors. It deteriorates steadily (in the S-region) to a saturating 30% (in the T-region) at smaller angles (figure 4.15).

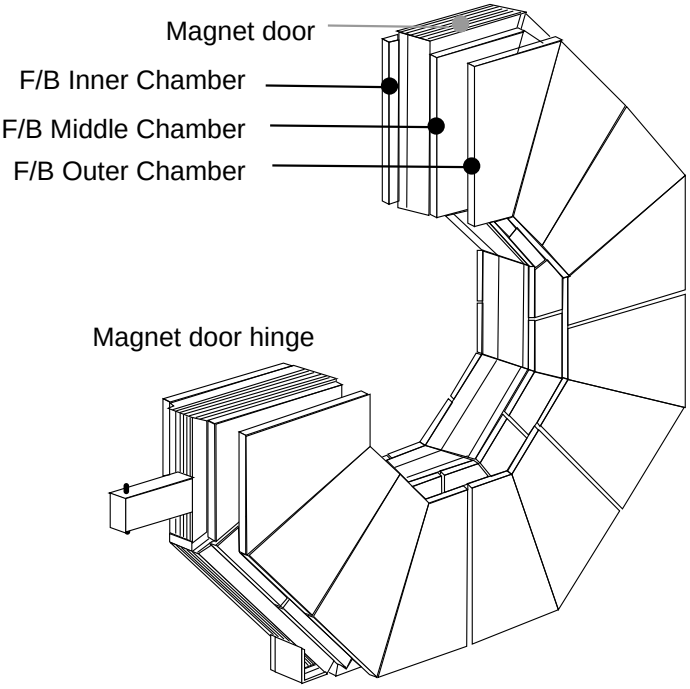

Figure 4.14: Forward backward muon chamber.

4.2 Energy Resolution of L3

These characteristic detector responses of photons, leptons and jets are exploited in the high resolution measurements at L3 to infer the properties of an event. Global energy resolution of few typical particles observed in the L3 detector are shown in figure 4.16 as a function of their energy.

4.3 Trigger & DAQ

The overall efficiency for selecting hadronic Z decays by the online trigger is greater than 99.9 %. The hadronic events are characterised by a large number of final state particles with most of the energy visible in the detector. Such events are identified by the logical OR of the level one [16] energy, TEC, and scintillation counter triggers. These three triggers have individual efficiencies of 99 %, 95 % and 95 % respectively. The energy trigger requires either

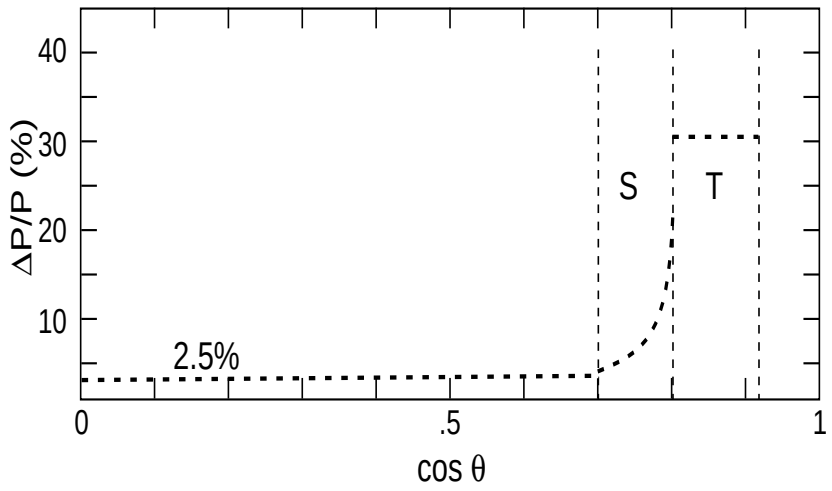

Figure 4.15: Momentum resolution for a 50 GeV muon as a function of the polar angle.

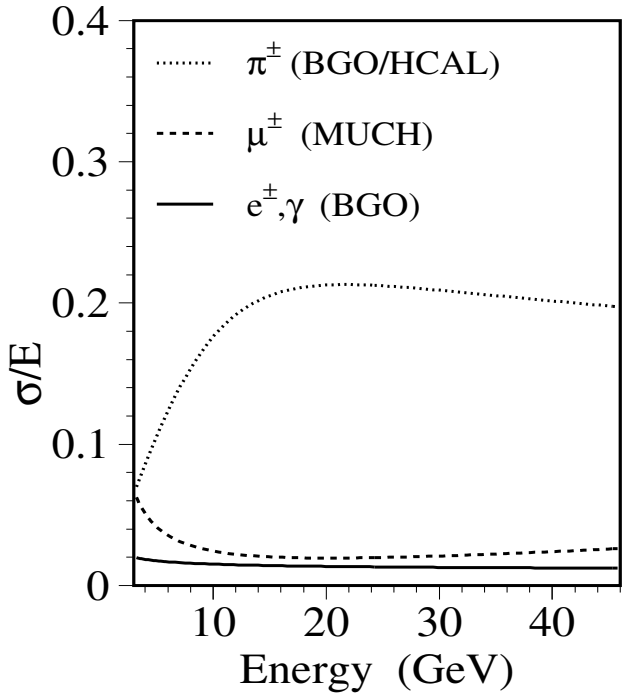

Figure 4.16: L3 detector resolution as a function of energy.

- a total energy of at least 25 GeV in the electromagnetic and hadron calorimeters, or
- a minimum energy of 15 GeV in the barrel or central region ($42^\circ < \theta < 138^\circ$) of calorimeters, or
- a minimum energy of 8 GeV in the barrel of the electromagnetic calorimeter alone.

The TEC trigger requires at least two tracks identified with a maximum acollinearity of 60°. The requirement in the scintillation counter trigger is a coincidence of at least 5 hits, in the counters during a 30 ns interval about the beam crossing time, which must extend over an azimuthal angular region of at least 90°.

An event must be selected by at least one of the three above-mentioned *first level triggers* in order to be recorded as a hadronic event, thereby reducing the 45 kHz bunch crossing rate of LEP to about 8 Hz first level trigger rate. The level one trigger analyses the trigger data of an individual sub-detector and either initiates the digitisation of the main data or clears the front end electronics before the next beam crossing. A negative decision at the first level does not produce any dead time. However, a positive decision from *any* of the individual level one triggers, initiates the detector data to be digitised and stored in multi-event buffers which takes around 500 μs, thereby causing the dead time for the data acquisition.

The successive *second* [17] and *third* [18] levels of the trigger system further filter events arising due to cosmic rays, electronic noise, uranium noise, and beam-gas interactions. The *second* level trigger acting on events with single level one trigger, uses the coarse digitized data from various sub-detectors, and additional informations from combined energy clusters in the calorimeters, loosely reconstructed tracks and the interaction point. It spends about 8 ms on an event without inducing any dead time. It has a rejection power of 20 to 30 % averaged over all first level triggers, and either passes all event information to an event builder memory or resets the event builder memories. The principle of the *third* level trigger (which is allowed ten times as much the time available to the previous levels) is similar to that of the second one, but accesses fully digitized data and bases its decision on recalculated and calibrated energies, fully reconstructed tracks and vertices which matched calorimetric clusters. On a positive third level trigger the data is transferred to the main acquisition system which is subsequently written to tapes, which is typically of the order of 2-3 Hz.

The L3 DAQ efficiency for 1999 was $\geq$ 91.5%: out of delivered luminosity of 253.7 pb^{-1} by LEP, L3 recorded 232 pb^{-1}.

4.4 Data Flow

Data events recorded online are reconstructed [19] offline, after taking into account calibration of the resolution and performance of the detector. Monte Carlo generated events

are passed into a detector simulation program, where the real detector response is modelled [20], and compared to the data after passing through process specific selection and user defined analysis.

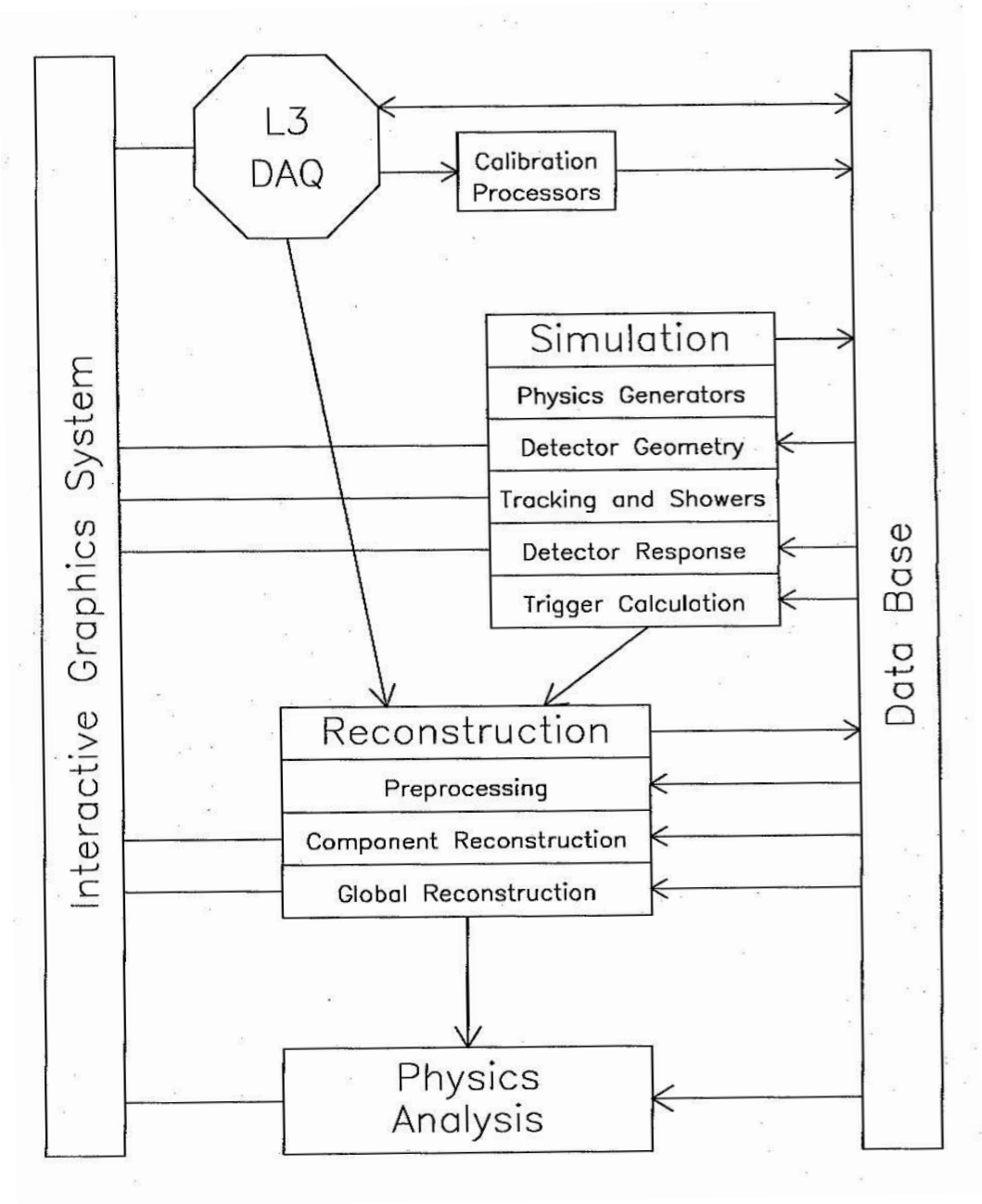

Figure 4.17: L3 Data Flow.

References

[1] ALEPH Collaboration, Nuclear Instr. & Methods **A294** (1990) 121.

[2] DELPHI Collaboration, Nuclear Instr. & Methods **A303** (1991) 233.

[3] L3 Collaboration, B. Adeva *et al.*, Nuclear Instr. & Methods **A289** (1990) 35.

[4] OPAL Collaboration, Nuclear Instr. & Methods **A305** (1991) 275.

[5] M. Acciarri *et al.*, Nuclear Instr. & Methods **A360** (1995) 103-109;
B. Alpat *et al.*, Nuclear Instr. & Methods **A315** (1992) 197-200.

[6] H. Akbari *et al.*, Nuclear Instr. & Methods **A315** (1992) 161-162;
F.Beissel *et al.*, Nuclear Instr. & Methods **A332** (1993) 33-55.

[7] A. Breskin *et al.* Nuclear Instr. & Methods **143** (1977) 29;
J. Chiba *et al.* Nuclear Instr. & Methods **206** (1983) 451.

[8] L3 Collaboration, O. Adriani *et al.*, Physics Reports, Volume 236 (1993) 1.

[9] J.A. Bakken *et al.* Nuclear Instr. & Methods **228** (1985) 294;
J.A. Bakken *et al.*, Nuclear Instr. & Methods **254** (1987) 535;
J.A. Bakken *et al.*, Nuclear Instr. & Methods **275** (1989) 81.

[10] B. Basti *et al.*, Nuclear Instr. & Methods **374** (1996) 293.

[11] H. Bergstein *et al.*, SC-N project, Vol I-III, Internal Report, I. Phys. Inst., RWTH-Aachen, Aachen -1995;
Ulrich Uwer, L3 Internal note **2003**, 1996.

[12] L3 Collaboration, A. Arefiev *et al.*, Nuclear Instr. & Methods **275** (1989) 71;
L3 Collaboration, A. Arefiev *et al.*, Nuclear Instr. & Methods **285** (1989) 403;
L3 Collaboration, O. Adriani *et al.*, Nuclear Instr. & Methods **A302** (1991) 53.

[13] R. D'Alessandro, Nuclear Instr. & Methods **289** (1990) 103;
L3 Collaboration, O. Adriani *et al.*, Nuclear Instr. & Methods **300** (1991) 493.

[14] L3 Collaboration, B. Adeva *et al.*, Nuclear Instr. & Methods **277** (1989) 187;
L3 Collaboration, B. Adeva *et al.*, Nuclear Instr. & Methods **323** (1992) 109.

[15] L3 Collaboration, A. Adam *et al.*, Nuclear Instr. & Methods **383** (1996) 342.

[16] L3 Collaboration, R. Bizzari *et al.*, Nuclear Instr. & Methods **A283** (1989) 799;
L3 Collaboration, P. Bagnaia *et al.*, Nuclear Instr. & Methods **A324** (1993) 101;
L3 Collaboration, P. Bagnaia *et al.*, Nuclear Instr. & Methods **A344** (1994) 212.

[17] L3 Collaboration, Y. Bertsch *et al.*, Nuclear Instr. & Methods **A340** (1994) 309;
L3 Collaboration, S.P. Beingessner *et al.*, Nuclear Instr. & Methods **A340** (1994) 322.

[18] L3 Collaboration, C. Dionisi *et al.*, Nuclear Instr. & Methods **A336** (1993) 78.

[19] S. Banerjee and F. Bruyant, L3 Note # 748 (1989).

[20] The L3 detector simulation is based on GEANT Version 3.15.
See R. Brun *et al.*, "GEANT 3", CERN DD/EE/84-1 (Revised), September 1987.
The GHEISHA program (H. Fesefeldt, RWTH Aachen Report PITHA 85/02 (1985)) is used to simulate hadronic interactions.

Chapter 5

The Process: $e^-e^+ \rightarrow \gamma/Z^\star \rightarrow$ *hadrons*

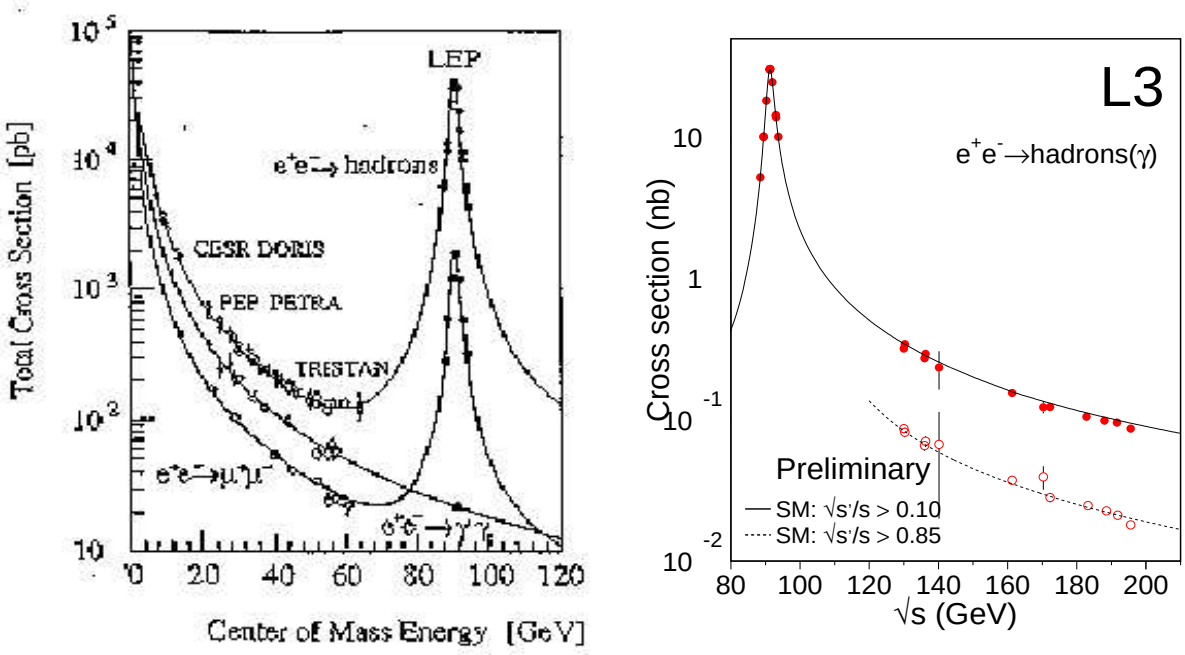

Figure 5.1: Cross section of $e^-e^+ \rightarrow$ *hadrons* up to (a) 120 GeV [1] and (b) 200 GeV [2].

The basic process underlying e^-e^+ annihilation into hadrons is $e^-e^+ \rightarrow q\overline{q}$ via the neutral gauge bosons mediators (γ, Z) of electro-weak interaction. At centre-of-mass energy ($\sqrt{s}$) close to the mass of Z boson (M_Z), total cross section is as high as 40 nb. The ratio of hadronic cross section to lepton pair production cross section at these energies

is given by:

$$\begin{aligned} R_{\rm had} &= \frac{\sigma(\mathrm{e^-e^+ \to Z^\circ \to \mathit{hadrons}})}{\sigma(\mathrm{e^-e^+ \to Z^\circ \to \mu^+\mu^-})} \\ &= 3\frac{\Sigma_q(\mathrm{v_q}^2 + \mathrm{a_q}^2)}{\mathrm{v_\mu}^2 + \mathrm{a_\mu}^2} \approx 20. \end{aligned}$$

Thus, the hadronic branching fraction of Z is large ($\approx 70\%$), and at LEP 1 hadronic Z decays is the dominant process with cross section around 30 nb (see figure 5.1a).

As we move up in energy from the Z peak, the hadronic cross section gets reduced substantially ($\sim$ 20 pb at 200 GeV) and the effect of initial state radiation becomes significant. Initial state radiation reduces the effective centre-of-mass energy of the remaining hadronic system. For a photon emitted with energy E_γ, the reduced centre-of-mass energy ($\sqrt{\mathrm{s}'}$) is given by:

$$\sqrt{\mathrm{s}'} = \sqrt{s\left(1 - \frac{2\mathrm{E}_\gamma}{\sqrt{\mathrm{s}}}\right)}$$

For two choices of $\sqrt{\mathrm{s}'}$, the hadronic cross section as measured by the L3 experiment is shown in figure 5.1b, which exhibits the characteristic 1/s fall with energy. At the LEP 2 phase, the cross section of hadronic production competes with the pair production of W and Z bosons. Production of these bosons followed by their hadronic decays poses as an irreducible background to the high energy quark pair production. Thus the study of the process $\mathrm{e^-e^+} \to \gamma/Z^\star \to$ *hadrons* provides valuable insight to the most of the standard model processes, and as well, serves as a dominant background to new particle searches.

5.1 L3 Data

$\sqrt{\mathrm{s}}$ (GeV)	Year (19__)	$\int \mathcal{L}\mathrm{dt}$ (pb^{-1})
91.2	91-94	142.4
130	95, 97	6.1
136	95, 97	5.9
161	96	10.8
172	96	10.2
183	97	55.3
189	98	176.3

Table 5.1: Luminosity recorded by L3.

L3 recorded data at different centre-of-mass energies ($\sqrt{\mathrm{s}}$) over the last decade (table 5.1). The total L3 data of hadronic events can be divided into three sub-samples depending upon the centre-of-mass energy less than, equal to and greater than $\mathrm{M_Z}$ [3, 4, 5, 6].

Tagging events with isolated photons from the large statistics Z peak data, mostly due to final state radiation emitted early in the evolution, allows one to study hadronic event at reduced centre-of-mass energy ($\sqrt{s'}$). The effective centre-of-mass energy is again given by the same formula applicable to the ISR radiation. Depending on the energy of the photon, properties of hadronic event sample were studied at 6 energy bins of reduced centre-of-mass energies $\sqrt{s'}$ = 30-50, 50-60, 60-70, 70-80, 80-84, 84-86 GeV [7].

Combining measurements from the reduced centre-of-mass energy study, with the measurements made at the energy points as given in the table 5.1, hadronic event structures have been studied in this thesis at each $\sqrt{s}$ over a wide energy range: from 30 to 189 GeV [6].

5.2 Modelling the Process

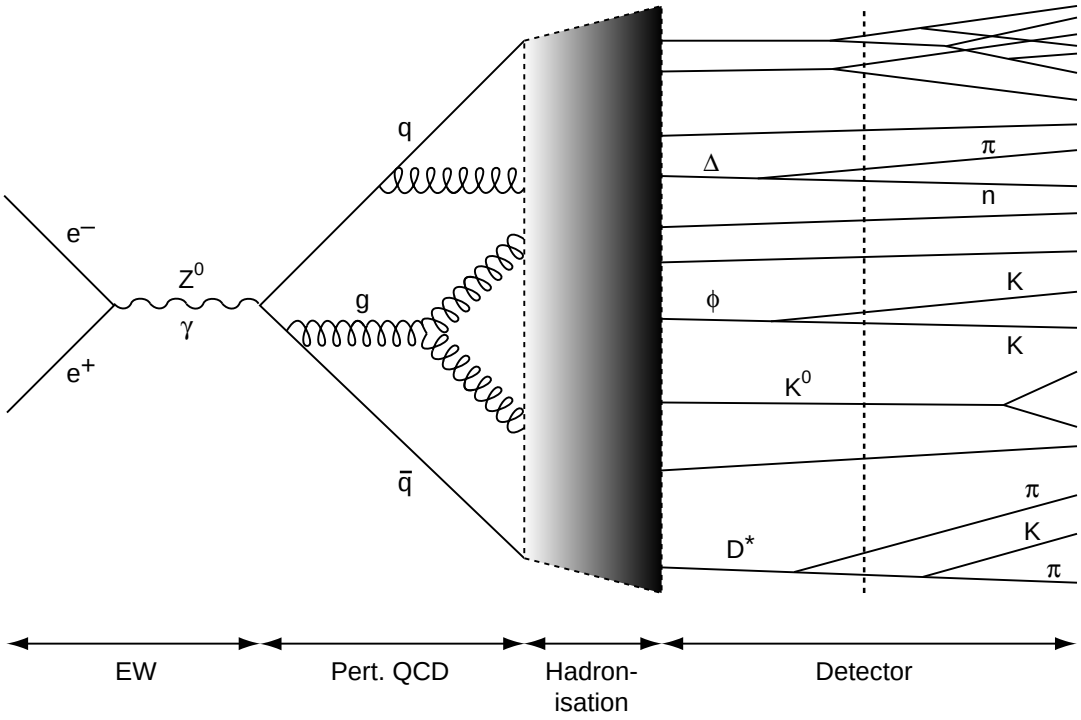

Figure 5.2: *Different phases of the process* $e^-e^+ \rightarrow \gamma/Z^\star \rightarrow$ *hadrons [8].*

At very high energies, e^-e^+ annihilation may produce tens to hundreds of hadrons in the final state. Analytical computation of scattering amplitude for such a multi-particle final state is not possible. In a more practical approach the individual sub-processes, classified for example on basis of the length scale of the interaction involved during the evolution of the process, are modelled separately using Monte Carlo simulations.

A schematic representation (see figure 5.2) of the sub-process used to model the process $e^-e^+ \rightarrow$ *hadrons* is given in the table 5.2.

Sub-process	length scale	Interaction
Quark-antiquark pair (and photon) production	$\sim 10^{-17}$ cm	Electro-weak
Gluon and quark radiation	$\sim 10^{-15}$ cm	Perturbative QCD
Fragmentation of quarks/gluons into hadrons	$\sim 10^{-13}$ cm	Non-perturbative QCD
Decays of unstable hadrons into stable particles	$> 10^{-13}$ cm	Electro-weak and QCD

Table 5.2: Schematic representation of the process $e^-e^+ \rightarrow$ *hadrons* [9].

For the perturbative QCD part, two approaches have been traditionally implemented in the generators: the *matrix element* (ME) and the *parton shower* (PS). The matrix element approach, resting on second order QCD calculations with a maximum of four primary partons generated, takes into account the exact kinematics and the full interference and helicity effects; whereas in the parton shower approach arbitrary number of partons are branched using approximations derived by simplifying the kinematics, interference and helicity structures, and modelling of multiple soft gluon emission. While the first one is better suited for α_s determinations, the latter approach, albeit with less predictive power, gives a good description of the substructure of multi-jet event.

For the non-perturbative part, study of the dynamic behaviour of quarks in colour fields with growing distance scale has led to the development of many phenomenological models for hadronisation, the most commonly used ones being: *independent fragmentation*, *string fragmentation* and *cluster fragmentation*. As the energy of the individual sub-systems at each branching falls down to the order of a few GeV, the non-perturbative modelling takes over. These models use different types of "grouping blocks" of the primary partons produced in the perturbative QCD phase, succeeded by iterative fragmentation of these building blocks in terms of few underlying branchings as shown in table 5.3.

Independent fragmentation	jet $\rightarrow$ hadron + remainder-jet
String fragmentation	string $\rightarrow$ hadron + remainder-string
Cluster fragmentation	cluster $\rightarrow$ cluster + cluster, or cluster $\rightarrow$ hadron + hadron

Table 5.3: Basic branching processes in different fragmentation models.

In the independent fragmentation, an incoherent summation of branchings are taken starting from each of the individual primary partons. The longitudinal momentum distribution for evolution of jets from a quark or gluon, described independently with branchings from the individual partons, and are controlled by separate parameters, e.g. b_q, d_q for quark jets and b_g, d_g for gluon jets. The transverse fragmentation profile is governed by an additional free parameter.

In the string fragmentation, the transverse momentum distribution is parametrised in

terms of a Gaussian:

$$\mathrm{f(p_T)} \;\sim\; \exp\left(-\frac{\mathrm{p_T}^2}{\sigma_\mathrm{Q}{}^2}\right)$$

The longitudinal momentum profile is described in terms of the lorentz boost invariant branching ratio z defined as:

$$z \;=\; \frac{(E+p_\parallel)_{hadron}}{(E+p_\parallel)_{quark}}$$

where E and $p_\parallel$ are the energy and momentum along the initial quark direction respectively. Light flavoured quarks (u,d,s) are fragmented using the a and b parameters in left-right symmetric Lund function:

$$f(z) \;\sim\; \frac{(1-z)^\mathrm{a}}{z}\exp(-\mathrm{b}m_T^2/z)$$

(where m_T is the transverse mass), while for the heavy flavours (c,b) a harder fragmentation function (with parameter ϵ_Q) given by Peterson *et al.* [10] is implemented:

$$f(z) \;\sim\; \frac{1}{z[1-\frac{1}{z}-\frac{\epsilon_Q}{(1-z)}]^2}$$

In the cluster fragmentation, colourless clusters, formed out of the primary partons at the end of the perturbative branching phase, are split (depending upon parameters CLMAX and CLPOW to be *tuned*) into lighter clusters before decaying if

$$\mathrm{M_{CL}}^{\mathrm{CLPOW}} \;>\; \mathrm{CLMAX}^{\mathrm{CLPOW}} + (\mathrm{M_1}+\mathrm{M_2})^{\mathrm{CLPOW}}$$

where $\mathrm{M_{CL}}$ is the mass of the cluster decaying into two sub-clusters of masses $\mathrm{M_1}$ and $\mathrm{M_2}$ respectively. In addition, the effective gluon mass (m_g) serves as a free parameter.

Based on different approaches to describe the perturbative evolution and non-perturbative hadronisation processes, several event generators have been developed. The perturbative phase is controlled in terms of the Λ_{QCD}, described up to leading logarithmic approximation (LLA), or next to leading logarithmic approximation (NLLA), or modified leading logarithmic approximation (MLLA). The generators used in L3, along with their specifications and a list of "free" parameters (which have been tuned using L3 data) are given in the table 5.4.

5.3 Monte Carlo Tuning

The description of hadronic production from $\mathrm{e^-e^+}$ annihilation depends on the parameter sets of the that Monte Carlo program. Numerous inputs from experimental observations have played a crucial role in the developments of these models. These models owe their

QCD Model	Shower Development	Fragmentation	Parameters
JETSET [11]	Matrix Element/Parton Shower	String	$\Lambda_{\rm LLA}$, $\sigma_{\rm Q}$, b
HERWIG [12]	Parton Shower	Cluster	$\Lambda_{\rm MLLA}$, CLMAX, CLPOW, m_g
ARIADNE [13]	Colour Dipole Parton Shower	String	$\Lambda_{\rm LLA}$, $\sigma_{\rm Q}$, b
COJETS [14]	Incoherent Parton Shower	Independent	$\Lambda_{\rm LLA}$, b_q, b_g, d_q, d_g

Table 5.4: Specifications and parameters of different QCD models.

success to these data in describing today's experiments. These models provide a way to unravel the effects of fragmentation in the experimental data and then can be compared with the perturbative QCD calculations directly.

Each Monte Carlo implementation has its own set of parameters. Tests of QCD thus depend on these parameters, and the optimisation of these parameter values is the first step for testing QCD [15].

Among the experimental measurements sensitive to model parameters, the event shape variables which characterise the global structure of hadronic events are the simplest. They are sensitive to the parameters of perturbative QCD as well as to those of the fragmentation models.

The main fragmentation parameters are *tuned* from the hadronic data at $\sqrt{s} \approx M_Z$ collected by the L3 detector [16] using the measured distributions of global event shape variables. The data used corresponds to 250 K hadronic events collected during the run in 1991. The observed distributions have been corrected [15] for detector effects − resolution and acceptance. The data have also been corrected for initial and final state radiations.

The event shape variables chosen to describe the lateral and longitudinal hadronic shower profiles include jet resolution parameter in the JADE algorithm [17] which corresponds to transition from $2 \rightarrow 3$ jets ($y_{23}^{\rm JADE}$), minor [18] calculated after dividing the event into two hemispheres by the thrust [19] axis and evaluated in the hemisphere corresponding to the narrow jet ($T_{\rm minor}^{\rm NS}$), the fourth Fox-Wolfram moment [20] [$H_4 = \sum_{a,b} \frac{\vec{p}_a \cdot \vec{p}_b}{s} P_4(\cos\theta_{ab})$ where P_4 is the fourth order Legendre polynomial]. The charge multiplicity distribution is also used as a tuning variable, where *charge multiplicity* is taken to be the number of *stable* (mean lifetime $> 3.3 \times 10^{-10}$ sec.) charged particles observed.

These three event shapes as well as the mean charged particle multiplicity from the Monte Carlo's were compared to L3 data from hadronic Z decays. Using the CERN program package MINUIT, the parameters are determined by minimising the χ^2 function defined as:

$$\chi^2 = \sum_{i,j} \frac{[{\rm Data}_{ij} - {\rm Theory}_{ij}(p_k)]^2}{\left(\sigma^{\rm stat}_{{\rm Data}_{ij}}\right)^2 + \left(\sigma^{\rm syst}_{{\rm Data}_{ij}}\right)^2 + \left(\sigma^{\rm stat}_{{\rm Theory}_{ij}}\right)^2}$$

where the individual contributions to χ^2 are summed over all bins (j) of the chosen four distributions (i). Points with insignificant statistics are ignored in the fits. The theoretical distribution is obtained by generating events on several points on a grid in the parameters space with a large number of events ($\geq$ 40 K). For a grid with k-parameters and n_p different values for a given parameter, one needs to generate events at $\Pi_{p=1}^{k}\, n_p$ points. The theoretical prediction for a given bin in a given distribution in between the grid points is obtained using a local multidimensional interpolation to the generated distributions using a polynomial of a given degree :

$$f_{ij}\,(\vec{p}_0 + \delta\vec{p}) \;=\; a_{ij}^{(0)} + \sum_{m} \left(a_{ij}^{(1)}\right)_m (\delta p_m) + \sum_{m,n} \left(a_{ij}^{(2)}\right)_{mn} (\delta p_m)(\delta p_n) + \cdots$$

Initial and final state radiations are switched off in these event generations.

To estimate the systematic errors, the fits have been repeated by changing (a) degrees of polynomial in the interpolation of the theoretical prediction; (b) the grid size by dropping a few grid points; (c) the fit range. Half of the maximum spread is attributed to the systematic error. To be conservative, the largest of the three different estimates is quoted.

5.3.1 Tuning of Herwig 5.9 and Jetset 7.4

With the release of the new version of HERWIG, default parameters have been *tuned* for HERWIG 5.9 [21, 22]. Parameter tuning has also been carried out for JETSET-PS 7.4 with Bose-Einstein effect not included (MSTJ(51) = 0) [21]. While the latter provides a comparison bench-mark for Bose-Einstein correlation studies at L3, the former serves as a bench-mark for colour reconnection effects in W^-W^+ decays from e^-e^+ annihilations.

Three decay schemes for unstable hadrons, using the decay mechanisms as incorporated in the HERWIG, JETSET and EURODEC [23] event generators, are interfaced with HERWIG. This is done by compiling the code with or without EURODEC generator and use of the decay flag BDEC. The three sets are referred to in our subsequent discussions as **n0** (no EURODEC and BDEC=0), **n3** (no EURODEC and BDEC=3) and **e3** (EURODEC and BDEC=3) respectively. In the last option (**e3**), only heavy flavour hadrons decay through EURODEC, while the light flavour hadrons decay through JETSET.

The predictions of these QCD models for other global event shape variables are obtained and compared with the measurements done at LEP I [15, 24]. The variables studied here are event thrust (T) [19], major (T_{major}), minor (T_{minor}), oblateness (O) [25], sphericity (S), aplanarity (A) [26], scaled jet mass squared (ρ_H and ρ_L) [27], C and D parameters [28], jet broadening variables (B_T, B_W) [29], Fox-Wolfram moments (H_i) [20], 3-jet resolution parameters in $k_\perp$ ($y_{23}^{k_\perp}$) [30] algorithm.

The values of the tuned parameters are summarised in tables 5.5 and 5.6. The χ^2 obtained from the various distributions with the tuned parameters are summarised in table 5.7. The overall χ^2 refers to 226 data points, while for the tuning variables there are 53 data points. Reasonable fits to the observed distributions were obtained. The mea-

sured distributions for the four fitted variables together with the theoretical predictions as obtained from the fit to HERWIG 5.9 are shown in figures 5.3, 5.4, 5.5.

Decay Model	Parameter	Fit Value	Stat. Error	Syst. Error
HERWIG	Λ_{MLLA} (GeV)	0.177	$\pm$ 0.003	$\pm$ 0.008
	CLMAX (GeV)	3.006	$\pm$ 0.035	$\pm$ 0.343
	CLPOW	2.033	$\pm$ 0.067	$\pm$ 0.524
JETSET	Λ_{MLLA} (GeV)	0.184	$\pm$ 0.001	$\pm$ 0.015
	CLMAX (GeV)	3.911	$\pm$ 0.035	$\pm$ 0.193
	CLPOW	2.000	$\pm$ 0.040	$\pm$ 0.480
EURODEC	Λ_{MLLA} (GeV)	0.178	$\pm$ 0.002	$\pm$ 0.023
	CLMAX (GeV)	3.933	$\pm$ 0.048	$\pm$ 0.445
	CLPOW	1.800	$\pm$ 0.018	$\pm$ 0.542

Table 5.5: Tuned Parameters for the HERWIG 5.9 Parton Shower Program.

Parameter	Fitted Value	Stat. Error	Syst. Error
Λ_{LLA} (GeV)	0.312	$\pm$ 0.011	$\pm$ 0.020
σ_{Q} (GeV)	0.343	$\pm$ 0.016	$\pm$ 0.009
b (GeV^{-2})	1.100	$\pm$ 0.030	$\pm$ 0.104

Table 5.6: Tuned Parameters for the JETSET 7.4 Parton Shower Program when effects of Bose Einstein correlation are not included.

Variables	# points	JETSET 7.4	HERWIG 5.9		
		No B.E.	**n0**	**n3**	**e3**
Thrust	13	8.6	14.4	14.1	13.7
ρ_{H}	13	21.3	10.2	6.8	14.0
$\mathrm{B_T}$	11	14.0	19.1	13.9	14.3
$\mathrm{B_W}$	8	38.8	32.6	33.6	32.2
$\mathrm{y_{23}^{JADE}}$	15	6.5	11.4	10.1	10.7
$\mathrm{y_{23}^{k_\perp}}$	16	17.9	7.1	6.0	9.0
Sphericity	14	16.2	9.3	6.4	6.7
Aplanarity	12	5.9	43.4	33.7	32.0
C-parameter	14	9.5	19.9	21.9	20.6
D-parameter	11	15.5	14.8	16.0	13.1
$\mathrm{T_{major}}$	14	4.8	7.9	9.3	11.6
$\mathrm{T_{minor}}$	12	9.1	42.3	40.1	42.6
Oblateness	12	37.6	19.2	36.8	31.3
$\mathrm{T_{minor}^{NS}}$	9	1.5	14.6	17.5	18.4
$\mathrm{H_3}$	12	4.3	5.5	5.2	5.9
$\mathrm{H_4}$	12	9.9	61.1	47.6	54.3
ρ_{L}	11	20.9	15.7	18.2	17.8
$< \mathrm{n_{ch}} >$	17	8.9	7.9	10.2	8.7
Overall	226	251.2	356.4	347.4	356.9
Tuned variables	53	(26.8)	(95.0)	(85.4)	(92.1)

Table 5.7: Goodness of matching between data and various QCD models with parameter sets from the current tuning, as determined by the χ^2 to the global event shape variables. The models studied here are JETSET 7.4 (with Bose Einstein correlation not included), HERWIG with decays of unstable hadrons done with HERWIG, JETSET and EURODEC.

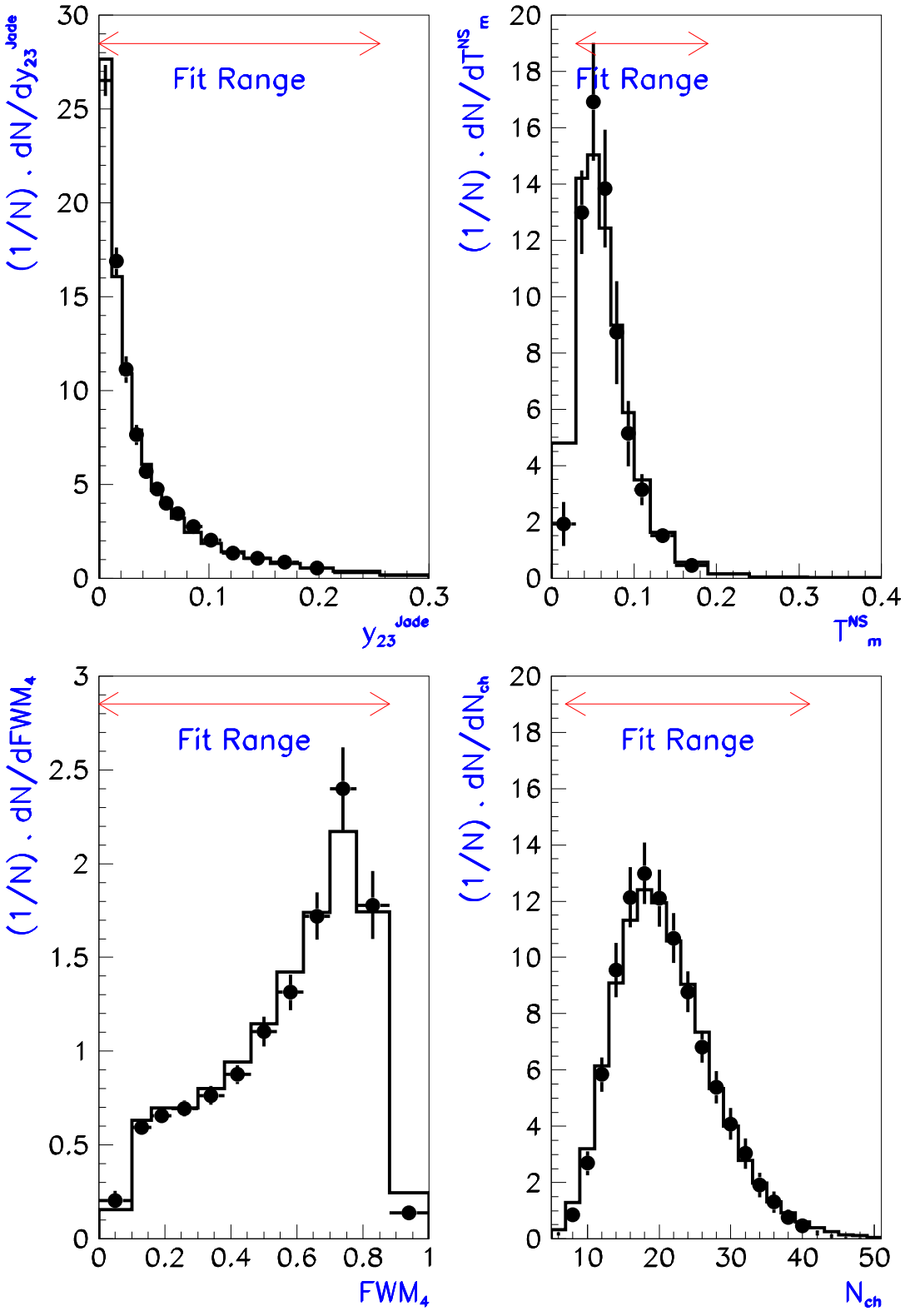

Figure 5.3: Measured distributions of y_{23}^{JADE}, $T_{\text{minor}}^{\text{NS}}$, H_4 and n_{ch} together with the predictions of HERWIG 5.9 in the **n0** scheme (when decays of unstable hadrons are done with HERWIG) using the parameters as obtained from the fit.

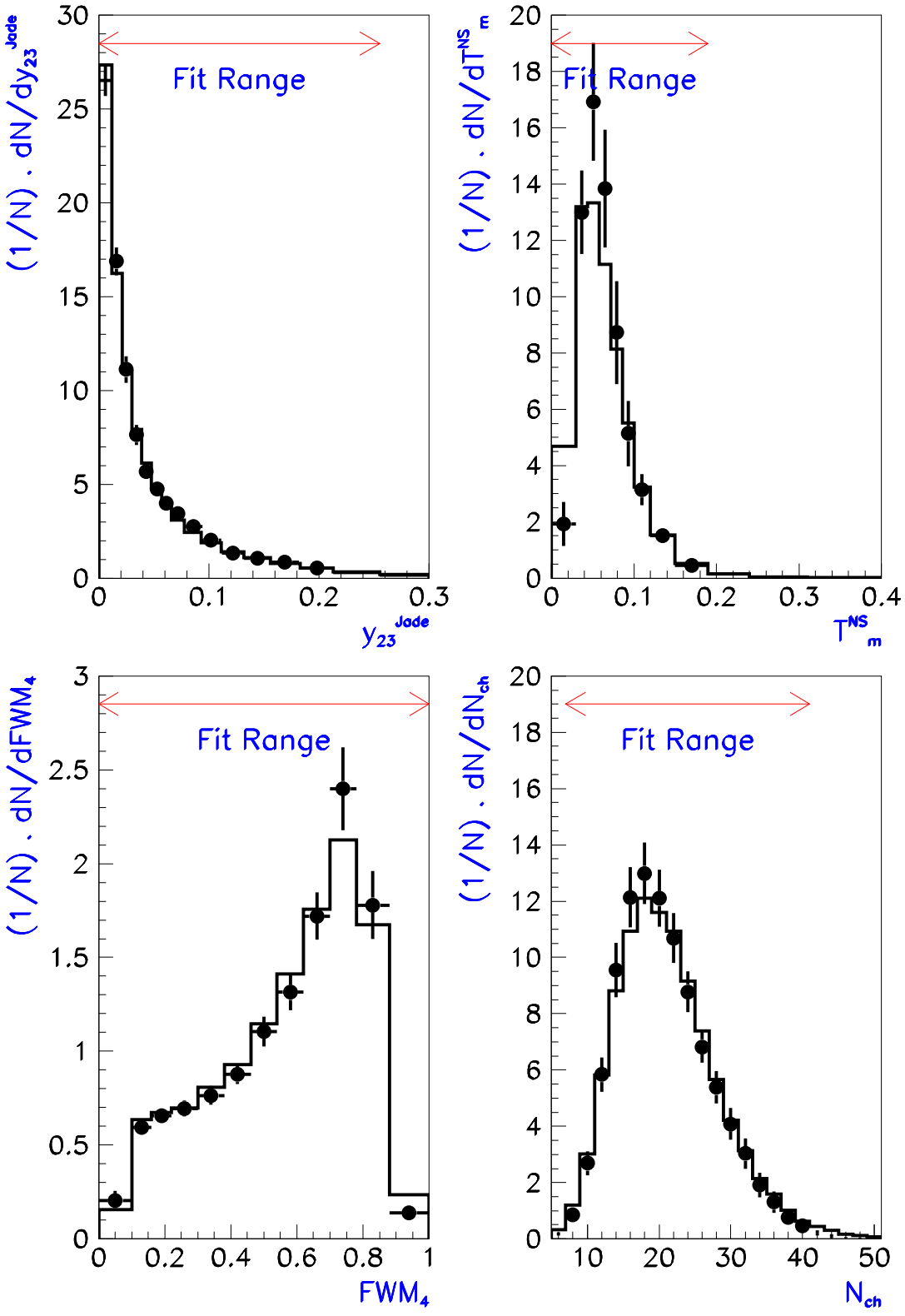

Figure 5.4: Measured distributions of y_{23}^{JADE}, $T_{\mathrm{minor}}^{\mathrm{NS}}$, H_4 and n_{ch} together with the predictions of HERWIG 5.9 in the **n3** scheme (when decays of unstable hadrons are done with JETSET) using the parameters as obtained from the fit.

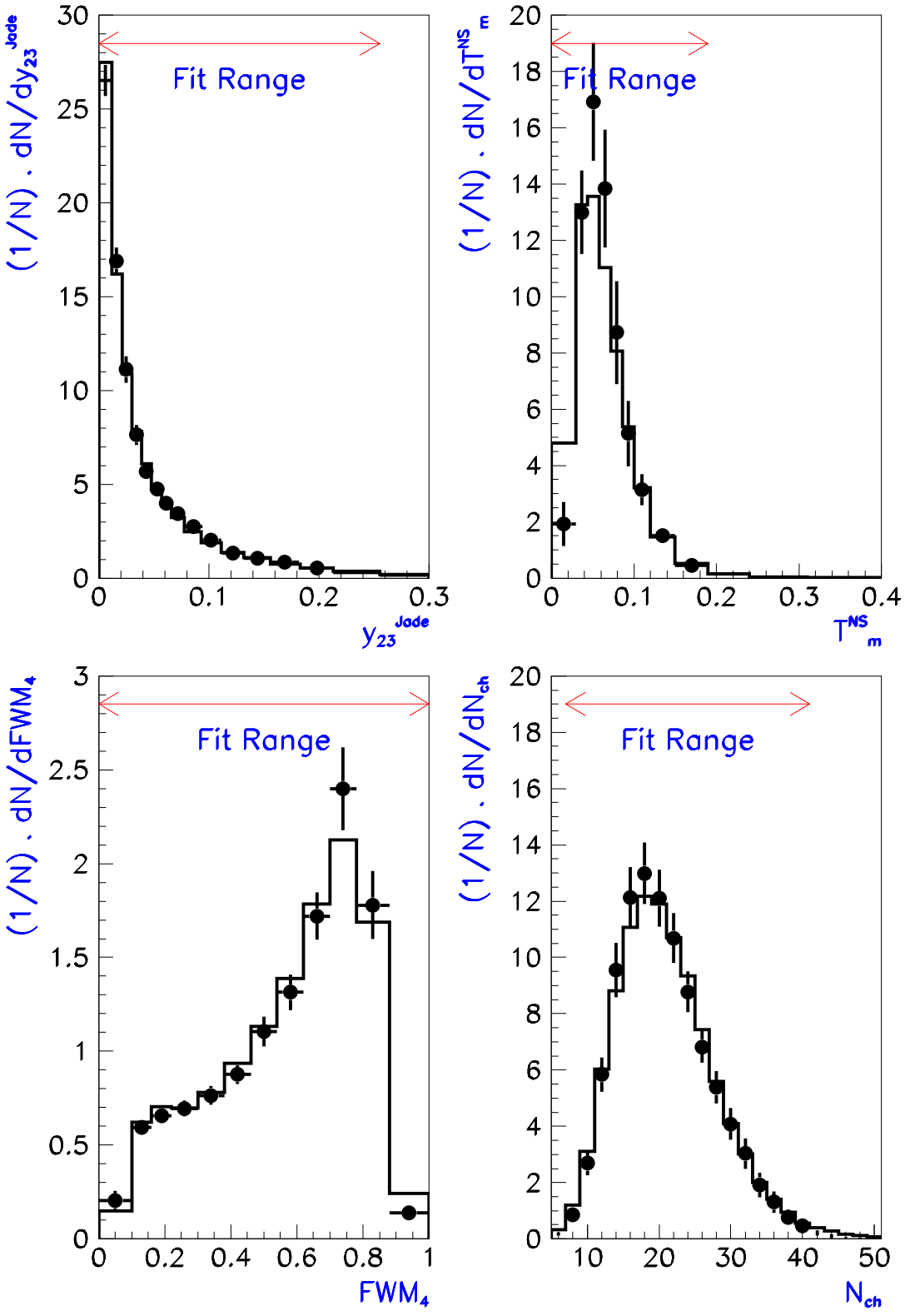

Figure 5.5: Measured distributions of y_{23}^{JADE}, $T_{\text{minor}}^{\text{NS}}$, H_4 and n_{ch} together with the predictions of HERWIG 5.9 in the **e3** scheme (when decays of unstable hadrons are done with EURODEC) using the parameters as obtained from the fit.

5.4 Energy Flow in Hadronic Events

In hadronic final state events from e^-e^+ annihilation, the produced neutral and charged particles are collimated as jets. A typical list of some of the *stable* particles produced along with their relative abundance in an hadronic event at the Z-resonance are listed in table 5.8 [9].

Neutral		Charged	
particle	#/event	particle	#/event
γ	21.5	$\pi^{\pm}$	17.1
K^0_L	1.1	$K^{\pm}$	2.2
n, $\overline{n}$	1.1	p, $\overline{p}$	1.2
ν, $\overline{\nu}$	0.3	$e^{\pm}$, $\mu^{\pm}$	0.4, 0.1

Table 5.8: Relative abundance of some of the *stable* particles produced in an typical hadronic event at the Z-peak.

At L3, the charged particles give rise to *hits* in the SMD and TEC, a directionally correlated collection of which is commonly referred to as *tracks*. Neutral particles pass through the tracking systems and deposits energy in the electromagnetic and hadron calorimeters. While the ECAL covers $\sim$ 1.1 nuclear interaction lengths, the sampling HCAL offers a material volume of 6-7 λ_{int} traversed by a particle/jet cascade depending upon the angle at which they come out from the interaction vertex. While an electromagnetic shower is usually completely contained in the ECAL, hadronic shower starts from the ECAL, and the energy deposited extends throughout the HCAL, with some leakage to the surrounding MUCH, in the form of punch-through objects.

5.4.1 Event Reconstruction

While passing through a detector, a particle leaves traces in the tracking detectors and energy deposits in the calorimeters in the form of correlated hits within a narrow solid angle. The task of pattern recognition is to relate these hits to a single particle. The degree to which trajectories of two particles can be resolved depends on the detector with finer resolution, which is the tracker for charged particles and the electromagnetic calorimeter for neutral particles. Two particle resolution of the electromagnetic calorimeter is rather good and one can use the ECAL as the seed of forming global clusters for both charged and neutral particles.

The event reconstruction [31] proceeds in two steps: first signals from each sub-detector are analysed and reconstructed locally, and then reconstructed objects from individual detectors are joined together and a global reconstruction is carried out. In the first step, analog signals from *hits* in the calorimeter compatible with 2 MeV threshold in the BGO or 9 MeV threshold in the hadron calorimeter are studied, giving rise to energy clusters.

Tracks are reconstructed in the central tracking chamber or the muon spectrometer by associating spatially adjacent hits. Energy clusters reconstructed from the calorimetric energy deposits are matched with the reconstructed tracks.

The reconstruction procedure then defines "objects" in the detector corresponding to hadron jets, isolated electrons, photons and muons. At this stage of the analysis, the information about muons reconstructed in the muon chambers is added to the calorimeter reconstruction information. An iterative procedure is applied to the "seed" to add all clusters in a 30° cone around the seed axis (the vector to the interaction vertex). An object axis is defined by calculating the energy-weighted vector sum of all the included cluster vectors, and a new 30° cone is defined about this axis, the clusters within which are in turn used to redefine the new object axis. This procedure is continued till when addition of new clusters within the new cone to this object does not affect the definition of its axis. Similarly, starting from the next most energetic cluster, new objects are built. The iteration of reconstruction procedure stops when the energy of the next new object is less than 7 GeV. The remaining low energy clusters are added to the closest existing objects, if it is not separated by more than 20° from the closest cluster in this object.

Finally, the objects are classified and their energies are determined by its composition. On the basis of the sub-detector informations, such a *smallest resolvable cluster* (SRC) may be of electromagnetic or hadronic origin, depending upon its longitudinal and transverse profile.

5.4.2 Clusters in the L3 Detector

A cluster is defined such that it resembles particle cascade with very small contamination from random noise. Individual sub-detectors have different response to the passage of an energetic particle, as compared to the pedestal level corresponding to fluctuations due to noise. For example, a 45GeV hadronic jet from a Z decay contains about 70 *hits* in the hadronic calorimeter in a volume compatible with its one module, while the noise level for the same module corresponds to about 4 *hits* [32].

For a global energy definition for a cluster, different sub-detector informations are combined in an off-line reconstruction procedure based on a geometric approach of the solid angle encountered by an outgoing particle/jet. Accordingly, the L3 detector is sub-divided into 12 regions as listed in table 5.9 (see figure 5.6).

Energy flow for *particle/jet* cascade have been reconstructed for two types of spatially correlated "clusters" by combining response from different sub-regions in the L3 detector with 100 MeV cut-off to remove contamination from random noise:

- clusters from energy deposited in the calorimeters alone (ASRC)

$$E^C = \sum_{i \neq 5,11,12} G_i(\sqrt{\mathrm{s}}) \cdot E_i^C$$

Regions	:	Sub-detectors
1,7,9	:	Electromagnetic Calorimeter (ECAL)
2,4,6,8,10	:	Hadron Calorimeter (HCAL)
3	:	Spaghetti Calorimeter (EGAP)
5	:	Active Lead Ring (ALR)
11	:	Muon Chamber (MUCH)
12	:	Time Expansion Chamber (TEC)

Table 5.9: Different regions of L3 detector for cluster definition

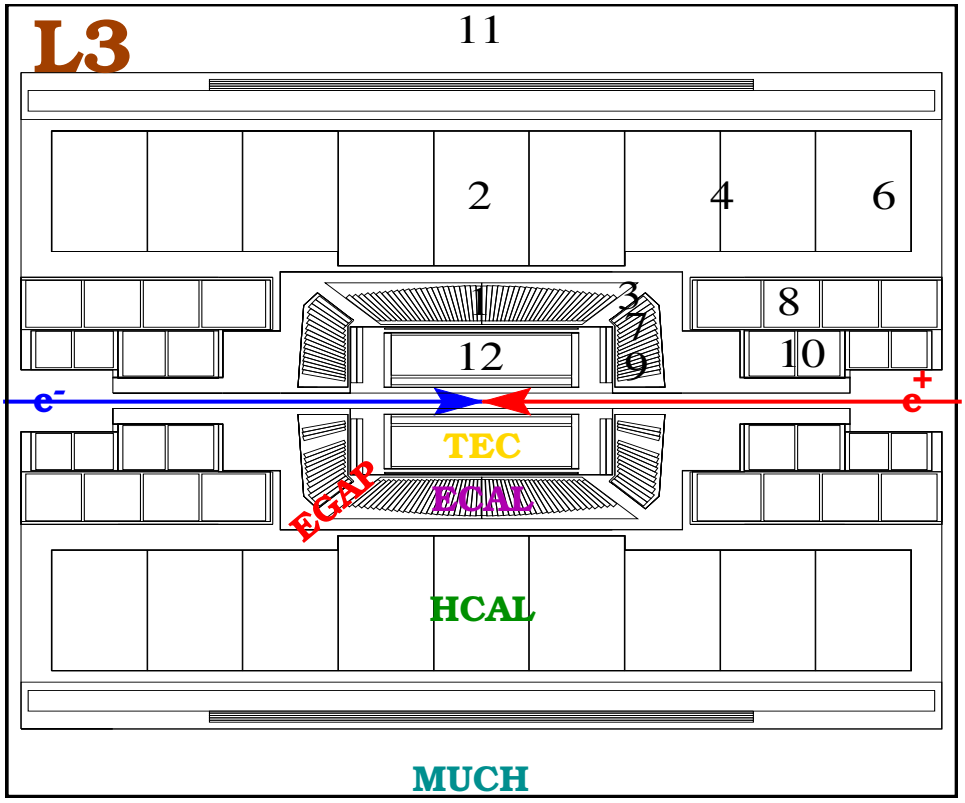

Figure 5.6: Different regions of L3 detector for cluster definition

- super-clusters from a non-linear combination of momentum & energy from charged tracks & calorimetric clusters (ECLU)

$$E^C = \sum_i G_i(\sqrt{s}) \cdot E_i^C + \sum_{j,k} A_{jk}(\sqrt{s}) \cdot C(E_j^C, E_k^C)$$

where E_i^c is the sum of uncorrected energies of all the constituents of the cluster from the region i, the correlation function for super-clusters has been chosen as

$$C(E_j^c, E_k^c) = \frac{E_j^c \cdot E_k^c}{E_j^c + E_k^c}$$

and the geometric weight factors G_i and A_{jk} are known as *G-factors* [33].

5.4.3 Energy Calibration

Hadronic events are very suitable for the off-line global energy calibration of the detector, because of its relative abundance (high cross section) and characteristic multi-particle final state. Thus, averaging over a sufficient number of hadronic events, energy response of a large fiducial volume of the detector can studied.

If $\overline{E}_i$ is the average energy in the geometric region i over a reasonably large number of hadronic events, then for the ASRC option, the average total energy and the variance are given by:

$$\begin{aligned} \overline{E} &= \sum_i G_i \overline{E}_i \\ \sigma^2 &= \overline{(E - \overline{E})^2} \\ &= \sum_{i,j} G_i G_j (\overline{E_i E_j} - \overline{E_i}\,\overline{E_j}) \end{aligned}$$

The above expression is generalised for ECLU option as well. Finally, the G-factors are fitted to minimise the function:

$$M = \left(\frac{\sigma}{\overline{E}}\right)^2 + \lambda \left(\frac{\sqrt{s}}{\overline{E}} - 1\right)^2$$

where the first term denotes the energy resolution and the second term imposes energy conservation at the centre-of-mass energy $\sqrt{s}$. λ, the Lagrange's multiplier, is assigned a large value.

5.4.4 Performance of ASRC and ECLU

There are several options in forming clusters using ASRC or ECLU algorithms which differ in level of particle identification, use of correlation function, etc. Some of these options has been studied here. Visible energy distribution shows a remarkable difference between the ASRC and ECLU G-factors. Figure 5.7 shows the scaled visible energy distribution of the calibration data from 1998 (at centre-of-mass energy $\sim M_Z$) for the ASRC (electromagnetic option) and ECLU (energy independent correlation function without explicit particle identifications) options. The smooth curves shown on the plot are results of fits to the observed distributions to a sum of Gaussian distributions:

$$f\left(\frac{E_{vis}}{\sqrt{s}}\right) = \sum_{i=1}^{2} \frac{w_i}{\sqrt{2\pi}\sigma_i} \exp\left[-\frac{(E_{vis}/\sqrt{s} - \mu_i)^2}{2\sigma_i^2}\right]$$

The fitted distribution agree well with the data. The resolution obtained is better with the ECLU option, as it takes into account the information of charged tracks as well as the

calorimetric clusters, along with the correlation among the different parts of the detectors. The evolution of the RMS of visible energy distributions is shown in table 5.10.

The angular resolution is studied by selecting on 2 jet events from 1998 calibration data at $\sqrt{s} \sim M_Z$. The best g-factors and the resolutions are shown in table 5.11 and figures 5.8 and 5.9 [33].

Year	$\sqrt{s}$(GeV)	ASRC		ECLU	
		DATA	MC	DATA	MC
1991	91.2	12.4	12.4	9.5	9.1
1992	91.2	12.9	12.7	9.5	9.6
1993	91.2	12.9	12.8	9.6	9.4
1994	91.2	12.9	12.7	9.6	9.4
1995	133	12.3	12.4	10.2	10.3
1996	161	13.0	12.6	10.5	10.1
1996	172	14.2	12.6	10.4	10.1
1997	133	12.6	12.5	12.1	11.5
1997	183	11.6	10.9	10.5	10.0
1998	189	11.4	10.6	10.0	9.6

Table 5.10: Visible energy resolutions (%) at different centre-of-mass energies.

Measurement	ASRC Algorithm				ECLU Algorithm			
	RMS (mrad)	w_i	μ_i (mrad)	σ_i (mrad)	RMS (mrad)	w_i	μ_i (mrad)	σ_i (mrad)
θ	44.3	0.71	1.0	34.9	45.1	0.64	0.0	33.1
		0.29	0.0	60.0		0.36	1.3	59.4
ϕ	57.5	0.70	-0.9	36.8	51.4	0.75	-0.3	31.8
		0.30	0.4	88.3		0.25	0.7	85.6

Table 5.11: Polar and azimuthal angular resolutions of jets measured from two jet sample in the 1998 calibration data.

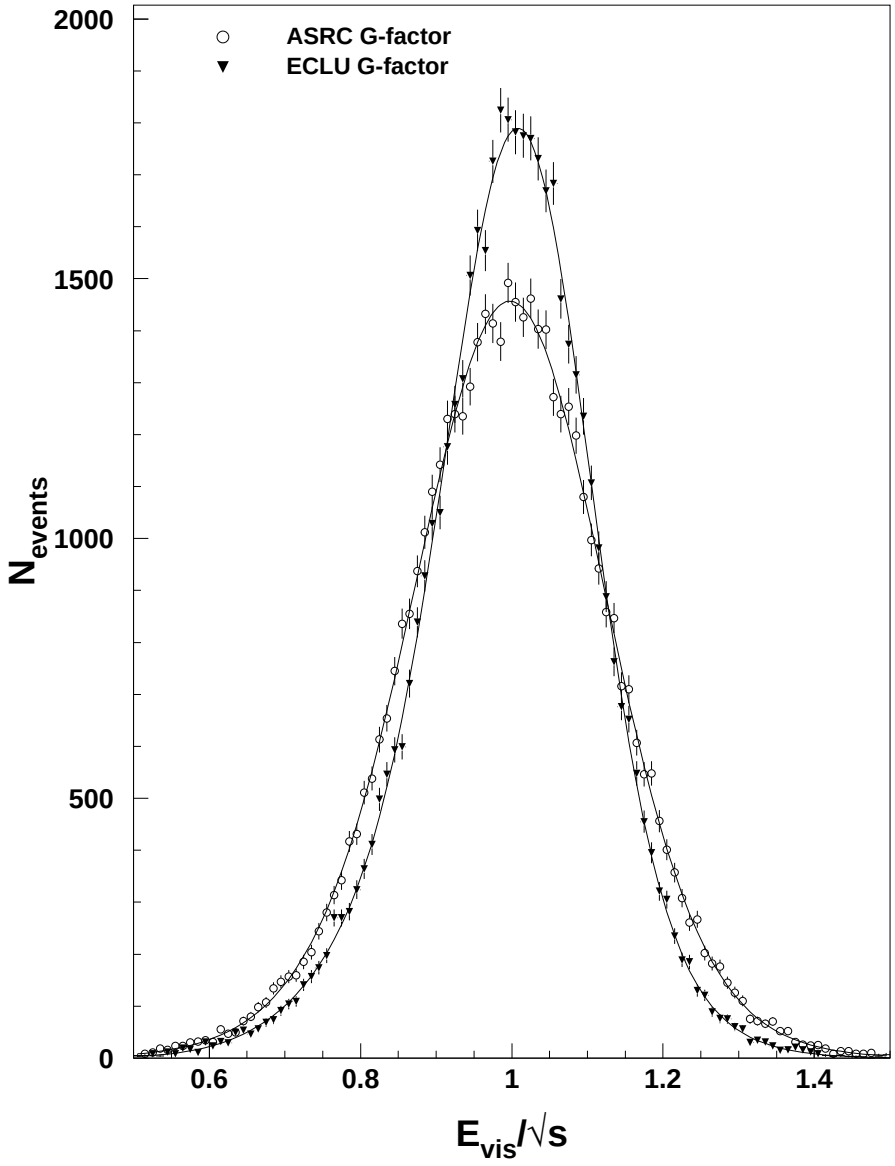

Figure 5.7: Distributions of scaled visible energy for ASRC's and ECLU's for 1998 calibration data with fits to a sum of 2 Gaussian distributions.

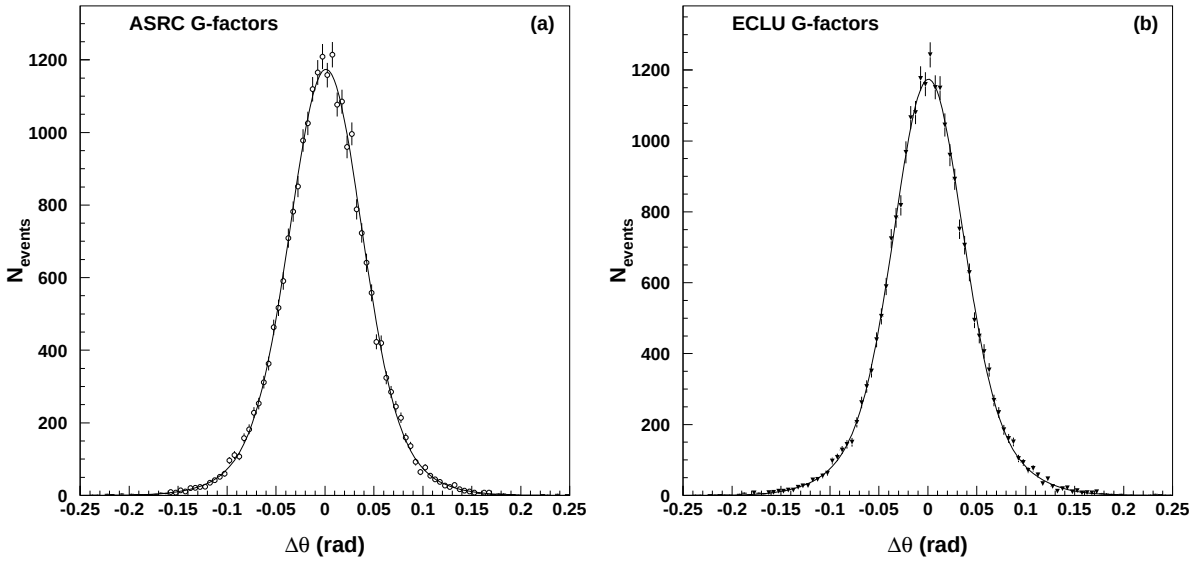

Figure 5.8: Polar angular resolution of jets measured from two jet sample in 1998 calibration data for (a) ASRC and (b) ECLU algorithms.

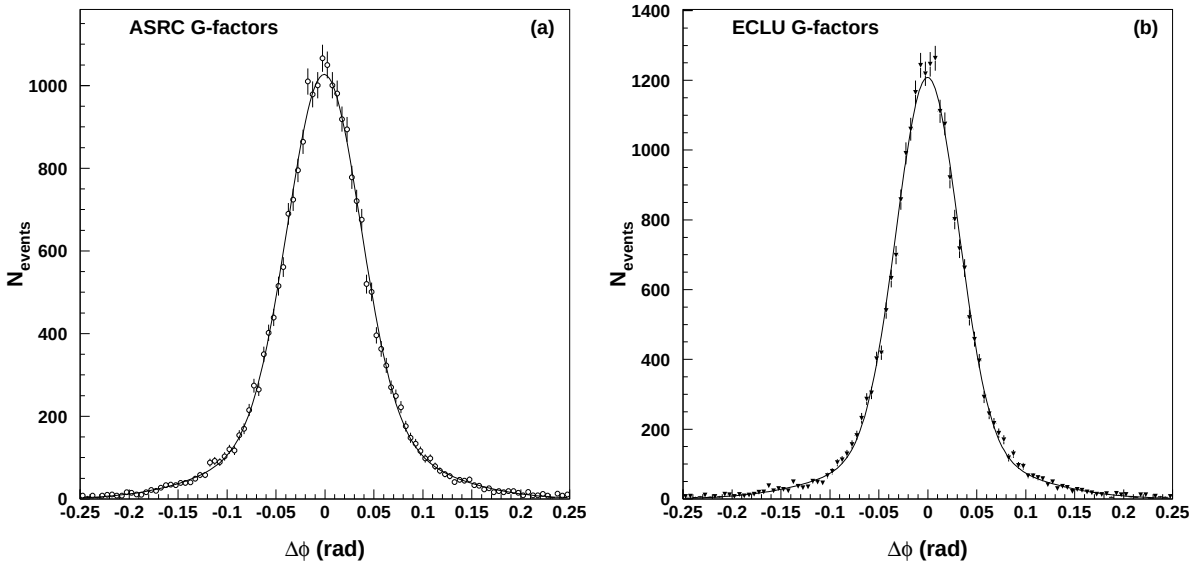

Figure 5.9: Resolution in azimuthal angle of jets measured from two jet sample in 1998 calibration data for (a) ASRC and (b) ECLU algorithms.

References

[1] W.J. Stirling, "Topical issues in Perturbative QCD", Lectures deliverd at CERN-JINR School of Physics, Casta-Papiernicka, August 1999.

[2] L3 Collaboration, contributed to the summer conferences 1999, L3 note #2440 (1999).

[3] L3 Collaboration, B. Adeva *et al.*, Z. Physik **C55** (1992) 39.

[4] L3 Collaboration, M. Acciarri *et al.*, Phys. Lett. **B411** (1997) 339.

[5] L3 Collaboration, M. Acciarri *et al.*, Phys. Lett. **B371** (1996) 137;
L3 Collaboration, M. Acciarri *et al.*, Phys. Lett. **B404** (1997) 390;
L3 Collaboration, M. Acciarri *et al.*, Phys. Lett. **B444** (1998) 569.

[6] L3 Collaboration, contributed to the summer conferences '99, L3 note #2414 (1999).

[7] Subir Sarkar, "Study of Hadronic Events in e^-e^+ Collisions using L3 Detector at Large Electron Positron (LEP) Collider at CERN", Ph.D. thesis, Tata Institute of Fundamental Research (1997).

[8] P.N. Burrows, "Precise tests of qcd in e^+e^- annihilation", Lectures given at the SLAC Summer Institute, SLAC-PUB-7434, August 19-30, 1996.

[9] T. Hebbeker, Physics Reports **217** (1992) 69.

[10] C. Peterson *et al.*, Phys. Rev. **D27** (1983) 105.

[11] JETSET 7.4 Monte Carlo Program:
T. Sjöstrand, Comp. Phys. Comm. **82** (1994) 74.

[12] HERWIG 5.9 Monte Carlo Program:
G. Marchesini and B.R. Webber, Nucl. Phys. **B310** (1988) 461;
I.G. Knowles, Nucl. Phys. **B310** (1988) 571;
G. Marchesini *et al.*, Comp. Phys. Comm. **67** (1992) 465.

[13] ARIADNE 4.08 Monte Carlo Program:
U. Pettersson, "ARIADNE: A Monte Carlo for QCD Cascades in the Color Dipole

Formulation", Lund Preprint, LU TP 88-5 (1988);
L. Lönnblad, "The Colour Dipole Cascade Model and the Ariadne Program", Lund Preprint, LU TP 91-11 (1991).

[14] COJETS 6.23 Monte Carlo Program:
R. Odorico, Nucl. Phys. **B228** (1983) 381;
R. Odorico, Comp. Phys. Comm. **32** (1984) 139, Erratum: **34** (1985) 43;
R. Mazzanti and R. Odorico, Nucl. Phys. **B370** (1992) 23;
R. Mazzanti and R. Odorico, Bologna preprint DFUB 92/1.

[15] L3 Collaboration, B. Adeva *et al.*, Z. Phys. **C55** (1992) 39;
Sunanda Banerjee, Swagato Banerjee, L3 Note #1978 (1996);
Swagato Banerjee, "Tuning of QCD Model Parameters Using LEP Data of Hadronic Z Decays", M.Sc. thesis, Tata Institute of Fundamental Research (1998).

[16] L3 Collaboration, B. Adeva *et al.*, Nucl. Inst. Meth. **A289** (1990) 35;
M. Chemarin *et al.*, Nucl. Inst. Meth. **A349** (1994) 345;
M. Acciarri *et al.*, Nucl. Inst. Meth. **A351** (1994) 300;
G. Basti *et al.*, Nucl. Inst. Meth. **A374** (1996) 293;
A. Adam *et al.*, Nucl. Inst. Meth. **A383** (1996) 342.

[17] JADE Collaboration, W. Bartel *et al.*, Zeitschrift für Physik **C33** (1986) 23;
JADE Collaboration, S. Bethke *et al.*, Physics Letters **B213** (1988) 235.

[18] MARK J Collaboration, D.P. Barber *et al.*, Physics Letters **B89** (1979) 139.

[19] S. Brandt *et al.*, Physics Letters **12** (1964) 57;
E. Fahri, Physical Review Letters **39** (1977) 1587.

[20] G.C. Fox, F. Wolfram, Physical Review Letters **41** (1978) 1581;
G.C. Fox, F. Wolfram, Nuclear Physics **B149** (1979) 413;
G.C. Fox, F. Wolfram, Physics Letters **B82** (1979) 134.

[21] Sunanda Banerjee, Swagato Banerjee, L3 Note # 2069 (1997).

[22] Sunanda Banerjee, Swagato Banerjee, L3 Note # 2247 (1998).

[23] EURODEC Monte Carlo Program:
A. ALi and B. van Eijk, CERN Program Library W 5048.

[24] S. Banerjee, S.Müller, L3 Note # 1441 (1993).

[25] MARK J Collaboration, D.P. Barber *et al.*, Phys. Rev. Lett. **43** (1979) 830.

[26] J.D. Bjorken and S.J. Brodsky, Phys. Rev. **D1** (1970) 1416.

[27] T. Chandrahoman and L. Clavelli, Nucl. Phys. **B184** (1981) 365;
MARK II Collaboration, A. Peterson *et al.*, Phys. Rev. **D37** (1988) 1;
TASSO Collaboration, W. Braunschweig *et al.*, Z. Physik **C45** (1989) 11.

[28] G. Parisi, Phys. Lett. **B74** (1978) 65;
J.F. Donoghue, F.E. Low and S.Y.Pi, Phys. Rev. **D20** (1979) 2759.

[29] S. Catani *et al.*, Phys. Lett. **B295** (1992) 269.

[30] Yu.L. Dokshitzer, Contribution to the Workshop on Jets at LEP and HERA, Durham (1990);
N. Brown and W.J. Stirling, Rutherford Preprint RAL-91-049;
S. Catani *et al.*, Phys. Lett. **B269** (1991) 432;
S. Bethke *et al.*, Nucl. Phys. **B370** (1992) 310.

[31] S. Banerjee and F. Bruyant, L3 Note # 748 (1989).

[32] L3 Collaboration, O. Adriani *et al.*, Nuclear Instr. & Methods **A302** (1991) 53.

[33] A. Ricker, L3 Note # 1394 (1993);
S. Banerjee, J. Casaus and S. Sarkar, L3 Note # 1939 (1996);
S. Banerjee, M. Rescigno and S. Sarkar L3 Note # 2394 (1999).

Chapter 6

Hadronic Event Selection at $\sqrt{s} > M_Z$

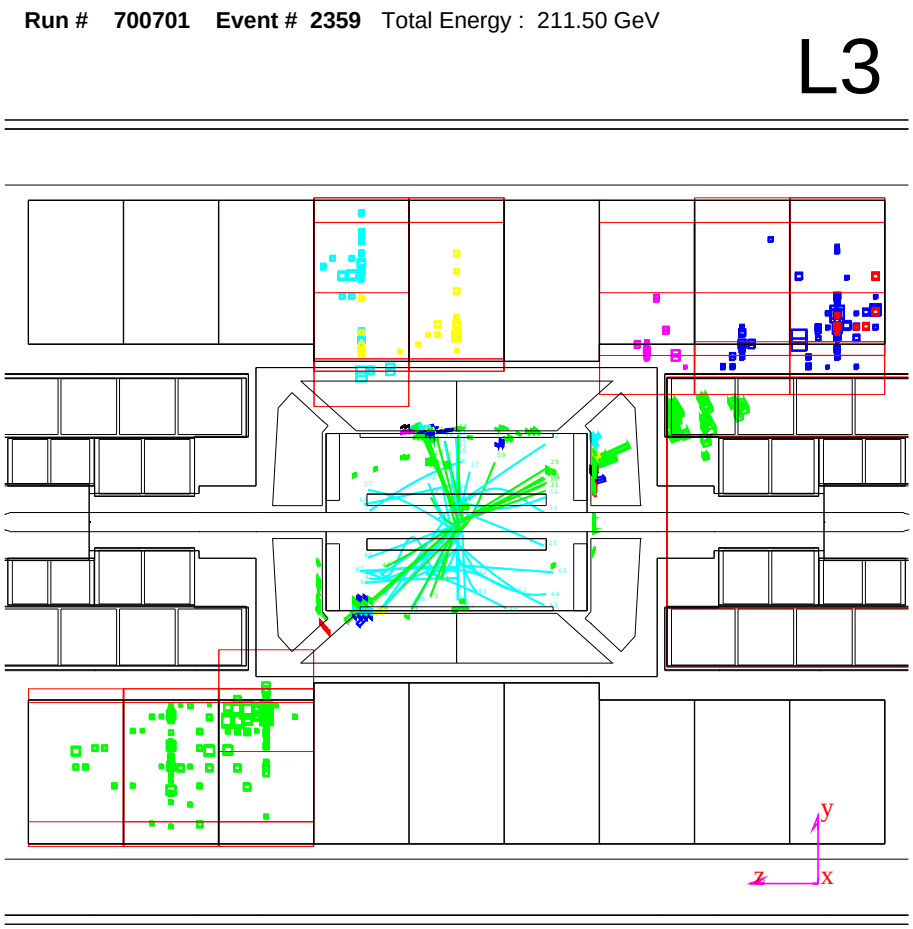

Figure 6.1: A three jet hadronic event at $\sqrt{s} = 189$ GeV from 1998 data taking period.

A typical hadronic event as seen in the L3 detector [1] is shown in the figure 6.1.

Hadronic events are characterised by:

- large number of particles observed in the final state, and
- large visible energy deposited in the detector.

6.1 Hadronic Event Selection

In terms of the directed energy measurements $\vec{\mathcal{E}}_i$ of the i^{th} cluster, with the *clusters* selected using an energy threshold of 100 MeV, some global selection variables like visible energy, missing energy, energy imbalance along the beam direction and in a plane perpendicular to the beam direction, and number of clusters are defined respectively as:

$$\begin{aligned} \mathrm{E_{vis}} &= \sum_{\mathrm{i}} \mid \vec{\mathcal{E}}_{\mathrm{i}} \mid \\ \vec{\mathcal{E}}_{\mathrm{miss}} &= -\sum_{\mathrm{i}} \vec{\mathcal{E}}_{\mathrm{i}} \\ \mathrm{E_{\parallel}} &= \hat{\mathrm{z}} \cdot \vec{\mathcal{E}}_{\mathrm{miss}} \\ \mathrm{E_{\perp}} &= \sqrt{(\hat{\mathrm{x}} \cdot \vec{\mathcal{E}}_{\mathrm{miss}})^2 + (\hat{\mathrm{y}} \cdot \vec{\mathcal{E}}_{\mathrm{miss}})^2} \\ \mathrm{N_{cl}} &= \sum_{\mathrm{i}} 1 \end{aligned}$$

where $\{\hat{x}, \hat{y}, \hat{z}\}$ are the three unit vectors in a right-handed orthogonal Cartesian coordinate system, with origin at the interaction point and z-axis pointing along the direction of the incoming electron and x-axis pointing towards the centre of the LEP ring.

For selecting hadronic events at $\sqrt{\mathrm{s}} > \mathrm{M_Z}$, one requires:

- $\mathrm{E}_{vis}/\sqrt{\mathrm{s}} > \mathrm{a}$: to reject processes with smaller effective centre-of-mass energy;
- $\mathrm{E_{\perp}/E}_{vis} < \mathrm{b}$: to reject processes with large missing energy;
- $\mathrm{N}_{cluster} > 12$: to reject processes like lepton pair production;

where the values of a and b as optimised at different $\sqrt{\mathrm{s}}$ are shown in the table 6.1.

$\sqrt{\mathrm{s}}$(GeV)	130	136	161	172	183	189
a	0.5	0.5	0.6	0.6	0.7	0.7
b	0.5	0.5	0.4	0.4	0.3	0.3

Table 6.1: Cuts on visible energy and transverse energy imbalance at different $\sqrt{\mathrm{s}}$.

In order to reject events compatible with cosmic background, another additional criteria is demanded: $\mathrm{N}_{tracks} > 0$.

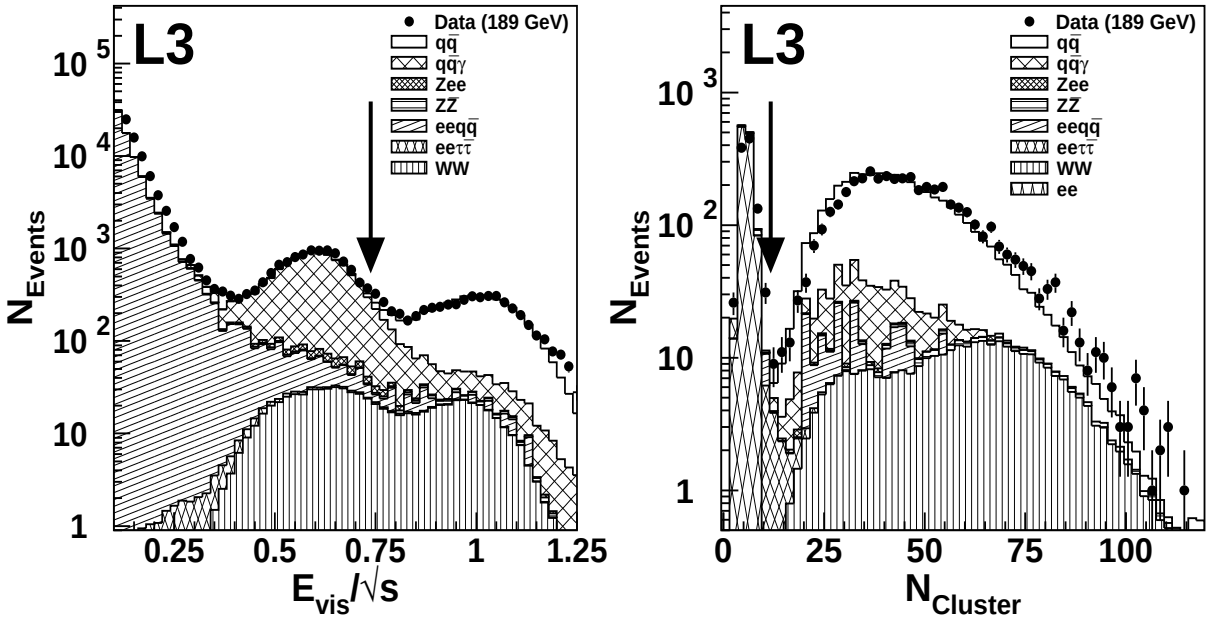

Figure 6.2: Distributions of scaled visible energy and number of clusters at $\sqrt{s} = 189$ GeV, with cuts shown as arrow on plots.

Monte Carlo events for the signal and different background processes have been passed through the L3 detector simulation [2], and are used to estimate the efficiency and purity of the selection criteria. Figures 6.2 show the distribution of some of the selection variables with *all other cuts* applied. The shaded regions shown are the contribution from the different backgrounds, whereas the empty region indicates the signal. The Monte Carlo predictions are shown one on top of the other so that the final histograms can be compared directly to data. All the Monte Carlo predictions are normalised by the number of selected hadron events to the observed luminosity in data, using cross sections from the programs and measured efficiency of selection.

The different Monte Carlo programs used for the signal and background processes along with representative cross sections at $\sqrt{s} = 189$ GeVare summarised in the table 6.2.

Process	:	Monte Carlo Programs	Cross section
$e^-e^+ \to qq(\gamma)$	:	JETSET PS [3] and PYTHIA [4]	98.43 pb
$e^-e^+ \to W^-W^+$	:	KORALW [5]	16.55 pb
$e^-e^+ \to$ 2-photon	:	PHOJET [6] (PYTHIA)	4.19 (13.74) nb
$e^-e^+ \to ZZ$	:	PYTHIA	0.97 pb
$e^-e^+ \to Ze^-e^+$	:	PYTHIA	3.35 pb
$e^-e^+ \to \tau^-\tau^+$	:	KORALZ [7]	8.21 pb
$e^-e^+ \to e^-e^+$	:	BHAGENE [8]	4.02 nb

Table 6.2: Monte Carlo programs used for different processes, and typical cross sections.

6.2 ISR Background

Since the initial and the final state of the process $e^-e^+ \rightarrow$ *hadrons* contain charged particles, in high energy collisions energetic photons are always radiated, as shown in the figure 6.3. Depending upon the source of radiation, from the initial state or from the primary quarks produced early in the final state, they are classified as ISR and FSR respectively. Photons may also be radiated from the decay of unstable particles produced at the end of hadronisation phase, but these tend to remain embedded in the neighbouring hadronic environment. High energetic photons from ISR and FSR, which are indistinguishable as observed in the detector, tend to isolate from the remaining hadronic activity. At $\sqrt{s} = M_Z$, the ISR is strongly suppressed owing to the Z peak resonance, but as we move up in energy, the probability for the initial states to lose energy through photon bremsstrahlung increases. This corresponding ISR background has to be subtracted in order to study the hadronic interactions at the true centre-of-mass energy of the e^-e^+ collision.

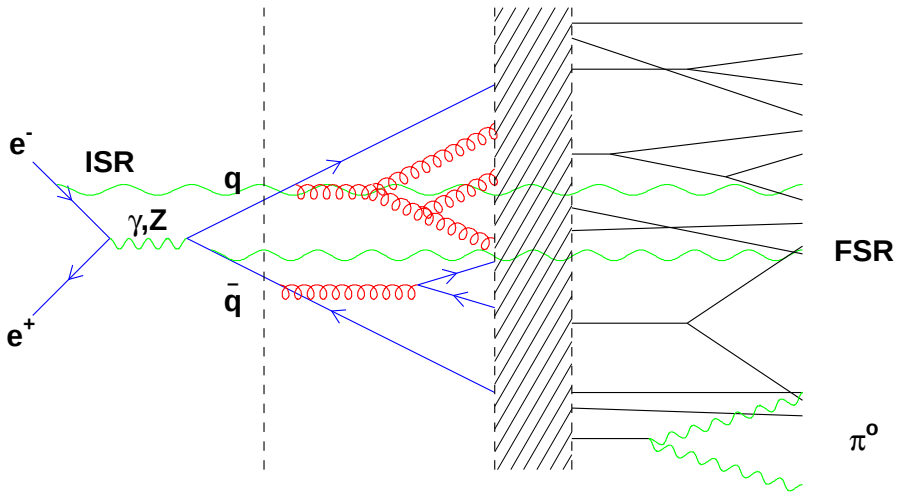

Figure 6.3: Photon radiations in the process $e^-e^+ \rightarrow$ *hadrons*.

The total cross section of $e^-e^+ \rightarrow q\overline{q}\gamma$ process can be expressed as a convolution of the ISR process and the underlying $e^-e^+ \rightarrow qq$ process at a lower effective centre-of-mass energy ($\sqrt{s'}$).

The differential cross section ($\frac{d\sigma}{dk}$) of the photon bremsstrahlung from a relativistic particle falls off with increasing photon energy roughly as $\frac{1}{k}$ [9]. Therefore, one expects large logarithmic terms of the form $(\alpha/\pi)\log(Q^2/m_e^2)$ for large values of momenta transfer (Q), associated with photon radiation from the electron and the positron in the initial state. The salient features of this ISR background is that the radiation is forward-peaked, and very often, these photons are lost in the beam pipe with characteristic missing longitudinal energy imbalance, and reduced centre-of-mass energy observed in the detector.

When energetic photons are radiated as ISR, at $\sqrt{s} > M_Z$, there is a strong tendency for the remaining e^-e^+ system to produce a Z^0, and for the effective reduced centre-of-mass energy of the remaining hadronic system to correspond to M_Z, because of the large hadronic cross section at the Z peak resonance. This is referred to as "radiative return to the Z".

Thus, depending upon the emission angle of the photon, which tend to be more often forward peaked, different sets of cuts have to be applied to reject events with ISR photons lost in the beam pipe and the remaining hadronic system to return to the Z.

6.2.1 Photons Collinear with Beam Direction

Two methods have been used to remove events with photon in beam pipe:

- First method uses the correlation between E_{vis} and $E_{\parallel}$ to discriminate well balanced events from unbalanced events with reduced visible energy deposited in the detector arising from an ISR photon lost in the beam pipe. In the plane of $E_{vis}/\sqrt{s}$ and $|E_{\parallel}|/E_{vis}$, events below a straight line are rejected as ISR events. The slope ($m \simeq 2$) of the line is increased with increasing $\sqrt{s}$ (above WW threshold), as the separation between unbalanced ISR events and true high energy hadronic events becomes more pronounced.

Equation of the line:

$$(E_{vis}/\sqrt{s}) > m(|E_{\parallel}|/E_{vis}) + C$$

$\sqrt{s}$(GeV)	m	C
130	2.5	0.5
136	2.5	0.5
161	1.5	0.5
172	2.0	0.5
183	2.4	0.3
189	2.4	0.3

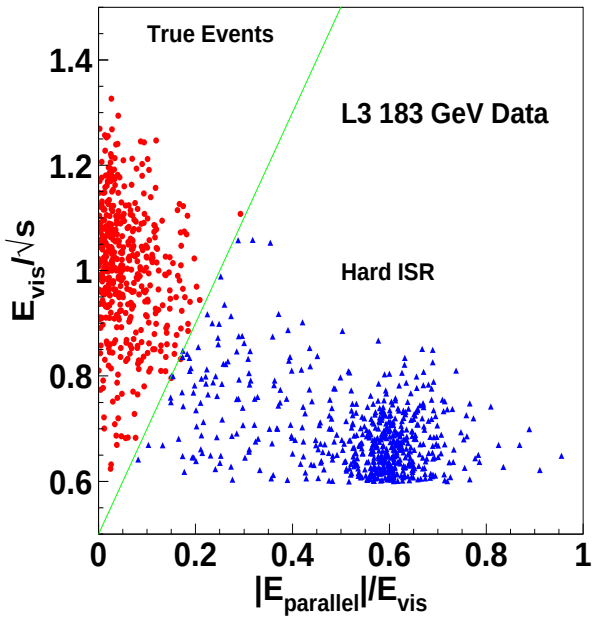

Figure 6.4: Two-dimensional cut in E_{vis} vs. $E_{\parallel}$ plane and scatter plot at $\sqrt{s} = 183$GeV.

The separation of the ISR background from the true high energy well-balanced hadronic events at $\sqrt{s} = 183$ GeV is shown in the figure 6.4. The optimal choice of the slope and the intercept have been obtained for each centre-of-mass energy

such that the product of efficiency and purity is maximised and are listed in the accompanying table.

- Alternatively, the effective centre-of-mass energy ($\sqrt{s'}$) is reconstructed, assuming photons have been radiated along beam-pipe. In this approach, the remaining hadronic event is forced into a two-jet topology, and the missing energy is attributed to have been carried away by the photon. Using kinematical considerations, one gets:

$$\sqrt{s'} = \sqrt{s}\sqrt{1 - \frac{2|\sin(\theta_1 + \theta_2)|}{\sin\theta_1 + \sin\theta_2 + |\sin(\theta_1 + \theta_2)|}}$$

where θ_1, θ_2 are the angles between the jets and the beam axis (see figure 6.5(a)).

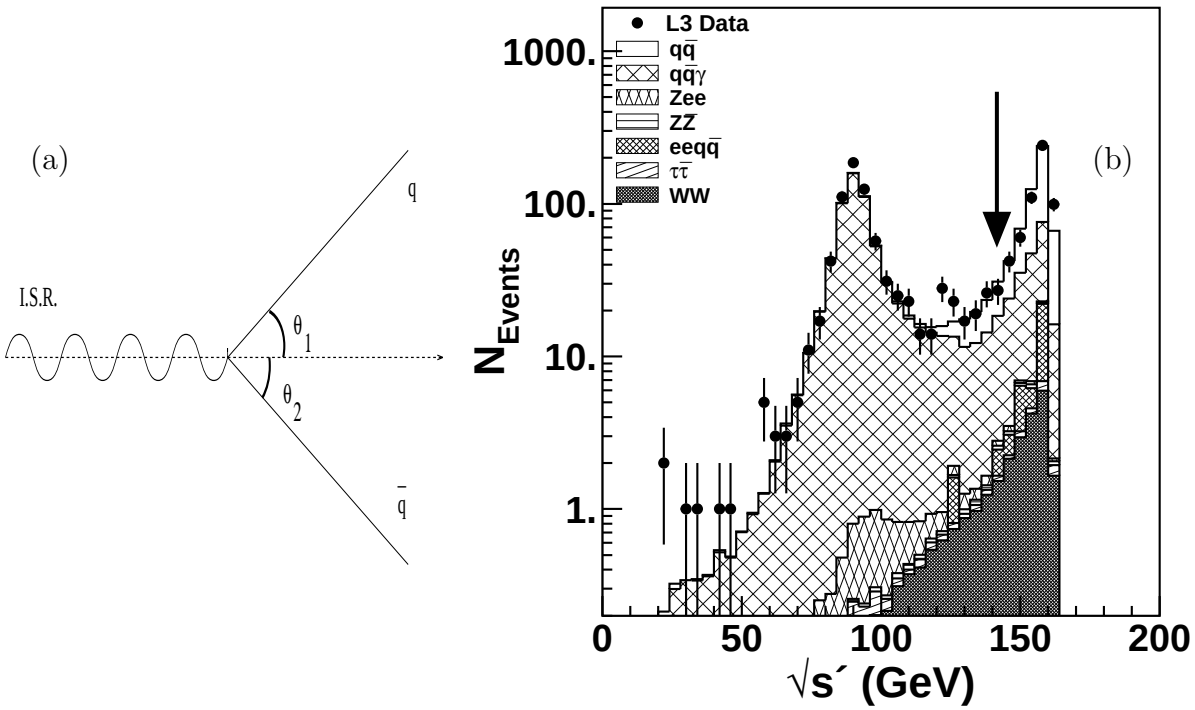

Figure 6.5: (a) The two jet and a photon topology is shown, where the ISR photon is along the beam axis.(b) Distribution of $\sqrt{s'}$ for ISR photon bremsstrahlung at $\sqrt{s} = 161$ GeV.

Figure 6.5(b) illustrates the $\sqrt{s'}$ distribution with all but ISR cuts applied to data at $\sqrt{s} = 161$ GeV. The ISR background is spread from just below unity, and peaks at $\sqrt{s'} = M_Z$ corresponding to the return to the Z, because of large hadronic cross section at Z peak resonance as explained earlier.

The true high energy hadronic events corresponding to the centre-of-mass energy close to e^-e^+ collision are chosen by applying the following criteria:

$$\frac{\sqrt{s'}}{\sqrt{s}} > .92$$

6.2.2 Energetic γ Seen in the Detector

The two principal criteria used for photon identification are: (a) isolated electromagnetic bump in the ECAL with reduced activity in the HCAL behind the bump; and (b) no associated track in the TEC.

The electromagnetic calorimeter has characteristically different response to particles losing energy in the detector electromagnetically and hadronically. The shower profile of energy deposited in the BGO crystals owing to the passage of photon and a jet are shown in the figure 6.6. These differences are exploited to identify a photon in the detector.

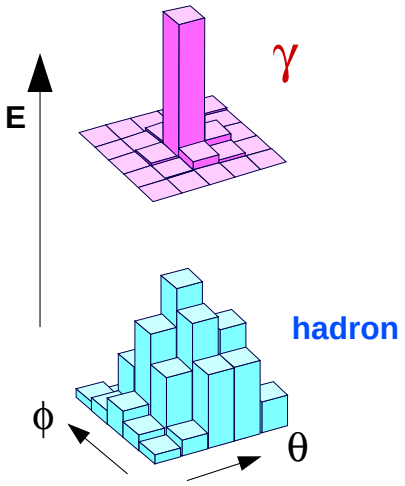

Figure 6.6: Shower profile of photon and hadronic jets in BGO.

The photon identification criteria used are:

- Electromagnetic bump with:

  1. sum of energy in (3x3) crystal matrix surrounding the most energetic crystal hit in the ECAL (E_9) > 0.5 GeV;
  2. the ratio of corrected energy of the cluster (assuming it to be electromagnetic) from energy deposited in the (3×3) and (5×5) crystal matrix surrounding the most energetic crystal hit in the barrel (endcap) electromagnetic calorimeter $\frac{E_9}{E_{25}} > 0.95$ (0.90);
  3. the electromagnetic chi-squared as obtained by comparing the lateral profile of energy deposited in the ECAL from test beam results $\chi^2_{EM} < 5.0$ (10.0);
  4. the ratio of total energy deposited in the HCAL behind ECAL to that deposited in the BGO crystals in ECAL $E_{HCAL}/E_{BGO} < 0.25$;
  5. $N_{crystals} > 4$, to reduce contamination from random noise.

The cuts on E_9/E_{25} and χ^2_{EM} are stricter in the barrel part ($|\cos\theta| < 0.7$) of the detector and somewhat relaxed in the endcap region (shown within parentheses above).

- No matching track:

  1. Good track is taken if it spans over at least 30 wires in the TEC, with transverse momentum $p_\perp \geq 100$ MeV, and distance of closest approach to the primary vertex $|\,\mathrm{DCA}\,| \leq 50$ mm
  2. $|\Delta\phi| > .01$ mrad, where $\Delta\phi$ is the difference of azimuthal angles between the bump in the BGO and its nearest track, measured at the face of the calorimeter with the track extrapolated using its nominal momenta.

When the photon is observed in the detector, the energy spectrum of most energetic identified photon shows two peaks: near origin, the well known infrared divergent behaviour falling off as inverse power of energy, and the second peak arising due to "return to the Z" (see figure 6.7). The signal, high energy hadronic events at scale close to the energy of e^-e^+ collision, is defined by the following criteria:

- $(E_\gamma)_{\max} \leq 15$ GeV for $e^-e^+ \rightarrow q\bar{q}\gamma$ at a $\sqrt{s} < 140$ GeV;
- $(E_\gamma)_{\max} \leq .18\sqrt{s}$ for $e^-e^+ \rightarrow q\bar{q}\gamma$ at a $\sqrt{s} > 140$ GeV.

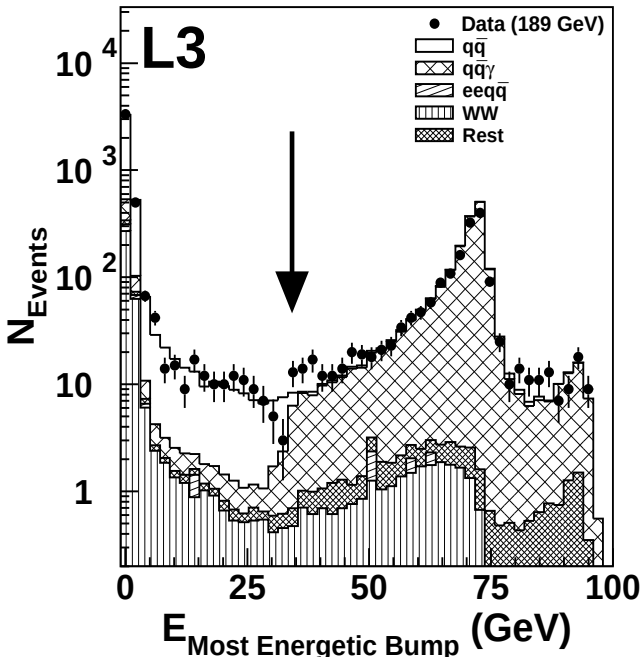

Figure 6.7: Comparison of the energy distribution of most energetic photon for Monte Carlo and data at $\sqrt{s} = 189$ GeV. The region to the left of the arrow is the signal.

The purity of the signal improves by 3% by demanding additional isolation condition for identification of the photon: $\frac{E_{15^\circ\text{Cone}}}{E_9} \leq .85$, where the ratio is that of energy deposited in a 15° cone about the most energetic crystal to the energy determined from the (3×3) matrix surrounding the central crystal.

6.3 W^-W^+ Background

For $\sqrt{s} > 161$ GeV, the $e^-e^+ \to W^-W^+$ process is an important background to $e^-e^+ \to$ *hadrons*. Different sets of cuts are used to reject the accompanying hadronic activity in semileptonic decays of the W boson and its purely hadronic decay mode.

6.3.1 Semileptonic Decays: $W^-W^+ \to q\bar{q}l\nu$

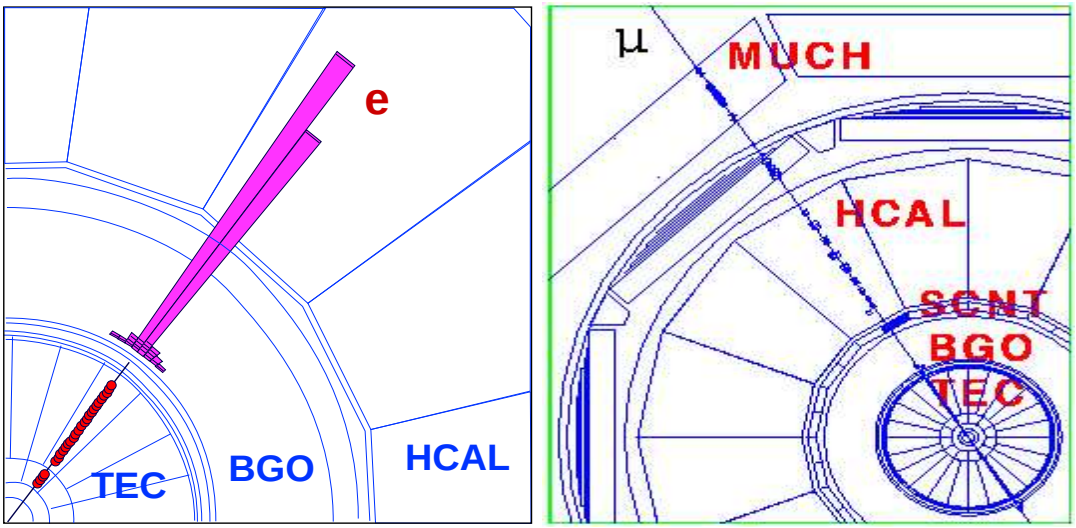

Figure 6.8: Representative signatures of electron and muon in the detector.

Characteristic detector response to passage of an energetic electron and muon are shown in the figure 6.8. These are used in the L3 detector, equipped with a central tracking device, excellent electromagnetic calorimeters, and a precise muon tracking system, to identify electrons and muons. The lepton identification criteria are:

- Electron: Electron is identified using the same conditions as identifying photon, as energetic electromagnetic bump in the ECAL, but with an associated track in the TEC ($|\Delta\phi| < .01$ mrad).
- Muon: Muon is identified as having:
  - at least 1 Z-segment and 2 P-segments (or a forward segment) hit in the muon chamber;

– with χ^2/d.o.f. < 8, so as to differentiate it from punch-through hadrons;

– having a matched track, with distance of closest approach from the interaction point (DCA) < 250 μm; and

– consistent with non-cosmic time-of-flight measurement in the scintillators.

The semileptonic decays of W^-W^+ into $q\bar{q}e\nu$ and $q\bar{q}\mu\nu$ is rejected by demanding:

- no energetic electrons ($E_e \geq 40$ GeV)
- no high-momentum muons ($P_\mu \geq 40$ GeV)

in the selected sample of hadronic events. The electron energy and muon momentum distribution for different processes is compared to the data at $\sqrt{s} = 189$ GeV, with all the other cuts applied, in the figure 6.9.

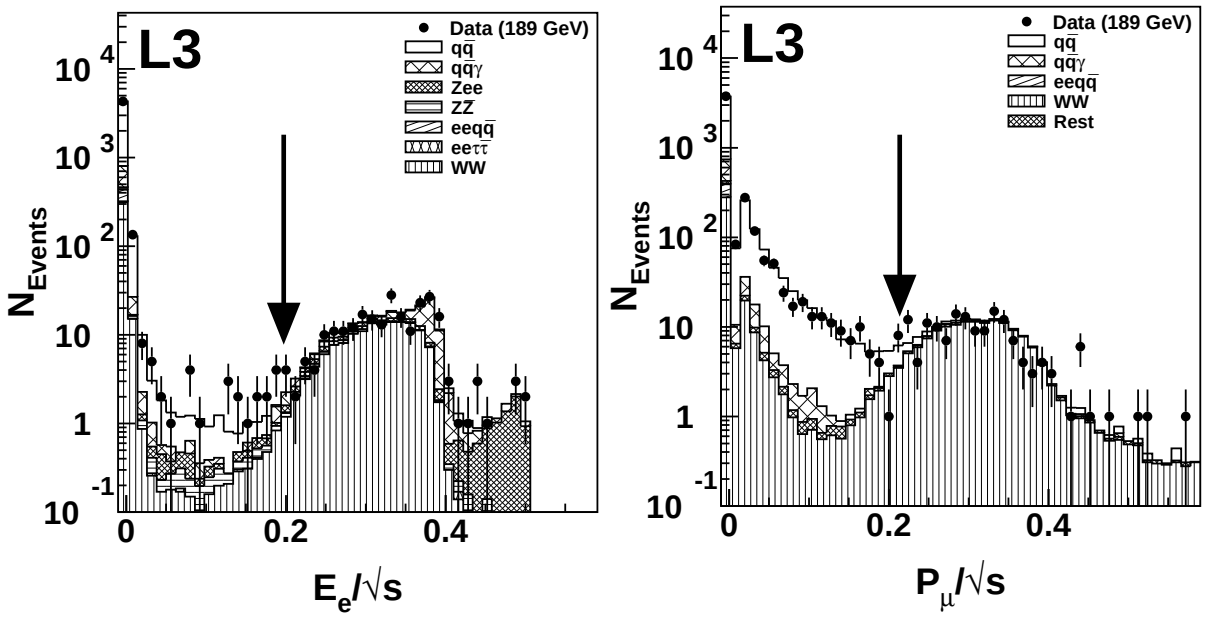

Figure 6.9: Electron energy and muon momenta spectra at $\sqrt{s} = 189$ GeV.

6.3.2 Hadronic Decays: $\mathbf{W^-W^+ \rightarrow q\bar{q}q\bar{q}}$

The hadronic branching fraction of W^-W^+ is $\sim 46\%$, and with a typical well-balanced, symmetric 4 jet structure, poses a severe background to hadronic events. In order to reject them, the first step is to force all events into a 4 jet topology, and then anti-select the event if *all* of the following criteria are satisfied:

- high multiplicity arising from 2 sets of $q\bar{q}$ decay: $N_{cluster} > 40, N_{track} > 15$;
- well-balanced event with large visible energy: $\frac{|E_\parallel|}{E_{vis}} < .2$;

- 4-jet topology with large 3 to 4 jet transition parameter in the Durham scheme [10]: $y_{34}^{D} > 0.0025$;
- symmetric 4-jet topology with energy of the most energetic jet $(E_{jet1}) < 0.395\sqrt{s}$, and ratio of energies of the most energetic to least energetic jet $(\frac{E_{jet1}}{E_{jet4}}) < 5$.

Using a energy-momentum conservation, a 4C kinematic fit using measured $\beta(=\frac{p}{E})$ for the jet energies, improves purity by 5% at $\sqrt{s} = 189$ GeV. The relative position of the cuts on fitted energy distributions and some of the other variables are shown in figure 6.10, where the WW rejection cuts have not been applied.

6.4 Event Statistics

The effect of selection can be understood in terms of the accepted background fraction in the sample of selected events. The effect of cuts on WW background, which appears predominantly in the 4 jet region on thrust distribution, is shown in the figure 6.11.

A summary of the selection at different centre-of-mass energy is presented in the table 6.3. The selected sample of events along with it efficiency and purity is shown, along with the accepted background contamination at each $\sqrt{s}$ between 130 to 189 GeV [11].

$\sqrt{s}$ (GeV)	130	136	161	172	183	189
Events	556	414	424	325	1500	4479
ε (%)	90.0	89.0	89.0	84.8	84.2	87.8
π (%)	80.6	81.5	81.2	82.6	82.4	81.1
ISR(%)	18.9	16.9	9.5	7.5	8.0	5.9
WW(%)	-	-	4.6	6.3	6.4	8.6
2-photon(%)	0.3	1.4	3.6	2.9	2.5	2.5
$\tau^{-}\tau^{+}$(%)	0.2	0.2	0.2	0.2	0.1	0.1
ZZ(%)	-	-	0.6	0.4	0.5	0.5
$Ze^{-}e^{+}$(%)	-	-	0.3	0.1	0.1	0.1

Table 6.3: Event statistics of the hadronic events for $130 \leq \sqrt{s} \leq 189$ GeV.

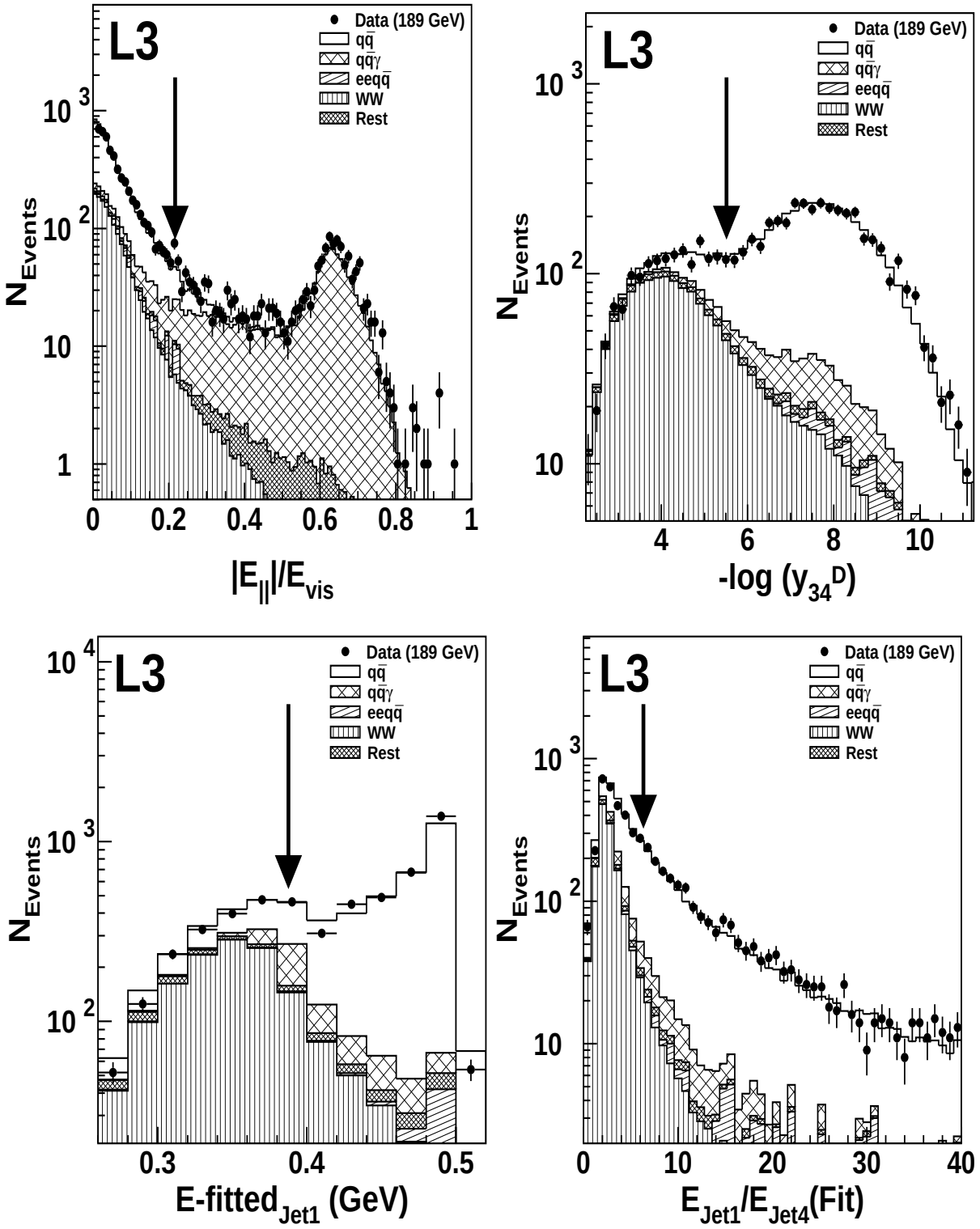

Figure 6.10: Monte Carlo distributions of parallel energy imbalance, 3 to 4 jet resolution parameter in Durham scheme, energy of the most energetic jet and ratio of the energies of most energetic to least energetic jets compared to data at $\sqrt{s} = 189$ GeV. In each of the plots, the WW rejection cuts have not been applied on the selection variable, and are shown by the arrow.

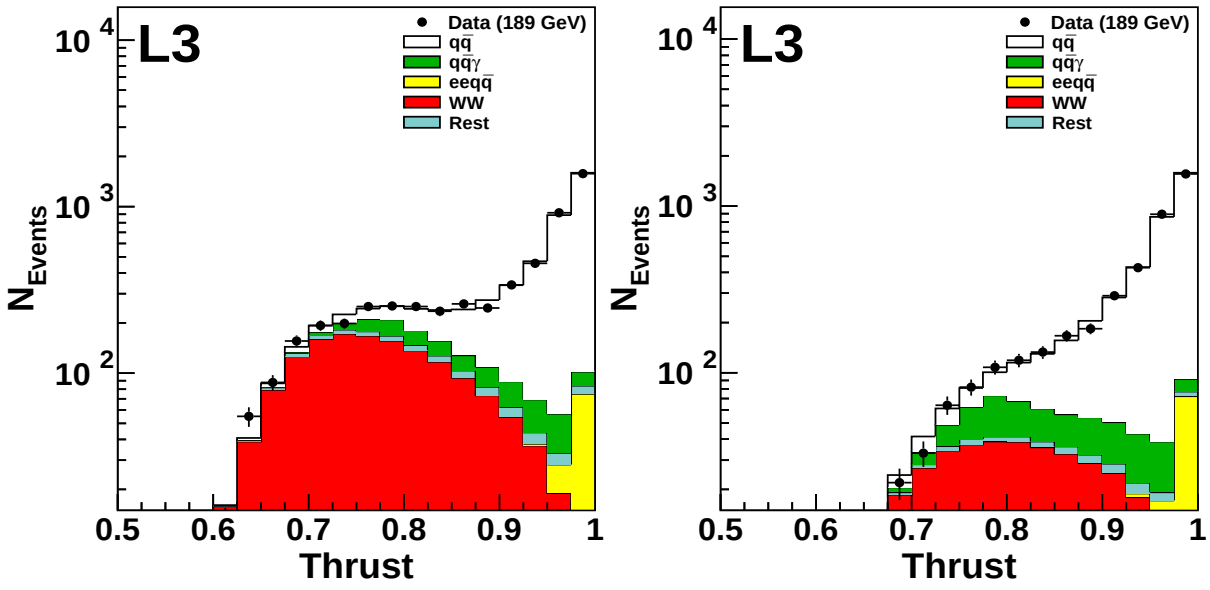

Figure 6.11: Signal and backgrounds at detector level shown on the thrust distribution (a) before WW rejection and (b) after WW rejection, at $\sqrt{s} = 189$ GeV.

References

[1] L3 Collaboration, B. Adeva *et al.*, Nucl. Inst. Meth. **A289** (1990) 35;
M. Chemarin *et al.*, Nucl. Inst. Meth. **A349** (1994) 345;
M. Acciarri *et al.*, Nucl. Inst. Meth. **A351** (1994) 300;
G. Basti *et al.*, Nucl. Inst. Meth. **A374** (1996) 293;
A. Adam *et al.*, Nucl. Inst. Meth. **A383** (1996) 342.

[2] The L3 detector simulation is based on GEANT Version 3.15.
See R. Brun *et al.*, "GEANT 3", CERN DD/EE/84-1 (Revised), September 1987.
The GHEISHA program (H. Fesefeldt, RWTH Aachen Report PITHA 85/02 (1985))
is used to simulate hadronic interactions.

[3] JETSET 7.4 Monte Carlo Program:
T. Sjöstrand, Comp. Phys. Comm. **82** (1994) 74.

[4] PYTHIA 5.7 Monte Carlo Program:
QCD parton shower and fragmentation process are taken from JETSET 7.4 [3];
T. Sjöstrand, CERN-TH-7112/93 (1993), revised august 1995;
T. Sjöstrand, Comp. Phys. Comm. **82** (1994) 74.

[5] M. Skrzypek *et al.*, Comp. Phys. Comm. **94** (1996) 216; Phys. Lett. **B372** (1996) 289.

[6] R. Engel, Z. Phys. **C66** (1995) 203;
R. Engel, J. Ranft and S. Roesler, Phys. Rev. **D52** (1995) 1459.

[7] S. Jadach, B.F.L. Ward and Z. Was, Comp. Phys. Comm. **79** (1994) 503.

[8] J.H. Field, Phys. Lett. **B323** (1994) 432;
J.H. Field and T. Riemann, Comp.Phys.Comm. **94** (1996) 53.

[9] Richard Fernow, "Introduction to experimental particle physics", chapter 2 "Electromagnetic Interactions", section 2.4. "Bremsstrahlung", Cambridge University Press, 1986.

[10] Yu. L. Dokshitzer, Contribution to the Workshop on Jets at LEP and HERA, Durham (1990);

N. Brown and W.J. Stirling, Rutherford Preprint RAL-91-049;
S. Catani *et al.*, Phys. Lett. **B269** (1991) 432;
S. Bethke *et al.*, Nucl. Phys. **B370** (1992) 310.

[11] L3 Collaboration, contributed to the summer conferences 1999, L3 note #2414 (1999).

Chapter 7

Systematics and Corrections

7.1 Backgrounds at Detector Level

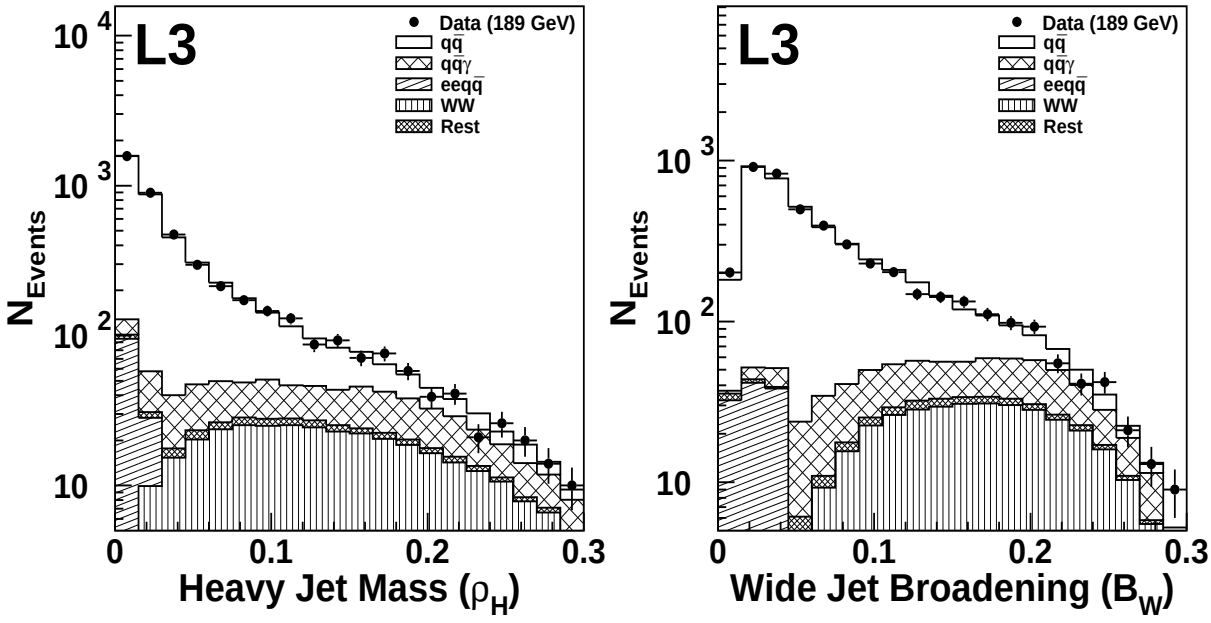

Figure 7.1: Data-Monte Carlo comparison for ρ_{H} and $\mathrm{B_W}$ at $\sqrt{\mathrm{s}} = 189$ GeV.

Monte Carlo events for the signal and background processes, passed through the L3 detector simulation program [1], describe the observed data in the L3 detector [2] quite well. As an example, the accepted signal and background events are compared to the data at $\sqrt{\mathrm{s}} = 189$ GeV, for the event shape variables heavy jet mass (ρ_{H}) and wide jet broadening ($\mathrm{B_W}$) in figure 7.2. So one can use Monte Carlo to correct the distributions for corrections of the data due to remaining background, and detector effects.

7.2 Corrections to Event Shape Distributions

The observed data from the detector contains some fraction of irreducible background in addition to the signal studied. The analysis must also take into account finite resolution effects and finite acceptance effects on the measurement.

In this spirit, the measured detector level distributions of event shape variables are corrected *bin-by-bin* for:

- remaining background;
- detector resolution;
- acceptance;
- initial/final state radiation.

After weighting the accepted background (N_{selected}) with a factor (ω) given by:

$$\omega = \frac{\sigma \cdot \mathcal{L}}{N_{\text{genarated}}},$$

for the ith background, the sum of the background contributions ($\sum_{\text{i}} \omega_{\text{i}} N^{\text{i}}_{\text{selected}}$) are subtracted from the data distributions.

Then, finite detector effect is corrected for using appropriate correction factors obtained from Monte Carlo studies. The total correction factor C is calculated for each bin as the product of two correction factors C_R and C_A, taking into account effects due to finite resolution and acceptance respectively:

$$\begin{aligned} \text{C} = \text{C}_\text{R} \cdot \text{C}_\text{A} \quad &= \quad \text{(fraction of events in detector reconstructed} \\ &\qquad \text{to genarator simulated with ISR/FSR turned off).} \end{aligned}$$

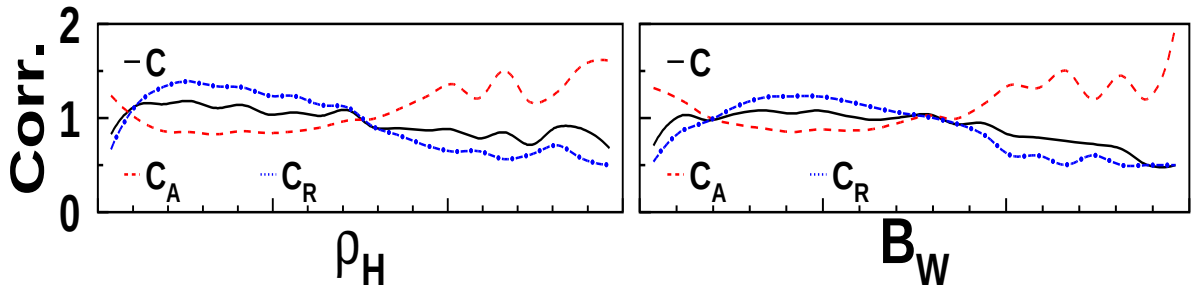

Figure 7.2: Correction factors for ρ_{H} and B_W at $\sqrt{\text{s}} = 189$ GeV.

Correction factors (C) for the event shape variables typically lie between 0.5 and 2.0. As an example, correction factors for the two event shape variables, heavy jet mass (ρ_{H}) and wide jet broadening (B_W), at $\sqrt{\text{s}} = 189$ GeV are shown in the figure 7.2. After such corrections, the data can be then compared with the perturbative QCD calculations directly at the level of particles.

7.2.1 Corrected Distributions

Monte Carlo distributions at the generator level are compared to the corrected data distributions for different types of models available.

Figures 7.3 shows the corrected thrust and the wide jet broadening distributions obtained at 183 GeV [3]. The data are compared with PYTHIA 5.7, HERWIG 5.6, ARIADNE 4.06 and COJETS 6.23 QCD models at particle level without ISR. The agreement is satisfactory.

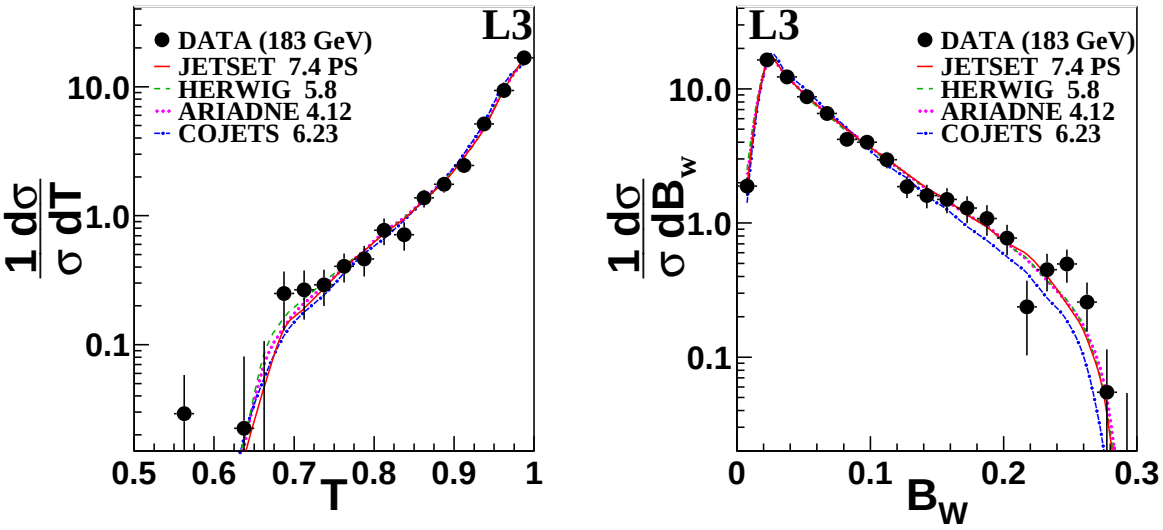

Figure 7.3: Corrected distribution of thrust, T and wide jet broadening, B_W at $\sqrt{s} = 183$ GeV in comparison with QCD model predictions. The errors shown are statistical only.

7.3 Systematic Studies

7.3.1 Sources and Estimates

To estimate the systematic error on the measured quantities, the analysis has been repeated taking into account the variation from the following sources:

➤ Due to detector:

- take two definitions of clusters, e.g. ASRC and ECLU;
- use barrel only ($|\cos(\theta_{thrust})| \leq 0.7$) as compared to the whole detector;
- using a theta dependent cut on the number of TEC wire hits in the definition of good tracks, as opposed to a constant cut.

The detector systematics is the dominant component of systematic errors and are similar at all energies.

➤ Due to background estimate:

- Use alternate selection:
  - ∗ for the ISR background, alternative selection with cut on $\sqrt{s'_{\rm reconstructed}}$ as compared to two-dimensional cut based on parallel imbalance is tried;
  - ∗ for W^-W^+ background, variations are tried with and without kinematic fitting, and also turning off WW-rejection during selections and correcting for the background using background subtraction alone.
- Vary accepted background for 2-photon processes by ± 30%.
- Vary background cross section for W^-W^+ background by ± 12% at $\sqrt{s}$ = 161 GeV where explicit WW rejection is turned off.

Systematic error due to ISR background decreases and due to W^-W^+ background increases with energy, as the accepted contamination follow similar trend (table 6.3).

➤ Due to choice of Monte Carlo:

- Vary signal Monte Carlo model (JETSET vs. HERWIG);
- Vary 2-photon Monte Carlo model (PYTHIA vs. PHOJET).

Systematics from this source is similar at all energies, and is the second most dominant component after detector effects.

Errors from similar sources are taken to be correlated over the entire energy range: $\sqrt{s}$ = 30 − 196 GeV, and uncorrelated among each other from different sources.

7.3.2 Statistical Component of Systematic Error

The statistical component of the systematic errors are estimated by:

☛ splitting Monte Carlo sample into luminosity weighted sub samples;

☛ treating each sub sample as data;

☛ taking the spread as estimate of the statistical component;

☛ subtracting the statistical component in quadrature from the systematic error.

The spread of the difference of $\langle\ 1-T\ \rangle$ using default and ISR variation for each luminosity weighted sub-sample at $\sqrt{s} = 161$ GeV is shown in the figure 7.4.

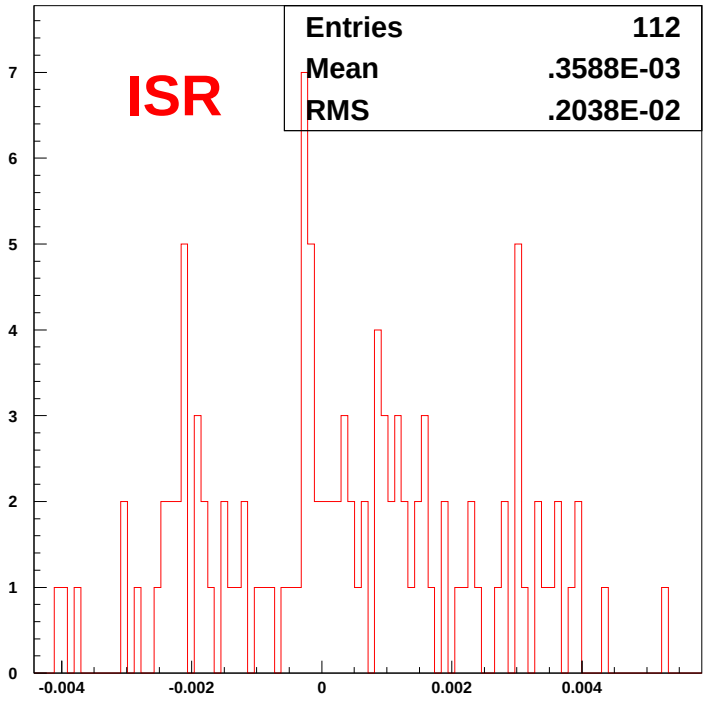

Figure 7.4: Statistical component of ISR systematics for $\langle\ 1-\mathrm{T}\ \rangle$ at $\sqrt{\mathrm{s}} = 161$ GeV.

7.3.3 Combining the Errors

For each source of the systematic variation, after subtracting the statistical component from the systematic errors, the half of the maximal spread is attributed to the systematic error. Then the contribution from the different sources are added in quadrature to estimate the final systematic error.

The effect of reduction of systematic errors for the different sources for $\langle\ 1-\mathrm{T}\ \rangle$ at $\sqrt{\mathrm{s}} = 161$ GeV is summarised in table 7.1.

Source	Systematic	Stat. Comp.	Final
Detector:			
G-Factor	0.0011	0.0008	0.0007
Track	0.0001	0.0001	–
Barrel	0.0006	0.0021	–
ISR	0.0007	0.0020	–
WW	0.0005	0.0000	0.0005
2-photon	0.0011	0.0000	0.0011
HERWIG	0.0003	0.0003	–
Total			0.0009

Table 7.1: Systematic errors on $\langle 1 - T \rangle$ at $\sqrt{\mathrm{s}} = 161$ GeV.

References

[1] The L3 detector simulation is based on GEANT Version 3.15.
See R. Brun *et al.*, "GEANT 3", CERN DD/EE/84-1 (Revised), September 1987.
The GHEISHA program (H. Fesefeldt, RWTH Aachen Report PITHA 85/02 (1985))
is used to simulate hadronic interactions.

[2] L3 Collaboration, B. Adeva *et al.*, Nuclear Instr. & Methods **A289** (1990) 35.

[3] L3 Collaboration, M. Acciarri *et al.*, Phys. Lett. **B444** (1998) 569.

Chapter 8

Aspects of Hard Gluon Radiation

8.1 Jet Rates

One of the characteristic feature of hard gluon radiation is the multi-jet topology. Jet rates have been studied using JADE [1] and DURHAM [2] algorithms, where the jet resolution parameters are defined as:

$$y_{cut}^{Jade} = 2\frac{E_i E_j}{E_{vis}^2}(1-\cos\theta_{ij}); \qquad y_{cut}^{Durham} = 2\frac{\min(E_i^2 E_j^2)}{E_{vis}^2}(1-\cos\theta_{ij})$$

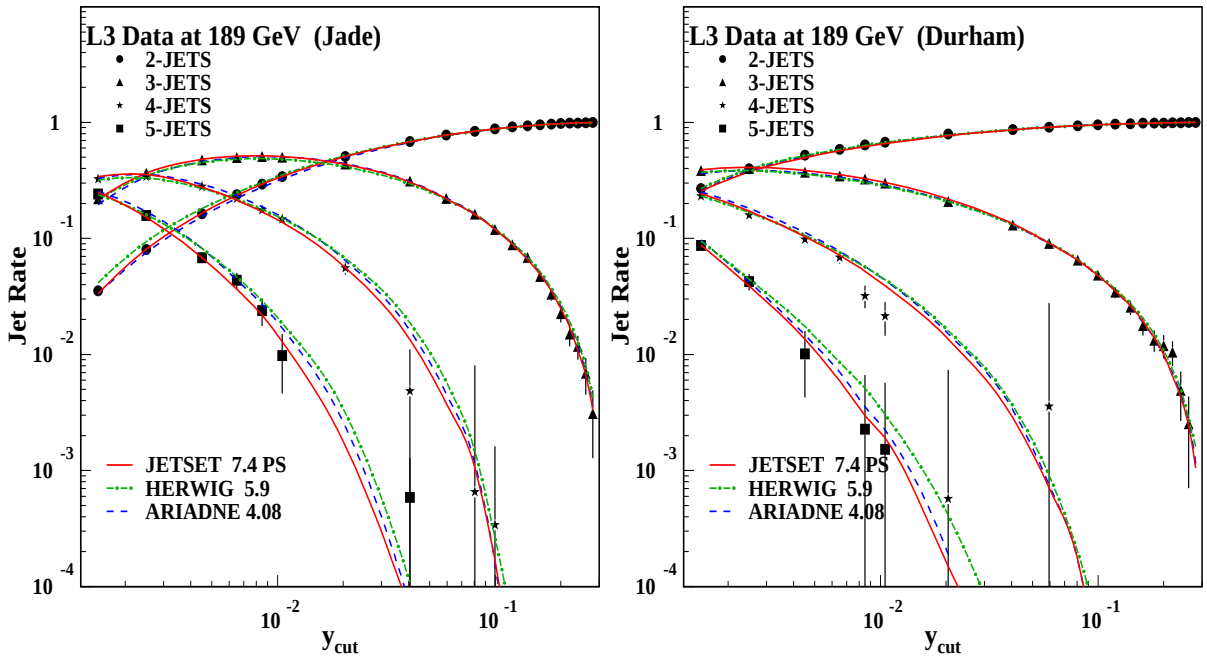

Figure 8.1: Jet rates with JADE and DURHAM algorithms. The errors are statistical only.

The detector corrected jet rates at $\sqrt{s}$ = 189 GeV are compared to Monte Carlo predictions in figure 8.1. The energy evolution of 3-jet rate at y_{cut} = 0.08, using JADE algorithm, is shown in the figure 8.2 along with QCD fits with (dotted line) and without scale variation (solid line). The jet rates have been fitted to $\mathcal{O}$ (α_s^2) calculations [3] with χ^2/d.o.f. = 13.57/17 by fixing the renormalisation scale at $\mu = \sqrt{s}$. The fit gives $\alpha_s(M_Z)$ = 0.1201 ± 0.0007, where the quoted error is statistical only.

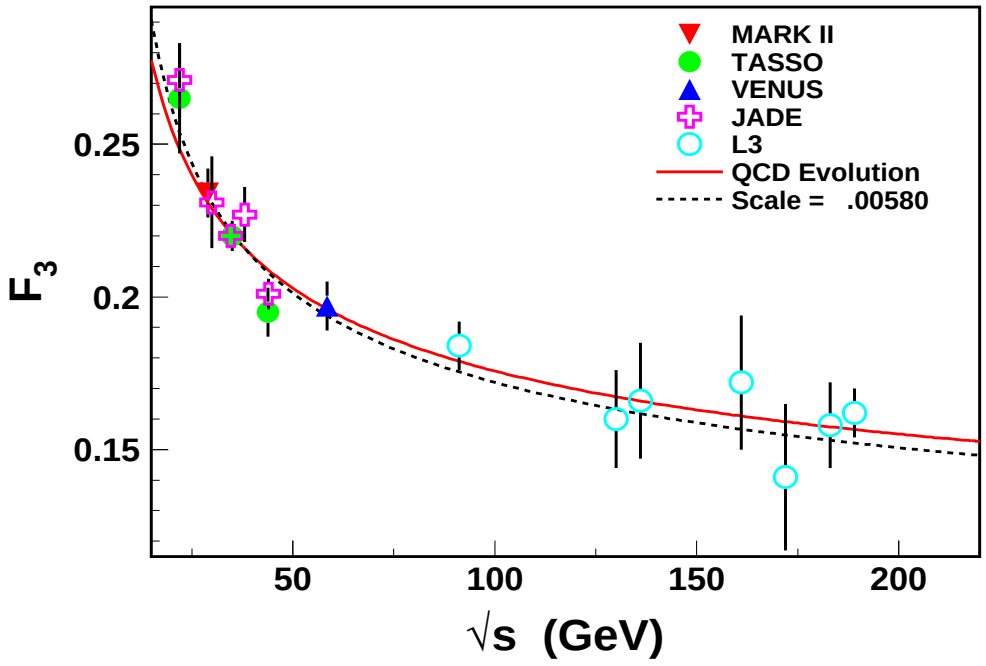

Figure 8.2: Energy evolution of three jet fraction at y_{cut} = 0.08 (JADE algorithm).

8.2 Event Shape Variables

Event shape variables bear the signature of relative abundance of multi-jet topology in a sample of hadronic events. Moments, errors and correlations among the moments of the event shapes are defined in the following manner:

$$\begin{aligned}
\textit{Moments} \quad &: \quad \mu_n = < x^n > = \frac{[\sum_i n_i x_i^n]}{[\sum_i n_i]}; \\
\textit{Error on Moments} \quad &: \quad \Delta^2_{\mu_n} = \sum_i [(\partial \mu_n / \partial n_i)^2 * (\Delta n_i)^2] \\
&\qquad (\partial \mu_n / \partial n_i) = [x_i^n - \mu_n]/N, \text{ where } N = \sum_i n_i \\
\textit{Covariance Matrix} \quad &: \quad M(i,j) = (\mu_{i+j} - \mu_i \mu_j)/N.
\end{aligned}$$

Assuming Poisson statistics, we have $\Delta n_i = \sqrt{n_i}$. Thus one can relate the error on the moments to the covariance matrix: $\Delta^2_{\mu_n} = \frac{1}{N}\left[\frac{\Sigma_i n_i x_i^{2n}}{\Sigma_i n_i}\right] - 2\frac{\mu}{N}\left[\frac{\Sigma_i n_i x_i^n}{\Sigma_i n_i}\right] + \frac{\mu_n^2}{N}$ $\boxed{= (\mu_{2n} - \mu_n^2)/N}$

= M(n, n). Although, this simplification using Poisson statistics helps to get a feel for the numbers, for event sample with finite impurity such simplifications are not exact. As for example, in case of background subtraction, the total event sample is the observed data minus the accepted background contamination. Taking this into account, errors are added in quadrature *bin-by-bin* and propagated numerically at each step.

8.2.1 Energy Evolution

The energy dependence of the mean event shape variables arises mainly from 2 sources:

- ✶ logarithmic energy scale dependence of α_s;
- ✸ power law ($1/Q^n$) dependence from non-perturbative effects.

The mean values of $(1-T)$ and wide jet broadening B_W are shown in Figure 8.3, along with predictions from JETSET PS, HERWIG, ARIADNE, COJETS and JETSET ME Monte Carlo models with constant parameter values over the entire energy range, obtained from tuning at $\sqrt{s} = M_Z$. QCD models can explain the energy evolution of the mean values of event shape variables.

The moments for *five* event shapes variables, thrust (T), scaled heavy jet mass (ρ_H), total (B_T) and wide (B_W) jet broadening variables and the C-parameter, for which improved analytical QCD calculations are available [4], have been measured. The first and second moments from $\sqrt{s} = 30$ to 189 GeV are summarised in the tables 8.1 and 8.2.

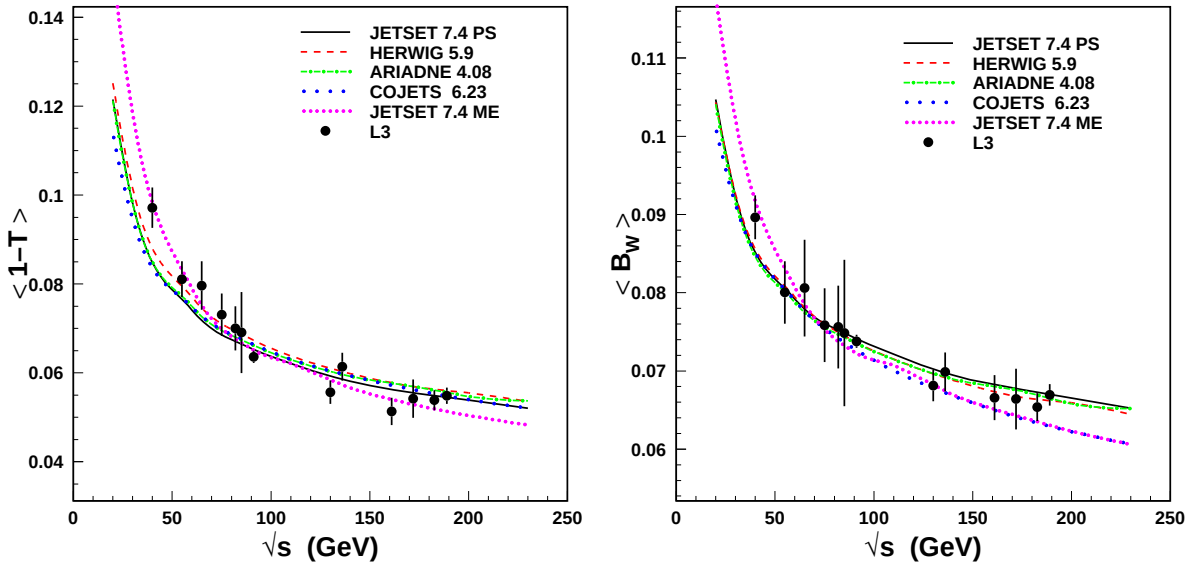

Figure 8.3: Distribution of mean 1−thrust, $< 1-T >$ and wide jet broadening, $< B_W >$ as a function of the centre-of-mass energy, compared to several QCD models.

$\sqrt{s}$ (GeV)	First moments of				
	$1-T$	ρ_{H}	$\mathrm{B_T}$	$\mathrm{B_W}$	C
30−50	.0971 ± .0030 ± .0034	.0747 ± .0023 ± .0023	.1399 ± .0027 ± .0016	.0896 ± .0021 ± .0018	.3667 ± .0084 ± .0073
50−60	.0811 ± .0027 ± .0029	.0632 ± .0021 ± .0023	.1223 ± .0025 ± .0054	.0800 ± .0020 ± .0034	.3091 ± .0080 ± .0131
60−70	.0796 ± .0021 ± .0051	.0603 ± .0015 ± .0047	.1213 ± .0019 ± .0079	.0806 ± .0014 ± .0060	.3049 ± .0059 ± .0232
70−80	.0731 ± .0015 ± .0045	.0560 ± .0011 ± .0027	.1157 ± .0015 ± .0048	.0758 ± .0011 ± .0046	.2851 ± .0044 ± .0177
80−84	.0700 ± .0018 ± .0046	.0546 ± .0015 ± .0035	.1116 ± .0017 ± .0057	.0756 ± .0014 ± .0051	.2759 ± .0055 ± .0191
84−86	.0691 ± .0022 ± .0088	.0544 ± .0017 ± .0085	.1102 ± .0021 ± .0086	.0749 ± .0017 ± .0092	.2722 ± .0068 ± .0289
91.2	.0636 ± .0003 ± .0013	.0539 ± .0002 ± .0013	.1102 ± .0002 ± .0011	.0738 ± .0001 ± .0008	.2599 ± .0004 ± .0054
130	.0556 ± .0022 ± .0014	.0452 ± .0018 ± .0007	.0976 ± .0023 ± .0008	.0681 ± .0019 ± .0007	.2277 ± .0072 ± .0052
136	.0614 ± .0029 ± .0011	.0467 ± .0022 ± .0004	.0999 ± .0029 ± .0011	.0699 ± .0024 ± .0006	.2357 ± .0089 ± .0038
161	.0513 ± .0030 ± .0008	.0421 ± .0025 ± .0007	.0923 ± .0032 ± .0018	.0666 ± .0027 ± .0010	.2052 ± .0098 ± .0028
172	.0542 ± .0037 ± .0022	.0440 ± .0028 ± .0018	.0950 ± .0046 ± .0031	.0664 ± .0031 ± .0023	.2281 ± .0159 ± .0133
183	.0539 ± .0020 ± .0011	.0424 ± .0014 ± .0004	.0918 ± .0020 ± .0015	.0654 ± .0015 ± .0010	.2157 ± .0063 ± .0073
189	.0548 ± .0013 ± .0013	.0442 ± .0009 ± .0009	.0918 ± .0013 ± .0018	.0669 ± .0009 ± .0010	.2160 ± .0040 ± .0041

Table 8.1: First moments of the five event shape variables at different energy points. The two errors are respectively the statistical and the systematic components.

$\sqrt{s}$ (GeV)	Second moments of				
	$1-T$	ρ_{H}	$\mathrm{B_T}$	$\mathrm{B_W}$	C
30−50	.0143 ± .0009 ± .0015	.0080 ± .0006 ± .0005	.0236 ± .0009 ± .0005	.0104 ± .0005 ± .0005	.1726 ± .0078 ± .0115
50−60	.0109 ± .0008 ± .0006	.0063 ± .0005 ± .0008	.0187 ± .0008 ± .0012	.0086 ± .0005 ± .0006	.1308 ± .0066 ± .0063
60−70	.0109 ± .0006 ± .0010	.0060 ± .0004 ± .0011	.0187 ± .0006 ± .0022	.0088 ± .0003 ± .0013	.1308 ± .0050 ± .0164
70−80	.0093 ± .0004 ± .0010	.0053 ± .0002 ± .0007	.0172 ± .0005 ± .0014	.0081 ± .0003 ± .0008	.1176 ± .0037 ± .0117
80−84	.0086 ± .0005 ± .0010	.0052 ± .0003 ± .0007	.0160 ± .0006 ± .0015	.0081 ± .0003 ± .0008	.1110 ± .0047 ± .0125
84−86	.0086 ± .0006 ± .0020	.0054 ± .0004 ± .0014	.0158 ± .0007 ± .0022	.0082 ± .0004 ± .0018	.1115 ± .0058 ± .0195
91.2	.0077 ± .0001 ± .0003	.0053 ± .0001 ± .0002	.0158 ± .0001 ± .0003	.0076 ± .0001 ± .0002	.1034 ± .0003 ± .0031
130	.0064 ± .0005 ± .0002	.0041 ± .0003 ± .0001	.0131 ± .0006 ± .0002	.0069 ± .0004 ± .0001	.0848 ± .0050 ± .0025
136	.0080 ± .0008 ± .0007	.0045 ± .0004 ± .0001	.0141 ± .0008 ± .0004	.0076 ± .0005 ± .0002	.0938 ± .0064 ± .0017
161	.0059 ± .0007 ± .0002	.0040 ± .0004 ± .0001	.0121 ± .0008 ± .0004	.0070 ± .0005 ± .0002	.0757 ± .0064 ± .0019
172	.0064 ± .0009 ± .0005	.0040 ± .0005 ± .0003	.0136 ± .0014 ± .0013	.0068 ± .0006 ± .0005	.0979 ± .0133 ± .0129
183	.0064 ± .0005 ± .0001	.0042 ± .0003 ± .0002	.0121 ± .0006 ± .0003	.0067 ± .0003 ± .0002	.0804 ± .0051 ± .0032
189	.0064 ± .0004 ± .0004	.0043 ± .0002 ± .0002	.0121 ± .0004 ± .0005	.0071 ± .0002 ± .0002	.0794 ± .0032 ± .0038

Table 8.2: Second moments of the five event shape variables at different energy points. The two errors are respectively the statistical and the systematic components.

8.3 Resummed LL & NLL + $\mathcal{O}\ (\alpha_s^2)$

Complete analytical QCD calculations are available for some event shape variables, up to second order and leading logarithmic terms have been resummed up to all orders [4]:

- Fixed order calculation exists up to $\mathcal{O}({\alpha_s}^2)$ for cumulative integrated cross-section $R(y)$ of event shape variables (y):

$$\begin{aligned} R(y,\alpha_s) &\equiv \int_0^y \frac{1}{\sigma}\frac{d\sigma}{dy} \\ &= \overline{\alpha}_s A(y) + {\overline{\alpha}_s}^2 \left[B(y) + 2\pi\beta_0 \ln(Q^2/s) A(y)\right] \end{aligned}$$

  with

$$\begin{aligned} \overline{\alpha}_s &= \frac{\alpha_s(Q)}{2\pi} \\ \beta_0 &= \frac{33 - 2n_f}{12\pi} \end{aligned}$$

  Here, $A(y)$, $B(y)$ are known numbers, computed by integrating ERT [5] matrix elements [$\mathcal{O}({\alpha_s}^2)$] using the program EVENT [6], EVENT2 [7]. While this second order calculation describes data well in the multi-jet region, it fails in the two jet region (small y).

- For certain variables leading logarithmic terms ($\sum {\overline{\alpha}_s}^n \mathrm{L}^{n+1}$) [8] and next-to-leading logarithmic terms ($\sum {\overline{\alpha}_s}^n \mathrm{L}^n$) [9] are resummed to all orders in $L \equiv \ln(1/y)$, with $\overline{\alpha}_s = \alpha_s/2\pi$. Using this description the two region can be described well.

	LL	NLL	Sub-leading			
$\mathcal{O}(\alpha_s)$	$\overline{\alpha}_s L^2$	$\overline{\alpha}_s L$	$\overline{\alpha}_s$	$\overline{\alpha}_s \mathcal{O}\left(\frac{1}{L}\right)$		
$\mathcal{O}({\alpha_s}^2)$	${\overline{\alpha}_s}^2 L^3$	${\overline{\alpha}_s}^2 L^2$	${\overline{\alpha}_s}^2 L$	${\overline{\alpha}_s}^2$	${\overline{\alpha}_s}^2 \mathcal{O}\left(\frac{1}{L}\right)$	
$\mathcal{O}({\alpha_s}^3)$	${\overline{\alpha}_s}^3 L^4$	${\overline{\alpha}_s}^3 L^3$	${\overline{\alpha}_s}^3 L^2$	${\overline{\alpha}_s}^3 L$	${\overline{\alpha}_s}^3$	${\overline{\alpha}_s}^3 \mathcal{O}\left(\frac{1}{L}\right)$
$\vdots$	$\vdots$	$\vdots$	$\vdots$	$\vdots$	$\vdots$	$\vdots$

Table 8.3: Expansion parameters of LLA and NLLA in orders of α_s.

One can combine the fixed order calculations with resummed calculations, after taking care of double counting of terms present in $\mathcal{O}\ ({\alpha_s}^2)$ fixed order and resummed calculations. This provides a better description of the event shape variables over a larger dynamical range. A cross-table showing the order of expansion used in terms of α_s for the LLA, NLLA, and sub-leading resummation are given in table 8.3. Four schemes have been used to perform the matching:

- **Log R Matching:** Take log of fixed order; expand in power series and match in $\ln R(y)$

- **Modified Log R:** Replace L in the resummed terms by $L' = \ln(y^{-1} - y_{\max}^{-1} + 1)$; carry out Log R matching
- **R Matching:** Remove $\mathcal{O}\left({\alpha_s}^2\right)$ terms from resummed $R(y)$; take fixed order calculation only
- **Modified R:** One sub-leading term included in the argument of exponent and subtracted after exponentiation

All matching algorithms are exact up to $\mathcal{O}\left({\alpha_s}^2\right)$.
The following kinematic constraints have to be imposed on the combined calculation:

$$\begin{aligned} R|_{y=y_{\max}} &= 1 \\ \left.\frac{dR}{dy}\right|_{y=y_{\max}} &= 0 \end{aligned}$$

These are needed to be added because they are obeyed only in the fixed order calculations and are not valid in general for the resummed expansion.

Some of the characteristic features are:

- ❒ resummed LL and NLL terms dominate at small y
- ❒ sub-leading terms are important at large y
- ❒ sub-leading terms are determined using Monte Carlo

Some of the advantage of this approach are:

- ❑ it can explain small y (high statistics) region
- ❑ it gives good fits at a reasonable scale ($Q \approx \sqrt{s}$)
- ❑ since more theoretical terms known, uncertainty due to uncalculated terms should be reduced

8.4 α_s from Event Shape Distributions

In order to determine α_s, we fit the measured distributions of the event shape variables to theoretical calculations based on $\mathcal{O}({\alpha_s}^2)$ perturbative QCD with resummed leading and next-to-leading order terms. These calculations are performed at parton level and do not include heavy quark mass effects. To compare the analytical calculations with the experimental distributions, the effect of hadronisation and decays has been incorporated using Monte Carlo programs.

Perturbative QCD cannot be used to calculate the contribution of the fragmentation process, which is an important ingredient to describe the multi-particle hadronic

final state observed in the detector. The Monte Carlo programs, which incorporate various phenomenological models, provide a bridge between partons and final state hadrons. These models provide a way to unravel the underlying parton structure, which can then be compared with the perturbative QCD calculations directly, from experimental data.

The parton level calculations, $f^{\rm pert}(y')$, is convoluted with the probability of finding a value y after fragmentation and decays for a parton level value y', $p^{\rm non-pert}(y', y)$:

$$f(y) \;=\; \int f^{\rm pert}(y') \cdot p^{\rm non-pert}(y', y)\, dy'$$

$p^{\rm non-pert}(y', y)$ is evaluated using Parton Shower Monte Carlo programs: JETSET (as default), HERWIG/ARIADNE (for cross-check).

The fit range is decided from the following considerations:

- ❒ theoretical calculations are reliable;
- ❒ detector and hadronisation corrections are small;
- ❒ data are well described by theory.

Good fits are obtained for each of these variable at all $\sqrt{\rm s}$. As an example, fits to five event shapes T, ρ, $\rm B_T$, $\rm B_W$ and C is shown in the figure 8.4.

Four or five $\alpha_{\rm s}$ values at each energy point are obtained from event shapes variables. The following errors on each measurement are considered:

- **Statistical** error is propagated from measurement errors
- **Experimental Systematic** error is determined from variation of
  (1) Detector effect
  (2) Background modelling
- Uncertainty due to **Hadronization** is obtained from variation of
  (1) Fragmentation models
  (2) Fragmentation parameters
- Uncertainty due to **Uncalculated higher orders** is estimated from variation of
  (1) Matching schemes
  (2) Scale from $0.5\sqrt{\rm s}$ to $2\sqrt{\rm s}$

Measured $\alpha_{\rm s}$ values at the six centre of mass energies of 130, 136, 161, 172, 183 and 189 GeV are summarised in Table 8.4.

The five dfferent event shape distributions are obtained from the same set of events and thus these distributions are correlated. But theoretical descriptions for different shape variables have different approximations. In order to have am independent estimation of the theoretical error, we compare $\alpha_{\rm s}$ measurements from many event shape variables which

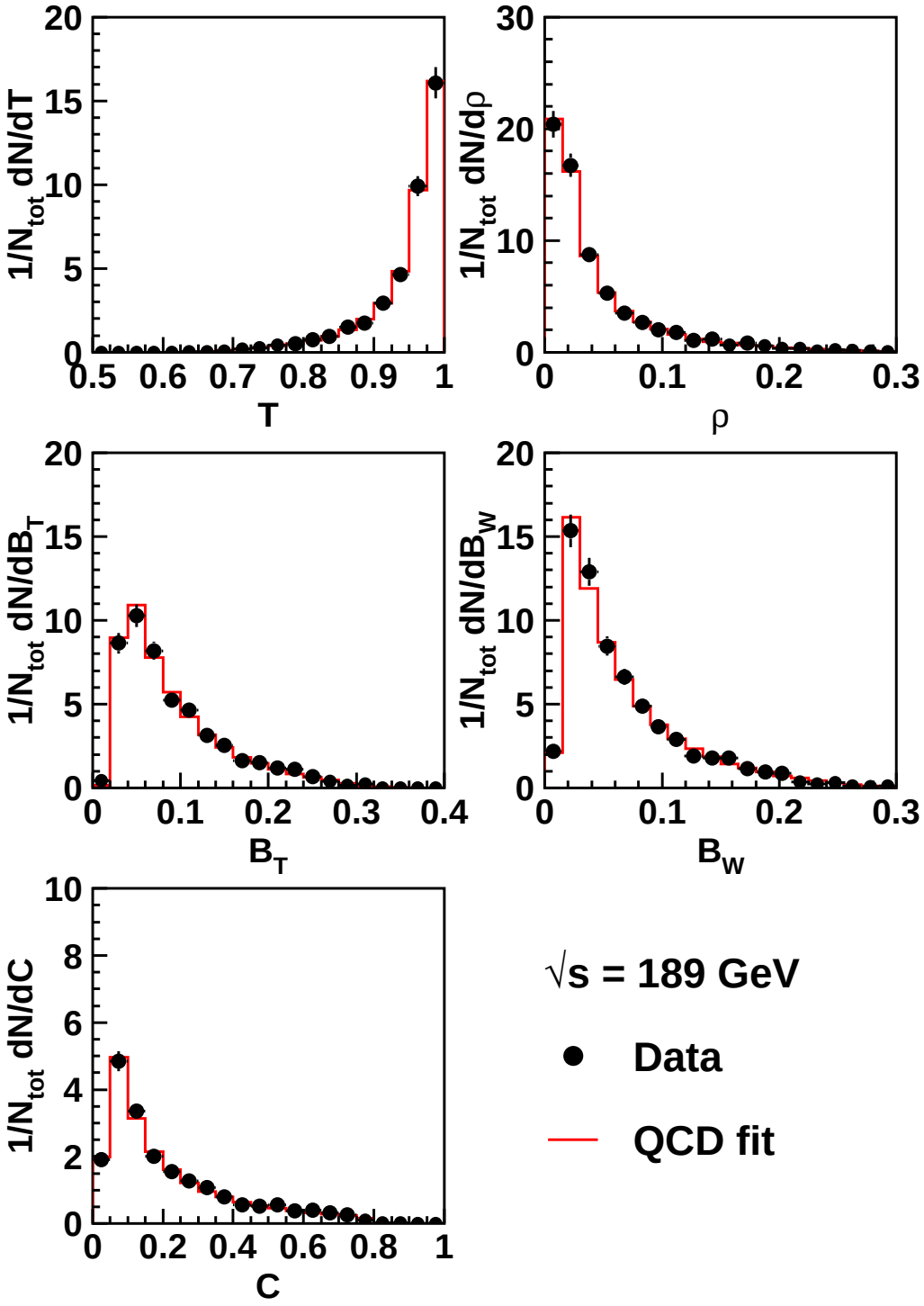

Figure 8.4: Measured distributions of thrust, T, scaled heavy jet mass, ρ, total, B_T, and wide, B_W, jet broadening, and C parameter in comparison with QCD predictions at 189 GeV. The experimental errors include statistical and systematic uncertainties. The theoretical distribution consists of $\mathcal{O}(\alpha_s{}^2)$ perturbative QCD with resummed leading and next-to-leading order terms and corrected for effects of hadronisation.

are affected differently by higher order corrections and hadronization effects. To obtain a combined value for the strong coupling constant we take the unweighted average of the five α_s values. We estimate the overall theoretical error from the simple average of the five theoretical errors or from half of the maximum spread in the five α_s values. Both these estimates yield similar results. The combined results are summarised in table 8.5. The earlier measurements at $\sqrt{s} = M_Z$ and at reduced centre-of-mass energies determined α_s from four event shape variables, T, ρ, B_T and B_W. So in table 8.5 we also provide the mean from these four measurements.

8.5 Energy Evolution of α_s

The *running* of the strong coupling constant is given by the Renormalization Group (RG) equations. The procedure of renormalization introduces a energy scale μ, which depends upon the renormalization scheme undertaken. For example, in the modified minimal subtraction ($\overline{MS}$) scheme, this represents the energy scale at which the ultraviolet divergences along with a constant term are subtracted. However, the concept of RG asserts that the observables of the theory remain independent of the choice of this scale μ. The RG equations of QCD are:

$$\mu^2 \frac{\partial \alpha_s}{\partial \mu^2} = -{\alpha_s}^2 \sum_{k=0} \beta_k {\alpha_s}^k$$

where the first three β-function co-efficients [10], in the $\overline{MS}$ scheme, in terms of n_f (the number of active quark flavours) are:

$$\begin{aligned} \beta_\circ &= \frac{33 - 2\,n_f}{12\pi} \\ \beta_1 &= \frac{153 - 19\,n_f}{24\pi^2} \\ \beta_2 &= \frac{77139 - 15099\,n_f + 325\,{n_f}^2}{3456\pi^3} \end{aligned}$$

Note that the first two beta functions are scheme independent. At LEP energies, well below top pair production, n_f is taken to be equal to *five*.

The solution at energy μ is related to the solution at energy $\mu_\circ$ (up to first order) by:

$$\alpha_s(\mu) = \frac{\alpha_s(\mu_\circ)}{1 + \beta_0 \alpha_s(\mu_\circ) \ln(\mu^2/\mu_\circ^2)},$$

For convenience, $\mu_\circ = M_Z$ is chosen to be the reference scale, and we write $\alpha_s \equiv \alpha_s(M_Z)$. A dimensional parameter Λ can also be used as the free parameter of QCD, interchangeably with α_s. This parameter Λ is defined as :

$$\Lambda = \mu_\circ \exp\left(\frac{1}{-2\beta_\circ \alpha_s(\mu_\circ)}\right)$$

Up to next-to-leading order, the energy (μ) dependence of the strong coupling constant is given by the following formula used extensively at LEP and related directly to the measurements at different energy scales:

$$\alpha_s(\mu) \;=\; \frac{1}{\beta_\circ \ln(\mu^2/\Lambda^2)}\left[1 - \frac{\beta_1 \ln\ln(\mu^2/\Lambda^2)}{\beta_\circ^2 \ln(\mu^2/\Lambda^2)}\right].$$

8.5.1 One Parameter Fit

The energy dependence of the measured α_s values is compared with the prediction from QCD in the figure 8.5. It should be noted that the theoretical errors are strongly correlated between these measurements. The higher order uncertainties should be the same and the uncertainties due to hadronisation corrections are comparable at these energies. The error appropriate to a measurement of the energy dependence of α_s can then be considered to be purely experimental.

The experimental systematic errors on α_s are dominated by the background uncertainties. Backgrounds are similar for all the individual low energy or high energy data points but differ between the low energy, Z peak and high energy data sets. The experimental systematic errors are then different and uncorrelated between the three data sets, but are taken as fully correlated between individual low energy or high energy measurements. The thirteen measurements in Figure 8.5 are shown with experimental errors only, together with a fit to the QCD evolution equation [11] with $\alpha_s(M_Z)$ as a free parameter. The fit gives a χ^2 of 13.5 for 12 degrees of freedom corresponding to a confidence level of 0.34 with a fitted value of α_s:

$$\alpha_s(M_Z) \;=\; 0.1215 \;\pm\; 0.0012 \;\pm\; 0.0061 \tag{8.1}$$

where the first error is experimental and the second error is theoretical. On the other hand, a model with constant α_s gives a χ^2 of 65.1 for 12 degrees of freedom (confidence level 2.7×10^{-9}).

8.5.2 Simultaneous Fit for $\mathbf{n_f}$

One can study the number of active flavours from the slope in the energy evolution of α_s. A fit has been performed with N_f as a free parameter along with α_s and obtain the number of active flavours:

$$N_f \;=\; 5.0 \;\pm\; 1.3 \;\pm\; 2.0$$

where the first error is experimental and the second is due to theoretical uncertainties. The errors have been estimated by using the covariance matrix determined from experimental and overall errors on α_s in the fit. This result agrees with the expectation $N_f = 5$, in the absence of a gluino contribution.

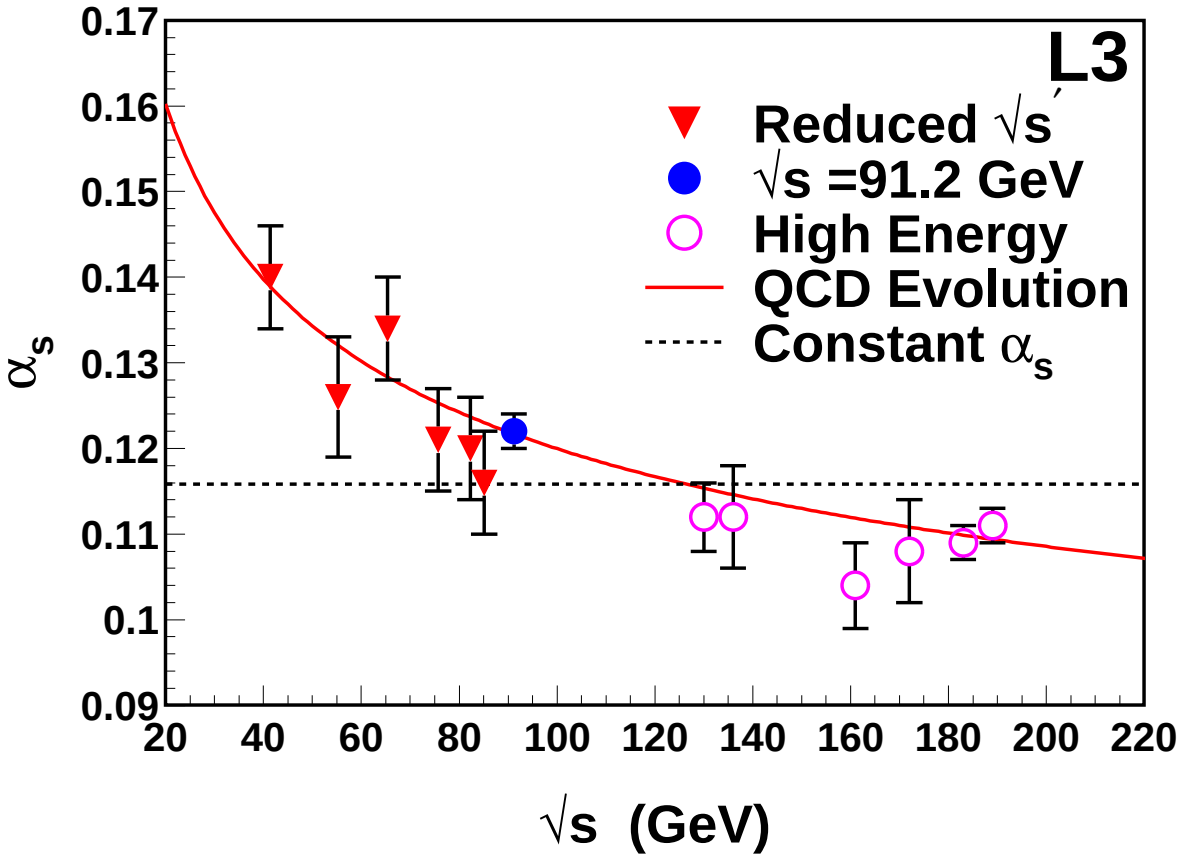

Figure 8.5: α_s measurements from event shape distributions as a function of the centre-of-mass energy. The errors shown are purely experimental. The solid and dashed lines are fits with the energy dependence of α_s as given by QCD and with constant α_s, respectively.

8.6 Power Law Behaviour

The non-perturbative contribution to the event shape variables can be parametrised using the power law ansatz [12], which relies on the assumption that soft gluon emission is controlled by *effective* $\alpha_{\rm eff}$, *different from* α_s *only in infrared region.* Another way of looking at this is an introduction of effective "fake" gluon mass in the dispersion relation, which freezes running of α_s in infrared region.

The energy dependence of moments of the event shape variables can be described as a sum of the perturbative contribution and a power law dependence due to non-perturbative contribution [12]. For example, the first moment of an event shape variable f can be written as

$$\langle f \rangle \;=\; \langle f_{\rm pert} \rangle \;+\; \langle f_{\rm pow} \rangle$$

where the perturbative contribution $\langle f_{\rm pert}\rangle$ can be expressed at $\mathcal{O}({\alpha_{\rm s}}^2)$ as:

$$\langle f_{\rm pert}\rangle \;=\; A\frac{\alpha_{\rm s}(Q)}{2\pi} \;+\; (B + A\cdot(\beta_0 \ln\mu - 2))\left(\frac{\alpha_{\rm s}(Q)}{2\pi}\right)^2 ,$$

with A and B being known numbers [6], [7], Q being the renormalisation scale and $\beta_0 = (11\cdot {\rm N_C} - 2{\rm N_f})/3$.

The power correction term is given by

$$\langle f_{\rm pow}\rangle \;=\; c_f \cdot \mathcal{P}$$

where $c_f = 2,\ 2,\ 1,\ \frac{1}{2}$ and 3π for the variables $1-T$, ρ, ${\rm B_T}$, ${\rm B_W}$ and C.

For linear variables (f = 1-T,C,$\rho_{\rm H}$), the effect is a shift "a shift $\propto 1/{\rm Q}$". $\mathcal{P}$ is supposed to have a universal form:

$$\mathcal{P} \;=\; \frac{4C_F}{\pi^2}\mathcal{M}\frac{\mu_I}{\sqrt{\rm s}}\left[\alpha_0(\mu_I) - \alpha_{\rm s}(\sqrt{\rm s}) - \beta_0\frac{{\alpha_{\rm s}}^2(\sqrt{\rm s})}{2\pi}\left(\ln\frac{\sqrt{\rm s}}{\mu_I} + \frac{K}{\beta_0} + 1\right)\right]$$

where α_0 is a non-perturbative parameter accounting for contributions to the event shape below an infrared matching scale μ_I (= 2 GeV), $K = (67/18 - \pi^2/6)\cdot C_A - 5{\rm N_f}/9$. The Milan factor $\mathcal{M}$ [12] is determined to be 1.49 for ${\rm N_f} = 3$.

For the jet broadening variables, there is an additional "logarithmic-skew" which can be described as a multiplicative factor F to $\mathcal{P}$:

$$F \;=\; \left(\frac{\pi}{2\sqrt{a\cdot C_F\alpha_{\rm CMW}}} + \frac{3}{4} - \frac{\beta_0}{6a\ C_F} + \eta_0 + \mathcal{O}(\sqrt{\alpha_{\rm s}})\right)$$

where η_0 is -0.6137, $a = 1$ (2) for ${\rm B_T}$ (${\rm B_W}$) and $\alpha_{\rm CMW}$, defined as

$$\alpha_{\rm CMW} \;=\; \alpha_{\rm s}\left(1 + K\frac{\alpha_{\rm s}}{2\pi}\right)$$

is determined at a scale $Q = \sqrt{\rm s}\cdot e^{-3/4}$.

The power law predictions have been extended to study the second moments of event shape variables. For variables $1-T$, ρ and C, the following result is expected to hold [13]:

$$\langle f^2\rangle \;=\; \langle f^2_{\rm pert}\rangle \;+\; 2\langle f_{\rm pert}\rangle\cdot c_f\mathcal{P} \;+\; \mathcal{O}\left(\frac{1}{Q^2}\right)$$

This assumes that the non-perturbative correction to the distributions just cause a shift. For jet broadenings the power corrections are not just a shift and the formula would be more complicated.

Fits to the first moments of the five event shape variables from $\sqrt{\rm s} = 30 - 189$ GeV have been performed with *two* free parameters:

❶ $\alpha_{\rm s}({\rm M_Z})$

❷ $\alpha_0(\mu_{\rm I}) = \frac{1}{\mu_{\rm I}}\int_0^{\mu_{\rm I}} dq\alpha_{\rm eff}(q)$.

The fit incorporates statistical as well as systematic errors on the data points. The systematic errors fall into six different categories: due to detector effects, due to backgrounds of the types π^0/η (applicable to reduced centre-of-mass energy samples), initial state radiation (relevant for high energy samples), W-pair (for $\sqrt{s} \geq 161$ GeV), 2-photon and due to Monte Carlo used in detector corrections (JETSET versus HERWIG). The diagonal terms of the covariance error matrix are constructed by summing in quadrature all the systematic terms and the statistical component. The off-diagonal terms are obtained only from the common systematic errors of each categories added in quadrature. α_0 and α_s are the only free parameters in the fit. The renormalisation scale is fixed at $Q = \sqrt{s}$. The results of the fit are summarised in table 8.6. The fits are also shown in the figure 8.6. The theoretical predictions are found to agree rather well with data for all the 5 event shape variables.

The four values of α_0 obtained from the four event shape variables ρ, B_T, B_W and C agree well within errors. The value obtained from $1-T$ is within $2 \cdot \sigma$ from the other four values. These measurements are in reasonable agreement with the predicted universality of the power law behaviour. The five estimates of α_0 and α_s values can be combined to get an overall α_0 and α_s from the power law fit:

$$\begin{aligned} \alpha_0 &= 0.537 \pm 0.069 \pm 0.079\,, \\ \alpha_s(M_Z) &= 0.1110 \pm 0.0045 \pm 0.0067\,. \end{aligned}$$

The first errors are experimental and are obtained from the average of the errors on α_0 and α_s from fits to the five variables. For the five variables, α_0 and α_s are affected differently by the limited theoretical description in the power law ansatz. Half of the maximum spread in the five values are taken as estimates of theoretical uncertainties which are quoted as the second error. A variation of μ_I in the range from 1 to 3 GeV gives an additional uncertainty on $\alpha_s(M_Z)$ of $\pm$ 0.001. This power law correction was first examined by DELPHI collaboration [14] for mean values $< 1-T >$ and $< \rho >$ and our measurement of α_0 is in agreement with their result.

Figure 8.7 shows the second moments compared to predictions as above where α_0 and α_s have been obtained from the corresponding fits to the first moments. As one sees from the figure the contributions of the $\mathcal{O}(\frac{1}{Q^2})$ term is not negligible for $1-T$ and C where the prediction is supposed to hold. The $\mathcal{O}(\frac{1}{Q^2})$ term has been parametrised as A_2/Q^2 and the five values of A_2, as obtained from the fits, are summarised in Table 8.6.

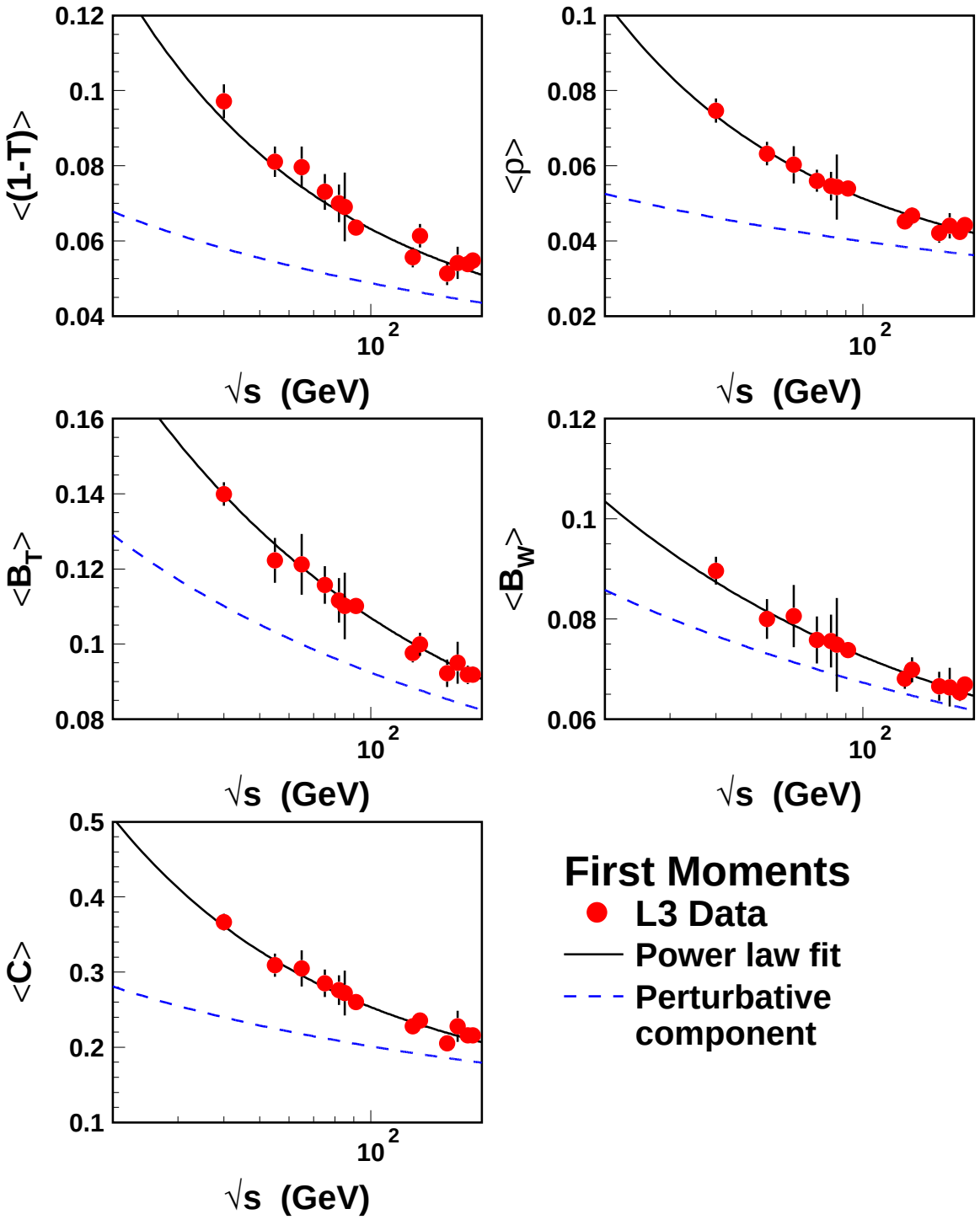

Figure 8.6: First moments of the five event shape variables, $1-T$, ρ, $\mathrm{B_T}$, $\mathrm{B_W}$, C compared to the results of a fit including perturbative and power law contributions.

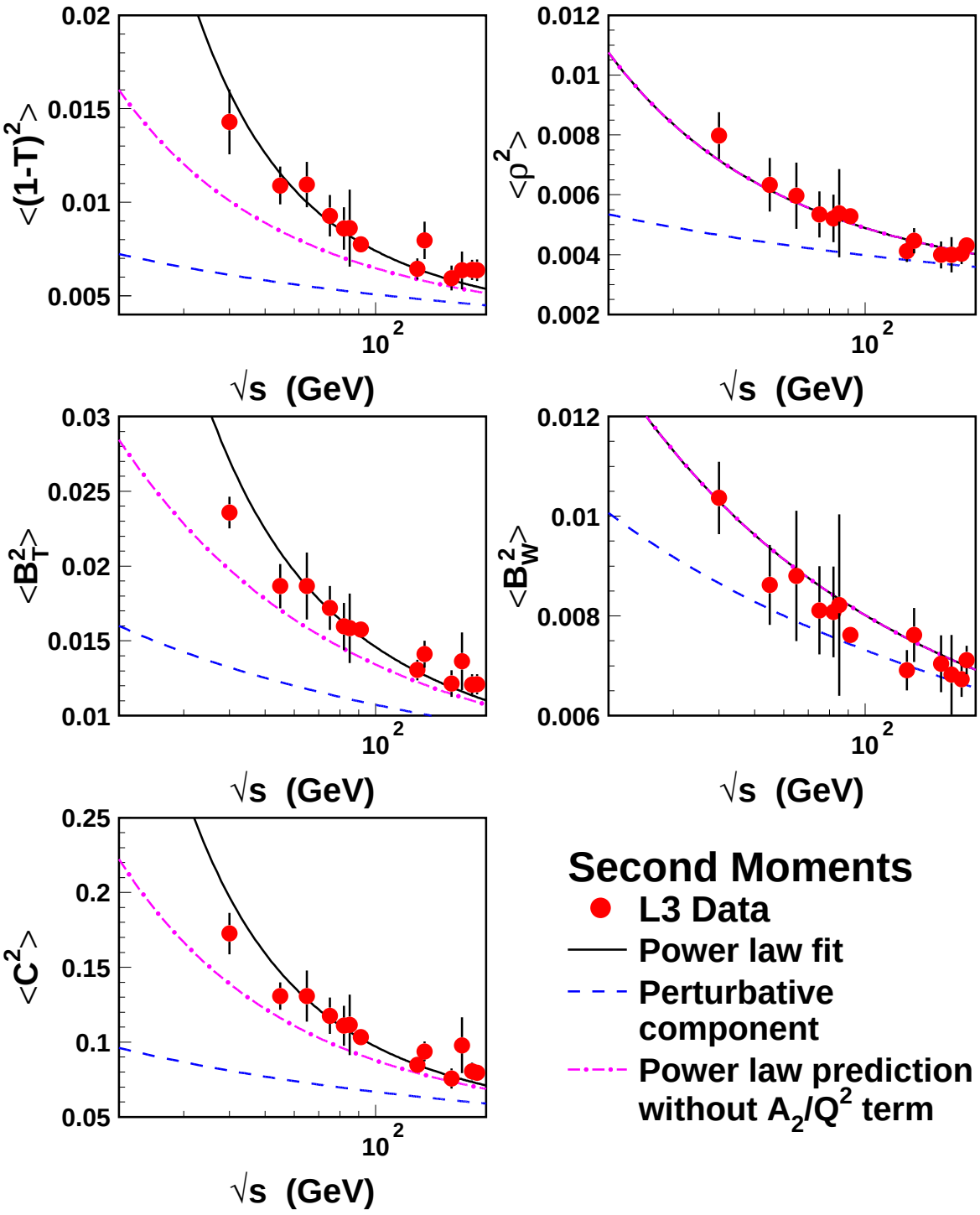

Figure 8.7: Second moments of the five event shape variables, $1-T$, ρ, $\mathrm{B_T}$, $\mathrm{B_W}$, C are compared to the results of a fit including perturbative and power law contributions. The parameters α_0 and α_s are fixed to the values obtained by the fits to the first moments.

	$(1-T)$	ρ	B_T	B_W	C
Fit Range	0.00−0.30	0.00−0.20	0.00−0.25	0.00−0.20	0.05−0.50
α_s(130 GeV)	0.1139	0.1134	0.1153	0.1063	0.1151
Statistical error	±0.0036	±0.0034	±0.0027	±0.0027	±0.0036
Systematic error	±0.0028	±0.0029	±0.0016	±0.0015	±0.0018
Overall experimental error	±0.0046	±0.0045	±0.0031	±0.0031	±0.0040
Overall theoretical error	±0.0056	±0.0038	±0.0062	±0.0088	±0.0066
χ^2/d.o.f.	6.9 / 10	8.4 / 9	9.1 / 11	12.0 / 12	8.5 / 8
α_s(136 GeV)	0.1166	0.1112	0.1141	0.1045	0.1089
Statistical error	±0.0047	±0.0037	±0.0034	±0.0032	±0.0043
Systematic error	±0.0024	±0.0013	±0.0010	±0.0026	±0.0020
Overall experimental error	±0.0053	±0.0039	±0.0035	±0.0041	±0.0047
Overall theoretical error	±0.0060	±0.0037	±0.0064	±0.0078	±0.0076
χ^2/d.o.f.	10.2 / 9	11.4 / 13	7.7 / 11	7.9 / 12	11.8 / 8
α_s(161 GeV)	0.1018	0.1012	0.1101	0.1032	0.1043
Statistical error	±0.0051	±0.0052	±0.0039	±0.0039	±0.0055
Systematic error	±0.0022	±0.0022	±0.0015	±0.0044	±0.0025
Overall experimental error	±0.0056	±0.0056	±0.0042	±0.0059	±0.0060
Overall theoretical error	±0.0050	±0.0034	±0.0066	±0.0068	±0.0057
χ^2/d.o.f.	8.2 / 9	5.7 / 13	7.9 / 11	5.6 / 12	4.9 / 8
α_s(172 GeV)	0.1109	0.1099	0.1071	0.1020	0.1121
Statistical error	±0.0055	±0.0050	±0.0043	±0.0039	±0.0064
Systematic error	±0.0026	±0.0016	±0.0044	±0.0022	±0.0024
Overall experimental error	±0.0061	±0.0052	±0.0062	±0.0045	±0.0068
Overall theoretical error	±0.0064	±0.0033	±0.0060	±0.0065	±0.0057
χ^2/d.o.f.	2.8 / 8	8.4 / 13	7.8 / 12	8.4 / 13	3.2 / 8
α_s(183 GeV)	0.1132	0.1075	0.1112	0.1036	0.1081
Statistical error	±0.0023	±0.0022	±0.0017	±0.0015	±0.0028
Systematic error	±0.0012	±0.0011	±0.0013	±0.0006	±0.0010
Overall experimental error	±0.0026	±0.0025	±0.0021	±0.0016	±0.0029
Overall theoretical error	±0.0054	±0.0038	±0.0060	±0.0071	±0.0054
χ^2/d.o.f.	4.2 / 11	6.4 / 13	15.9 / 12	6.3 / 13	5.2 / 8
α_s(189 GeV)	0.1168	0.1108	0.1114	0.1033	0.1118
Statistical error	±0.0014	±0.0013	±0.0011	±0.0010	±0.0018
Systematic error	±0.0012	±0.0010	±0.0014	±0.0012	±0.0014
Overall experimental error	±0.0018	±0.0016	±0.0018	±0.0016	±0.0023
Overall theoretical error	±0.0057	±0.0033	±0.0067	±0.0078	±0.0055
χ^2/d.o.f.	4.4 / 11	8.2 / 13	28.0 / 12	10.6 / 13	5.7 / 8

Table 8.4: α_s measured at $\sqrt{s} = 130, 136, 161, 172, 183, 189$ GeV from the fits of the event shape variables to theoretical predictions with combined fixed order and resummed calculations, along with the estimated experimental and theoretical errors and fit qualities.

$\sqrt{s}$ (GeV)	α_s (from T, ρ, B_T, B_W)	α_s (from T, ρ, B_T, B_W, C)
30−50	$0.1400 \pm 0.0056 \pm 0.0107$	
50−60	$0.1260 \pm 0.0073 \pm 0.0088$	
60−70	$0.1340 \pm 0.0060 \pm 0.0087$	
70−80	$0.1210 \pm 0.0064 \pm 0.0082$	
80−84	$0.1200 \pm 0.0057 \pm 0.0089$	
84−86	$0.1160 \pm 0.0061 \pm 0.0082$	
91.2	$0.1221 \pm 0.0020 \pm 0.0066$	
130	$0.1122 \pm 0.0038 \pm 0.0060$	$0.1128 \pm 0.0038 \pm 0.0063$
136	$0.1116 \pm 0.0042 \pm 0.0060$	$0.1111 \pm 0.0043 \pm 0.0061$
161	$0.1041 \pm 0.0052 \pm 0.0054$	$0.1041 \pm 0.0054 \pm 0.0054$
172	$0.1075 \pm 0.0054 \pm 0.0056$	$0.1084 \pm 0.0056 \pm 0.0055$
183	$0.1089 \pm 0.0022 \pm 0.0056$	$0.1088 \pm 0.0023 \pm 0.0055$
189	$0.1106 \pm 0.0017 \pm 0.0058$	$0.1105 \pm 0.0018 \pm 0.0058$

Table 8.5: Summary of α_s values as determined from event shape variables at different centre-of-mass energies.

Observable	α_0 (2 GeV)	$\alpha_s(M_Z)$	χ^2/d.o.f.	A_2 (GeV^2)
$1-T$	0.634 ± 0.092	0.1104 ± 0.0065	11.5/11	5.48 ± 0.56
ρ	0.524 ± 0.063	0.1027 ± 0.0050	5.5/11	$0.00\ ^{+0.01}_{-0.00}$
B_T	0.517 ± 0.044	0.1160 ± 0.0029	3.5/11	13.75 ± 0.88
B_W	0.476 ± 0.100	0.1134 ± 0.0042	4.1/11	$0.00\ ^{+0.01}_{-0.00}$
C	0.536 ± 0.044	0.1125 ± 0.0038	6.3/11	11.58 ± 0.88

Table 8.6: Determination of α_0 (2 GeV) and $\alpha_s(M_Z)$ from fits to the first moments of the event shape distributions together with A parameters for the second moments.

References

[1] JADE Collaboration, W. Bartel *et al.*, Z. Physik **C33** (1986) 23;
JADE Collaboration, S. Bethke *et al.*, Phys. Lett. **B213** (1988) 235.

[2] Yu.L. Dokshitzer, Contribution to the Workshop on Jets at LEP and HERA, Durham (1990);
N. Brown and W.J. Stirling, Rutherford Preprint RAL-91-049;
S. Catani *et al.*, Phys. Lett. **B269** (1991) 432;
S. Bethke *et al.*, Nucl. Phys. **B370** (1992) 310.

[3] S. Bethke *et al.*, Nucl. Phys. B370(1992) 310;
OPAL Collaboration, Phys Lett. B235 (1990) 389.

[4] S. Catani *et al.*, Phys. Lett. **B263** (1991) 491;
S. Catani *et al.*, Phys. Lett. **B272** (1991) 368;
S. Catani *et al.*, Phys. Lett. **B295** (1992) 269;
S. Catani *et al.*, Nucl. Phys. **B407** (1993) 3;
S. Catani *et al.*, Phys. Lett. **B427** (1998) 377.

[5] R.K. Ellis, D.A. Ross, and E.A. Terrano, Nuclear Physics **B178** (1981) 421.

[6] Z. Kunszt and P. Nason in "Z Physics at LEP 1", CERN Report 89-08, Vol.I., p. 373.

[7] EVENT2 Program: S. Catani, M. Seymour, Phys. Lett. **B378** (1996) 287.

[8] K. Konishi, A. Ukawa, and G. Veneziano, Nuclear Physics **B157** (1979) 45;
R. Odorico, Nuclear Physics **B172** (1980) 157;
G.C. Fox and S. Wolfram, Nuclear Physics **B168** (1980) 285;
T.D. Gottschalk, Nuclear Physics **B214** (1983) 201.

[9] J. Kalinowski, K. Konishi, and T.R. Taylor, Nuclear Physics **B181** (1981) 221;
J. Kalinowski *et al.*Nuclear Physics **B181** (1981) 253;
J.F. Gunion and J. Kalinowski, Physical Review **D29** (1984) 1545;
J.F. Gunion, J. Kalinowski, and L. Szymanowski, Physical Review **D32** (1985) 2303.

[10] W. Caswell, Physical Review Letters **30** (1974) 244;
D.R.T. Jones, Nuclear Physics **B75** (1974) 531;
O.V. Tarasov, A. A. Vladimirov, A. Y. Zharkov, Physics Letters **B93** (1980) 429.

[11] Particle Data Group, C. Caso *et al.*, Eur. Phys. J. **C3** (1998) 1.

[12] Yu.L. Dokshitzer, B.R. Webber, Phys. Lett. **B352** (1995) 451;
B.R. Webber, HEP-PH-9510283;
Yu.L. Dokshitzer *et al.*, Nucl. Phys. **B511** (1997) 396;
Yu.L. Dokshitzer *et al.*, J.HEP. 05 (1998) 3;
Yu.L. Dokshitzer *et al.*, Eur. Phys. J. direct **C3** (1999) 1;
Yu.L. Dokshitzer, HEP-PH-9911299.

[13] Yu.L. Dokshitzer and B.R. Webber, Phys. Lett. **B404** (1997) 321;
B.R. Webber, Nucl. Phys. Proc. Suppl. **71** (1999) 66;
G. Salam, private communication.

[14] Delphi Collaboration, P. Abreu *et al.*, Phys. Lett. **B456** (1999) 322.

Chapter 9

Aspects of Soft Gluon Radiation

Effect of soft gluon radiation has been studied in charged particle multiplicity distributions and in inclusive momentum spectra of charged particles. Both these studies require a good identification and selection of charged particles and this is done using the tracks in the tracking detector TEC.

9.1 Good Tracks

In the hadronic events, good tracks are selected using the following quality cuts:

# of Hits	$\geq$	30
Span	$\geq$	30
| DCA |	$\leq$	50 mm
$p_\perp$	$\geq$	100 MeV

where # of hits counts the number of used hits in the readout wires of the outer and the inner TEC, span is the difference between the first and last wire hit, DCA is the distance of closest approach of the reconstructed track to the primary vertex, and $p_\perp$ is the transverse momentum of the track.

The cut on DCA is varied to study systematic effects. Instead of using a constant cut of the number of wires hit in the forward region of the TEC, for systematics the following criteria has also been used to take care of the limited angular coverage of the outer TEC:

$\theta \geq 41^\circ$:	Span ≥ 30, # of Hits ≥ 20
$41^\circ > \theta \geq 21^\circ$:	Span ≥ 10, # of Hits $\geq 0.66 \times$ Span
$21^\circ > \theta$:	# of Hits $\geq 0.66 \times$ Span

The distribution of observed number of good tracks at $\sqrt{s} = 189$ GeV is compared at the detector level with Monte Carlo predictions in figure 9.1. A real detector simulation is used for the Monte Carlo generated events to take care of the detector inefficiency and running time fluctuations of the performance of the different sectors of the TEC.

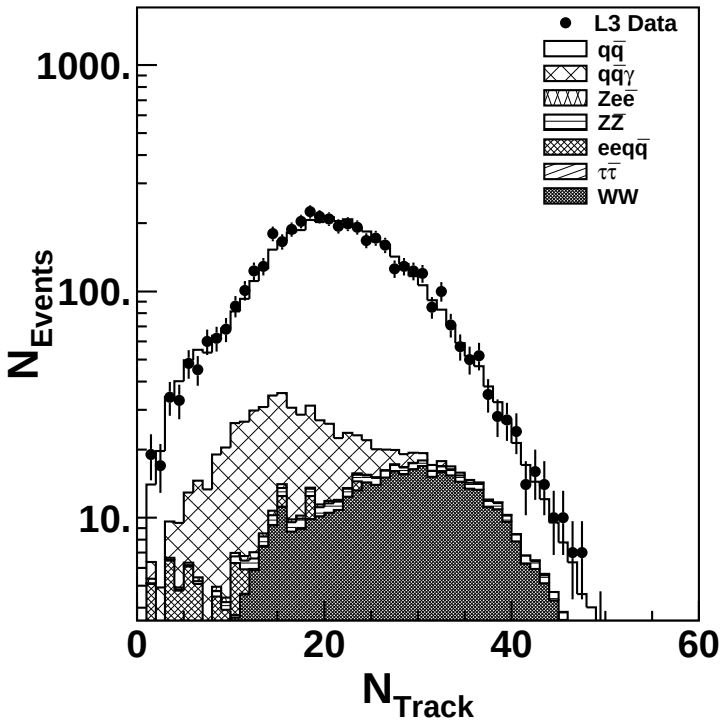

Figure 9.1: Data-Monte Carlo comparison of number of good tracks at $\sqrt{s} = 189$ GeV.

9.2 Charged Particle Multiplicity

The detector level distribution of track multiplicity is first corrected for accepted background contamination on a bin-by-bin basis. The detector correction is taken care of using an unfolding matrix, which calculates the probability for a given number of charged particles in the generator level to migrate into an observed number of tracks in the detector. For the event statistics at $\sqrt{s} > M_Z$, accuracy of this procedure is better than systematic uncertainties due to the detector and background correction.

Figure 9.2 shows detector corrected charged particle multiplicity distributions at $\sqrt{s} =$ 91 and 189 GeV. A characteristic feature of this spectrum is that it "shifts" and "broadens" with increasing energy.

The energy evolution of mean charged multiplicity as measured at L3 is shown in the figure 9.3, and listed in the table 9.1. Most of the Monte Carlo models agree well with the data, with the exception of:

- ▲ COJETS with incoherent parton shower and independent fragmentation gives higher multiplicity at high energies;
- ▼ JETSET ME with a second order implementation (and hence with very few partons) cannot describe evolution.

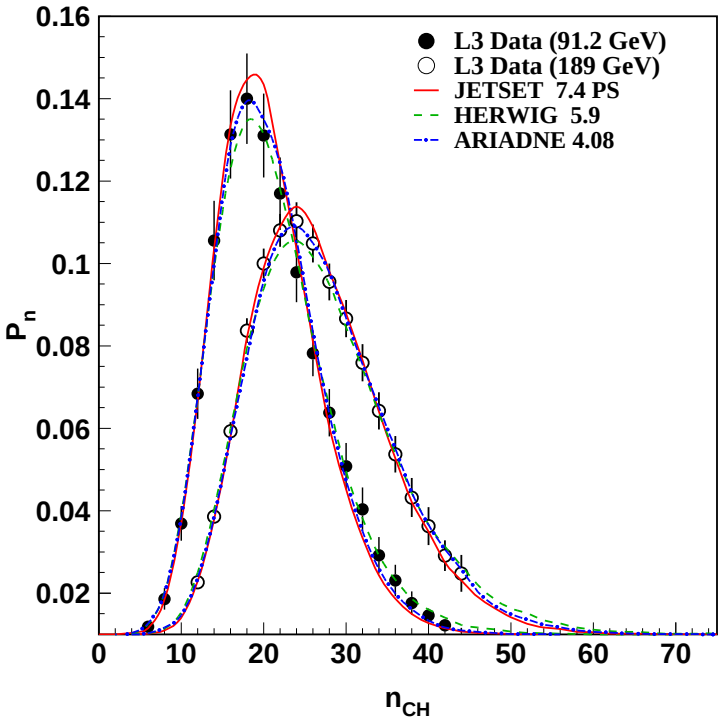

Figure 9.2: Detector corrected charged particle multiplicity distributions at $\sqrt{s} = 91$ and 189 GeV.

$\sqrt{s}$ (GeV)	$\langle N_{ch} \rangle$
91.2	$20.79 \pm 0.03 \pm 0.52$
130.	$24.90 \pm 0.50 \pm 0.80$
136.	$24.20 \pm 0.70 \pm 0.80$
161.	$25.45 \pm 0.38 \pm 0.32$
172	$26.61 \pm 0.47 \pm 0.30$
183.	$27.04 \pm 0.24 \pm 0.43$
189.	$26.84 \pm 0.20 \pm 0.25$

Table 9.1: Results on $\langle N_{ch} \rangle$ measured at different centre-of-mass energies. The errors are statistical and systematic respectively.

9.3 Inclusive Momentum Spectra

Inclusive momentum spectra of charged particles have been studied at different centre-of-mass energies in term of the variable ξ $(= \ln\left(\frac{1}{x}\right))$ where x is the momentum of the particle scaled to the beam energy $(2p/\sqrt{s})$. The spectra for x and ξ at $\sqrt{s} = 189$ GeV are shown in the figure 9.4. The observed distribution is then corrected from the effect of the remaining background by estimating the background using Monte Carlo and then subtracting on a *bin-by-bin* basis. The resulting distribution is then corrected for the

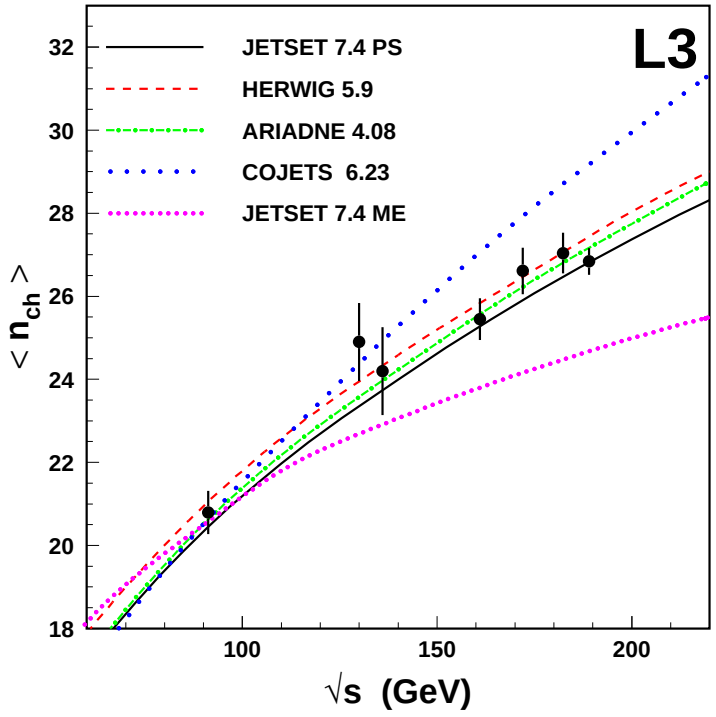

Figure 9.3: Energy evolution of mean charged particle multiplicity.

detector effects (resolution and acceptance) *bin-by-bin* using Monte Carlo events from PYTHIA [1] with parameters tuned using L3 event shape data [2].

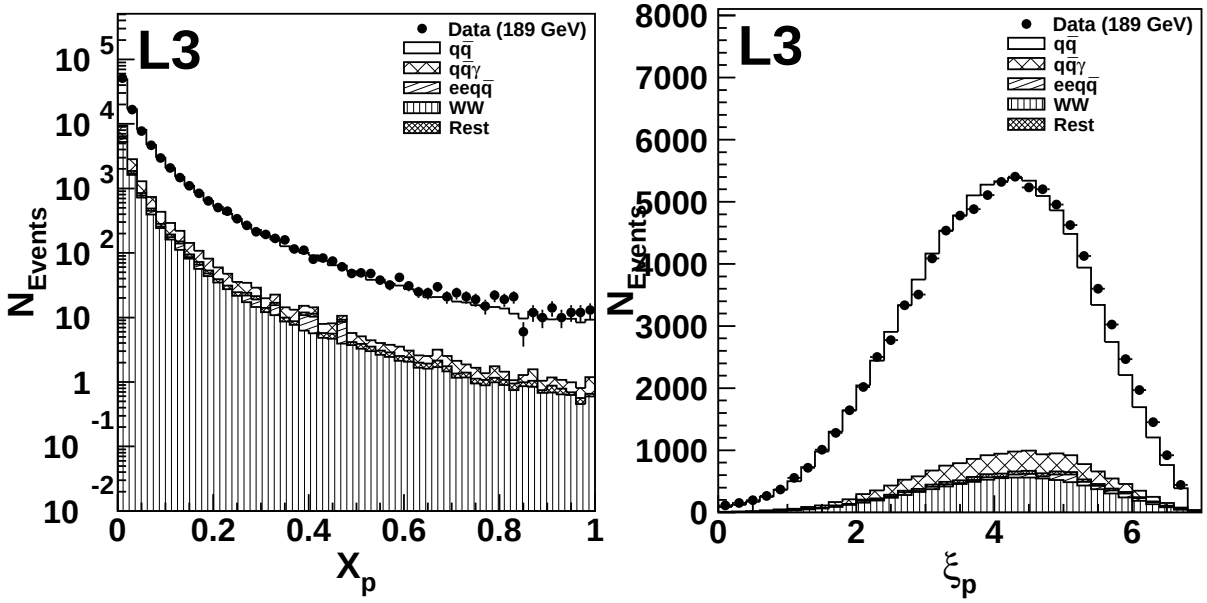

Figure 9.4: Detector level distributions for x_p and ξ_p variables at $\sqrt{s} = 189$ GeV.

The theoretical predictions for ξ distribution have been already discussed in chapter 2 (section 2.3.1). The corrected ξ distribution is fitted to a Gaussian or to a skewed Gaussian (Fong-Webber parametrisation) function at each centre-of-mass energy restricting the fit range to values of ξ where the distribution falls up to 60% of its maximum value. The Gaussian parametrisation works better at small ξ values, but the skewed Gaussian gives a better description of the data in the large ξ (small x) region. For these fits, the statistical errors on the measurements are taken to be uncorrelated whereas the systematic errors are taken to be maximally correlated.

The peak position ($\xi^\star$) of the ξ distribution are fitted to analytical expressions as described in section 2.3.1. The fitted values are given in table 9.2. Figure 9.5 shows the quality of the fit performed at $\sqrt{\mathrm{s}} = 189$ GeV.

The value of $\xi^\star$ obtained from the Fong-Webber parametrisation is taken as the central value and the results from the Gaussian fit as a measure of the systematic error. The $\xi^\star$ value at $\sqrt{\mathrm{s}} = 91.2$ GeV, shown in the table 9.2 is obtained by re-fitting the ξ distribution measured earlier [3].

$\sqrt{\mathrm{s}}$ (GeV)	$\xi^\star$
91.2	$3.71 \pm 0.01 \pm 0.05$
133.	$3.90 \pm 0.04 \pm 0.05$
161.	$3.92 \pm 0.05 \pm 0.04$
172	$4.06 \pm 0.05 \pm 0.05$
183.	$4.08 \pm 0.02 \pm 0.04$
189.	$4.06 \pm 0.01 \pm 0.03$

Table 9.2: Results on $\xi^\star$ measured at different centre-of-mass energies. The errors are statistical and systematic respectively.

To estimate the systematic errors, the fits have been repeated changing

(a) the functional form (Gaussian or skewed Gaussian);

(b) the quality cuts on track selection;

(c) the hadronic selection criteria to vary the backgrounds within one σ;

(d) the model (HERWIG [4]) used for detector corrections (default being PYTHIA).

The half of the maximum spread is attributed to the systematic error at each energy point.

The energy evolution of $\xi^\star$ is given by :

$$\xi^\star \;=\; Y(\frac{1}{2} + a\sqrt{\frac{\alpha_\mathrm{s}(Y)}{32\mathrm{N_c}\pi}} - a^2\frac{\alpha_\mathrm{s}(Y)}{32\mathrm{N_c}\pi} + ...),$$

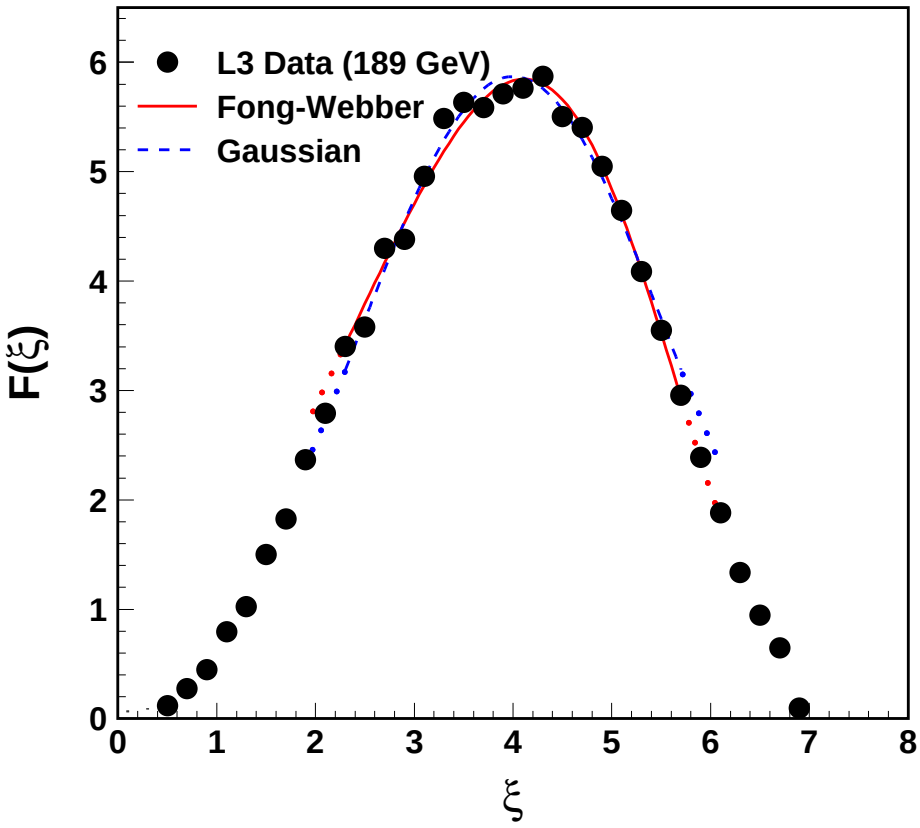

Figure 9.5: Corrected ξ-spectrum at $\sqrt{s} = 189$ GeVtogether with the fits to Gaussian and skewed Gaussian distributions.

where

$$\begin{aligned} Y &= \ln(E_{beam}/\Lambda), \text{ and} \\ a &= \frac{11}{3}N_c + \frac{2}{3}\frac{N_f}{{N_c}^2} \end{aligned}$$

The first term is given by the double logarithm approximation (DLA), and the other correction terms arise in the next-to-leading order [5] (MLLA) QCD predictions.

Figure 9.6 shows the energy evolution of $\xi^\star$ measurements done in the current analysis at and above the Z-peak. It also shows data from TASSO [6] and other LEP experiments [7, 8, 9].

Fits to the L3 and TASSO data have been performed using the theoretical predictions given above. In the fits, the statistical error is taken as fully uncorrelated and the systematic errors from the same experiment are taken to be fully correlated. The correlation of systematic errors among different experiments have been ignored. For the TASSO data, the statistical and systematic components of the errors have been separated using the published number of events at each centre-of-mass energies. There the statistical errors is assumed follow a Poisson distribution and that the detector correction factors are taken to be of order unity.

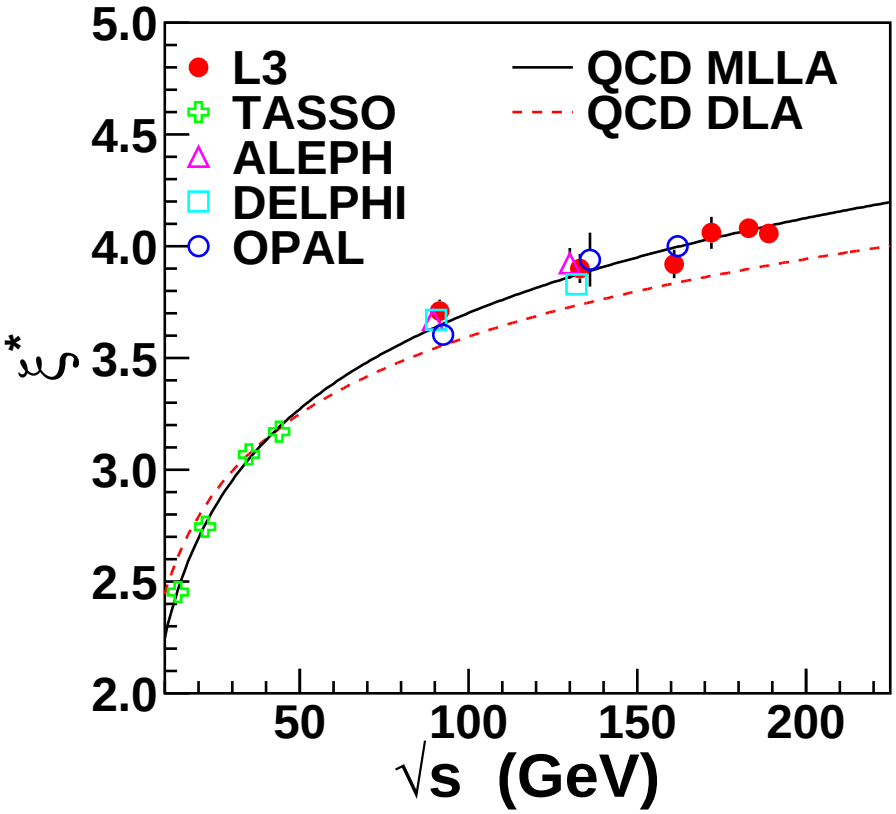

Figure 9.6: Energy evolution of $\xi^{\star}$.

The data are found to be in better agreement with QCD predictions computed to the next-to leading orders. The fit to the DLA parametrisation gives rise to a χ^2 of 37.9 for 10 degree of freedom whereas the MLLA predictions give a fit with χ^2 of 10.9 for 10 degrees of freedom. The results of the fits are shown in figure 9.6 as the smooth curves.

References

[1] T. Sjöstrand, CERN-TH/7112/93 (1993), revised August 1995;
T. Sjöstrand, Comp. Phys. Comm. 82 (1994) 74.

[2] Sunanda Banerjee, Swagato Banerjee, L3 Note # 1978 (1996).

[3] L3 Collaboration, B. Adeva *et al.*, Phys. Lett. **B259** (1991) 199.

[4] G. Marchesini and B.R. Webber, Nucl. Phys. **B310** (1988) 461;
I.G. Knowles, Nucl. Phys. **B310** (1988) 571;
G. Marchesini *et al.*, Comp. Phys. Comm. **67** (1992) 465.

[5] Yu.L. Dokshitzer *et al.*, Basics of Perturbative QCD, Editions Frontieres, Gif-sur-Yvette, 1991.

[6] Tasso Collaboration, W. Braunschweig *et al.*, Z. Physik **C47** (1990) 187.

[7] Aleph Collaboration, R. Barate *et al.*, CERN preprint CERN-PPE/96-186.

[8] Delphi Collaboration, P. Abreu *et al.*, Phys. Lett. **B275** (1992) 231;
Delphi Collaboration, P. Abreu *et al.*, Z. Physik **C73** (1997) 229.

[9] Opal Collaboration, M.Z. Akrawy *et al.*, Phys. Lett. **B247** (1990) 617;
Opal Collaboration, G. Alexander *et al.*, Z. Physik **C72** (1996) 191;
Opal Collaboration, K. Ackerstaff *et al.*, Z. Physik **C75** (1997) 193.

Chapter 10

Search for Colour Singlet Exchange

10.1 Introduction

Three jet events of Mercedes type from hadronic Z decays have been studied to search for colour singlet exchanges in e^-e^+ annihilations.

Energy deposits in the calorimeters are combined to form clusters with varying thresholds for ECAL and HCAL, in order to have a better agreement between Data and Monte Carlo for the number of clusters. Alternatively, tracks in the TEC have been used to restrict the analysis to charged particles observed in the detector. By using a b-tag algorithm, one identifies two of the jets as due to quarks (being probable b-jet candidates) and thus the remaining jet due to gluon.

Using the JADE algorithm (with $y_{cut} = 0.05$), well separated three jet events of Mercedes type are selected for this study. The angles (θ_{ij}) between the jets (i and j) projected onto the *event plane*, defined by the two most energetic jets, are restricted to lie within 30° interval with respect to a perfect Mercedes 120° separation. A fixed degree cone is defined around each jet and the remaining region in the event plane is taken as *gaps*.

Measured particle and angular asymmetries (defined in section 2.4) in these gaps are compared to models with colour singlet and colour octet exchange, and their relative contributions are estimated.

10.2 L3 Data

Data from 1994-1995 at $\sqrt{s} \sim M_Z$ is used. The criteria for event selection of Mercedes type three jet events are given in the table 10.1.

E^C, $E^C_\parallel$ and $E^C_\perp$ are respectively the total energy observed in the calorimeters, the energy imbalance along the beam direction and the energy imbalance in the plane perpendicular to the beam direction. The cut on the number of calorimetric clusters, $N_{cluster}$, with energy greater than 100 MeV rejects low multiplicity events such as $\tau^-\tau^+$ final states.

Calorimeter based	Charged-track based
$N_{cluster} > 12$	$N_{track} \geq 5$, $\phi_2 < 170°$
$0.6 < E^C/\sqrt{\mathrm{s}} < 1.4$	$0.15 < E^T/\sqrt{\mathrm{s}}$
$\lvert E^C_{\parallel} \rvert / E^C < 0.4$	$\lvert E^T_{\parallel} \rvert / E^T < 0.75$
$E^C_{\perp}/E^C < 0.4$	$E^T_{\perp}/E^T < 0.75$
$N^{\mathrm{JADE}}_{jets} = 3$ ($\mathrm{y_{cut}} = 0.05$)	$N^{\mathrm{JADE}}_{jets} = 3$ ($\mathrm{y_{cut}} = 0.05$)
$\theta_{12}, \theta_{23}, \theta_{31} \ \varepsilon \ [90°, 150°]$	$\theta_{12}, \theta_{23}, \theta_{31} \ \varepsilon \ [90°, 150°]$

Table 10.1: Selection criteria for Mercedes type three jet events from hadronic Z decays.

N_{track} is the number of selected tracks. E^T, $E^T_{\parallel}$, and $E^T_{\perp}$ are, respectively, the absolute momentum sum, the longitudinal and the transverse momentum imbalances computed from the tracks. ϕ_2 is the second largest angle in the $R-\phi$ plane between two neighbouring tracks. This last requirement removes the remaining background due to back-to-back $\tau^-\tau^+$ events where both the τ's decay through 3-prong final state. Each track is required to have a span of at least 30 $R-\phi$ hits (out of 62 wires), a distance of closest approach to the interaction point of less than 20 mm in the plane perpendicular to the beam axis, and a measured transverse momentum with respect to the beam direction of greater than 100 MeV. The track polar angles are taken from matched calorimetric clusters.

10.3 Flower Plots and Angle Rescaling

In order to compare the angular distribution of particles in the event plane, defined by the two most energetic jets, the angular separation between jets need to be standardised. However, due to detector resolution the cuts on energy imbalance allow for some fluctuation of the angle between the jets.

In the left part of figure 10.1, the distribution of particles on the event plane is shown, with the radius of the rays proportional to the number of particles in that direction, as observed in selected Mercedes type three jet events, per degree interval from 1995 data sample. The clustering of the rays correspond to the 3 jets, where the angle between jets are scattered around 120°. Angles of all the particles for the event are rescaled in the right hand side of the figure 10.1, such that the angle between the jets is strictly 120°.

A more conventional flower plot is shown in the figure 10.2, with measured and rescaled angles for a sample of 3-jet events. Henceforth, in the discussion the angles are rescaled, and thus events can be superimposed to enable an event-by-event comparison of the angles between the particles.

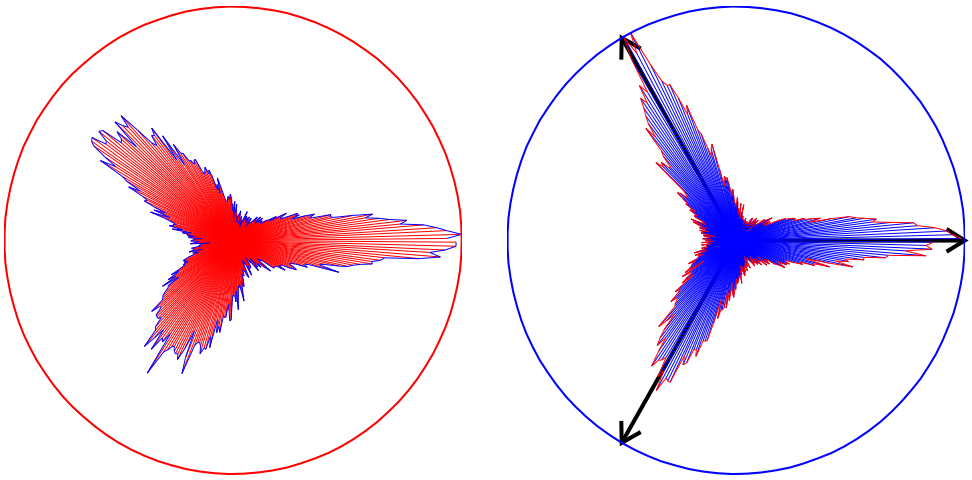

Figure 10.1: Angular distribution of particles projected for a typical three jet event.

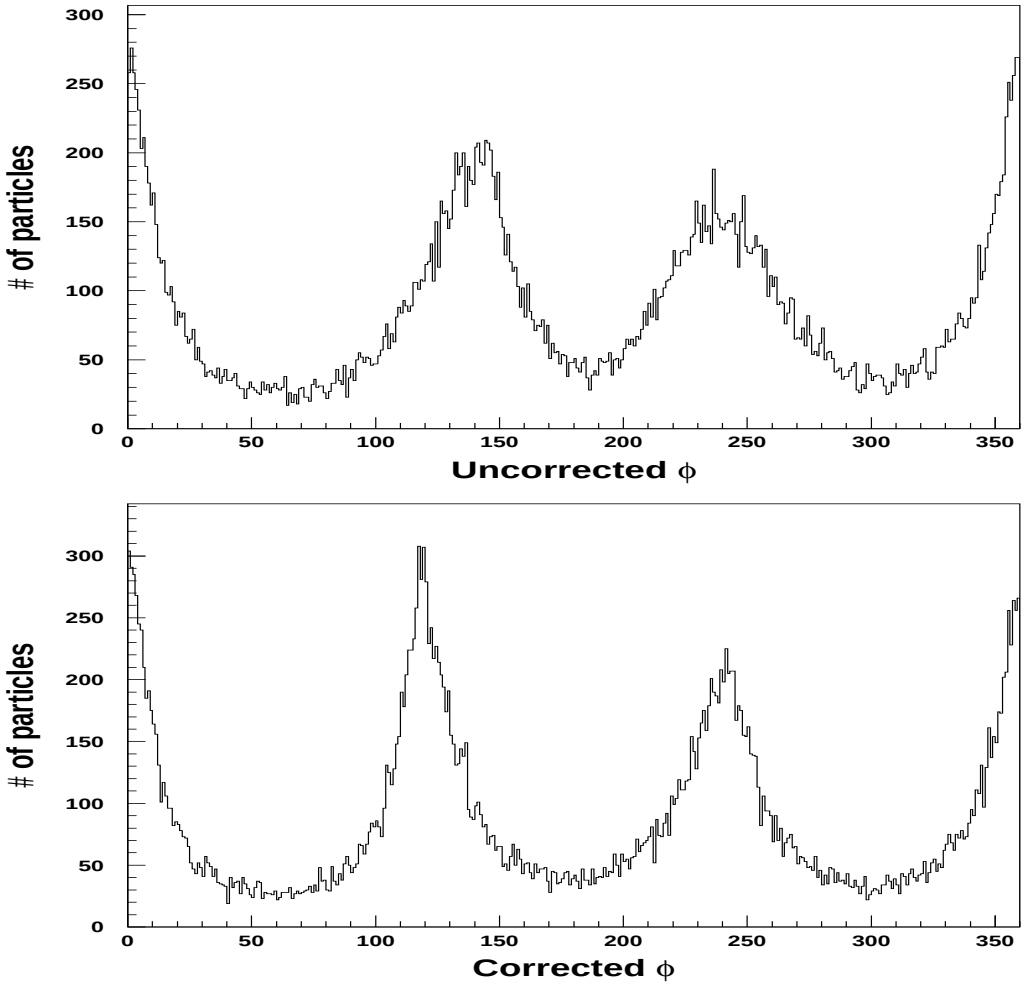

Figure 10.2: Flower plot for a sample of three jet events.

10.4 Model for Colour Singlet Exchange

A toy model based on the colour flow of $q\overline{q}\gamma$ events is used to obtain the desired colour flow in colour singlet exchange [1]. Events of type $q\overline{q}\gamma$ with photon mass as in gluon jet mass distribution are generated, and the photon is then replaced by a boosted two jet event, as illustrated in the figure 10.3. In terms of string fragmentation, coloured strings are thus confined to the $q\overline{q}$ gap, and leads to increased the hadronic activity in this gap and suppressed in the remaining ones. The different hadronisation options studied are given in the table 10.2.

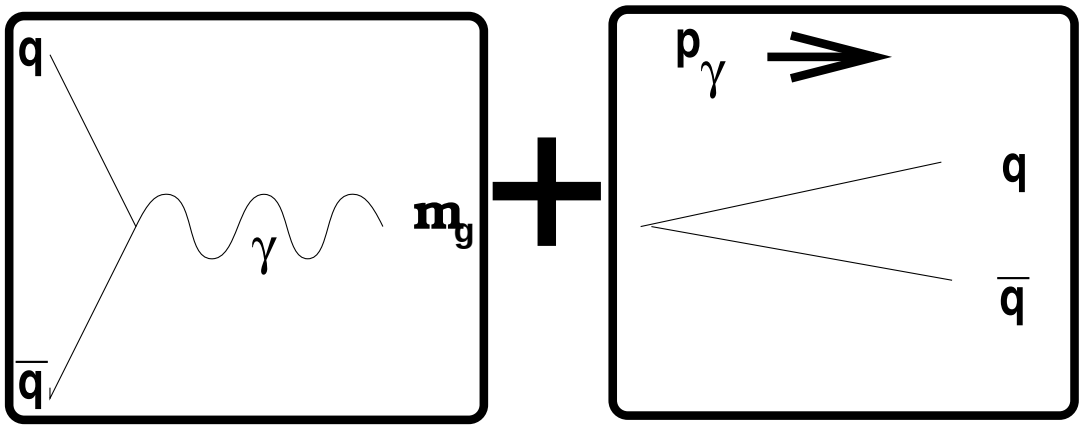

Figure 10.3: Model for colour singlet exchange.

OPTION	Nature of Fragmentation
0	$q\overline{q}$ generated in gluon rest frame, boosted back to the overall CMS, then usual parton shower.
1	The gluon is decayed as though it were a J/ψ. (with its own mass)
2	The gluon is fragmented as a single jet.
3	The gluon is decayed as though it were an η_c.

Table 10.2: Fragmentation options for colour singlet exchange.

	CSE 0	CSE 1	CSE 2	CSE 3	JETSET
Total	54.2	58.3	54.9	58.3	56.8
$q\overline{q}$ GAP (15° cone)	7.2	7.6	7.4	7.6	6.2
$q\overline{q}$ GAP (20° cone)	5.7	6.0	5.9	6.0	4.7

Table 10.3: Average number of particles generated for different models.

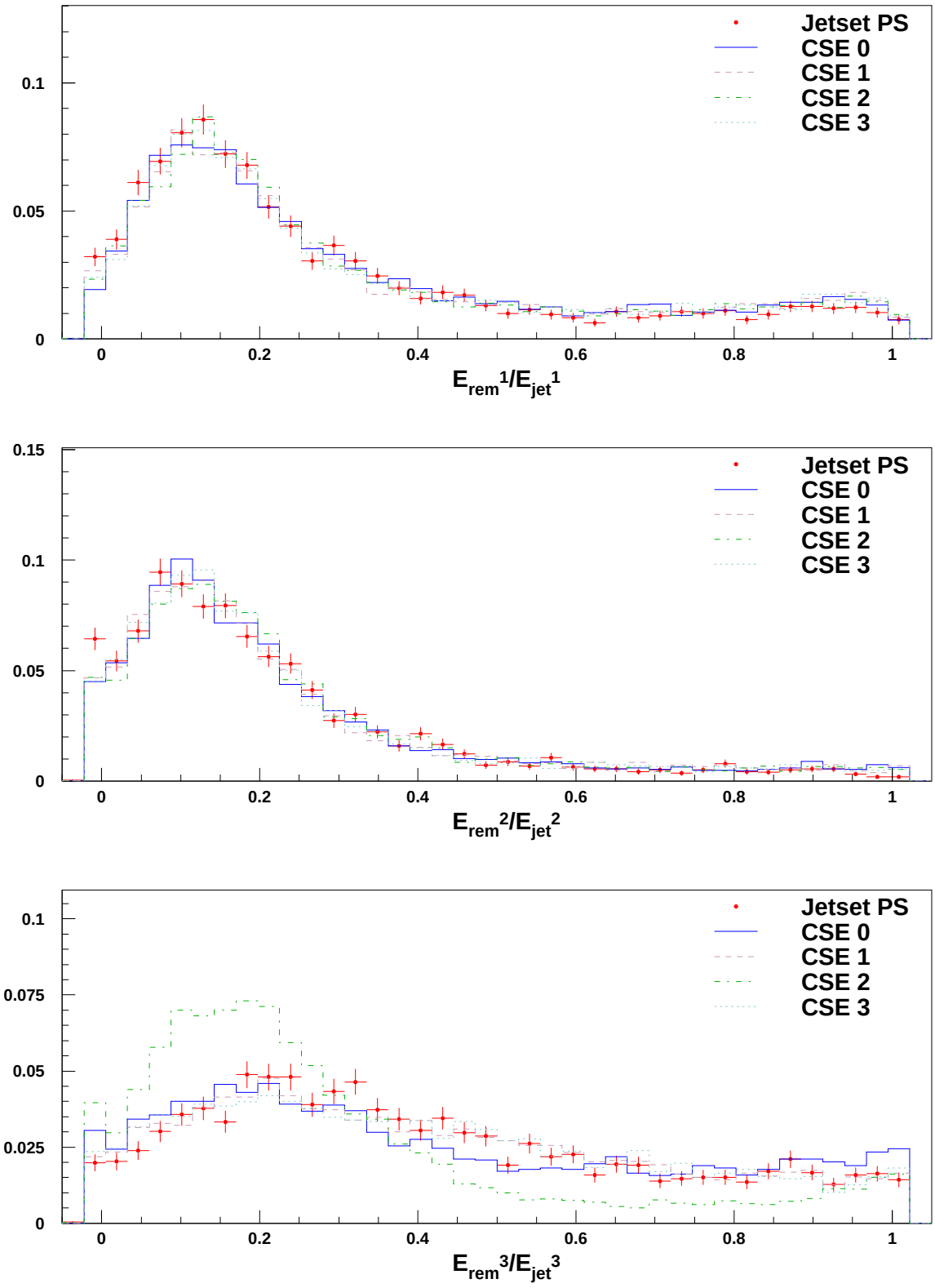

Figure 10.4: Comparison for E_{rem} of the different models.

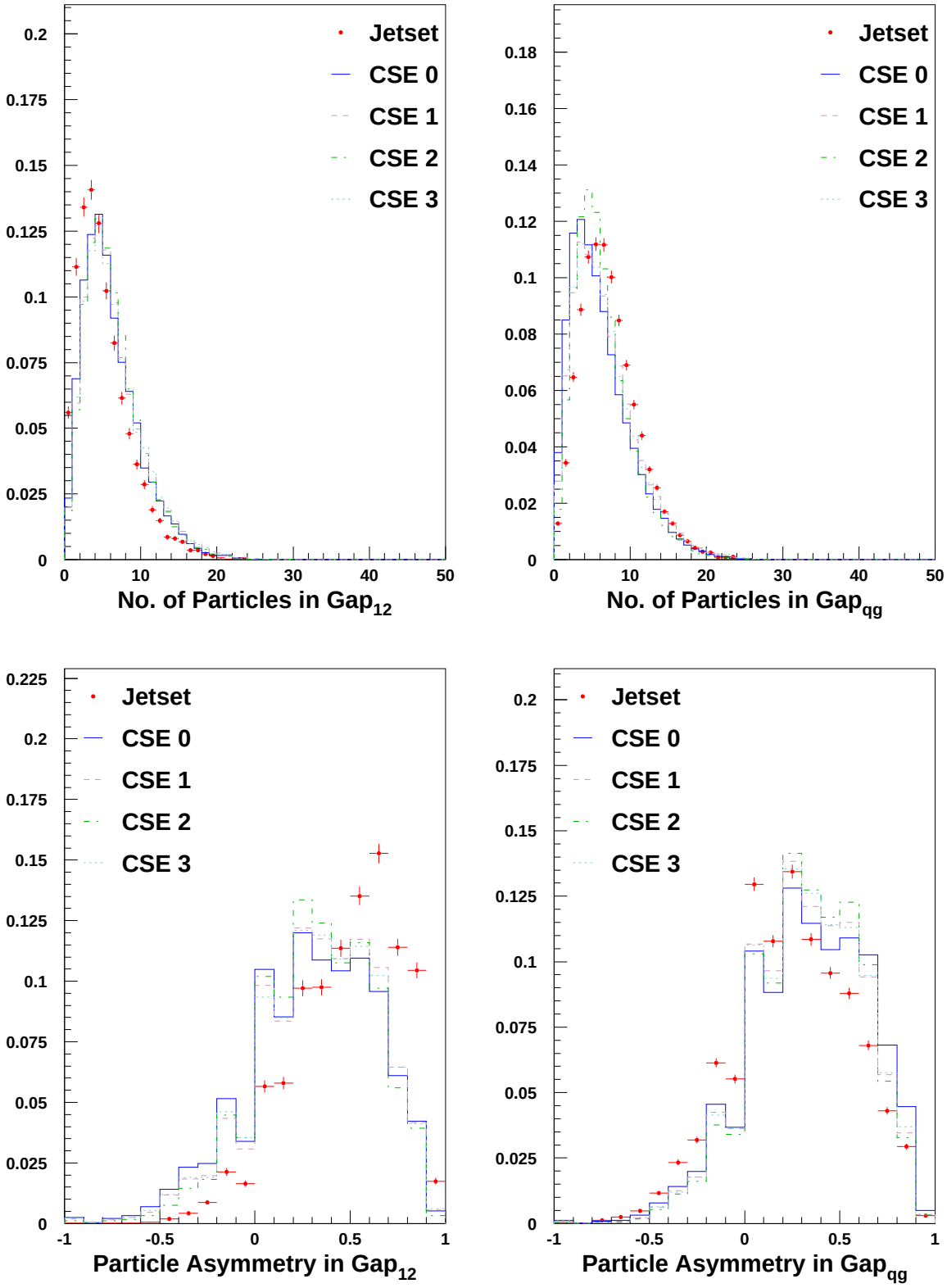

Figure 10.5: Comparison for number of particles and asymmetries in the gaps of the different models.

The total number of particles obtained from these models (labelled as CSE0, CSE1, CSE2, CSE3) are compared to that from the standard hadronic Monte Carlo generator JETSET [2] in the table 10.3. Also the number of particles in the $q\overline{q}$ gap is compared for two definitions of the cone angle around the Mercedes jets.

With jets ordered to have primary quarks in the two most energetic jets, generator level prediction for the fraction of the jet energy remaining outside a 15° cone, are shown in figure 10.4 for the different models. The colour singlet option 2 (fragmented as single jet) gives maximum difference from Jetset. The figure 10.5 compares predictions for particles and particle asymmetries, which are seen to be sensitive to differences in modelling the colour flow between gaps. The histograms for the gaps 23 and 31 are added to gain in statistics and are labelled as gap_{qg}.

The option 0 is taken to be default for colour singlet modelling and the extreme option 2 is taken for systmatic studies for further comparison with data. These options are then passed through the L3 detector simulation [3].

10.5 Clusters in L3 Detector

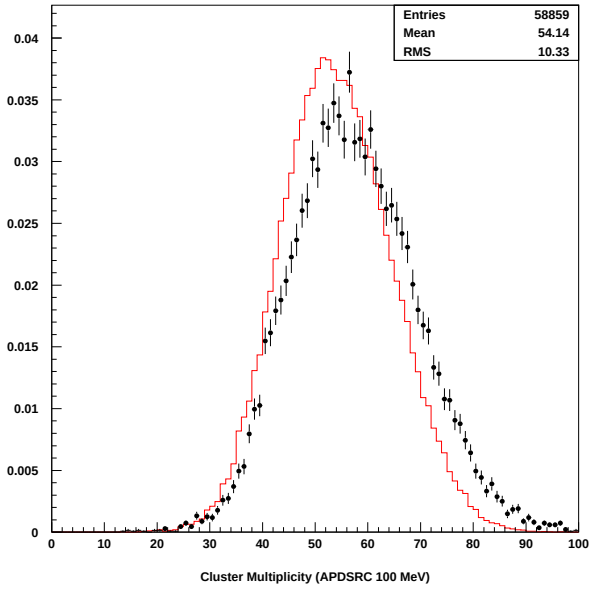

Figure 10.6: Distribution of cluster multiplicity with 100 MeV threshold.

Figure 10.6 shows the distribution of clusters with 100 MeV threshold for hadronic events for data and JETSET Monte Carlo passed through detector simulation. The data points are shown with error bars and the expectation in solid lines. This necessitates a closer look at the clusters and redefinition of them, in order to make a detailed analysis of the particle distribution of particles in the gaps of Mercedes type three jet events.

Two options have been tried for obtaining a better description between data and Monte Carlo:

- Special treatment for noise in HCAL :
  (100 MeV in ECAL with a minimum of 2 crystals hit)
  OR (100 MeV in ECAL and 900 MeV in HCAL)
  OR (1800 MeV in HCAL alone) ;

- look at charged particles only with a minimum transverse momentum of 100 MeV, DCA less than 20 mm, and hits and span of at least 20 wires in the TEC.

A comparison of the number of clusters for the different types of clusters are given in the table 10.4. The distributions for track and cluster multiplicities are shown in the figure 10.7. These two options studied for all further analyses.

Selection	Data	JETSET
Standard cluster	56.96	53.64
Special cluster	39.97	39.00
Track	23.44	23.41

Table 10.4: Number of clusters for different options compared to 1995 data and JETSET Monte Carlo.

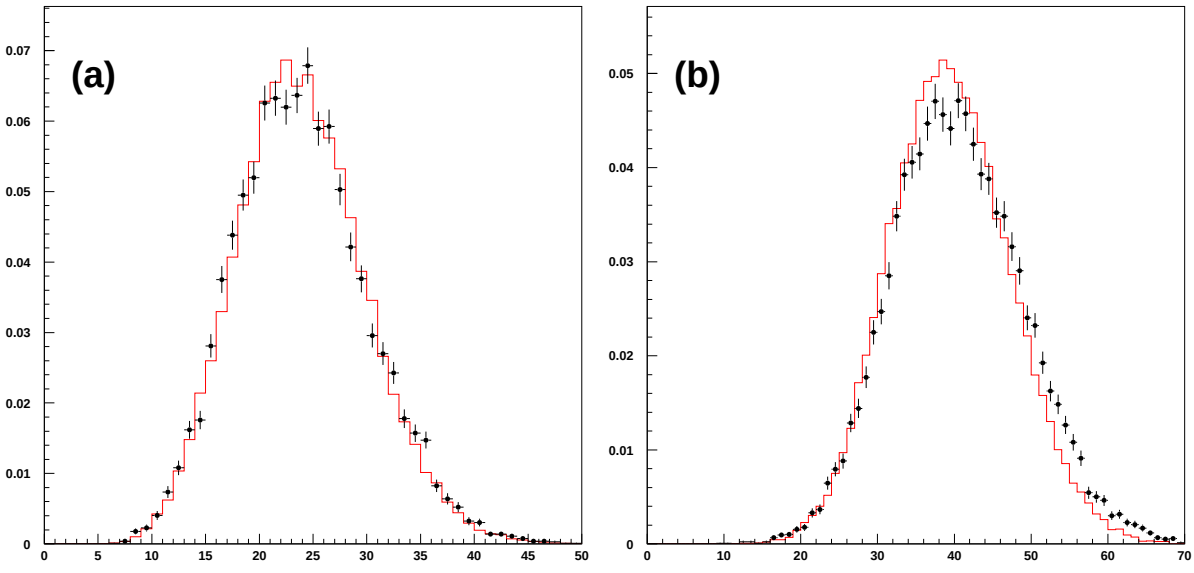

Figure 10.7: Distributions of (a) charged particle multiplicity and (b) cluster multiplicity with special selection criteria.

10.6 Gluon Jet Identification

In order to look at difference in gaps between ($q\overline{q}$) jets and other jets, the identification of gluon jet is necessary.

As one cannot use fragmentation properties to distinguish between quark jets and gluon/CS jets, jets tagged as b-jets are identified as quark jets.

For limited statistics CSE Monte Carlo, one uses the generator level criteria of associating the primary quarks direction with two jets, and taking the remaining jet is from CSE.

10.6.1 B-tagging

As the first step, the interaction vertex (V) is estimated by iteratively fitting all the good tracks measured in the detector over events recorded using simillar detector conditions. Criteria for good tracks for this measurement is: Span > 12, # of Hits > 10, $p_\perp > 150$ MeV, $|\ DCA_{r\phi}\ | < 10$ mm and $|\ DCA_{r\phi}\ | < 5(\sigma^2_{DCA_{r\phi}} \oplus \sigma^2_V)$, $|\ DCA_{sz}\ | < 100$ mm, where Monte Carlo studies have provided the following results:

	RMS in DCA along		
	x-axis (μm)	y-axis (μm)	z-axis (μm)
Non $b\bar{b}$ events	51.0	10.0	118.0
$b\bar{b}$ events	81.0	11.0	154.0

The decay lengths with respect to jet-direction: $L_{r\phi}$ and L_{sz}, in the planes $r\phi$ and sz respectively, are defined as in the figure 10.8.

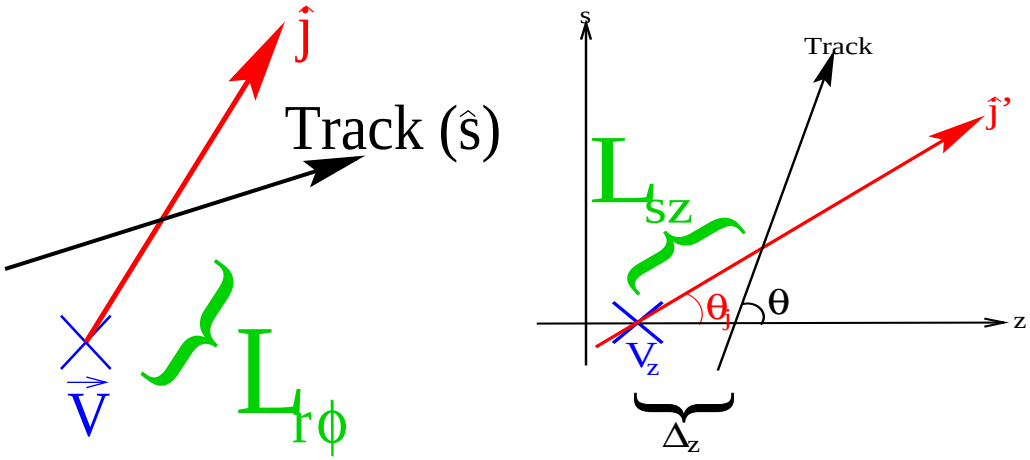

Figure 10.8: Decay lengths with respect to jet direction in the r-ϕ and s-z planes.

Lower resolution and larger pattern recognition ambiguities of measurements in the sz plane are complemented by measurements from the SMD. The measurements in the two

planes are combined by defining a weighted decay length (L):

$$\mathrm{L} = \frac{\mathrm{L}_{r\phi}/\sigma^2_{\mathrm{L}_{r\phi}} + \mathrm{L}_{sz}/\sigma^2_{\mathrm{L}_{sz}} - \frac{(\mathrm{L}_{r\phi}+\mathrm{L}_{sz})c_{\phi z}}{\sigma^2_{\mathrm{L}_{r\phi}}\sigma^2_{\mathrm{L}_{sz}}}}{1/\sigma^2_{\mathrm{L}_{r\phi}} + 1/\sigma^2_{\mathrm{L}_{sz}} - \frac{2c_{\phi z}}{\sigma^2_{\mathrm{L}_{r\phi}}\sigma^2_{\mathrm{L}_{sz}}}}$$

The correlations among the measurements of (x, y, z) coordinates of the primary vertex contribute to the correlation coefficient, $c_{\phi z}$. In addition, a symmetric error of 15 mrad comes from the uncertainty in the jet direction and this is common to $\mathrm{L}_{r\phi}$ and L_{sz}. All these correlations typically contributes only $\sim 1\%$ to the error of L, the major contribution coming from propagation of the errors from tracking, vertex and jet direction errors into the errors on $\mathrm{L}_{r\phi}$, L_{sz}.

The decay length significance $\mathrm{S} = \mathrm{L}/\sigma_{\mathrm{L}}$ has non-zero values because of: statistical fluctuations and also from the presence of a displaced secondary vertex, arising from boosted b-hadron with decay length ~ 3 mm.

From this decay length significance, a probability, P(S), that a track is consistent with zero lifetime hypothesis is constructed such that it is flat for zero lifetime, and peaks at zero for finite lifetime. The weighted discriminant for n tracks in a jet is defined as $B^{\mathrm{w}}_n = -\log(\prod_{j=1}^{n} P_n)$. Distributions of the weighted discriminant and variation of efficiency and purity with the discriminant are shown in the figure 10.9 [4].

10.6.2 Gluon Tagging

A combination of energy ordering criteria and anti b-tagging of jets is used to improve the gluon purity. Jets from primary quarks are tagged at the generator level as quark jets and the remaining jet as the gluon jet.

From generator level studies with JETSET PS, for events with three jets (labelled in decreasing order of energy) with $\mathrm{y_{cut}} = 0.05$ (JADE), the following probabilities have been estimated:

Quark in Jet 1 = 98 %
Quark in Jet 2 = 93 %
Gluon in Jet 3 = 88 %

The purity of the third jet decreases when one takes care of detector effects. If one carries out detector reconstruction of Monte Carlo events from JETSET PS program according to the run condition of 1995 data taking period, the probabilities of gluon in the least energetic jet in three jet samples are 85.4% and 67.7% when jets are reconstructed from clusters and tracks respectively. For Mercedes criteria, these probabilities reduce to 64.8% and 49.2% respectively. The probability is smaller for jets made from tracks alone, because of TEC inefficiency and smaller acceptance of the TEC.

By demanding b-tag discriminant (B) for jets and for the event to be:

$$\mathrm{B}_{event} > 2;\ \mathrm{B}_{Jet1},\ \mathrm{B}_{Jet2} > 2,\ \mathrm{B}_{Jet3} < 2.$$

the probabilities that the third jet is a gluon jet is estimated to be 88.0% and 78.9% respectively for clusters and tracks in Mercedes type three jet events.

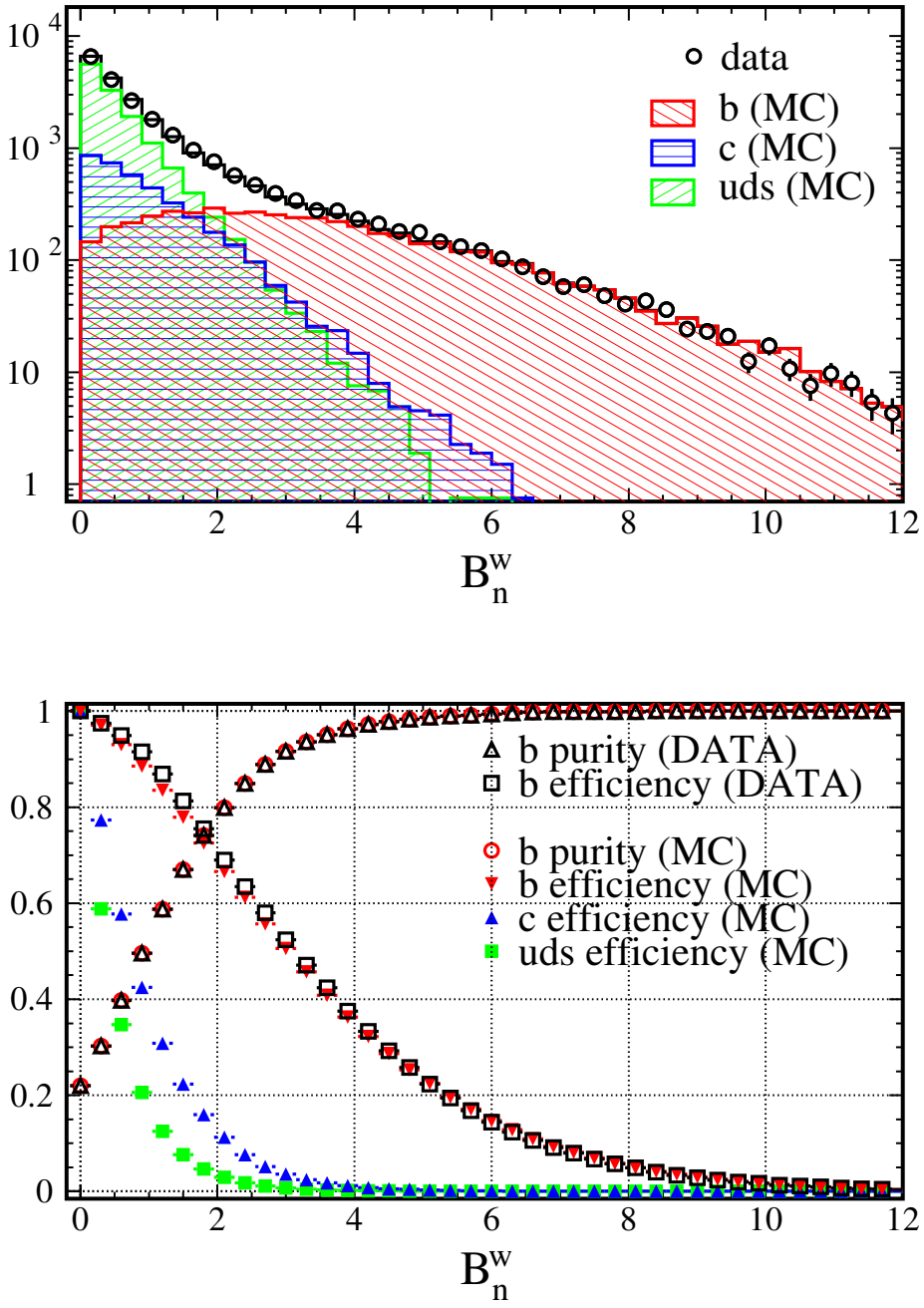

Figure 10.9: Distribution of weighted discriminant and variation of efficiency and purity with the discriminant.

10.7 Comparison of Rates

L3 data, analysed from hadronic Z decays, correspond to a luminosity of 40.4 pb^{-1} from 1994 (bcd) and 13.0 pb^{-1} from 1995 data taking periods. Owing to inefficiency of SMD and poorer agreement between data and JETSET for the 1994a period, the corresponding events have not been included in the study.

	1994		1995	
	Clusters	Tracks	Clusters	Tracks
Data	1,195,383	1,051,027	387,560	338,433
JETSET	3,573,885	3,157,768	1,558,313	1,355,976
CSE0	91,418	85,345	29203	27065
CSE2	89,640	83,400	35310	32607

Table 10.5: Event statistics for 1994-1995 periods.

	3-jet		Mercedes	
	Clusters	Tracks	Clusters	Tracks
Data-1994	0.223	0.265	0.036	0.032
MC-1994	0.228	0.264	0.038	0.032
Data-1994	0.231	0.277	0.035	0.030
MC-1994	0.246	0.264	0.038	0.032

Table 10.6: Fraction of three jet and Mercedes type events for 1994-1995 period.

The number of hadronic events for 1994 (1995) period is given in table 10.5. Monte Carlo expectations are determined from event samples where the generated events are reconstructed with corresponding real detector condition for each of the data raking periods. The fraction of three jet events and Mercedes type events are compared with data and Monte Carlo (JETSET) and listed in the table 10.6. Using the b-tag information, the fraction of events with primary quarks in the first two jets are estimated to be 0.00059 (0.000432) and 0.00056 (0.00042) respectively for jets reconstructed from clusters and tracks corresponding to 1994 (1995) data taking periods from real detector simulation of JETSET, which are consistent within statictical fluctuations.

In the following, the distributions from 1994 and 1995 data are added. Also the gaps 23 and 31 are added and referred to as $\mathrm{gap_{qg}}$.

10.7.1 Energy Ordering

Figures 10.10 and 10.11 show the distributions of the smallest angle of a particle from the bisector in the quark-gluon gap and the corresponding asymmetry distributions, where the jets are reconstructed from the clusters and the core of the jet defined by a 20° or a 15° cone is left out in defining the gap angle. The jets are ordered with decreasing energy and the least energetic jet is identified as the gluon jet. As one can see from the figures that JETSET PS model is in agreement with the data and the different colour singlet models differ from JETSET and also from the data. The change in definition of the jet core does not make any appreciable difference in the comparison of data with various Monte Carlo models. Figure 10.12 shows the same distributions with the jets reconstructed from tracks and using a jet core definition with a 20° cone. Again the data are in better agreement

with JETSET PS model predictions.

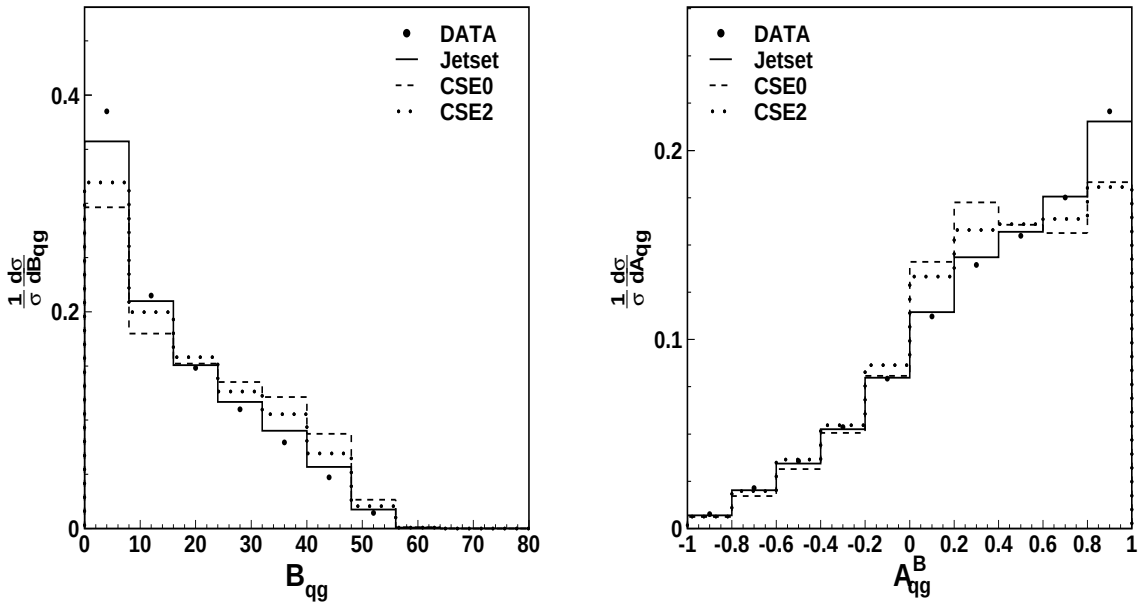

Figure 10.10: Angles from the bisector and corresponding asymmetries for 20° cone with energy ordered jets with clusters.

The definition of gap angle as the largest angular separation in the appropriate inter-jet region is also studied. Figure 10.13 shows this distribution for the inter-jet region between jets 1 and 2 (the two quark jets) and the corresponding asymmetry plot. Again the jets are obtained with clusters and central 20° cone around the jet axis are left out in these distributions. The data favour JETSET PS model in preference to the colour singlet models.

The analyses using clusters and tracks select 56419 and 42432 events in the data respectively. All these angular and asymmetry distributions are fitted to a combination of colour octet exchange (as obtained from JETSET) and a colour singlet contribution. All the fits give fraction of events due to colour singlet exchange consistent with zero. The asymmetry distributions give good fits with acceptable χ^2/d.o.f. The fit results only from the asymmetry distributions are shown in the following tables. The results for fit for relative fraction of colour singlet contribution to the data are given in tables 10.7 and 10.8. Colour singlet exchanges can be ruled out up to a level of 0.3 % from these asymmetry distributions.

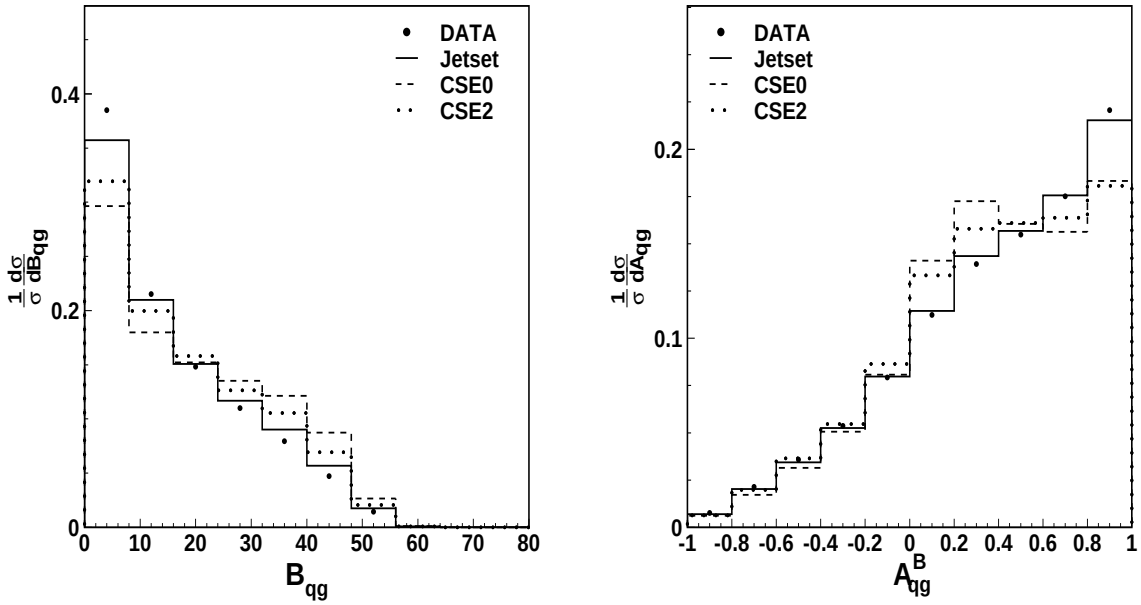

Figure 10.11: Angles from the bisector and corresponding asymmetries for 15° cone with energy ordered jets with clusters.

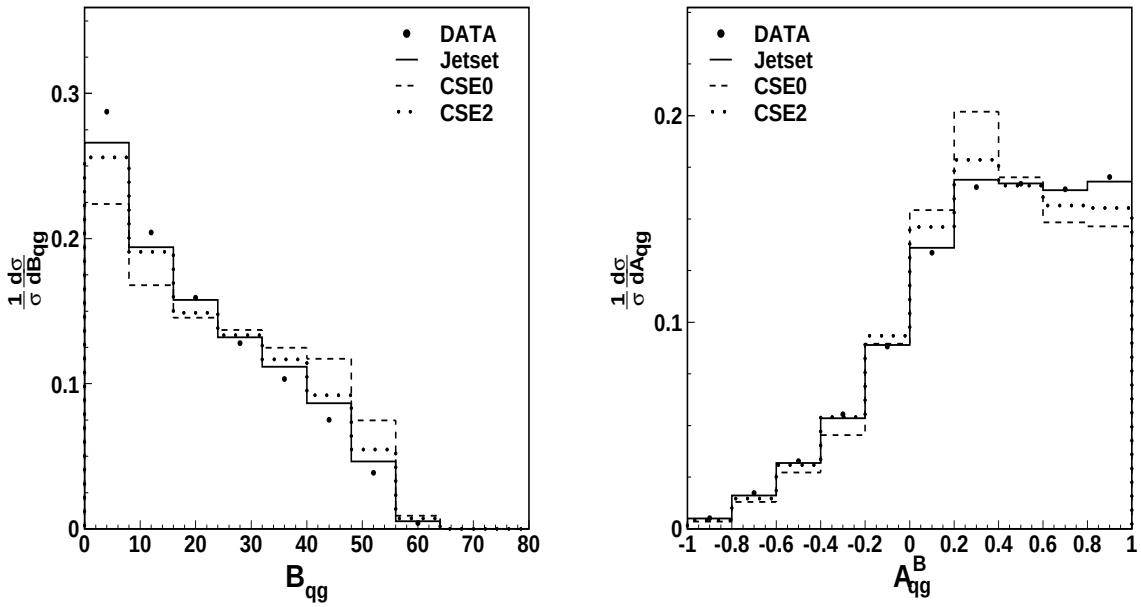

Figure 10.12: Angles from the bisector and corresponding asymmetries for 20° cone with energy ordered jets with tracks.

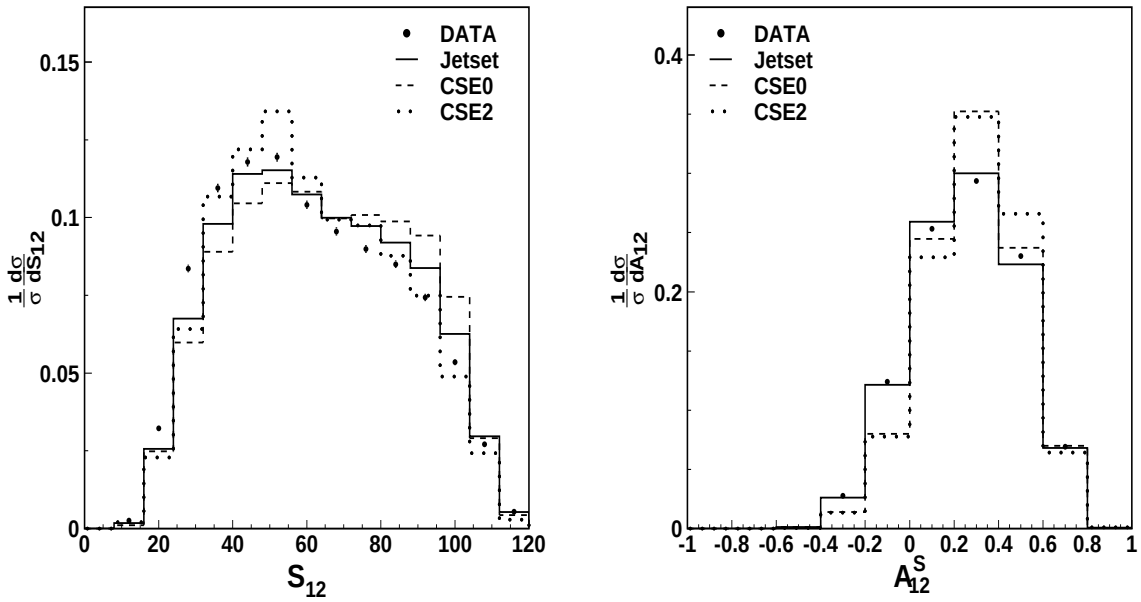

Figure 10.13: Maximum separation gap angle and corresponding asymmetries for 20° cone with energy ordered jets with clusters.

Variable used	95% CL Upper Bound	
	CSE0 Model	CSE2 Model
A^B_{12}	0.005	0.011
A^B_{qg}	0.003	0.005
A^S_{12}	0.009	0.020
A^S_{qg}	0.038	0.042

Table 10.7: 95% CL upper bound on the fraction of events due to colour singlet exchange from studies of asymmetry distributions with energy ordered jets using clusters.

Variable used	95% CL Upper Bound	
	CSE0 Model	CSE2 Model
A^B_{12}	0.009	0.046
A^B_{qg}	0.006	0.015
A^S_{12}	0.160	0.188
A^S_{qg}	0.085	0.116

Table 10.8: 95% CL upper bound on the fraction of events due to colour singlet exchange from studies of asymmetry distributions with energy ordered jets using tracks.

10.7.2 Gluon Tagged Events

A similar analysis is carried out with events where the gluon jet can be identified with b-tag results. This analysis provides a much purer gluon jet content. Figures 10.14 and 10.15 show the distributions of the smallest angle of a particle from the bisector in the quark-gluon gap and the corresponding asymmetry distributions, where the jets are reconstructed from the clusters and the core of the jet defined by a 20° or a 15° cone is left out in defining the gap angle. Figure 10.16 shows the same distributions with the jets reconstructed from tracks and using a jet core definition with a 20° cone. Figure 10.13 shows the distribution of the largest angular separation in the inter-jet region between the two quark jets and the corresponding asymmetry plot. The data are better described by JETSET PS model and the different colour singlet models differ significantly from the data.

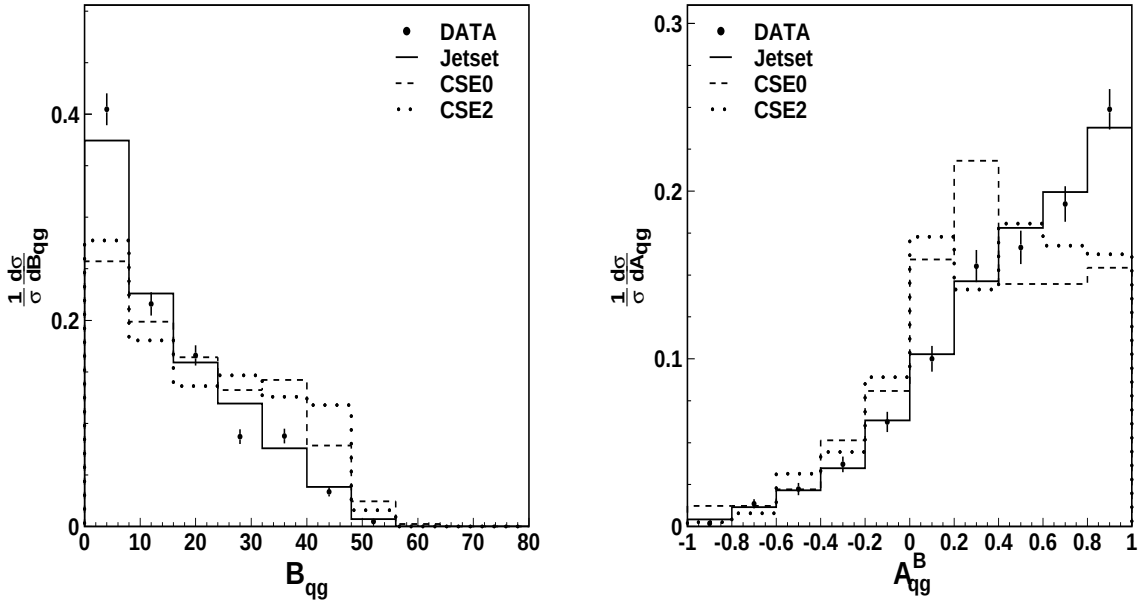

Figure 10.14: Angles from the bisector and corresponding asymmetries for 20° cone with gluon tagged jets with clusters.

The number of events in the data are 850 and 661 respectively for the cluster based and track based analyses. The angular distributions and asymmetries to a combination of colour octet and colour singlet exchanges are also fitted. The fits are consistent with no colour singlet exchange and 95% CL upper limit of fraction of events due to colour singlet exchange are summarised in tables 10.9 and 10.10.

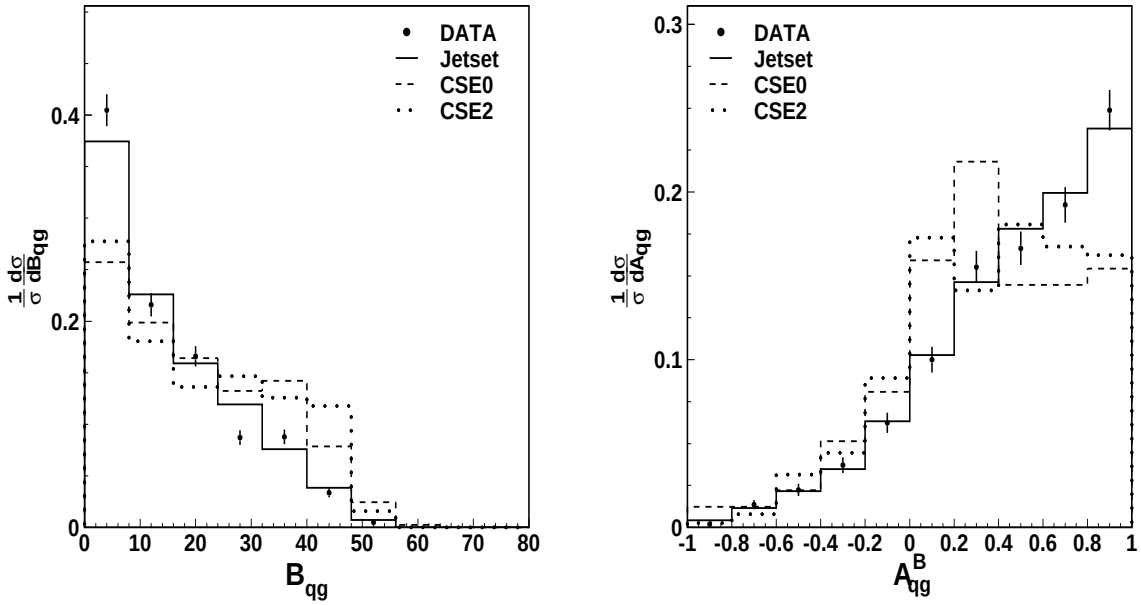

Figure 10.15: Angles from the bisector and corresponding asymmetries for 15° cone with gluon tagged jets with clusters.

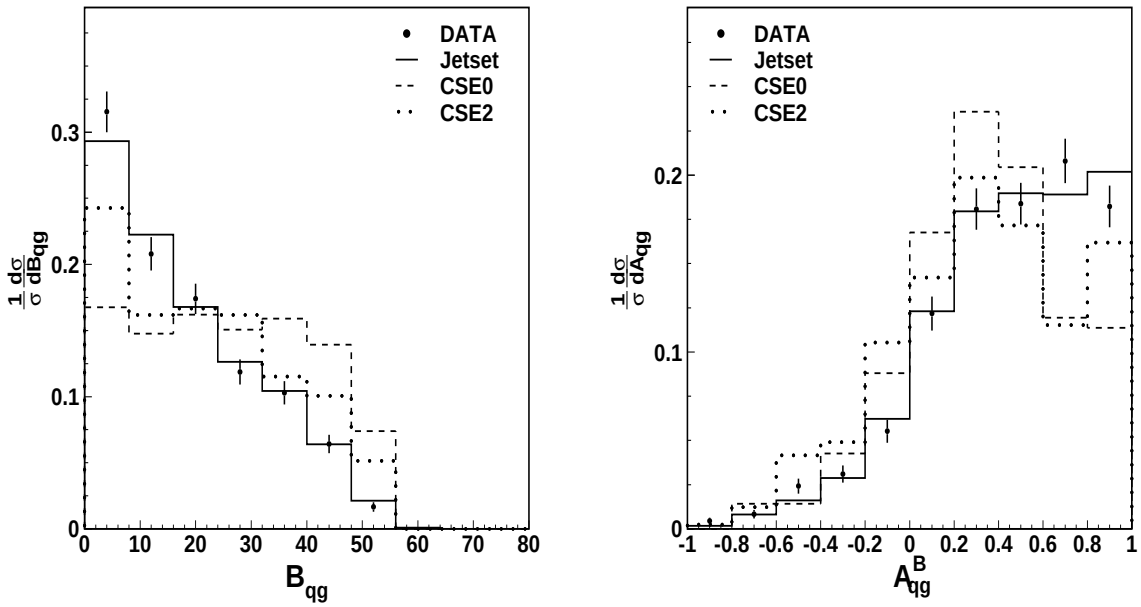

Figure 10.16: Angles from the bisector and corresponding asymmetries for 20° cone with gluon tagged jets with tracks.

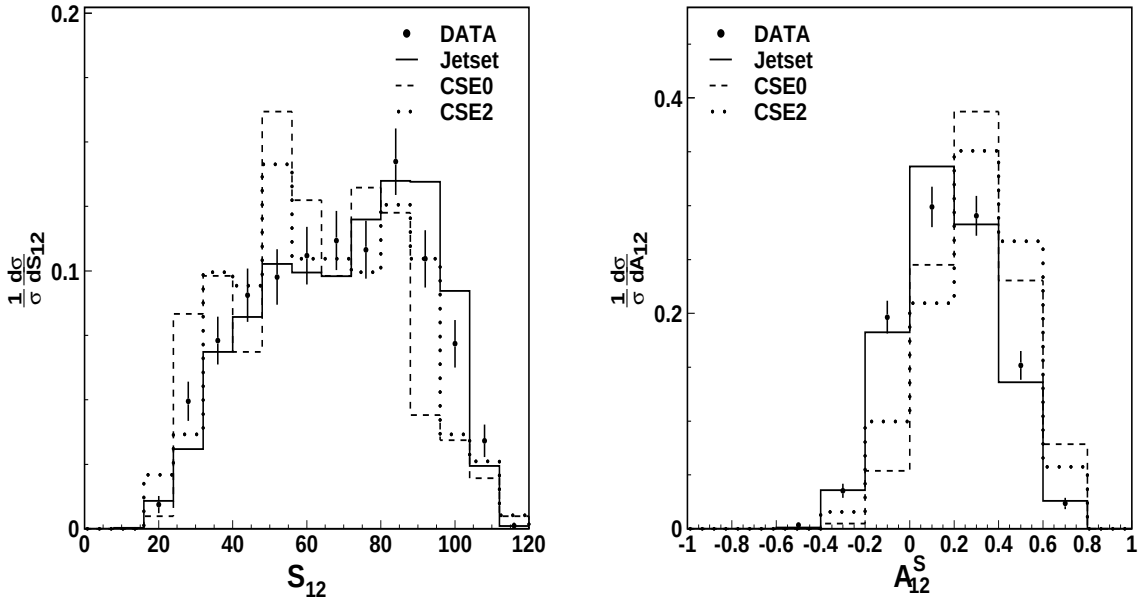

Figure 10.17: Maximum separation gap angle and corresponding asymmetries for 20° cone with gluon tagged jets with clusters.

Variable used	95% CL Upper Bound	
	CSE0 Model	CSE2 Model
A^B_{12}	0.162	0.206
A^B_{qg}	0.168	0.088
A^S_{12}	0.142	0.211
A^S_{qg}	0.081	0.197

Table 10.9: 95% CL upper bound on the fraction of events due to colour singlet exchange from studies of asymmetry distributions of jets reconstructed from clusters and identified using b-tag information.

Variable used	95% CL Upper Bound	
	CSE0 Model	CSE2 Model
A^B_{12}	0.259	0.274
A^B_{qg}	0.137	0.188
A^S_{12}	0.217	0.246
A^S_{qg}	0.128	0.208

Table 10.10: 95% CL upper bound on the fraction of events due to colour singlet exchange from studies of asymmetry distributions of jets reconstructed from tracks and identified using b-tag information.

References

[1] John Field, private communication.
Wesley Metzger, private communication.
Peter Molnar, private communication.
Micheal Unger, private communication.

[2] JETSET 7.4 Monte Carlo Program:
T. Sjöstrand, Comp. Phys. Comm. **82** (1994) 74.

[3] The L3 detector simulation is based on GEANT Version 3.15.
See R. Brun *et al.*, "GEANT 3", CERN DD/EE/84-1 (Revised), September 1987.
The GHEISHA program (H. Fesefeldt, RWTH Aachen Report PITHA 85/02 (1985))
is used to simulate hadronic interactions.

[4] Aaron Dominguez, private communication.
Ian Fisk, private communication.
Chris Tully, private communication.

Chapter 11

Summary

Event shape variables have been studied over a large energy range: from 30 to 189 GeV from the same experiment. This has resulted measurements with correlated systematic errors among the different energy points. Good agreement is seen between data and QCD models with coherent parton shower and with parameters tuned using data at $\sqrt{s} = M_Z$. Jet rates have been observed to follow the expected QCD energy evolution. Using $\mathcal{O}({\alpha_s}^2)$+NLLA calculations, the strong coupling constant has been measured:

$$\boxed{\alpha_s(M_Z) = 0.1215 \pm 0.0012 \text{ (exp)} \pm 0.0061 \text{ (theo)}}$$

From fit to the slope of the running of α_s, active number of flavours is measured to be:

$$\boxed{n_f = 5.0 \pm 1.3 \text{ (exp)} \pm 2.0 \text{ (theo)}}$$

From Power law parametrisation, the first moments of five event shapes have been fitted to a power law parametrisation. The universality of the parametrisation has been tested within 10% accuracy. The non-perturbative parameter, α_0, accounting for contributions to the event shape below an infrared matching scale of 2 GeV has been estimated as:

$$\boxed{\alpha_0(2GeV) = 0.537 \pm 0.069 \text{ (exp)} \pm 0.079 \text{ (theo)}}$$

Power law correction studies have been extended to the second moments where a non-negligible contribution of $\mathcal{O}(\frac{1}{Q^2})$ term is found for the event shape variables $1 - T$ and C.

Evidence of destructive interference from soft gluon emission between jets has been observed in charged particle inclusive momentum spectra.

Colour singlet exchange in e^-e^+ annihilation has been studied using asymmetries in the gaps of Mercedes type three jet events from hadronic Z decays.

Publications of Swagato Banerjee

[1] L3-note #1978, July 1996.
Tuning of QCD model parameters using the LEP data of Hadronic Z decays
– Sunanda Banerjee and Swagato Banerjee.

[2] L3-note #2059, March 1997.
QCD Results at $\sqrt{s}$ = 161 GeVand 172 GeV
– Sunanda Banerjee, Swagato Banerjee, Dominique Duchesneau, Subir Sarkar.

[3] L3-note #2069, April 1997.
Tuning of Parameters for HERWIG 5.9 and JETSET 7.4 (without B.E. Correlation)
– Sunanda Banerjee and Swagato Banerjee.

[4] L3-Note #2176, Oct 1997.
Charged Particle Momentum Spectra at $\sqrt{s}$= 130 - 172 GeV
– Sunanda Banerjee, Swagato Banerjee, Dominique Duchesneau.

[5] L3-Note #2177, Oct 1997.
QCD Results from L3 at $\sqrt{s}$ = 130 - 172 GeV(LEP QCD Working Group Report)
– Sunanda Banerjee, Swagato Banerjee, Dominique Duchesneau.

[6] L3-Note #2228, March 1998.
QCD Results at $\sqrt{s}$ = 183 GeV
– Sunanda Banerjee, Swagato Banerjee, Dominique Duchesneau.

[7] L3-Note #2245, March 1998.
Progress on the Combination of QCD observables at LEP1.5 and LEP2.
– The LEP QCD Working Group.

[8] L3-Note #2247 April 1998.
Tuning of Parameters for HERWIG 5.9
– Sunanda Banerjee and Swagato Banerjee.

[9] L3-Note #2364, March 1999.
QCD Results at $\sqrt{s}$ = 189 GeV
Sunanda Banerjee, Swagato Banerjee, Dominique Duchesneau.

[10] L3-Note #2414, June 1999.
Hadronic Event Structures from 30 to 189 GeVand power law corrections.
– Sunanda Banerjee, Swagato Banerjee, Dominique Duchesneau, Subir Sarkar.

[11] L3-Note #2422d, June 1999.
"Rapidity gap events in 3jets", talk presented at L3 Annual General Meeting 1999, Lyon, France.
– Swagato Banerjee.

Published journals:

Co-author of 92 publications from the L3 Collaboration, since 25 April 1997. Some selected ones are:

1. L3 Collaboration, M. Acciarri *et al.*, Phys. Lett. B 404 (1997) 390-402.
   CERN preprint CERN-PPE/97-42; 25 April 1997, L3 preprint 115.
   QCD Studies and Determination of α_s in e^-e^+ collisions at $\sqrt{s} = 161$ GeVand 172 GeV.

2. L3 Collaboration, M. Acciarri *et al.*, Phys. Lett. B 444 (1998) 569-582.
   CERN preprint CERN-EP/98-148, 21 September 1998, L3 preprint 162.
   QCD Results from Studies of Hadronic Events produced in e^-e^+ Annihilations at $\sqrt{s} = 183$ GeV.